

Spring 5-10-2018

DENSITY AND VELOCITY MEASUREMENT OF ARI AND ARII USING LASER INDUCED FLUORESCENCE (LIF) IN A LARGE-SCALE HELICON PLASMA

Ralph F. Kelly
University of New Mexico

Follow this and additional works at: https://digitalrepository.unm.edu/ece_etds

 Part of the [Other Electrical and Computer Engineering Commons](#)

Recommended Citation

Kelly, Ralph F.. "DENSITY AND VELOCITY MEASUREMENT OF ARI AND ARII USING LASER INDUCED FLUORESCENCE (LIF) IN A LARGE-SCALE HELICON PLASMA." (2018). https://digitalrepository.unm.edu/ece_etds/409

This Dissertation is brought to you for free and open access by the Engineering ETDs at UNM Digital Repository. It has been accepted for inclusion in Electrical and Computer Engineering ETDs by an authorized administrator of UNM Digital Repository. For more information, please contact disc@unm.edu.

Ralph F. Kelly

Candidate

Electrical and Computer Engineering

Department

This dissertation is approved, and it is acceptable in quality and form for publication:

Approved by the Dissertation Committee:

Mark Gilmore, Chairperson

Edl Schamiloglu

Gary Cooper

Todd Pedersen

**DENSITY AND VELOCITY MEASUREMENT OF ARI AND ARII USING
LASER INDUCED FLUORESCENCE (LIF) IN A LARGE-SCALE HELICON
PLASMA**

By

RALPH F. KELLY

B.S., Physics, University of Florida (UF), 2003
M.S., Physics, Auburn University (AU), 2006

DISSERTATION

Submitted in Partial Fulfilment of the
Requirements for the Degree of

**Doctor of Philosophy
Engineering**

The University of New Mexico
Albuquerque, New Mexico

May 2018

Acknowledgements

I would like to thank my dissertation committee members for their help and support: Mark Gilmore, Edl Schamiloglu, Gary Cooper, and Todd Pedersen. In particular, I would like to thank Mark Gilmore for acquiring the laser that allowed me to perform this research and helping me finish this dissertation. I would like to thank Gary Cooper for being willing to continue as a committee member even though he already retired. I would like to thank Todd Pedersen for being willing to be my outside expert, and for his help and assistance.

I would also like to thank Earl Scime, Amy Keese, Derek Elliott, Zachary Short, and the rest of the West Virginia University (WVU) research group for their help and assistance. Amy Keese allowed me to use the collisional-radiative (CR) model she used. Earl Scime was willing to have me go to WVU to learn about their system and about iodine cells. It was an educational trip.

I would like to thank Dustin Fisher who helped with theory and computer code. This research would have been much harder without his help.

I would like to thank Tiffany Desjardins for her help, knowledge and support. She was always willing to answer questions and provide information.

I would like to thank Yue Zhang for his help, and friendship.

I would also like to thank Maren Hatch and Robert Dwyer for their help with data acquisition and equipment set-up.

I would like to thank the Senior Design Group (Nicholas Boynton, Luan Nguyen, Jorge Romero, and Andrew Scruggs) who got this project started for me.

Finally, I would like to thank my fiancée, Kathy Wolf, for her patience and understanding while I was finishing this research. It was not easy for her as I was spending long hours in the lab writing. I love you, Kathy!

**DENSITY AND VELOCITY MEASUREMENT OF ARI AND ARII USING
LASER INDUCED FLUORESCENCE (LIF) IN A LARGE-SCALE HELICON
PLASMA**

By

Ralph F. Kelly

B.S., Physics, University of Florida (UF), 2003
M.S., Physics, Auburn University (AU), 2006
Ph.D., Engineering, University of New Mexico, 2017

ABSTRACT

Helicon plasma sources are widely used in basic plasma science, as well as for materials processing. These plasmas typically operate at high gas fill pressure, and therefore have significant densities of neutral particles. However, the role of neutrals in the overall plasma dynamics, such as ion flows, remains poorly understood. There are at least two possible mechanisms for neutrals to influence ion flows. One is an $\mathbf{F} \times \mathbf{B}$ drift, where \mathbf{F} is the force exerted on ions by neutrals through collisions. The second is through Pedersen conductivity which is dependent on the ratio of the ion cyclotron frequency, ω_{ci} , to the ion-neutral collision frequency, ν_{in} .

To investigate this interaction, a laser induced fluorescence (LIF) system has been developed for the Helicon-Cathode (HelCat) linear helicon plasma device at the University of New Mexico (UNM). The LIF system is based on a > 250 mW, tunable diode laser with a tuning range between 684 and 699 nm. One neutral and one ion metastable energy state can be excited. For neutral argon (ArI) LIF, the laser pumps the metastable ($^2P^0_{3/2}$) $4s$

$^2[3/2]_2^0$ level to the $(^2P_{1/2}^0)4p\ ^2[1/2]_1$ level using 696. 7352 nm light. The fluorescence radiation from decay to the $(^2P_{1/2}^0)4s\ ^2[1/2]_0^0$ level at 772. 6333 nm is observed. Two ion transitions are also explored, one of which yielded usable results.

The system design, measurements, and analysis for axial, radial and azimuthal velocity of ArI is presented. The neutral flow is found to be axially away from the source, radially outward from the center of the machine, and azimuthally in the electron diamagnetic direction. It is less than 50 m/s in all directions. The neutral temperature is ~ 0.05 eV. A collisional-radiative (CR) model is used to estimate the neutral ground state density profile, which is used to calculate the neutral-driven $F \times B$ drift. Swept, compensated probe data are used to calculate $E \times B$ velocity, modified by the Pedersen conductivity, and diamagnetic drifts. A total drift is calculated and compared to Mach probe measurements of ion flow. Although the combined drifts fail to account for the measured ion flow, results indicate that the neutrals do influence the flow.

Table of Contents:

Table of Contents:.....	vii
List of Figures	x
List of Tables	xix
Chapter 1: Motivation and Introduction	1
1.1 Motivation	1
1.1.1 Equations of Motion in Plasma with Ion-Neutral Collisions	8
1.1.2 Pedersen Conductivity.....	12
1.2 History of LIF as a diagnostic for plasmas	15
1.3 Quantum Mechanics of Laser Induced Fluorescence (LIF).....	24
1.3.1 Notation.....	24
1.3.2 Transition Probabilities	28
1.3.3 Zeeman Splitting	32
1.3.4 Spectral Line Broadening Mechanisms	39
1.3.5 CR model.....	41
1.4 LIF Schemes.....	48
1.4.1 The 696 nm Neutral Line	50
1.4.2 The 688 nm Ion Line.....	51
1.4.3 The 686 nm Ion Line.....	52

Chapter 2: Experimental Setup and Techniques	53
2.1 The HelCat Plasma Device	53
2.2 The LIF System.....	57
2.2.1 The Laser.....	60
2.2.2 Wavemeter	61
2.2.3 Optics	61
2.2.4 DAQ Trigger Circuit.....	65
2.2.5 Iodine Cell.....	67
2.3 Neutral LIF.....	71
2.3.1 Axial Velocity Measurements.....	73
2.3.2 Radial Velocity Measurements	81
2.3.3 Azimuthal Measurements.....	86
2.4 ArII (singly-ionized argon) LIF	89
2.4.1 688 Ion Line	89
2.4.2 686 Ion Line	91
2.5 Summary of LIF Measurements.....	101
2.6 Swept Probe.....	103
2.7 Mach Probe	113
Chapter 3: Experimental Results and Analysis.....	121
3.1 Neutral Density, Temperature and Flow Measurements.....	121

3.1.1	Measurements using Axial Laser Injection.....	124
3.1.2	Measurements using Radial Laser Injection	126
3.1.3	Azimuthal Measurements.....	128
3.2	Comparison with Mach Probe Measurements	131
3.3	CR Model Fit.....	132
3.4	Calculation of Remaining Drift Velocities and Comparison to Mach Probe Flow Measurements.....	138
3.5	Ion Line (ArII) Data	146
Chapter 4: Conclusion and Future Work		148
4.1	Conclusions	148
4.2	Future Work	154
Appendix A.....		172
Appendix B.....		175

List of Figures

Figure 1.1.1. Mach probe data showing ion flow in the electron diamagnetic direction (EDD) with a fill pressure of 2.5 mTorr argon, RF power of ~1800W at 10 MHz, and the magnetic field of ~ 0.035 T [19].	6
Figure 1.1.2. Calculated ion drift velocity, ($\mathbf{E} \times \mathbf{B}$ drift + diamagnetic drift) with a fill pressure of 2.5 mTorr argon, RF power of ~1800W at 10 MHz, and the magnetic field of ~ 0.035 T [19].	6
Figure 1.1.3. 2D diagram showing the resultant ion velocity given perpendicular electric and magnetic fields and ion-neutral collision effects. Figure reproduced from that shown in [16].	15
Figure 1.3.1. Partial Grotrian diagram showing the transitions out of the upper state with energy levels labeled [58].	30
Figure 1.3.2. Graphical representation of the splitting of the energy levels due to the Zeeman effect showing the different possibilities for ΔM .	34
Figure 1.3.3. Graphical representation of the Zeeman splitting showing the central frequency, f_0 , and the relative intensities of the split lines.	36
Figure 1.3.4. Energy level diagram for argon energy levels used in the CR model [70].	45
Figure 1.4.1. Energy level (Grotrian) diagram for the three-level LIF neutral argon scheme used in this research.	50
Figure 1.4.2. First ArII three-level LIF scheme attempted for this research. This scheme was proposed by <i>Severn, et al</i> , [32].	51
Figure 1.4.3. ArII LIF scheme suggested by <i>E. E. Scime</i> [77].	52
Figure 2.1.1. The Helcat plasma device. The helicon source is behind the aluminum plate on the left.	53
Figure 2.1.2. Side view of HelCat showing the locations of Ports 4, 5, and 6. The helicon source is to the right of the vertical aluminum box.	54
Figure 2.1.3. Argon plasma discharge in Helcat as viewed from the helicon antenna end.	56
Figure 2.1.4. Typical Langmuir (ion saturation current) trace for 10 mTorr argon plasma with 1800 W of RF power at 10 MHz and a magnetic field of 0.044 T at Port 6.	56
Figure 2.1.5. Relative ion density profile for 10 mTorr argon plasma with 1800 W of RF power at 10 MHz and a magnetic field of 0.044 T at Port 6.	57

Figure 2.2.1. Schematic layout of LIF system for axial measurements.....	58
Figure 2.2.2. Injection side of the LIF system with parts labeled.....	59
Figure 2.2.3. Collection side of the LIF system with parts labeled.	59
Figure 2.2.4. Display on Data Acquisition (DAQ) computer. Upper trace is raw LIF response from PMT. Lower trace is power spectrum of raw data.	60
Figure 2.2.5. Typical plot of the neutral LIF signal response vs. frequency for sweep of the laser through the full frequency range. The double peak is due to Zeeman splitting of the atomic levels. This data is for 10 mTorr argon, with 1800 W of RF power at 10 MHz and magnetic field of 0.044 T.....	61
Figure 2.2.6. Side view of HelCat showing custom made yoke to hold the aluminum extrusion to the 8 in. conflat port.	63
Figure 2.2.7. Close-up view of the custom yoke used to attach the optics to the 8 in. conflat port. It is constructed such that it sits over the bolt heads.	63
Figure 2.2.8. Collection side optical lens assembly.....	64
Figure 2.2.9. Side view of HelCat with the collection optics attached at Port 6. The lens assembly, PMT, and test laser are indicated.	65
Figure 2.2.10. Data Acquisition (DAQ) triggering circuit.....	66
Figure 2.2.11. Line spectrum of Iodine for the region of interest. Closest two lines to the neutral argon resonance are indicated on the plot [81].	68
Figure 2.2.12. Laser table showing iodine cell heater box.	69
Figure 2.2.13. Iodine cell response to laser sweep through resonances of interest. The upper trace is the output sweep of the laser and the lower trace is the response from the iodine cell. The spikes in the lower trace are where the iodine cell fluoresces as the laser sweeps through a resonance.	70
Figure 2.2.14. Iodine Cell response vs. laser frequency sweep across the resonances shown in Figure 2.2.13.	71
Figure 2.3.1. Injection laser hitting probe tip inside the vacuum chamber.....	72
Figure 2.3.2. Test laser shining through collection optics on probe tip.....	72
Figure 2.3.3. Neutral LIF fluorescence response vs. argon pressure for the laser at full power and set to the first Zeeman split peak frequency (430280.95 GHz). Same scan performed at $r = 0$ cm, $r = 6$ cm, and $r = 10$ cm. 10 mTorr was chosen as the working pressure to ensure good LIF response without overloading the vacuum pumps.....	74

Figure 2.3.4. Calibration curve to convert from laser head input current to laser power after the beam splitter.....	75
Figure 2.3.5. Neutral LIF fluorescence signal response vs. input laser power. Saturation occurs above ~40mW. Laser power of 20 mW used to avoid power broadening. 75	
Figure 2.3.6. Typical raw LIF data signal.....	76
Figure 2.3.7. Plot of partial plasma data shot showing the raw PMT signal, the chopper signal and the DAQ trigger signal. The laser “on/off” conditions coincide with the chopper “high/low” signal. The DAQ turns on on a “down” of the chopper signal.	77
Figure 2.3.8. Typical neutral argon LIF amplitude response as a function of frequency for $f-f_0$	77
Figure 2.3.9. Neutral argon LIF fluorescence response vs. argon pressure at Port 4 with the laser at full power and set to the first Zeeman split peak frequency (430280.95 GHz). Scans performed at $r = 0$ cm, $r = 6$ cm, and $r = 10$ cm.....	78
Figure 2.3.10. Neutral argon LIF amplitude vs. laser power for Port 4 with argon at 10 mTorr and $r = 6$ cm.	79
Figure 2.3.11. Neutral LIF amplitude vs. injected laser frequency for Port 4 and $r = 6$ cm with argon at 10 mTorr and laser at full power.	80
Figure 2.3.12. Neutral argon LIF amplitude vs. argon pressure for Port 5 and $r = 6$ cm with the laser at full power and set at 430280.95 GHz.	80
Figure 2.3.13. Injection side optics set for radial LIF measurements at Port 6.	81
Figure 2.3.14. Radial neutral argon LIF amplitude vs. injection laser frequency at Port 6 and the collection optics at the end of the machine for $r = 0$ cm with 10 mTorr argon.	82
Figure 2.3.15. Fabricating a new yoke to hold the collection side optic on the 60-degree port.	83
Figure 2.3.16. Collection side optics mounted on 60-degree port using new yoke, optical bread board, and ThorLabs PRO1 High-Precision Rotation Mount.....	83
Figure 2.3.17. Schematic of the vacuum chamber showing the relative locations of the injection laser and the collection optics for radial laser injection at Port 6. The direction of the scan is also shown.	84
Figure 2.3.18. Neutral LIF amplitude vs. argon pressure for radial laser injection with laser at full power at 430280.90 GHz at Port 6.	84

Figure 2.3.19. Neutral LIF amplitude vs. laser power for radial laser injection at Port 6 with 10 mTorr argon.	85
Figure 2.3.20. Typical neutral LIF amplitude vs. laser frequency for radial laser injection at Port 6 with 10 mTorr argon.....	85
Figure 2.3.21. Adjustable optical mount to move the injection laser in a vertical direction.	86
Figure 2.3.22. Optical mount to allow the injection laser beam to be directed into the chamber and moved vertically.	87
Figure 2.3.23. Schematic view of injection and collection optics showing direction of scan for azimuthal LIF measurements.	87
Figure 2.3.24. Schematic showing how raising the laser vertically can probe the azimuthal (tangent-radial) velocity. The injection laser and the collection optics are aligned to intersect at a point tangential to a radius.....	88
Figure 2.3.25. Typical neutral LIF amplitude vs. frequency for azimuthal measurements at Port 6 with 10 mTorr argon and 20 mW of injection laser power.....	89
Figure 2.4.1. ArII LIF amplitude vs. argon pressure for the 688.8512 nm ion pump line at Port 4 and $r = 6$ cm with the laser at full power.....	90
Figure 2.4.2. ArII LIF amplitude vs. argon pressure for the 688.8512 nm ion pump line at Port 5 at $r = 6$ cm with the laser at full power.....	90
Figure 2.4.3. ArII LIF amplitude vs. laser frequency for argon at 1 mTorr at Port 6 at $r = 5$ cm with the laser at full power.....	91
Figure 2.4.4. 686 ion line LIF amplitude vs. argon pressure at Port 6 with the injection laser at full power and set at 436813.90 GHz.	92
Figure 2.4.5. Power spectrum of ArII LIF for the 686-ion line with 1.0 mTorr argon and no laser. The peak at 600 Hz is due to plasma fluctuations.....	92
Figure 2.4.6. Power spectrum of LIF response for the 686-ion line with 1.0 mTorr argon and the laser on. The peak at 600 Hz is due to plasma fluctuations.	93
Figure 2.4.7. Power spectrum of LIF response for the 686-ion line at Port 6 with 1.5 mTorr argon and the laser on. The peak shifted indicating that it is due to plasma fluctuations.....	93
Figure 2.4.8. 686 ion LIF amplitude vs. laser frequency at Port 6 with 10 mTorr argon and $r = 0$ cm.	94

Figure 2.4.9. 686 ion LIF amplitude vs. argon pressure at Port 5 with the injection laser at full power and set at 436813.90 GHz.	95
Figure 2.4.10. 686 ion LIF response vs. frequency at Port 5 with 10 mTorr argon at $r = 0$ cm and laser at full power.	95
Figure 2.4.11. 686 Ion LIF amplitude vs. argon pressure at Port 4 with the laser at full power.	96
Figure 2.4.12. 686 Ion LIF amplitude vs. power for Port 4 with 2.5 mTorr argon and $r = 0$ cm.	96
Figure 2.4.13. 686 ion LIF amplitude vs. laser frequency for Port 4 with 2.5 mTorr argon and $r = 0$ cm.	97
Figure 2.4.14. Injection side optics showing quarter-wave plate installed after the chopper. Also visible are the corner of the laser head, the beam splitter and the linear polarizer.	98
Figure 2.4.15. 686 ion LIF response vs. frequency for Port 4 with 2.5 mTorr argon, $r = 0$ cm, and quarter-wave plate at 45 degrees.	98
Figure 2.4.16. 686 ion LIF amplitude vs. laser frequency for Port 4 with 2.5 mTorr argon, $r = 0$ cm, and quarter-wave plate at - 45 degrees.	99
Figure 2.4.17. 686 ion LIF response vs. frequency at Port 4 with 2.5 mTorr and $r = 0$ cm. The red trace is the actual fit line to the data, the blue traces are the confidence intervals, and the purple and green traces are the double Gaussian fit under the main peak.	99
Figure 2.4.18. 686 ion LIF response vs. frequency at Port 4 with 2.5 mTorr and $r = 2$ cm. The signal to noise ratio was such that this was the last radial position for which data was acquired.	100
Figure 2.6.1. Schematic of RF-compensated probe [82].	103
Figure 2.6.2. Actual RF-compensated probe showing one of the inductors and the ground back to the plasma (copper wrapped around the ceramic stub).	104
Figure 2.6.3. Schematic of electronics used to apply variable bias voltage to the RF-compensated probe.	105
Figure 2.6.4. Typical raw data from the RF-compensated, swept probe. The red trace is the bias voltage, V_{bias} , and the blue trace is the probe voltage, $V_{\text{probe}} = I_{\text{probe}} * R$	106
Figure 2.6.5. Typical I-V curve for the swept, RF-compensated probe.	106
Figure 2.6.6. Ideal Current(I) versus voltage (V) trace from [89].	107

Figure 2.6.7. Typical exponential fit to the data for the exponential part of the I-V curve.	108
Figure 2.6.8. Plot of the log of the current vs. the bias voltage for the exponential part of the I-V curve.	108
Figure 2.6.9. Electron temperature found from the swept, RF-compensated probe.	109
Figure 2.6.10. Ion density profile for 10 mTorr argon at Port 6 with 1800 W of RF power at 10 MHz, and magnetic field of 0.044T.	110
Figure 2.6.11. Absolute Ion Density profile for 10 mTorr argon at Port 6 with 1800 W of RF power at 10 MHz, and magnetic field of 0.044T.	111
Figure 2.6.12. Swept probe current vs. bias voltage, I-V, curve showing plasma potential found from the "knee" of the curve.	112
Figure 2.6.13. Plasma potential vs. radius with 10 mTorr argon, 1800 W of helicon power at 10 MHz, and magnetic field of 0.044 T.	112
Figure 2.7.1. Model of the new Mach probe tip design using fused quartz.	114
Figure 2.7.2. New Quartz Mach probe tip with electrodes installed. Tantalum electrodes can be seen extending beyond the quartz because the ends are open. The tips were adjusted to be recessed in the quartz tube once the rest of the probe was assembled.	114
Figure 2.7.3. . Mach probe tip after being in the plasma. The discoloration is a combination of carbon and sputtered tantalum. It is conductive and causes "shorts" (~ 1 Mohm resistance paths) between the tips. The aluminum coupling holds the tip to the rest of the probe shaft.	115
Figure 2.7.4. Quartz Mach probe tip after fusing the end and cleaning with EtchAll. ...	115
Figure 2.7.5. Drawing of a six-sided Mach probe tip with the magnetic field direction and the angle to it indicated [82].	116
Figure 2.7.6. Schematic of electrical circuit used for the Mach probe measurements [82].	118
Figure 2.7.7. Typical plot of ion current collected by the Mach probe for 10 mTorr argon with 1800 W of RF power at 10 MHz and a magnetic field of 0.044 T.	119
Figure 2.7.8. Parallel (to the magnetic field) ion velocity (in Mach number) vs. radius for 10 mTorr argon with 1800 W of RF power at 10 MHz and a magnetic field of 0.044 T. Negative Mach number indicates flow away from the sources.	119

Figure 2.7.9. Perpendicular (azimuthal) ion velocity (in Mach number) vs. radius for 10 mTorr argon with 1800 W of RF power at 10 MHz and a magnetic field of 0.044 T. Positive Mach number is in the electron diamagnetic direction (EDD)..... 120

Figure 3.1.1. Typical neutral LIF signal response vs. frequency. f_0 , the resonant frequency is indicated by the vertical red line. The Doppler shift is shown by the displacement from f_0 . Zeeman splitting, and full width at half maximum (FWHM) are indicated. 121

Figure 3.1.2. LIF amplitude vs. radius for ArI using axial laser injection and the collection optics located at Port 6 with 10 mTorr argon, 1800 W of helicon power at 10 MHz, and magnetic field of 0.044 T..... 125

Figure 3.1.3. Temperature vs. radius for ArI using axial laser injection and the collection optics located at Port 6 with 10 mTorr argon, 1800 W of helicon power at 10 MHz, and magnetic field of 0.044 T..... 125

Figure 3.1.4. Velocity vs. radius for ArI using axial laser injection and the collection optics located at Port 6 with 10 mTorr argon, 1800 W of helicon power at 10 MHz, and magnetic field of 0.044 T. Negative velocity indicates neutral argon flow away from the helicon source..... 126

Figure 3.1.5. LIF amplitude vs. radius for ArI using radial laser injection with 10 mTorr argon, 1800 W of helicon power at 10 MHz, and magnetic field of 0.044 T..... 127

Figure 3.1.6. Temperature vs. radius for ArI using radial laser injection with 10 mTorr argon, 1800 W of helicon power at 10 MHz, and magnetic field of 0.044 T..... 127

Figure 3.1.7. Radial velocity vs. radius for ArI with 10 mTorr argon, 1800 W of helicon power at 10 MHz, and magnetic field of 0.044 T. The negative velocity indicates neutral argon flow radially outward from the center of the machine. 128

Figure 3.1.8. Neutral LIF amplitude vs. radius for azimuthal laser injection with 10 mTorr argon, 1800 W of helicon power at 10 MHz, and magnetic field of 0.044 T..... 129

Figure 3.1.9. Neutral temperature vs. radius for azimuthal laser injection with 10 mTorr argon, 1800 W of helicon power at 10 MHz, and magnetic field of 0.044 T..... 130

Figure 3.1.10. Azimuthal velocity vs. radius with 10 mTorr argon, 1800 W of helicon power at 10 MHz, and magnetic field of 0.044 T. The negative velocity indicates neutral flow in the electron diamagnetic direction (EDD)..... 130

Figure 3.2.1. Comparison between axial (parallel to the magnetic field) Mach probe (ion) and ArI velocities with 10 mTorr argon, 1800 W of helicon power at 10 MHz, and magnetic field of 0.044 T. Negative velocity is away from the helicon source.. 131

Figure 3.2.2. Comparison of azimuthal ArI and ion velocities with 10 mTorr argon, 1800 W of helicon power at 10 MHz, and magnetic field of 0.044 T. Negative velocity is in the ion diamagnetic direction (IDD).	132
Figure 3.3.1. Neutral density profile used in CR model with electron beam for 10 mTorr argon, 1800 W of helicon power at 10 MHz, and magnetic field of 0.044 T.	134
Figure 3.3.2. Fit of CR model with electron beam compared to radial LIF amplitude with 10 mTorr argon, 1800 W of helicon power at 10 MHz, and magnetic field of 0.044 T.	134
Figure 3.3.3. Neutral density profile without electron beam for 10 mTorr argon, 1800 W of helicon power at 10 MHz, and magnetic field of 0.044 T.	135
Figure 3.3.4. Fit of CR model without electron beam compared to radial LIF amplitude with 10 mTorr argon, 1800 W of helicon power at 10 MHz, and magnetic field of 0.044 T.	136
Figure 3.3.5. Estimated radial force on the ion due to ion-neutral collisions vs. radius for 10 mTorr argon, 1800 W of helicon power at 10 MHz, and magnetic field of 0.044 T	137
Figure 3.3.6. $\mathbf{F} \times \mathbf{B}$ drift (azimuthal ion) velocity vs. radius due to ion-neutral collisions for 10 mTorr argon, 1800 W of helicon power at 10 MHz, and magnetic field of 0.044 T. Negative velocity indicates flow is in the ion diamagnetic direction.	137
Figure 3.3.7. Neutral radial velocity calculated from diffusion equation using ground state neutral density from CR model vs. radius for 10 mTorr argon, 1800 W of helicon power at 10 MHz, and magnetic field of 0.044 T.	138
Figure 3.4.1. Radial \mathbf{E} -field calculated from the plasma potential profile vs. radius for 10 mTorr argon, 1800 W of helicon power at 10 MHz, and magnetic field of 0.044 T.	139
Figure 3.4.2. $\mathbf{E} \times \mathbf{B}$ drift vs. radius for 10 mTorr argon, 1800 W of helicon power at 10 MHz, and magnetic field of 0.044 T. The drift is in the electron diamagnetic direction (EDD).	140
Figure 3.4.3. Radial ion drift velocity vs. radius as determined by Equation 3.4.5. This drift is for 10 mTorr argon, 1800 W of helicon power at 10 MHz, and magnetic field of 0.044 T. Negative velocity indicates flow toward the center of the chamber. ...	141
Figure 3.4.4. $\mathbf{E} \times \mathbf{B}$ drift and $\mathbf{E} \times \mathbf{B}$ drift with Pedersen conductivity correction vs. radius for 10 mTorr argon, 1800 W of helicon power at 10 MHz, and magnetic field of 0.044 T.	142
Figure 3.4.5. Comparison of radial ion velocity vs. radius as determined by Equations 3.4.5 and 3.4.7. This drift is for 10 mTorr argon, 1800 W of helicon power at 10 MHz,	

and magnetic field of 0.044 T. Negative velocity indicates flow toward the center of the chamber.....	142
Figure 3.4.6. Comparison of azimuthal ion velocity calculated for the $E \times B$ drift, the $E \times B$ drift with Pedersen conductivity, and the ion velocity from the equation of motion. This drift is for 10 mTorr argon, 1800 W of helicon power at 10 MHz, and magnetic field of 0.044 T. The drift is in the electron diamagnetic direction (EDD).	143
Figure 3.4.7. Ion diamagnetic drift vs. radius for 10 mTorr argon, 1800 W of helicon power at 10 MHz, and magnetic field of 0.044 T.....	144
Figure 3.4.8. Total calculated ion drift velocity vs. radius for 10 mTorr argon, 1800 W of helicon power at 10 MHz, and magnetic field of 0.044 T. Positive is in the electron diamagnetic direction (EDD).	145
Figure 3.4.9. Comparison between the total calculated azimuthal ion drift velocity and the measured ion velocity vs. radius for 10 mTorr argon, 1800 W of helicon power at 10 MHz, and magnetic field of 0.044 T. Positive is in the electron diamagnetic direction (EDD).	145
Figure 3.5.1. LIF amplitude vs. radius for 686 ion line using axial laser injection and collection optics at Port 4 with 2.5 mTorr argon, 1800 W of helicon power at 10 MHz, and magnetic field of 0.044 T.....	146
Figure 3.5.2. Axial Temperature vs. radius for the 686 ion line LIF measurements using axial laser injection and collection optics at Port 4 with 2.5 mTorr argon, 1800 W of helicon power at 10 MHz, and magnetic field of 0.044 T.....	147
Figure 3.5.3. Axial velocity vs. position for the 686 ion line LIF measurements using axial laser injection and collection optics at Port 4 for 2.5 mTorr argon, 1800 W of helicon power at 10 MHz, and magnetic field of 0.044 T. Negative velocity is away from the source.	147
Figure 4.1.1. Pictorial description of the plasma rotation about the center of the machine. The left side shows normal plasma rotation around a central axis, while the right side shows the plasma rotating as a unit around the center of the machine.	150
Figure 4.1.2. Camera images of unfiltered visible light from plasma in HelCat at two different times during the plasma discharge for 10 mTorr argon and magnetic field of 0.044 T. The images have been colorized to show areas of high and low ionization. The high ionization region rotates off the central axis. View is looking axially toward the helicon source.	150

List of Tables

Table 1.3.1. Transition probabilities for calculating the linewidth of the ArI LIF scheme.....	29
Table 1.3.2. Transition probabilities doe calculating the linewidth of the ArII LIF scheme.....	31
Table 1.3.3. Zeeman splitting for the π transitions ($M = M_1 = M_2$)	35
Table 1.3.4. Zeeman Splitting for $\Delta M = 1$ ($M_1 - M_2 = 1$) (not showing the symmetric negative shift)	36
Table 1.3.5. Zeeman splitting for the π transitions ($M = M_1 = M_2$)	37
Table 1.3.6. Zeeman Splitting for $\Delta M = 1$ ($M_1 - M_2 = 1$) (not showing the symmetric negative shift)	37
Table 1.3.7 The 65 effective argon levels included in the CR model code and properties associated with excitation by electrons from the ground state to each level. A is an optically allowed, P is a parity-forbidden, and S is a spin-forbidden transition....	44
Table 2.5.1. Summary of LIF schemes attempted and the results.....	101
Table 3.1.1. Measured values of Zeeman splitting for $B = 0.044T$	122

Chapter 1: Motivation and Introduction

1.1 Motivation

Plasma is defined as a collection of charged particles exhibiting some properties of a gas, but differing from a gas as being a good conductor of electricity and in being affected by a magnetic field [1]. Plasma dynamics are dominated by the charged particles, but neutral particles can influence the dynamics as well. Although the importance of neutrals in some plasmas, such as the earth's ionosphere, was recognized long ago, the role of neutrals in other plasmas, i.e. laboratory and fusion plasmas has only recently received much attention. From laboratory plasmas to fusion plasmas to ionospheric plasmas and space plasma, neutral particles can influence the dynamics of the plasma. Unfortunately, since these particles are electrically neutral, standard methods of observation, i.e., electric probes, do not work.

In 1975, *Stern* and *Johnson* were some of the first to report the use a laser to excite an atomic transition in singly ionized argon. Their experiments were on a hot-cathode DC discharge, and they were able to measure transverse ion velocities up to 5×10^5 cm/s [2]. This diagnostic became known as laser induced fluorescence (LIF) and works by causing an atomic transition in an atom, or ion by the absorption of laser light. This transition pushes (excites) an electron from a lower energy state to a higher energy state. Since the upper energy state is generally unstable, the electron will drop back (decay) to a lower energy state. In most transitions to a lower energy state, there are more than one possible energy state the electron can decay to. If the decay is to a state other than where the electron started from, the energy emitted will be at a different wavelength than that used to excite the electron. Since the emitted light is at a different wavelength, it can be observed, and

not confused with the light from the laser. It is generally helpful to modulate the laser in some fashion to differentiate the observed response from background plasma light. The method of laser induced fluorescence (LIF) is well suited to the observation of neutral particles as it is non-invasive, and new lasers can be tuned to the atomic transitions of the neutral particles.

Neutral particles can affect the plasma in many ways other than simply by collisions. In a paper from 1997, *Beverini, et al*, stated that “it is well known that the dynamics of weakly ionized noble gas plasma are largely dominated by the kinematics of neutral metastable states [3].” *Schrenk* defines a metastable state as:

an excited state of an atom which does not (according to the selection rules) combine with the ground state of the atom. [...] The excited states for which the probability of returning to the ground state by emission of energy is very low also cannot be reached from the lower state by the direct absorption of energy. These states can be populated by an indirect process, such as energy transfer by collisions with high-energy particle [4].

As examples of some of the effects neutrals can have on a plasma, *Magee, et al*, state that “neutral depletion in low temperature radio frequency (RF) plasmas can lead to an increase in plasma transport, resulting in a decreasing plasma density [5].” *Houshmandyar* and *Scime* stated in 2012, that in laboratory plasmas, “neutral collisions damp waves, increase transport, and perhaps even impart momentum to ions and dust [6].” in 2006, *Keesee* stated that “the neutral gas that is present in all plasmas can play a significant role in radiation losses, diffusion, momentum transport, and cooling [7].” In an experiment by *Aramaki, et al*, “a class of vortices, which rotate in the opposite direction to

the $\mathbf{E} \times \mathbf{B}$ drift, has been observed. A force acting on the ions due to charge exchange interaction between the ions and neutrals is thought to play an essential role in generating anti- $\mathbf{E} \times \mathbf{B}$ rotation [8].” In 2009, *Shuzo, et al*, stated that “Neutral heating and neutral depletion have been observed in a high-density plasma for chemical vapor deposition [9].” In 2016, *Kelly, et al*, stated that neutral particles “can also exert both pressure and torque on the plasma through the $|F_r \times B_z|/qB^2_z$ force, where F_r is the radial neutral-ion drag force, B_z is the axial magnetic flux density, and q is the ion charge [10].”

One of the basic plasma parameters is beta, β , which is defined as the ratio of the thermal pressure to the magnetic pressure:

$$\beta = \frac{\sum n k_B T}{\frac{B^2}{2\mu_0}} \quad (1.1.1)$$

where the summation is over the ions and electrons, n and T are the respective densities and temperature, k_B is the Boltzmann constant, B is the magnetic field strength, and μ_0 is the permittivity of free space. For the conditions of the experiment described herein and developed in later sections, $\beta \approx 0.001$, which indicates that the plasma is low beta. Since beta is small, the diamagnetic effect is also small, and it can be assumed that the magnetic field is axially uniform [11].

Neutrals are also important in magnetic fusion plasmas. For example, *Elliott* states that “neutral particle dynamics play an important role in the fusion plasma edge and must be considered to create predictive models of such systems. Neutrals have a large impact on fueling, energy, and momentum transport, and thus particle confinement. Changes in the neutral density in the plasma edge are known to affect critical bulk plasma properties such as the L to H transition in tokamaks [12].” In addition, “penetration by neutrals also plays an important role in cross field transport of particles and energy in fusion plasmas [13].”

Neutral particles play an important role in the physics of the ionosphere as well. In the ionosphere, the neutral density is much greater than the plasma density throughout the entire vertical range. (The point where the plasma density becomes greater than the neutral density is generally considered the boundary between the ionosphere and the plasmasphere above it [14].) The ratio of the ion gyro frequency to the ion-neutral collision frequency influences the flow of plasma, and the E-layer is particularly susceptible to the effects of the neutral ‘wind’ as the neutral density changes with elevation above the earth [15], [16], and [17].

In planets with radiation belts, “plasma-neutral interactions involve the transfer of charge, momentum and energy in ion-neutral and electron-neutral collisions. Important examples are the resonant charge exchange interaction between an ion, and its parent neutral ($H^+ + H \leftrightarrow H + H^+$), and the accidentally resonant charge exchange reaction ($O^+ + H \leftrightarrow H^+ + O$) [18].”

As a final example of possible neutral particles influencing ion motion, research on the linear helicon-cathode (HelCat) device at the University of New Mexico is being conducted to understand the interaction between ions and neutrals. HelCat is a cylindrical plasma device 4 m long and 50 cm in diameter. It has external electromagnets capable of creating a uniform magnetic field along the length of the chamber. Typical operating parameters are: fill pressure ~ 2.5 mTorr argon, helicon (RF) power ~ 1800 W at 10 MHz, and background magnetic field (B) ~ 0.044 T. These parameters can be varied, and the cathode can be operated in conjunction with the helicon antenna, or alone, making HelCat extremely versatile. HelCat will be described in more detail in Section 2.1.

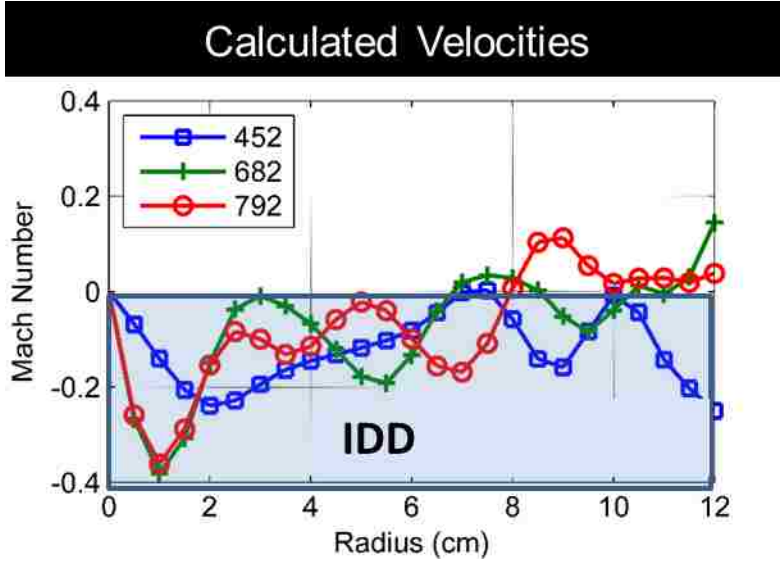
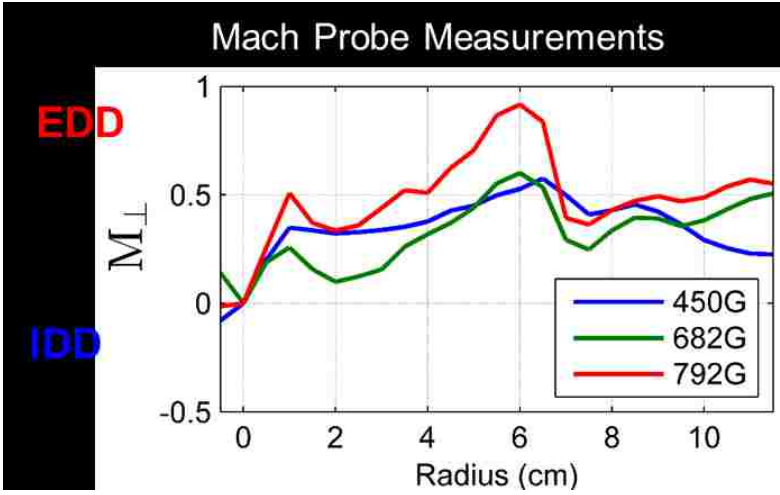
In a cylindrical plasma device, such as HelCat, the azimuthal ion flow should be dominated by the $\mathbf{E} \times \mathbf{B}$ drift and the diamagnetic drift, as the effects of a gravity drift would be negligible, and since the magnetic field is uniform, any drifts associated with a non-uniform magnetic field would not materialize. In a helicon plasma, we assume the electric field to be steady-state, thereby, eliminating the polarization drift, which would be small if it did appear.

In a poster presented by *Gilmore* in 2015, he showed a plot of Mach probe data collected by *Desjardins* which showed the ion flow in HelCat to be in the electron diamagnetic direction (EDD) as reproduced in Figure 1.1.1 [19]. In contrast the calculated drift velocity of the ions ($\mathbf{E} \times \mathbf{B}$ drift + diamagnetic drift), indicated that the ions should be flowing in the ion diamagnetic direction (IDD), as shown in Figure 1.1.2.

The diamagnetic drift is defined as [11]:

$$v_D = - \frac{\nabla p \times \mathbf{B}}{qnB^2} \quad (1.1.2)$$

where v_D is the diamagnetic drift, ∇p is a pressure gradient with $p = nkT$, n is the plasma density, k is the Boltzmann constant, T is the temperature (ion, or electron), q is the ion, or electron charge, and \mathbf{B} is the magnetic field. As HelCat is a cylindrical device with \mathbf{B} directed along the axis of the machine, and the pressure gradient is mainly in the radial direction, this leads to an azimuthal drift. Because ions and electrons have opposite charges, they will drift in opposite directions.



Since the measured values did not agree with the calculated values, other mechanisms that could account for the discrepancy were discussed and investigated. These mechanisms included: errors in probe measurements, Reynold's stress [20], neutral effects [21] [5] [22], finite Larmor radius (FLR) effects, high electron-ion collisionality [23], recoil from detaching blob like structures, and angular momentum imparted to the ions from the helicon source. Some of these possibilities have been investigated and ruled out. The high collisionality does cause a force in the electron diamagnetic direction, $\vec{F}_{thermal} = .71n\nabla T_e \times \vec{B}$, but this force is not large enough to overcome the $\mathbf{E} \times \mathbf{B}$ velocity. The finite Larmor radius (FLR) was deemed insufficient to explain the observed ion flow. The Reynold's stress was ruled out as the experiments *Desjardins* was performing involved biasing the plasma to suppress fluctuations. With the fluctuations suppressed, the Reynold's stress was reduced to effectively zero, and the ion flow increased in the electron diamagnetic direction (EDD) [19]. In addition, new Mach probe data from a redesigned probe still show the ion flow in the electron diamagnetic direction [24], which give some additional confidence in the measurements.

Blob structures detaching from the plasma were also ruled out as being insufficient to account for the observed flow. Momentum from the helicon source has not been pursued as there is no known mechanism for this effect. That left the question of whether neutral effects could account for the observed ion flows. These effects include: neutral collisions and a neutral 'wind.' The neutral collisions can act as a 'drag' force and reduce the $\mathbf{E} \times \mathbf{B}$ velocity, as shown in Equation 1.1.3. The neutral wind can create an $\mathbf{F} \times \mathbf{B}$ drift that can influence the ion flow [19], as shown in Equation 1.1.4, and Equation 1.1.5.

$$\mathbf{v}_{ExB} = \frac{\mathbf{E} \times \mathbf{B}}{B^2 \left(1 + \frac{v_{in}^2}{\omega_{ci}^2} \right)} \quad (1.1.3)$$

$$\mathbf{F}_{ni} = v_i m_i n_i \mathbf{v}_n \quad (1.1.4)$$

$$\mathbf{v}_{F_{ni} \times B} = \frac{1}{q} \frac{\mathbf{F}_{ni} \times \mathbf{B}}{B^2} = \frac{m_i n_i v_i}{q} \frac{\mathbf{v}_n \times \mathbf{B}}{B^2} \quad (1.1.5)$$

It should be noted that the force, \mathbf{F} , in equation 1.1.4 is a force density, and to obtain an $\mathbf{F} \times \mathbf{B}$ drift velocity, it is necessary to divide by the ion density n_i .

Prior to this dissertation research, no measurement of neutral particle energy, or velocity existed in HelCat. To try to resolve the discrepancy in the ion flows, a neutral particle LIF system was developed. The laser used was a Toptica tunable diode laser with < 250 mW output laser power and tunable between 684 nm and 699 nm. (The laser will be described in more detail in Section 2.2.1.) The goal of this research is to understand the neutral particle dynamics and interaction with the ions. This research is intended to answer the questions:

1. Do the neutrals affect the ion flow?
2. Is this interaction enough to explain the observed ion flow as measured by Mach probes?

In addition, since this laser acquired is tunable, two ion fluorescence lines will be investigated.

1.1.1 Equations of Motion in Plasma with Ion-Neutral Collisions

Many basic plasma treatments ignore the effects of neutral particle interactions. For example, Chen writes “the fluid equation of motion including the effects of charged particle collisions” as:

$$m_i n \frac{dv_i}{dt} = en(\mathbf{E} + \mathbf{v}_i \times \mathbf{B}) - \nabla p_i - \nabla \cdot \boldsymbol{\pi}_i + \mathbf{P}_{ie} \quad (1.1.6)$$

$$m_e n \frac{dv_e}{dt} = -en(\mathbf{E} + \mathbf{v}_e \times \mathbf{B}) - \nabla p_e - \nabla \cdot \boldsymbol{\pi}_e + \mathbf{P}_{ei} \quad (1.1.7)$$

where M is the mass of the ions, m is the mass of the electrons, v_i and v_e are the velocity of the ions and the velocity of the electrons, n is the plasma density, \mathbf{E} and \mathbf{B} are the electric and magnetic fields, p_i and p_e are the pressure due to ion and electrons defined as nkT , and $\boldsymbol{\pi}_j$ is the anisotropic viscosity tensor which contains like-particle collisions, and since these collisions do not give rise to much diffusion, the $\nabla \cdot \boldsymbol{\pi}_j$ terms can be ignored. “The terms \mathbf{P}_{ie} and \mathbf{P}_{ei} represent, respectively, the momentum gain of the ion fluid caused by collisions with electrons, and vice versa.” Since these terms “represent the friction between the two fluids, the conservation of momentum requires”

$$\mathbf{P}_{ie} = -\mathbf{P}_{ei} \quad (1.1.8)$$

These can be written in terms of the collision frequency as:

$$\mathbf{P}_{ei} = mn(\mathbf{v}_i - \mathbf{v}_e)v_{ei} \quad (1.1.9)$$

where v_{ei} is the electron-ion collision frequency [11].

This includes electron-ion collisions, but how do we need to change the equations of motion if we want to include ion-neutral collisions? For this, we turn to ionospheric research as the neutrals do play an important role in the motion of the plasma in the ionosphere. *Rishbeth* and *Garriott* [15] write the equations of motion as

$$\begin{aligned} m_i \left(\frac{d\mathbf{V}_i}{dt} \right) = 0 = m_i \mathbf{g} - \nabla P_i + e(\mathbf{E} + \mathbf{V}_i \times \mathbf{B}) - m_i v_{in}(\mathbf{V}_i - \mathbf{U}) \\ - m_e v_{ei}(\mathbf{V}_i - \mathbf{V}_e) \end{aligned} \quad (1.1.10)$$

$$\begin{aligned} m_e \left(\frac{d\mathbf{V}_e}{dt} \right) = 0 = m_e \mathbf{g} - \nabla P_e - e(\mathbf{E} + \mathbf{V}_e \times \mathbf{B}) - m_e v_{en}(\mathbf{V}_e - \mathbf{U}) \\ - m_e v_{ei}(\mathbf{V}_i - \mathbf{V}_e) \end{aligned} \quad (1.1.11)$$

Where \mathbf{U} is the neutral velocity, and ν_{in} is the ion-neutral collision frequency. If we ignore the effects of gravity and the electron-ion collision term, we get:

$$m_i \left(\frac{d\mathbf{V}_i}{dt} \right) = e(\mathbf{E} + \mathbf{V}_i \times \mathbf{B}) - \nabla P_i - m_i \nu_{in} (\mathbf{V}_i - \mathbf{U}) \quad (1.1.12)$$

From this equation, we can define a “force per unit volume experienced by particles of type a, F_{ab} , due to collisions with particles of type b” as:

$$\mathbf{F}_{ab} = -\mathbf{F}_{ba} = n_a m_a \nu_{ab} (\mathbf{V}_b - \mathbf{V}_a) \quad (1.1.13)$$

And re-write the equation of motion as given by Vranješ, et al. [22]

$$\begin{aligned} m_i n_i \left(\frac{\partial}{\partial t} + \mathbf{V}_i \cdot \nabla \right) \mathbf{V}_i &= q_i n_i (-\nabla \phi + \mathbf{V}_i \times \mathbf{B}_0) - \nabla p_i \\ &\quad - m_i n_i \nu_{in} \mathbf{V}_i + \mathbf{F}_{ni} \end{aligned} \quad (1.1.14)$$

Where ν_{in} is the ion-neutral collision frequency. “The force \mathbf{F}_{ni} describes the momentum transferred in the ion-neutral charge transfer interactions which is given by:”

$$\mathbf{F}_{ni} = \nu_{in} m_i n_i \mathbf{V}_n. \quad (1.1.15)$$

The neutral flow, \mathbf{V}_n , can be determined by the diffusion flux $\mathbf{V}_n = -D_n \nabla n_n / n_n$ [22], or by measurement with neutral LIF.

The above formulation gives the force of the neutrals on the ions due to the neutral velocity, but it does not account for the effect of the ion-neutral collisions on the ion velocity itself. To be complete and include this term, the equations of motion can be written as:

$$\begin{aligned} m_i n_i \left(\frac{\partial}{\partial t} + \mathbf{V}_i \cdot \nabla \right) \mathbf{V}_i &= q_i n_i (-\nabla \phi + \mathbf{V}_i \times \mathbf{B}_0) - \nabla p_i - \nabla \cdot \\ &\quad \boldsymbol{\pi}_i - \mathbf{R} - m_i n_i \nu_{in} \mathbf{V}_i + m_i n_i \nu_{in} \mathbf{V}_n \end{aligned} \quad (1.1.16)$$

Assuming a steady state solution and the convective term is small (this term may be not be small and may lead to Reynolds stress as discussed in Section 4.2, but for this derivation it will be ignored), the left side of this equation disappears. The anisotropic viscosity tensor

π_i and the collisional momentum transfer term, \mathbf{R} , are assumed to be small and are neglected (to see that \mathbf{R} may be small compared to the $\mathbf{V}_i \times \mathbf{B}$ term, see Appendix A). The pressure term ∇p_i only contributes to the ion velocity through the diamagnetic drift ignored for now. With these assumptions, Equation 1.1.16 becomes:

$$0 = q_i n_i (-\nabla\phi + \mathbf{V}_i \times \mathbf{B}_0) - m_i n_i v_{in} \mathbf{V}_i + m_i n_i v_{in} \mathbf{V}_n \quad (1.1.17)$$

Solving this equation for the ion velocity in the cylindrical geometry of HelCat, we get:

$$v_{i\theta} = -\frac{k^2}{k^2+1} \frac{E_r}{B_0} + \frac{1}{k^2+1} v_{n\theta} - \frac{k}{k^2+1} v_{nr} \quad (1.1.18)$$

$$v_{ir} = \frac{k}{k^2+1} \frac{E_r}{B_0} + \frac{1}{k^2+1} v_{nr} + \frac{k}{k^2+1} v_{n\theta} \quad (1.1.19)$$

Where $v_{i\theta}$ and v_{ir} are the ion velocity in the azimuthal and radial directions, E_r is the electric field in the radial direction, B_0 is the magnetic field in the axial direction, $k = \frac{\omega_{ci}}{v_{in}}$ (ω_{ci} is the ion gyrofrequency, and v_{in} is the ion-neutral collision frequency), and $v_{n\theta}$ and v_{nr} are the neutral velocity in the azimuthal and radial directions.

With respect to the ionosphere, *Bjorna* states that “the ion-neutral collision frequency is an important parameter in characterizing the ionospheric plasma in the lower E region. For instance, the collision frequency is needed for calculating conductivities and electric currents and can be used to estimate the density of the neutrals [25].” *Tolmacheva* states that since the “frequency of ion-neutral collisions affects the energy and momentum transfer processes”, the collision frequency “should be taken into account when the low-frequency processes associated with the plasma conductivity are analyzed [26].”

1.1.2 Pedersen Conductivity

Since this research involves neutral particle dynamics in plasmas, a comparison to a plasma where the neutral particles do play a role might be in order. One such plasma is the earth's ionosphere. In this environment, the neutral particles can have a significant effect depending on such parameters as the ion-neutral collision frequency, the magnetic field strength, and the strength and direction of the neutral particle flow, or wind.

In 1927, Pedersen pointed out “that the geomagnetic field renders the electrical conductivity anisotropic [27].” He then deduced that if there was an electric field, \mathbf{E} , applied perpendicular to the existing magnetic field, \mathbf{H} , the electrical conductivity would have the form [28];

$$\sigma_1 = n_i e^2 \left\{ \frac{v_{en}}{m_e(\omega_{ce}^2 + v_{en}^2)} + \frac{v_{in}}{m_i(\omega_{ci}^2 + v_{ci}^2)} \right\} \quad (1.1.20)$$

where n_i is the ion, or electron density, e is the electronic charge, m_e and m_i are the mass of the electron and the ion, v_{in} and v_{en} are the ion-neutral and electron-neutral collision frequencies, and ω_{ci} and ω_{ce} are the cyclotron frequencies (qB/m).

This is now referred to as the *Pedersen* conductivity. In addition to this conductivity, there can “be a flow of electric current perpendicular to both \mathbf{E} and \mathbf{H} . This is the *Hall* current” and because of the relative mobilities of the electrons and ions the current is in the anti- $\mathbf{E} \times \mathbf{B}$ direction. The Hall conductivity has the form [28];

$$\sigma_2 = n_i e^2 \left\{ \frac{\omega_{ce}}{m_e(\omega_{ce}^2 + v_{en}^2)} - \frac{\omega_{ci}}{m_i(\omega_{ci}^2 + v_{in}^2)} \right\} \quad (1.1.21)$$

“For an electric field applied parallel to the magnetic field the conductivity, which may be termed the ‘longitudinal conductivity,’ is independent of \mathbf{H} ,” and is of the form [28];

$$\sigma_0 = n_i e^2 \left(\frac{1}{m_e \nu_{en}} + \frac{1}{m_i \nu_{in}} \right) \quad (1.1.22)$$

Baumjohann states that in the ionosphere, at the geomagnetic equator, the direction of the magnetic field is south to north, and the Pedersen current flows eastward parallel to the primary ionospheric electric field. The electric field drives a Hall current which flows vertically downward and causes charge separation with negative charges at the top and positive charges at the bottom of the highly conducting layer (the E layer). This charge separation creates a secondary electric field pointed vertically upward. This secondary electric field creates a secondary Hall current flowing in the eastward direction. The combination of the eastward primary Pedersen current and eastward secondary Hall current give rise to what is referred to as the Cowling conductivity as defined below [17].

Rewriting these conductivities in a slightly different form, we get;

$$\text{Longitudinal or Direct:} \quad \sigma_0 = n_i e^2 (k_{0e} + k_{0i}) \quad (1.1.23)$$

$$\text{Transverse or Pedersen:} \quad \sigma_1 = n_i e^2 (k_{1e} + k_{1i}) \quad (1.1.24)$$

$$\text{Hall:} \quad \sigma_2 = n_i e^2 (k_{2e} + k_{2i}) \quad (1.1.25)$$

$$\text{Cowling:} \quad \sigma_3 = (\sigma_1^2 + \sigma_2^2) / \sigma_1 \quad (1.1.26)$$

Where:

$$k_0 = \frac{1}{mv} = \frac{1}{Be} \frac{\omega}{v} \quad (1.1.27)$$

$$k_1 = \frac{1}{mv} \frac{v^2}{v^2 + \omega^2} = \frac{1}{Be} \frac{v\omega}{v^2 + \omega^2} \quad (1.1.28)$$

$$k_2 = \frac{1}{mv} \frac{\omega v}{v^2 + \omega^2} = \frac{1}{Be} \frac{\omega^2}{v^2 + \omega^2} \quad (1.1.29)$$

with m , v , ω , e defined as before, and B is the magnitude of the magnetic field [15].

For an electric field and neutral wind parallel to the magnetic field, the electric field causes a drift qE/mv directed along \mathbf{B} . A neutral wind with velocity, U , causes a drift

$mvU/mv = U$, and “both electron and ions are driven along a field line at a speed equal to the wind component parallel to \mathbf{B} . [15]”

If there is an electric field and a neutral wind perpendicular to the magnetic field, then there are different possible responses depending on the ratio of v/ω . The first case is if $v \gg \omega$, then $k_1 = k_0 \gg k_2$. In this case the plasma is highly collisional, and the magnetic field does not have much influence on particle motion. “An electric field produces a current parallel to itself, and a wind carries ions and electrons at its own velocity.

“If $v \approx \omega$ then $k_1 \approx k_0$, and both fields and winds produce drift velocities inclined to themselves (that is, the drift velocity will be at an angle to the electric field, or wind, and the angle will be dependent on the ratio of v and ω). This gives rise to the interesting situation that exists in the ionospheric E region.” (It will be shown in Section 4.1 that this is the case for the current research).

Finally, if $v \ll \omega$, then $k_1 \ll k_2 \approx 1/Be$. “An electric field causes both electrons and ions to drift in the same direction ($\mathbf{E} \times \mathbf{B}$) with speed E/B . A wind produces a Hall drift of speed $(v/\omega) U$, in the direction ($\mathbf{U} \times \mathbf{B}$) for positive ions and the opposite direction for electrons [15].”

The current density due to these conductivities can be expressed as;

$$\mathbf{j} = \boldsymbol{\sigma} \cdot \mathbf{E} = n_i e (\mathbf{V}_i - \mathbf{V}_e) \quad (1.1.30)$$

where \mathbf{V}_i and \mathbf{V}_e are the ion and electron velocities [15] [17]. This says that the conductivities and the E field produce a current, and this gives rise to an ion velocity. The direction of the velocity can be more clearly understood written in the form [16]:

$$\mathbf{v}_i = \frac{k_i}{1+k_i^2} \frac{\mathbf{E}}{B} + \frac{k_i^2}{1+k_i^2} \frac{\mathbf{E} \times \mathbf{B}}{B^2} \quad (1.1.31)$$

where

$$\tan\theta = k_i = \frac{\omega_{ci}}{v_{in}} \quad (1.1.32)$$

Given this form for the velocity of the ions, it is easy to see that the motion will be a combination of the current due to the \mathbf{E} field, and the $\mathbf{E} \times \mathbf{B}$ drift, and the angle, θ , with respect to the \mathbf{E} field will be dependent on the ratio of ω_{ci} to v_{in} (Figure 1.1.3). This says that in addition to the $\mathbf{E} \times \mathbf{B}$ drift, the ions will “advance in the direction of E_{\perp} [29].” If Equation 1.1.31 is written in component form, it would be similar to Equation 1.1.18 and Equation 1.1.19 except that it does not include the neutral velocity terms.



It will be shown in Section 3.4 that the magnitudes of ω_{ci} and v_{in} are approximately equal in HelCat helicon plasmas, and the $\mathbf{E} \times \mathbf{B}$ drift is modified by the factor shown in Equation 1.1.31.

1.2 History of LIF as a diagnostic for plasmas

Laser induced fluorescence (LIF) has been used as a diagnostic for plasma since at least 1975 [2]. Since that time, there have been many improvements, many different applications, and different approaches used. These include using LIF to observe basic

laboratory plasmas, industrial plasmas, fusion plasmas, and medical applications. The following gives a brief description of the history and use of LIF as a diagnostic with special attention to its use when applied to neutral particles in laboratory plasmas.

In 1975, *Stern* and *Johnson* performed experiments “using a cw (continuous wave) argon-II laser with 0.5 W focused to 0.5 mm” in a hot-cathode dc discharge. Ions in the excited state $4s^2P_{3/2}$ were excited further to the $4p^2D_{5/2}$ state with 488nm laser light. This state then decayed to the $4s^4P_{3/2}$ state with the emission of a photon at 422.8 nm. The laser intensity was modulated to differentiate between fluorescence and spontaneous emission. They were able to measure “a typical mean speed $v \approx 1.7 \times 10^5$ cm/s,” and transverse (to the electric field) velocities “as large as 5×10^5 cm/s and equivalent to a 6 eV temperature [2].”

By 1991, in a review article, *Wieman* claimed that “laser sources that can be tuned to particular atomic transitions are now a standard tool in most atomic physics laboratories.” The tunable diode laser had mostly replaced the dye laser as the laser of choice due to improved “reliability, power, and wavelength coverage, while steadily decreasing in cost.” In addition, the amplitude was very “stable compared to most other laser sources so that it is relatively simple to make sensitive absorption and fluorescence measurements [30].”

In 1993, *Muraoka* and *Maeda* gave a good description of LIF in a review article. They stated “Laser-induced fluorescence (LIF) is the technique in which the laser frequency ν is tuned to match a transition of a group of atoms or molecules, whose energy difference is E_{12} , by a relation $h\nu = E_{12}$, (where h is Planck's constant), and the resultant fluorescence is observed. By the resonant nature of the excitation, the fluorescence

intensity is many orders of magnitude larger than other sources of scattering, such as Rayleigh. Raman or Thomson scattering, if the relevant number densities are the same order of magnitude. Therefore, the LIF technique is very selective of species to be detected,” and because it is sensitive yields high spatial and temporal resolution [31].

In 1997, *Beverini, et al*, single-mode tunable diode laser to observe the transition from the metastable $4s\ ^3P_2$ energy state to the $4p\ ^3D_2$ state in Ar I at 801.479nm. Their “plasma was produced by four DC hot filament discharges placed symmetrically on the surface” of their vacuum chamber. For this research, they used the laser absorption technique in which the laser was directed through the vacuum chamber and the resultant reduction in power was recorded as a function of frequency by a “Si photovoltaic diode.” From their measurements, they were able to determine “the atomic temperature, $T = (376 \pm 20)$ K and the metastable state population density, $N_I = (8.8 \pm 0.8) \times 10^8$ atoms/cm.” In addition, they calculated the averaged collision frequencies [3]:

$$v_{i0} = (5 \pm 1) \times 10^3\ \text{s}^{-1}, \text{ ionization rate for the ground state,}$$

$$v_{m0} = (2 \pm 1) \times 10^3\ \text{s}^{-1}, \text{ metastable creation rate from ground state, and}$$

$$v_{i0m} = (10 \pm 1)\ \text{s}^{-1}, \text{ metastable ionization rate from the } 3P_2 \text{ state.}$$

Also in 1997, *Severn, et al*, continued the idea of three-level schemes for argon ion LIF. They proposed several schemes that could be used for LIF measurements. The 611.66 nm line and the 668.61 nm line have been used quite extensively. (The 688.85 nm line was attempted in the course of this dissertation research and will be discussed in more detail in Section 2.4.1) The experiments were performed in the Irvine Torus, “a plasma discharge device with a thermionic emission plasma source.” They compared three different LIF systems using the above-mentioned excitation lines: a dye laser, a master oscillator power

amplifier (MOPA) diode laser, and a diode laser as the seed laser for a MOPA. An iodine (I₂) cell was used as an absolute calibration for all three systems. They found that the MOPA by itself was the worst of the three due to “multimode output of the laser.” The combined seed laser and MOPA had the best overall response, and a family of ion velocity distribution functions was created by changing the output power of the laser system [32].

In 2001, *Engeln, et al*, presented LIF measurements from the expanding, accelerating plasma produced with a cascade arc source. Operating at sub-atmospheric pressure, the thermal arc “produces a thermal plasma (source temperature $T \approx 0.8\text{eV}$) that expands through a nozzle into a vessel at low pressure. [...] The shock on the side of the supersonic part of the expansion is called the barrel shock. The plane normal to the expansion axis where M (the Mach number) = 1 is called the Mach disc. Behind the shock wave the gas flows sub-sonically into the background gas as constant static pressure.” For this research, a single-mode cw external cavity diode laser was used to initiate the ArI transition from the metastable $1s_5$ state to the $2p_9$ state at 811.53nm, or the transition from the metastable $1s_4$ state to the $2p_7$ state at 810.37nm. They were able to collect data for both axial and radial, temperature and velocity distribution functions. From the distribution functions they were able to fit the data before and after the shock with a single Gaussian, and during the shock with two Gaussian profiles. From this they conclude that “the measured non-Maxwellian distributions can well be described with the sum of two Maxwellian distributions. It is concluded the one distribution originates from gas accelerated and cooled in the supersonically expanding plasma jet, while the other one originates from background gas penetrating in the valley of the barrel shock structure [33].”

Scime's group at West Virginia University have been working on LIF since at least 2003. They have produced many papers and dissertations some of which will be discussed now. In a paper from 2003, *Boivin* and *Scime* used the same tunable diode laser to observe an ArII transition pumped with 668.61nm laser light, and a HeI transition pumped with 667.99nm laser light. This was the first known LIF experiment on HeI [34]. *Keesee, et al*, continued this work in 2004 by the addition of an ArI transition with the same laser at 667.91nm, and the use of an iodine (I₂) cell used as an absolute calibration reference [35]. *Scime, et al*, showed that time-resolved LIF measurements were possible through the use of a lock-in amplifier and a digital oscilloscope [36]. In 2006, *Keesee* earned a Ph.D. performing LIF on argon, both neutral and ionized. For the neutral argon (ArI), a collisional-radiative (CR) model was used to produce a ground state density profile from the excited state measurements she acquired. In addition, the same LIF setup was used on the Chi-Kung plasma device at the Australian National University (ANU), where data was collected to produce ion velocity profiles [7]. This work was also presented in a 2007 paper in which passive spectroscopy was included to test the fit of the CR model [37], [38]. Also in 2006, *Biloiu, et al*, presented work indicating that they had reduced the time resolution of time-resolved LIF to $\sim 30 \mu\text{s}$ "by replacing the mechanical chopper with a high-speed acousto-optic modulator and by digital signal processing of the raw data [39]." *Biloiu* earned a Ph.D. in 2009 using a continuous wave (CW) ring dye laser for LIF measurements on Ar II and Xe II [40]. In 2010, *Thakur* earned a Ph.D. working with LIF as well. For this research, standard LIF techniques were used to obtain ion velocity distribution functions for ArII and compared those with measurements made with continuous wave cavity ring down spectroscopy (CW-CRDS) [41]. In 2012, *Houshmandyar* and *Scime* continued the work with neutrals and the CR model applying them to He I plasma. For this work, they switched

from the diode laser to “a 10W Spectra-Physics Millennium Pro double YAG laser that pumps a Sirah Matisse-DR tunable ring dye laser.” With this system, they were able to measure both axial and radial neutral density profile and velocity distribution functions [6]. In 2014, *VanDervort, et al*, optimized a confocal LIF system which allows LIF measurements to be taken using only one viewport. This is significant in that, until this development LIF needed two viewports; the laser input port and the observation port. This method allows access to locations that were not available before [42]. Finally, in 2016, *Short, et al*, presented work using a different excitation scheme for ArI. In this method, they used the $1s^2$ to $2p^3$ transition pumped with 841.052 nm laser light to produce neutral velocity distribution functions (NVDF) at lower operating pressures than what *Keesee* used [43].

Several papers have been devoted to the observation and explanation of a tripolar vortex in argon plasma in the high-density plasma experiment (HYPER-I) device at the National Institute for Fusion Science. This is an electron cyclotron resonance (ECR) device using a microwave source operated at 2.45 GHz. The input power can be varied from 40 W to 5 kW. First reported in 2003, they used emission spectroscopy to observe the 425.9362 nm (in air) line corresponding to the transition from the $(^2P^0_{1/2})5p^2[1/2]_0$ upper state to the $(^2P^0_{1/2})^2[1/2]_1^0$ lower state for neutral particle motion in the plasma. The 487.9863 nm line corresponding to the transition from the $3s^23p^4(^3P)4p^2D^0_{5/2}$ upper state to the $3s^23p^4(^3P)4s^2P_{3/2}$ lower state was used for ions. They found that the observed rotation about the vortices was in the anti- $\mathbf{E} \times \mathbf{B}$ direction. They theorized that there should be an inward force to explain the rotation, and that this force could be “a net momentum

transfer between the ions and the neutrals [44].” The equation of motion presented was originally given by *Vranješ, et. al.* [22].

In subsequent experiments, they used a tunable diode laser to perform LIF on neutral argon. They used the 696.7352 nm line to excite the transition from the $(^2P^0_{3/2})4s^2[3/2]^0_2$ metastable state to the $(^2P^0_{1/2})4p^2[1/2]_1$ state, and observed the fluorescence from the upper state to the $(^2P^0_{1/2})4s^2[1/2]^0_1$ state at 826.6794 nm. “Moving the collection optics along the horizontal axis,” they were able to collect distribution functions at different radial positions. From these measurements, they were able to determine that there was a radially inward neutral flow with a maximum velocity of 70 m/s [45]. In 2009, they changed their LIF set up to use saturated-absorption spectroscopy and Doppler LIF with the same laser as before. In this change the original Doppler LIF is still used, but a 0.01% neutral density (ND) filter is used to attenuate the beam that has already passed through the plasma. This attenuated beam is then reflected back through the plasma along the same path as that of the pump beam. “This backward beam is used as the probe beam of the saturated absorption spectroscopy.” The power of the backward beam is weak enough to avoid saturation (power broadening) which would affect the LIF measurements. With this system, the ‘Lamb dip’ is used as the frequency standard, since the line width of the Lamb dip is significantly narrower than the doppler broadened line obtained with the LIF system. Using this technique, they were able to refine the neutral velocity measurements to ~10m/s with a dispersion of ± 2 m/s [8], [9], and [46].

Other groups have been working on LIF as well. In 2006, *Woo, et al.*, developed an LIF system for the Diversified Plasma Simulator (DiPS) at the Electric Probes Applications Laboratory at Hanyang University on Seoul, South Korea. This machine has a LaB₆ disk-

type dc plasma source. They found that *Keesee's* original iodine cell measurements were shifted by 0.002 nm relating to an error in velocity space of 900 m/s. To remedy this situation, they injected laser beams from both directions into the iodine cell. Doing so eliminated any effects that might occur due to iodine flowing in the cell. With this system, they were able to show that “the wavelengths of the iodine cell measured by the wavemeter were shifted by 0.05 pm [47].”

In 2013, *Bieber, et al*, used the 696.7352 nm line to excite the metastable neutral argon state $(^2P^0_{3/2})4s^2[3/2]^0_2$ to the $(^2P^0_{1/2})4p^2[1/2]_1$ state in a helicon plasma in 2013. He used the 772.6333 nm emission from the upper state to the $(^2P^0_{1/2})4s^2[1/2]^0_0$ state as the observation line. (This is the same LIF scheme used in the research presented here.) For this research, the magnetic field was varied, and the resulting change in the intensity of the LIF signal was recorded. This change in intensity was attributed to a change in the density of the initial metastable state. From these experiments, it was concluded the metastable states “are depopulated with increasing confinement magnetic field,” and that “electron impact interactions are the process leading to this destruction phenomenon [48].”

In 2014, *Teshigahara, et al*, developed a 2-D LIF system for the Large Mirror Device (LMD) using a system of optical mounts and mirrors. This allowed them to record data in both the axial and the radial directions [49]. In a continuation of work on LMD, *Kuwahara, et al*, presented work in 2015 in which they extended the capabilities of their LIF system to include neutral Argon (Ar I) [50].

One example of other applications of LIF can be seen in the work by *Nakano, et al*, in which they measured the ion velocity distribution functions (ivdf) for chlorine ions, Cl^+ in an electron cyclotron resonance (ECR) discharge. The “doppler broadened and shifted

laser induced fluorescence profiles of Cl^+ metastable ions are different from the ivdfs (of Ar^+) because of overlapping of isotropic transitions from ^{35}Cl and ^{37}Cl .” For this research, they were interested in application to chip manufacturing. As such, their results reflect this point of view, and are summarized as follows [51]:

1. The ion transport in Cl_2 ECR plasmas is qualitatively similar to that found in the corresponding Ar plasmas. However, the presheath electric field induced by the platen is smaller in the Cl_2 plasma suggesting that the electron temperature is also smaller in this system.
2. As in Ar plasmas, bimodal v_z ivdfs are observed on Cl_2 and are attributed to the presence of two primary sources of ionization: (1) the source and (2) the throat where the plasma expands into the reactor.
3. As a result of the plasma expansion, ions are accelerated across a potential step or double layer at the source throat
4. As expected, the presence of a wafer platen directly influences ion transport by creating a presheath.
5. A magnetic cusp is found to have little influence on the $f(v_z)$ and $f(v_x)$ distributions, but is useful for improving the uniformity of the ion flux to a wafer surface.

As a second example of LIF being used for other applications, *Dougal, Williams* and *Pease* used LIF “to study the migration of metal vapor expelled from the aluminum electrodes of a spark gap.” In this research, they used a dye laser and were able to produce “two-dimensional maps of the presence of ground-state Al vapor in an operating spark gap [52].”

As a final example of the use of LIF for applications other than laboratory plasmas, *Rex* and *Fink* used LIF spectroscopy to observe nicotinamide adenine dinucleotide (NADH) which is a “main substrate for energy transfer in the first complex of the mitochondrial respiratory chain, located in the inner membranes of the mitochondria,” and may have a direct relationship to neurodegenerative disorders like Morbus Parkinson and Alzheimer’s disease. They found that the reduced NADH absorbed at 340nm and the fluorescence was at 465nm. Advances in the development of small, efficient, short pulsed lasers and detections systems allowed “the determination of intra-cellular NADH with high spatial resolution.” They conclude by stating that LIF spectroscopy “is a reliable method which allows the spatial and temporal characterization of functional changes in the brain associated with metabolic changes *in vitro* and *in vivo* [53].”

1.3 Quantum Mechanics of Laser Induced Fluorescence (LIF)

1.3.1 Notation

Since laser induced fluorescence (LIF) relies on atomic transitions in the target atom, or molecule, an understanding of the energy levels, quantum mechanics, and the notation associated with atomic energy levels is required.

We start with a description of the notation used to describe the energy levels of the atom, argon in this case. The *Springer Handbook of Atomic, Molecular, and Optical Physics* states that “a one electron atomic state is defined by the quantum numbers nlm_jm_s , or $nljm_s$, with n and l representing the principle quantum number and the orbital angular momentum quantum number. The allowed values of n are the positive integers, and $l = 0, 1, \dots, n - 1$.” The quantum number j is “the angular momentum obtained by coupling the

orbital and spin angular momenta of an electron, i.e., $j = l + s$,” where s is the spin angular momentum, and $j = l \pm \frac{1}{2}$. “The magnetic quantum numbers m_l , m_s , and m_j represent the projections of the corresponding angular momenta along a particular direction.” These magnetic quantum numbers can take the values; $m_s = \pm \frac{1}{2}$, $m_l = -l, -l + 1, \dots, l$, and $m_j = -j, -j + 1, \dots, j$.

There can be more than one electron with the same principle quantum number. These are said to belong to the *shell* for that number. A *subshell* consists of electrons with that same n and l values and are equivalent. A configuration of N equivalent electrons is designated nl^N , with the N omitted for $N = 1$. “A configuration of several subshells is written $nl^N n' l'^N$. the numerical values of l are replaced by letters in writing a configuration, according to the code:” $l = 0, 1, 2$ becomes s for 0, p for 1, d for 2; and $l = 3, 4, 5, \dots$ becomes f for 3, g for 4, h for 5... Note that e and j are not used [54]. Putting this in a different form for clarity, we get [55]:

L or l : 0 1 2 3 4 5 6 7 8 9 10...

L ; S P D F G H I K L M N ...

l : s p d f g h i k l m n ...

The Pauli “exclusion principle states *no two electrons in an atom can have the same values for the four quantum numbers n , l , m_l , and m_s* ” Stated differently, the principle “states that *no two electrons can exist in an atom with exactly the probability of location.* [56]”. “Thus, the maximum number of equivalent electrons is $2(2l + 1)$. A subshell having this number of electrons is *full, complete, or closed*, and a subshell having a smaller number of electrons is *unfilled, incomplete, or open*. The $3p^6$ configuration represents a full

subshell, and $3s^23p^63d^{10}$ represents a full shell for $n = 3$. [54]” With this in mind, the ground state of argon which has eighteen electrons is: $1s^22s^22p^63s^23p^6$.

Now that we know how to write the ground state, we need to consider how to indicate an electron in an excited state. There are several schemes to indicate an electron is in an excited state and how it couples to the core ion.

The first of these schemes is the “Russell-Saunders coupling, also called L-S coupling.” This is generally used when describing the coupling between two electrons. In this case the interaction energy of the two orbital angular momenta and the spins is greater than the interaction on either electron’s spin to its own orbital momentum [7]. Stated differently, this coupling “takes place when the spin-orbit coupling is weak compared to the electrostatic [57].” In this case the spin angular momenta combine to give; $|s_1 - s_2| \leq S \leq s_1 + s_2$, where S is the total spin momentum. Likewise, the orbital momenta combine to give; $|l_1 - l_2| \leq L \leq l_1 + l_2$, where L is the total orbital momentum. The total orbital momentum and the spin momentum then combine to give; $|L - S| \leq J \leq L + S$, where J is the total angular momentum. The magnitude of J is given by $\sqrt{J(J + 1)}$ [7].

“The combination of a particular S value with a particular L value comprises a spectroscopic term, the notation for which is ^{2S+1}L . the quantum number $2S + 1$ is the multiplicity of the term. The S and L vectors are coupled to obtain the total angular momentum, $J = L + S$, for a level of a term: the level is denoted as $^{2S+1}L_J$ [54].”

The parity of a configuration, or term is defined by “whether $\sum_i l_i$ is even, or odd, the sum being taken over all electrons.” The parity is indicated by the addition of a degree symbol as a superscript to the right of the angular momentum L on odd parity terms, as in the following example: $^2P_{3/2}^0$ [54].

A second type of coupling is the j-j coupling. In this case the electrostatic interaction is weak compared to the spin-orbit interaction [57]. That is, the interaction energy between the spin and orbital momenta of an individual electron is greater than the interaction energy between the spin and orbital momentum of two electrons. In this case the l_i and s_i combine to form j_i , where $|l_i - s_i| \leq j_i \leq l_i + s_i$. The total angular momentum, J , is then obtain by coupling the j_i 's, as $|j_1 - j_2| \leq J \leq j_1 + j_2$ [7].

A third scheme for describing the coupling between and excited electron and the “parent ion” is that developed by Giulio Racah. This coupling “takes place when the electrostatic interaction is weak compared to the spin-orbit interaction of the parent ion, but is strong compared to the spin coupling of the external electron.” This is referred to as (jl), or Racah coupling. “In this case the total angular momentum j of the parent ion and the orbital angular momentum l of the external electron couple together and have a resultant \mathbf{K} ; then \mathbf{K} is coupled with the spin of this electron, and their result is \mathbf{J} [57].” This notation has the form of $nl[K]_J$, or $nl'[K]_J$, where the prime indicates that the parent ion has a total angular momentum of $1/2$ [7]. If the L-S coupling of the parent ion is included as is done in the NIST spectral line tables, the notation has the form: $nl^N \left({}^{2S_1+1}L_{1J_1}^0 \right) nl^{2S+1}[K]_J^0$, where the subscript 1 indicates values from the parent ion. As an example, the energy state that will excited with the laser is the $3s^2 3p^5 \left({}^2P_{3/2}^0 \right) 4s^2 [3/2]_2^0$ [58].

Since this is the notation that is used by NIST [58], this is the notation that will be used throughout the rest of this text except for the section on the CR model where the notation used in Table 1.3.7 is consistent with that of *Keese* [7].

The notation for ArII is similar with the comments that since there is one less electron, the nl^N has $N = 4$, and the (jl) coupling term is not enclosed in brackets; for example: $3s^23p^4(^3P)3d^2P_{3/2}$.

1.3.2 Transition Probabilities

The notation indicates what energy level an atom, or ion is in. It does not give much information about how it got into this state, but it does give information as to what states are available for the atom, or ion to move to. The selection rules dictate which states are available for an atom, or ion in a given state. These selection rules are as follows [54] [59]:

$$\Delta n = \text{arbitrary}$$

$$\Delta l = \pm 1$$

$$\Delta J = 0, \pm 1$$

$$\Delta m = 0, \pm 1$$

These rules indicate that an electron can move to any principle quantum number, but is restricted by the orbital angular momentum to transitions of $l = \pm 1$. For example, a $4s$ electron can go to a $6p$ level, but not to a $6d$ level.

“Every spectral line is now believed to be emitted (or absorbed) in connection with the transition of an atom (or molecule) between two definite (quantized) states, of different energy-content – the frequency of the radiation being exactly proportional to the change of energy [60].” Since the input laser linewidth is on the order of 1MHz, the wavelength of the spectral line will be dominated by the energy difference between the two levels:

$$\lambda = hc(E_i - E_k)^{-1} \quad (1.3.1)$$

Where h is Plank’s constant, c is the speed of light, and E_i and E_k are the upper and lower energy levels [61]. The uncertainty in either energy level is given by:

$$\Delta E_j = \frac{h}{2\pi\tau_j} \quad (1.3.2)$$

where τ_j is the lifetime of level j . The lifetime can be found from [62]:

$$\tau_i = \frac{1}{\sum_{l<j} A_{jl}} \quad (1.3.3)$$

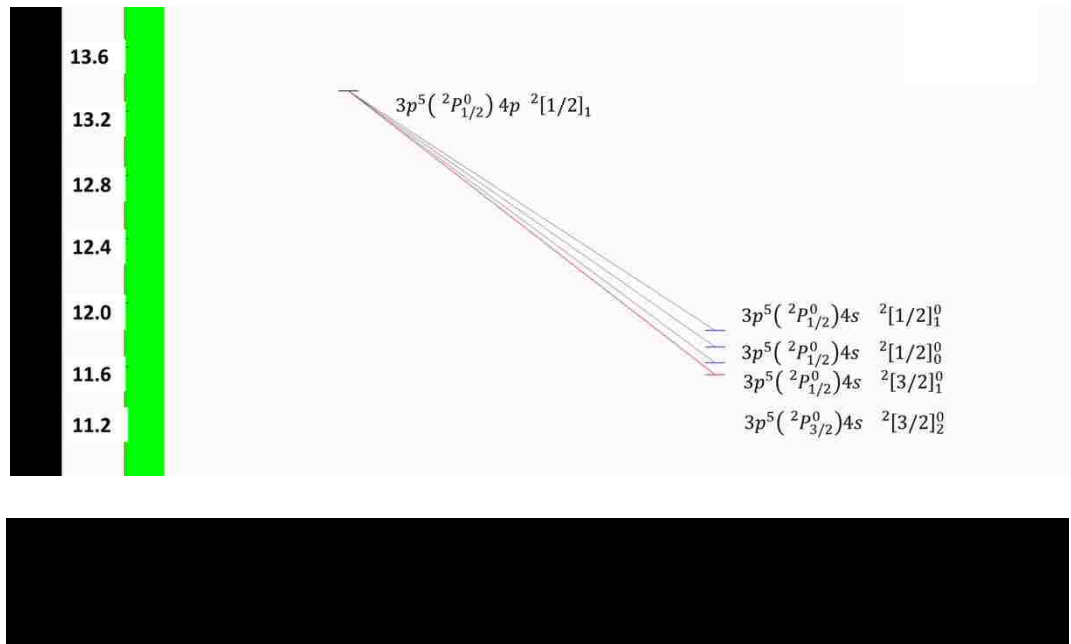
This is the sum of the Einstein transition probabilities, A_{jl} , for spontaneous transitions from level j to level l . The uncertainty in the energy can be written in terms of the frequency, using the relation $E = h\nu$, as [7]:

$$\Delta\nu_{ij} = \frac{1}{2\pi} (\sum_{m<i} A_{im} + \sum_{n<j} A_{jn}) \quad (1.3.4)$$

For Ar I LIF in this research, the linewidth of the 696.7352nm transition from the $3s^2 3p^5 ({}^2P_{3/2}^0) 4s$ state to the $3s^2 3p^5 ({}^2P_{1/2}^0) 4p$ state will depend only on the transitions out of the upper state as the lower state is metastable and transition probabilities out of that state are negligible. Table 1.3.1 lists the transitions out of the upper state and the respective transition probabilities. Using these values, the linewidth is $\Delta\nu = 5.33\text{MHz}$. Since this is much larger than the laser linewidth, “the natural linewidth limits the spectral resolution of the LIF diagnostic [7].” Figure 1.3.1 shows the energy level (Grotrian) diagram for the transitions out of the upper energy state.

Table 1.3.1. Transition probabilities for calculating the linewidth of the Ar I LIF scheme.

Upper State	Lower State	A_{ij} (10^8 s^{-1})
$3s^23p^5(^2P^0_{1/2})4p \ ^2[1/2]_1$	$3s^23p^5(^2P_{3/2})4s \ ^2[3/2]^0_2$	0.0639
$3s^23p^5(^2P^0_{1/2})4p \ ^2[1/2]_1$	$3s^23p^5(^2P_{1/2})4s \ ^2[3/2]^0_1$	0.00087
$3s^23p^5(^2P^0_{1/2})4p \ ^2[1/2]_1$	$3s^23p^5(^2P_{3/2})4s \ ^2[1/2]^0_0$	0.117
$3s^23p^5(^2P^0_{1/2})4p \ ^2[1/2]_1$	$3s^23p^5(^2P_{1/2})4s \ ^2[1/2]^0_1$	0.153



The same procedure was used to determine the ArII natural linewidth. In this case the upper level is $3s^23p^4(^3P)4p \ ^2P^0_{3/2}$, and the lower level is $3s^23p^4(^3P)3d \ ^2P_{3/2}$ with the transition centered at 686.3162nm. Once again, the lower state is metastable, and

the values are given in Table 1.3.2. There are more transitions out of the upper state than are listed here. However, there are no transition probabilities listed for many of them. With this limitation, the linewidth is calculated as, $\Delta\nu = 11.21$ MHz, which is much greater than the laser linewidth, and “the natural linewidth limits the spectral resolution of the ArII LIF diagnostic [7].”

Table 1.3.2. Transition probabilities doe calculating the linewidth of the Ar II LIF scheme.

Upper State	Lower State	A_{ij} (10^8 s ⁻¹)
$(^3P)4p \ ^2P^0_{3/2}$	$(^3P)3d \ ^4D_{5/2}$	0.002
$(^3P)4p \ ^2P^0_{3/2}$	$(^3P)3d \ ^2P_{1/2}$	0.002
$(^3P)4p \ ^2P^0_{3/2}$	$(^3P)3d \ ^2P_{3/2}$	0.024
$(^3P)4p \ ^2P^0_{3/2}$	$(^3P)4s \ ^4P_{5/2}$	0.016
$(^3P)4p \ ^2P^0_{3/2}$	$(^3P)4s \ ^4P_{3/2}$	0.02
$(^3P)4p \ ^2P^0_{3/2}$	$(^3P)4s \ ^4P_{1/2}$	0.0002
$(^3P)4p \ ^2P^0_{3/2}$	$(^3P)4s \ ^2P_{1/2}$	0.64

1.3.3 Zeeman Splitting

The spectral lines of neutrals, or ions, will be split into sublevels in a magnetic field. This effect was first observed by Zeeman in 1897 when he observed “that a discharge, located between the poles of a magnet, emitted broadened spectral lines the widths of which were related to the field strength.” In 1898, Preston used better quality magnets and “observed that the spectral lines were, in fact, not broadened, but split into a symmetrical multiplet about the original spectral line when the atoms of the discharge were in a homogeneous magnetic field.” The original line remained when the field was applied, but additional lines appeared symmetrically about the original and the displacement was proportional to the magnetic field strength.

“Further observations showed that the radiations emitted in the presence of a magnetic field were polarized” This contrasts with the radiation from a conventional discharge with no magnetic field, which is non-polarized. “The center line of the Zeeman triplet was found to be plane polarized” with the direction of polarization parallel to magnetic field, “while the two satellites were plane polarized” perpendicular to the magnetic field. “These orientations were classified as π and σ transitions, respectively [56].”

The general equation that gives the change in energy due to the magnetic field is:

$$\Delta E = \mu_B B g_j M_j \quad (1.3.5)$$

where ΔE is the change in energy, μ_B is the Bohr magneton, B is the magnetic field strength in Tesla, g_j is the Landé factor for each level, and M_j is the magnetic orbital quantum number [63].

The magnetic orbital quantum numbers, M_j , follow the normal selection rules, so they can change at most by ± 1 . That is:

$$\Delta M_j = 0, \pm 1 \quad (1.3.6)$$

with:

$$M_j = J, J - 1, J - 2, \dots - J \quad (1.3.7)$$

“With the addition that the combination $M = 0 \rightarrow M = 0$ is forbidden for $\Delta J = 0$ [64].”

Marr states that “transitions for $\Delta M_j = 0$ are called the π components and result in the original emission line, while transitions with $\Delta M_j = \pm 1$ provide satellite (σ components) on either side of the original line [56].”

Most of the Landé factors can be found on the NIST website under the tab for LEVELS [58]. If the Landé factor is not available on the NIST website, it can be calculated using the following formula:

$$g_j = 1 + \frac{J(J+1) - L(L+1) + S(S+1)}{2J(J+1)} \quad (1.3.8)$$

where J is the total angular momentum, L is the orbital angular momentum, and S is the angular momentum, or spin [63]. These values can be found from the term symbol for a given electron configuration and are listed on the NIST website. The term symbols have the form:

$$^{2S+1}L_{J=L\pm S} \quad (1.3.9)$$

For a two-level transition, the energy difference would be:

$$\Delta E = \mu_B B (g_1 M_1 - g_2 M_2) \quad (1.3.10)$$

So, we need to know the Landé factors and the magnetic orbital quantum numbers for the given transition.

For the neutral Argon line, the transition is from the $3s^23p^5(^2P_{3/2}^0)4s^2[3/2]_2$ energy state to the $3s^23p^5(^2P_{1/2}^0)4p^2[1/2]_1$ energy state. For both states, $L = P = 1$, and $S = 1/2$. For the lower state, $J = 3/2$, and $M_j = 3/2, 1/2, -1/2, -3/2$. And, for the upper state, $J = 1/2$, so $M_j = 1/2, -1/2$. This is shown graphically in Figure 1.3.2. The Landé factors for these states can be found on the NIST website.



In addition to the magnitude of the Zeeman splitting, there is the intensity of the lines once they are split. There are three different scenarios regarding the value of the total angular momentum for a given transition: $J \rightarrow J$, $J \rightarrow J + 1$ and $J \rightarrow J - 1$. The intensities of all Zeeman components for a $J \rightarrow J$ transition are given by the expressions [56]:

$$M \rightarrow M (\pi \text{ components}) I_{\pi} = 4KM^2 \quad (1.3.11)$$

$$M \rightarrow M \pm 1 (\sigma \text{ components}) I_{\sigma} = K (J \pm M + 1) (J \mp M) \quad (1.3.12)$$

The intensities of all Zeeman components for a $J \rightarrow J + 1$ transition are given by the expressions [56]:

$$M \rightarrow M (\pi \text{ components}) I_{\pi} = 4K (J + M + 1) (J - M + 1) \quad (1.3.13)$$

$$M \rightarrow M \pm 1 (\sigma \text{ components}) I_{\sigma} = K (J \pm M + 1) (J \pm M + 2) \quad (1.3.14)$$

Since the initial and final states can be interchanged the intensities for a $J \rightarrow J - 1$ are given by the expression (1.7a and 1.7b). K is a constant related to the initial line intensity. The total intensity of all Zeeman components is given by:

$$I = \sum_{M'M''} I_{\pi} + \sum_{M'M''} I_{\sigma} \quad (1.3.15)$$

The statistical weight of any given Zeeman components is thus:

$$w = \frac{1}{2} I_{\pi} / I, \text{ or } w = \frac{1}{2} I_{\sigma} / I \quad (1.3.16)$$

the $\frac{1}{2}$ factor being related to the symmetry of the Zeeman pattern [63].

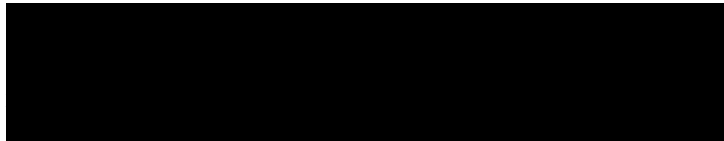
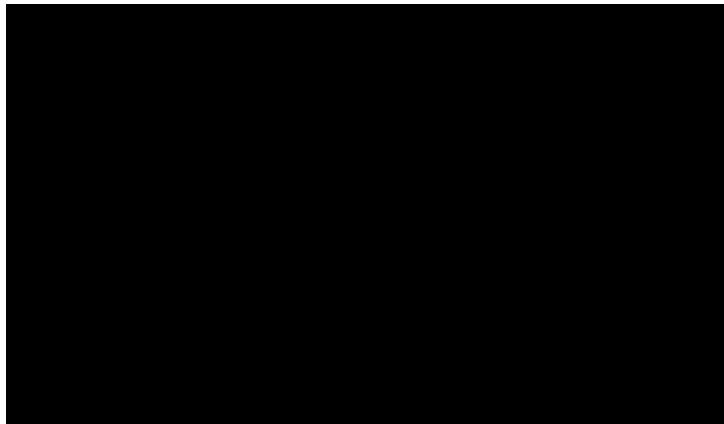
Table 1.3.3 shows the values of M , g_1 , g_2 , $(g_1 - g_2)M$, the change in energy, ΔE , in Joules and GHz, and the weight of the lines for the $\Delta M = 0$ transitions for neutral argon. Table 2 shows the same values for the $\Delta M = 1$ transitions. The values for the symmetrically negative shift are not shown as those values are the same, only negative. The data for the Zeeman splitting shown in Section 3.1 is in good agreement with the value shown in Table 1.3.4. This is shown graphically in Figure 1.3.3.

Table 1.3.3. Zeeman splitting for the π transitions ($M = M_1 = M_2$).

M	g_1	g_2	$(g_1 - g_2) M$	$\Delta E (*10^{-24})$	$\Delta E/h = \Delta \text{GHz}$	Weight
1/2	1.506	1.38	0.063	0.0257	0.0388	0.25
-1/2	1.506	1.38	-0.063	-0.0257	-0.0388	0.25

Table 1.3.4. Zeeman Splitting for $\Delta M = 1$ ($M_1 - M_2 = 1$) (not showing the symmetric negative shift).

M_1	M_2	g_1	g_2	ΔE (*10 ⁻²⁴)	$\Delta E/h=\Delta\text{GHz}$	Ave Zeeman Shift (GHz)	Weight
3/2	1/2	1.506	1.38	0.6402	0.9662	0.9274	0.1875
1/2	-1/2	1.506	1.38	0.5888	0.8886	0.9274	0.0625



As will be described in Section 1.4, two different schemes were tried for argon ions (ArII). For the 688.8512nm line, no useful data was acquired. As such, the Zeeman splitting for this line was not calculated. For the 686.3162nm ion line, the transition is from the $3s^2 3p^4 ({}^3P) 3d [{}^2P]_{3/2}$ energy level to the $3s^2 3p^4 ({}^3P) 4p [{}^2P^0]_{3/2}$ energy level. Once again, $L = P = 1$ and $S = 1/2$ for both levels. And, since $J = 3/2$ for both levels, $M_j = 3/2$,

1/2, -1/2, -3/2. The Landé factor for the upper energy level can be found on the NIST website as 1.244. The Landé factor for the lower level can be calculated from Equation 2 as 1.333. The values for this transition are shown in Table 1.3.5, and Table 1.3.6. As will be shown in Section 3.5, these values are in good agreement with the measured Zeeman splitting.

Table 1.3.5. Zeeman splitting for the π transitions ($M = M_1 = M_2$).

M_1	M_2	g_1	g_2	$\Delta E (*10^{-24})$	$\Delta E/h = \Delta \text{GHz}$	Weight
3/2	3/2	1.333	1.244	0.0547	0.0825	0.225
1/2	1/2	1.333	1.244	0.0182	0.0275	0.025

Table 1.3.6. Zeeman Splitting for $\Delta M = 1$ ($M_1 - M_2 = 1$) (not showing the symmetric negative shift).

M_1	M_2	g_1	g_2	ΔE (*10 ⁻²⁴)	$\Delta E/h = \Delta \text{GHz}$	Ave Zeeman Shift	Weight
3/2	1/2	1.333	1.244	0.4894	0.7386	.7936	0.075
1/2	-1/2	1.333	1.244	0.5258	0.7936	.7936	0.100
-1/2	-3/2	1.333	1.244	0.5623	0.8486	.7936	0.075

The measured LIF intensity will not have a Dirac delta function line shape as shown in Figure 1.3.2. *Keesee* states that the LIF intensity line shape will be “a convolution of thermal (Doppler) broadening and Zeeman splitting. Because the Doppler width and the Zeeman splittings are on the order of gigahertz, other effects such as the natural linewidth of the line and the Stark broadening are ignorable [7].” Boivin states that “Doppler broadening can be understood if the motion of a particle is considered, i.e., the motion of a radiating particle toward or away from an observer leads to a frequency shift of the emitted line, the Doppler shift. In plasmas, the random motions of the radiating particles cause a Doppler broadening of the lines [61].” As such, the fitting function for this data was based on a double Gaussian assuming thermal doppler broadening of the signal, Zeeman splitting from the background magnetic field, and a possible Doppler shifted frequency, $f - f_0$:

$$I(f) = I(f_0) \left(e^{-\left(\frac{(f-f_0-\Delta f_z-\frac{V_0 f_0}{c})^2}{\alpha_D T}\right)} + a_1 e^{-\left(\frac{(f-f_0+\Delta f_z-\frac{V_0 f_0}{c})^2}{\alpha_D T}\right)} \right) \quad (1.3.17)$$

Where

$$\alpha_D = \frac{2k_B f_0^2}{mc^2} \quad (1.3.18)$$

And $I(v)$ is the measured LIF signal intensity, $I(f_0)$ is the amplitude of the measured signal, Δf_z is the is the Zeeman shift, T is the temperature in eV, $V_0 f_0/c$ is the overall Doppler shift due to bulk flow of the species observed, and “ α_D scales the width of the thermal broadening for the argon species of mass m . [7]”

1.3.4 Spectral Line Broadening Mechanisms

There are several mechanisms that contribute to the broadening of spectral lines. These include Doppler broadening (discussed above), *Stark* and *Zeeman* broadening, instrument broadening, and power broadening. *Boivin* provides a good analysis of the *Stark* and *Zeeman* broadening theory and calculations, and states that the electron density, N_e , of the plasma should be greater than 10^{15} cm^{-3} ($N_e > 10^{15} \text{ cm}^{-3}$) for *Stark* broadening to have an impact on the width of the spectral lines [61]. Since the normal electron density in HelCat is on the order of $N_e \sim 10^{12} \text{ cm}^{-3}$, *Stark* broadening should not have a measurable effect.

For Zeeman broadening, the π and σ components were calculated were calculated in Section 1.3.3, along with their relative statistical weights. The π components are symmetrically distributed around the central resonant frequency. The distribution is assumed to be Gaussian and the variance given by:

$$\sigma^2 = \frac{\sum_i (\lambda_i - m_\lambda)^2}{n} \quad (1.3.19)$$

where λ_i is a Zeeman component wavelength, m_λ is the average wavelength (the central wavelength in this case), and n is the number of Zeeman splittings. The full width at half maximum (FWHM) of the broadened line is given by [61]:

$$FWHM = \Delta\lambda_{z\pi} = 2(2Ln2)^{1/2}\sigma \quad (1.3.20)$$

Using the values in Table 1.3.3, the Zeeman broadening for the π components is $\Delta\lambda_{z\pi} = 0.0913 \text{ GHz}$ which is negligible when compared to the Doppler broadening which is used to find the temperature and is on the order of 2 GHz as shown in Figure 3.1.1.

The σ components can have Zeeman broadening as well. In this case, the average wavelength is calculated first. This give the average shift from the central frequency, and

is used as m_l in Equation 1.3.19. Then the calculations are performed as before, and using the values in Table 1.3.4, $\Delta\lambda_{z\sigma} = 0.0913 \text{ GHz}$, which is the same as the broadening for the π components. (This is pure coincidence, it does not always happen this way.) As such, Zeeman broadening should not be an issue for this research.

For the instrument broadening, there are two distinct types. One is associated with the laser linewidth. As will be discussed in Section 2.2.1, the linewidth of the laser is less than 1MHz ($\lambda_{\text{laser}} < 1\text{MHz}$). The other instrument broadening is related to the dispersion of fluorescence detection system. Since the fluorescence detection system uses (Section 2.2.3.2) a 1nm bandpass filter and a photomultiplier, broadening from the collection optics is negligible [61].

The last broadening mechanism is saturation, or power broadening. As *Goeckner* and *Goree* point out, “saturation occurs when the stimulated photon emission rate is equivalent to the photon absorption rate and greater than the spontaneous photon emission rate. Increases in laser intensity will not change this balance. When saturation occurs at frequencies in the wings of the laser line, the measured fluorescence line is broadened [65].” If this broadening mechanism is not addressed, errors in the temperature measurement will likely ensue [61], [37].

Goeckner and *Goree* state that “optimizing the laser intensity requires a balance of a strong fluorescence signal with minimal saturation broadening.” Three experimental methods for optimizing the laser intensity can be employed. The first involves setting the laser to get a good fluorescence signal, then while keeping the plasma parameters constant, reducing the laser power. The magnitude of the fluorescence signal is recorded and plotted

on a log-log plot. The optimum laser intensity occurs when the slope of the line is 0.015 [65].

The second method involves changing the laser intensity again. However, in this method, the fluorescence intensity is plotted versus laser power. This should display two asymptotic shapes; one for high and one for low laser intensities. “The optimum laser intensity is one-half the intensity at which the asymptotes intersect [65].”

The third method for optimizing the laser intensity involves finding the maximum signal strength and then reducing the laser intensity until the fluorescence signal is reduced by a factor of 5 [65].

As shown in Section 2.3.1.1, method number two was used in the course of this research. The laser power was increased and a plot of neutral LIF fluorescence response versus laser power was created. From the plot it is easy to see that the LIF signal does saturate above ~ 40 mW. Therefore, 20 mW was chosen as the working power for the laser so as to be below the saturation region, but still collecting a strong fluorescence signal.

1.3.5 CR model

One major drawback of LIF is that it can only probe one atomic, or ionic state at a time. A laser tuned to each of the transitions of the plasma would be required to get a complete description of the plasma. Since it is the neutral ground state that is of interest, a Collisional-Radiative (CR) model was employed to give an estimate of the ground state. There are several different CR models available [66], [67], [68]. They all have similarities which include:

1. Electron impact excitations from the ground state and de-excitations,

2. Electron impact transitions between two excited levels,
3. Electron impact ionization and recombination to the ground state,
4. Electron impact ionization and recombination to an excited state,
5. Radiative recombination to the ground state, or an excited state,
6. Radiative re-excitation

The one used by *Keesee* [7] seemed to be suited to HelCat plasmas, and The investigator cooperated with the adoption of this technique.

This model was originally developed by *Vlček* and allows for the input of an arbitrary electron energy distribution function (EEDF) [69]. This model also includes “sixty-five effective energy levels of neutral argon” along with “atom-atom inelastic collisions and diffusion losses [7].” The code was modified by *Bogaerts et al.* “to include more details of the two 4s metastable levels and fast argon ion and atom impact ionization [70].” This code was further modified by *Keesee* “to match the physical dimensions of HELIX (the hot helicon experiment at West Virginia University) and include only the CR processes relevant to our plasma conditions [37].” The code was modified again by *D. M. Fisher* for use in this research to reflect the physical dimensions of HelCat, and be more user friendly. More information about the Cr model and the Fortran code used in the CR model are given in Appendix B.

The dissertation by *Keesee* states “the effective levels used in the CR model code are given in Table 1.3.7, numbered in order of their ionization energies. Also included in the table is the excitation energy in eV for electron-impact excitation from the ground state, the statistical weight (number of states of that energy, $g_n = 2J+1$), and whether the transition is optically allowed, parity-forbidden, or spin-forbidden for each level. The argon

energy levels can be divided into two subgroups, one in which the parent ion has a quantum number $j = 1/2$ denoted by a prime, and the other in which the parent ion has a quantum number $j = 3/2$. A diagram of the argon energy levels divided into the two subsystems is shown in Figure 1.3.4 with the effective level numbers used in the CR model.” Table 1.3.7 was reproduced from *Keese* [7].

Table 1.3.7 The 65 effective argon levels included in the CR model code and properties associated with excitation by electrons from the ground state to each level. A is an optically allowed, P is a parity-forbidden, and S is a spin-forbidden transition

Effective level number, n	Designation npqnl[KJ]	Excitation energy (eV)	Statistical weight, gn	Nature of transition
1	3p ⁶ 1s	0.000	1	-
2	4s [3/2] ₂	11.548	5	S
3	4s [3/2] ₁	11.624	3	A
4	4s' [1/2]0	11.723	1	S
5	4s' [1/2]1	11.828	3	A
6	4p [1/2]1	12.907	3	P
7	4p [3/1]1,2 + [5/2]2,3	13.116	20	P
8	4p' [3/2]1,2	13.295	8	P
9	4p' [1/2]1	13.328	1	P
10	4p [1/2]0	13.271	1	P
11	4p' [1/2]0	13.480	1	P
12	3d [1/2]0,1 + [3/2]2	13.884	9	S
13	3d [7/2]3,4	13.994	16	S
14	3d' [3/2]2 + [5/2]2,3	14.229	17	P
15	5s'	14.252	4	A
16	3d [3/2]1 + [5/2]2,3 + 5s	14.090	23	A
17	3d' [3/2]1	14.304	3	A
18	5p	14.509	24	P
19	5p'	14.690	12	P
20	4d + 6s	14.792	48	A
21	4d' + 6s'	14.976	24	A
22	4f	15.083	28	-
23	4f	14.906	56	-
24	6p'	15.205	12	-
25	6p	15.028	24	-
26	5d' + 7s'	15.324	24	A
27	5d + 7s	15.153	48	A
28	5f', g'	15.393	64	-
29	5f, g	15.215	128	-
30	7p'	15.461	12	-
31	7p	15.282	24	-
32	6d' + 8s'	15.520	24	-
33	6d + 8s	15.347	48	A
34	6f', g', h'	15.560	108	-
35	6f, g, h	15.382	216	-
36	8p'	15.600	12	-
37	8p	15.423	24	-
38	7d' + 9s'	15.636	24	-
39	7d + 9s	15.460	48	-
40	7f', g', h' i'	15.659	460	-
41	7f, g, h, i	15.482	320	-
42	8d', f, ...	15.725	240	-
43	8d, f, ...	15.584	480	-
44	9p', d', f', ...	15.769	320	-
45	9p, d, f, ...	15.592	640	-
46	10s', p', d', f', ...	15.801	400	-
47	10s' p, d, f, ...	15.624	800	-
48	11s', p', d', f', ...	15.825	484	-
49	11s, p, d, f, ...	15.648	968	-
50	12s', p, d', f', ...	15.843	576	-
51	12s, p, d, f, ...	15.666	1152	-
52	13s', p', d', f', ...	15.857	676	-
53	13s, p, d, f, ...	15.680	1352	-
54	14s', p', d', f', ...	15.868	784	-
55	14s, p, d, f, ...	15.691	1568	-
56	15s', p', d', f', ...	15.877	900	-
57	15s, p, d, f, ...	15.700	1800	-
58	16s', p', d', f', ...	15.884	1024	-
59	16s, p, d, f, ...	15.707	2048	-
60	17s', p', d', f', ...	15.890	1156	-
61	17s, p, d, f, ...	15.713	2312	-
62	18s', p', d', f', ...	15.895	1296	-
63	18s, p, d, f, ...	15.718	2592	-
64	19s', p', d', f', ...	15.899	1444	-
65	19s, p, d, f, ...	15.722	2888	-

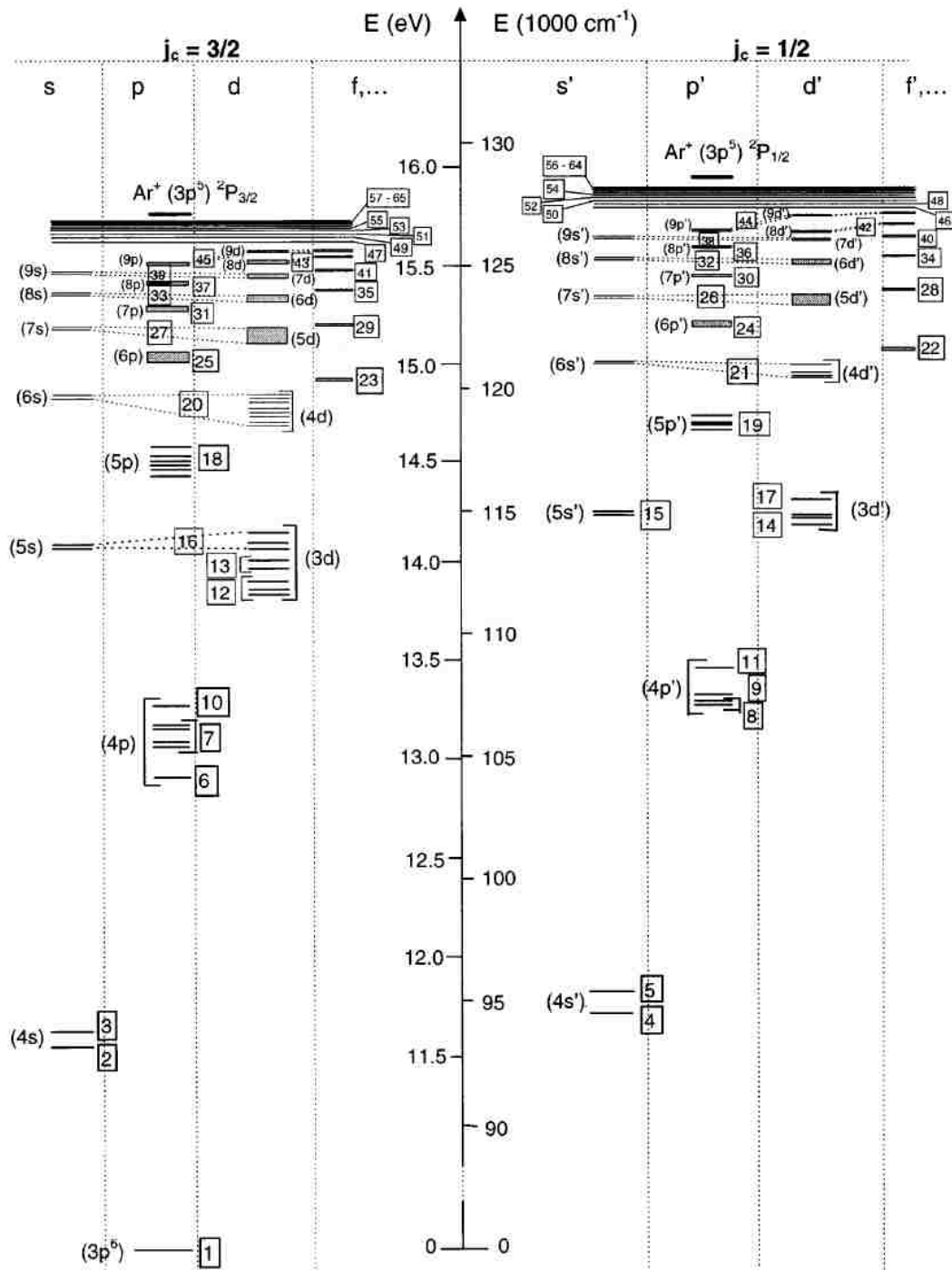


FIG. 1. Energy level scheme of the argon atom, illustrating all the effective levels incorporated in the model.

Keesee describes the processes included in the CR model with the following: “the density of the ground state ($n = 1$) at the edge of the plasma is calculated using the ideal gas law, $nI=P/kT$, where P and T are the source pressure and neutral argon temperature, respectively. A non-uniform ground state density spatial profile can be defined in the model. The sixty-four equations describing the densities of the excited states based on all included processes are simultaneously solved at each time step until a convergence is reached. The processes included in our version of the CR model are:

1. Electron impact excitation and de-excitation between all levels.
2. Thermal argon atom impact excitation and de-excitation between all levels.
3. Radiative decay and photo-excitation between all levels.
4. Electron impact ionization from and three-body recombination to all levels.
5. Thermal argon atom impact ionization from and three-body recombination to all levels.
6. Radiative recombination to all levels.
7. Diffusion and consequent de-excitation at the walls of metastable levels. (The lifetime of the other levels makes diffusion negligible.)
8. Two- and three-body collisions with thermal ground state atoms for metastable levels. (The densities of the other levels make these types of collisions negligible.)
9. Metastable-metastable collisions causing ionization of one of the atoms. (The densities of the other levels make these types of collisions negligible.)

All processes, except diffusion, are calculated locally at each radial position. The calculation of parameters for each of the above processes is” described in detail in by *Keesee* [7].

The electron energy distribution function (EEDF) used in the code was based on measured electron density and radial temperature profiles collected with an RF-compensated swept probe described in Section 2.6. *Keesee* states that “a spatially localized, energetic electron beam could then be added to the Maxwellian distribution to study the effects of a beam on the neutral argon excited levels. The radial profiles of electron density, the EEDFs, and the fill pressure measured at the edge of the chamber are input variables for the code. The radial profile of the neutral ground state density in the code is varied to find the ground state profile that is most consistent with the spectroscopic and fluorescence measurements [7].”

The code has built in ground state profiles that could be used to model a depletion in the ground state density. These include:

- 1: Flat ground state profile
- 2: Parabolic profile with depletion percentage, P
- 3: Profile using Langmuir Probe (LP) data for certain parameters
- 4: Profile with depletion of some width (wid)
- 5: 2 off-axis depletions. of width (wid) centered at some radius r
- 6: user defined profile

We added the user defined profile as the first five profiles did not do an adequate job of fitting the experimental data. The profile we used was based on a double depletion and a “pchip” fit in MatLab. The central depletion region was 30% below the fill pressure density and 2 cm wide, and the second depletion region was 50% below the fill pressure density with a sloped profile centered at 5 cm. It was found that this profile could be adjusted to

match the data well, and this profile could be adjusted, and an electron beam added to fit the data as well. This is discussed in more detail in Section 3.3.

1.4 LIF Schemes

Laser induced fluorescence (LIF) has been used for many years and in many different fields.

Boivin states that “in a typical LIF measurement, the frequency of a very narrow bandwidth laser is swept across a collection of ions or atoms that have a thermally broadened velocity distribution. The atoms or ions absorb a photon when it is at the appropriate frequency in its rest frame. After a short time, depending on the lifetime of the excited state, the atom or ion emits a photon of either the same frequency or another frequency. Measurement of intensity of the emitted photons as a function of laser frequency constitutes a LIF measurement. The shift in the center frequency and the width of the absorption spectrum feature for the entire ensemble of atoms or ions is then used to determine the flow velocity and temperature of the particle distribution. Optimally, a three-level system involving an absorption line different from the fluorescence emission is used to reduce the effects of scattered light and background emission at the pump wavelength. [34]”

There are multiple methods for making LIF measurements. These include, but are not limited to the three-level scheme, the two-photon absorption laser induced fluorescence (TALIF), and the single line method.

The TALIF method was first developed by Magee et al, in 2012 at West Virginia University. This method uses two counter-propagating laser beams of the same wavelength

to excite ground state neutral hydrogen atoms. *Magee, et al*, state that because “TALIF is absorption spectroscopy, the measured signal is related to the Doppler-shift of the absorbed light, rather than the emitted light [71].” This method of LIF has been extended to other gases and is becoming more popular [5], [72], [13], [12], and [73].

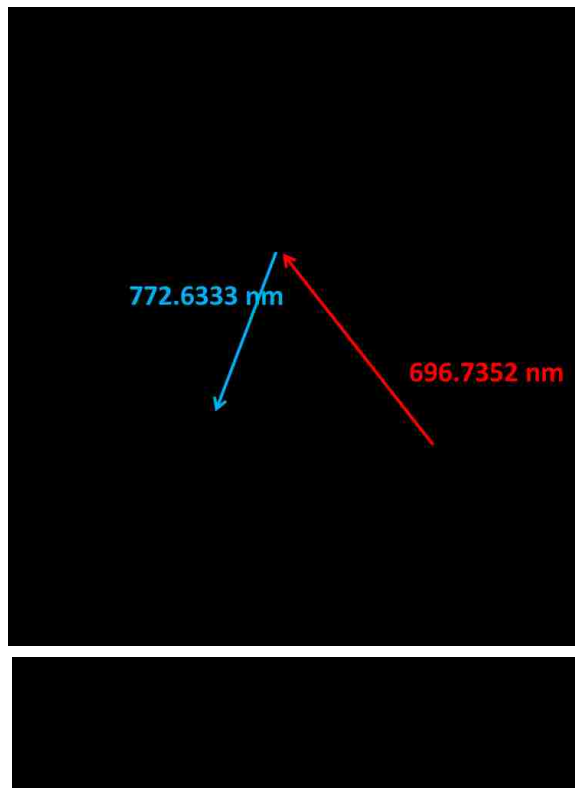
Another method of LIF is to use a laser with a broadband spectrum (FWHM ~5nm) and pump the entire span. The observed fluorescence was at the same wavelength as the pumped line, but can be distinguished because the bandwidth of the incident laser was considerably broader than the detection wavelength [74].

For the research presented here, the three-level LIF scheme is employed where the laser pumps a neutral, or ion, from a lower energy state to a higher energy state. As the particle, neutral or ion, decays from the higher state, the light emitted is observed. Generally, the pumped state is a metastable and the decay from the excited state back to this state is not statistically probable. In addition, *Schef, et al*, state that “metastable states can decay radiatively only by forbidden transitions...While a ‘normal’ excited state in a neutral, or lowly charged ion has a lifetime of a few nanoseconds, a metastable state may live for milliseconds, or even seconds [75].” This ensures that the light emitted as the particle drops to a lower energy state is not at the same wavelength as the light needed to pump it. There are many three-level schemes, some of which have been used by [32], [7], [45], and [43]. The best way to plot the energy levels of interest on an energy level, or Grotrian diagram. In these diagrams the vertical axis indicates increasing energy upward, and the horizontal axis is “given over to the scheme of classification of states by orbital and spin quantum numbers [76].” The next sections describe the schemes used in this research.

1.4.1 The 696 nm Neutral Line

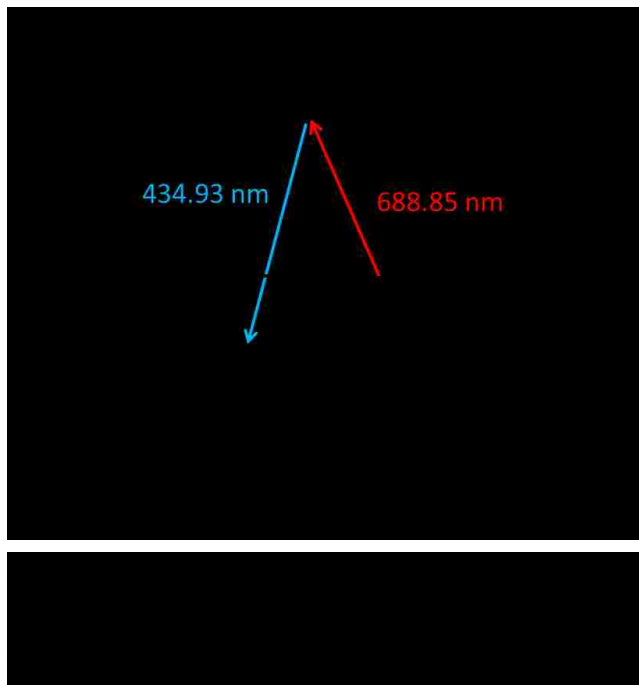
The LIF scheme used for observation of the neutral argon (ArI) particles was based on the three-level scheme shown in Figure 1.4.1. This scheme starts by pumping the $(^2P_{3/2}^0)4s\ ^2[3/2]_2^0$ metastable state with 696.7352nm laser light. This pushes the metastable neutral argon to the excited state $(^2P_{1/2}^0)4p\ ^2[1/2]_1$ level. This level then decays to the $(^2P_{1/2}^0)4s\ ^2[1/2]_0^0$ state by the emission of a photon at 772.6333nm. Both transitions have a relative intensity of 10,000 [58]. This relative intensity is important as it indicates that this is a strong resonance line in the ArI spectrum.

This is the same scheme used by Bieber, et all in 2013. In that research, the quoted values for the pump laser and the observed wavelength are the NIST values for these transitions in “air” as opposed to “vacuum” [48].



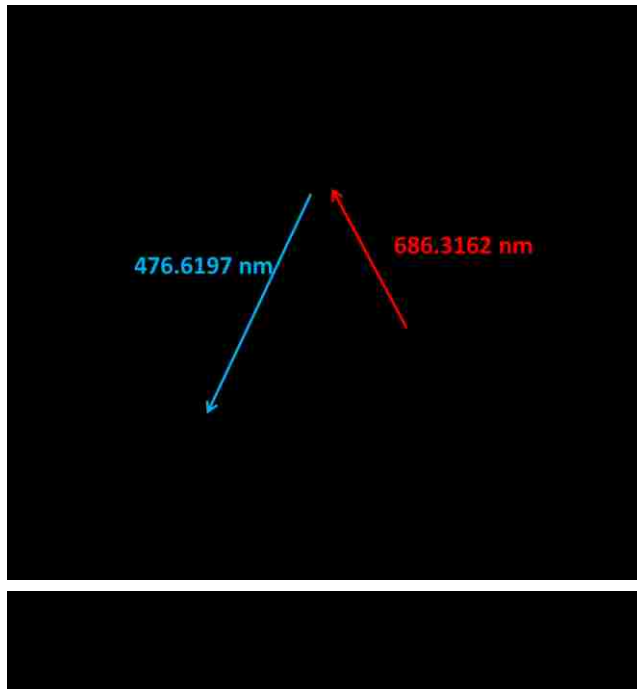
1.4.2 The 688 nm Ion Line

Two different three-level LIF schemes were tried for the argon ion (ArII) measurements. The first was a scheme proposed by Severn [32], Figure 1.4.2. For this scheme, the laser is set to pump the $(^3P)3d\ ^4F_{7/2}$ ion state with 688.8512nm light. This pushes the ion to the $(^3P)4p\ ^4D_{7/2}^0$ state which decays to the $(^3P)4s\ ^4P_{5/2}$ state by the emission of a photon at 434.9286nm. The excitation transition has a relative intensity of 26, while the de-excitation transition has a relative intensity of 1995 [58]. The low relative intensity for the excitation line made it unusable for this research as will be detailed in Section 2.3.2.



1.4.3 The 686 nm Ion Line

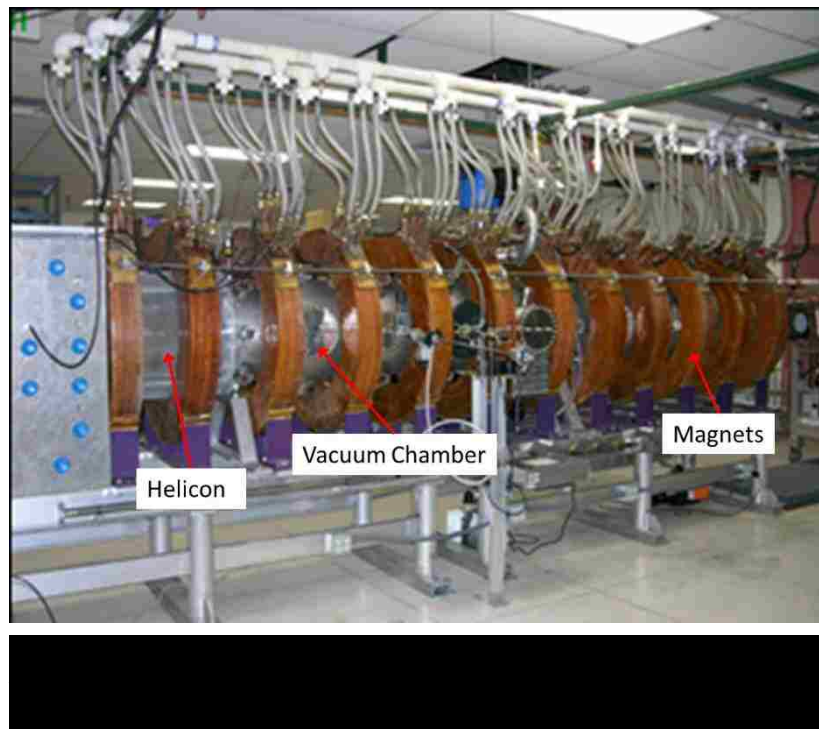
The second three-level ArII LIF scheme use was proposed by Dr. Earl Scime [77]. This scheme was to use 686.3162nm laser light to pump the $(^3P)3d\ ^2P_{3/2}$ state to the $(^3P)4p\ ^2P_{3/2}^0$ state. This would then decay to the $(^3P)4s\ ^2P_{1/2}$ state with the emission of a photon at 476.6197nm, Figure 1.4.3. These transitions have relative intensities of 112 for the excitation line, and 2344 for the de-excitation line [58]. Although the relative intensity for the excitation line is not large, it did provide results as will be discussed in Section 2.3.3.



Chapter 2: Experimental Setup and Techniques

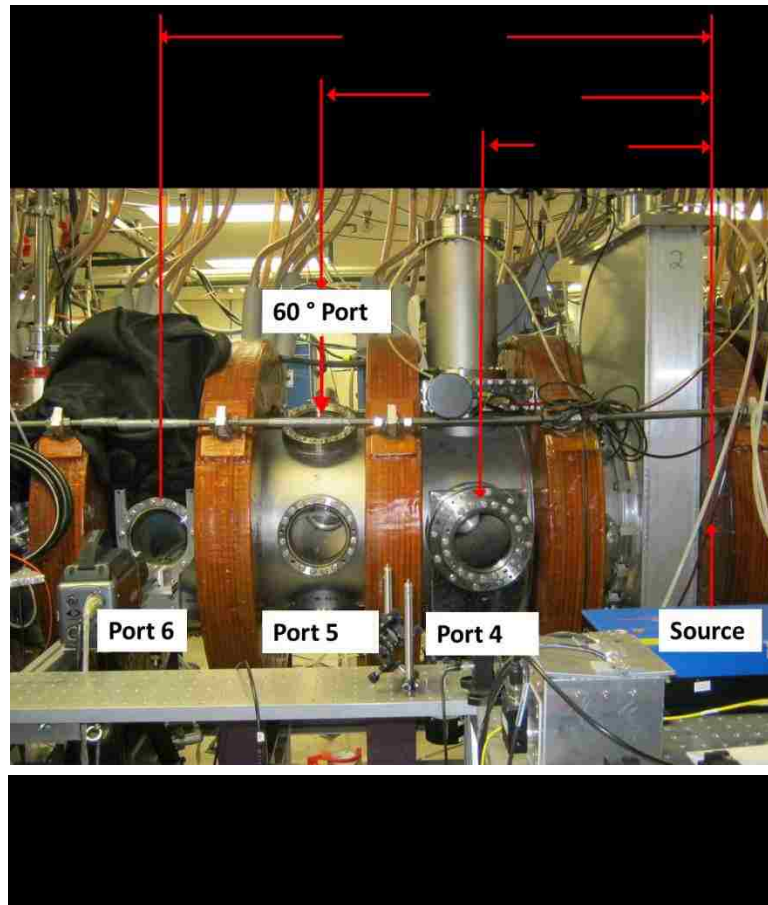
2.1 The HelCat Plasma Device

All of the experiments described in this text were performed using the HelCat (Helicon-Cathode) linear plasma device, shown in Figure 2.1.1. HelCat is a “4 m long, 50 cm in diameter cylindrical vacuum chamber in two 2-meter sections. Each section has multiple 10 in and 8 in conflat ports. The chamber has a large rectangular window (20 cm × 40 cm) at the end of the chamber (at the cathode location) which provides a good view of the entire cross-section of the chamber. Vacuum is maintained at $\sim 5 \times 10^{-7}$ Torr (6.0×10^{-5} Pa) by two 1000 L/min turbo molecular pumps, one at the mid-chamber and the other at the end behind the cathode source.” The pumps have independent valves and backing systems. A roughing pump system ($p \sim 0.667$ Pa) is installed for multiple probe diagnostic systems, along both sides of the linear vacuum chamber [78].



Magnetic fields are produced by thirteen water-cooled, solenoidal electromagnetic coils, as shown in Figure 2.1.1. For these experiments, the magnet current was maintained at 100A, corresponding to a magnetic field of 440G (44mT). Magnetic field ripple is measured to be $< 1\%$ along the chamber axis and $\sim 3\%$ at the plasma edge near $r = 20$ cm [79].

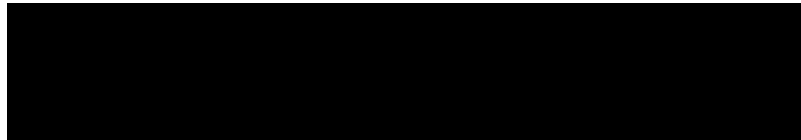
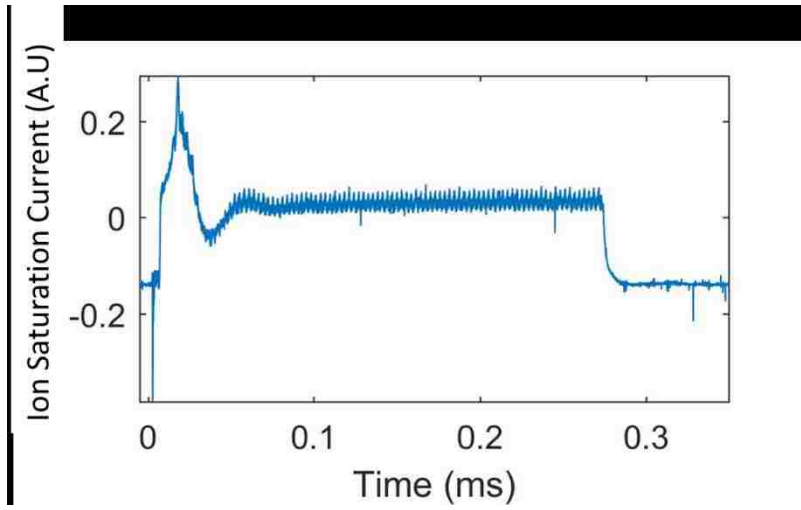
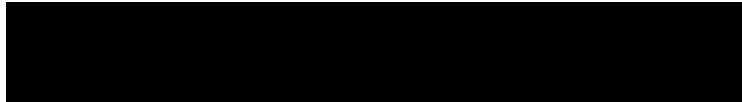
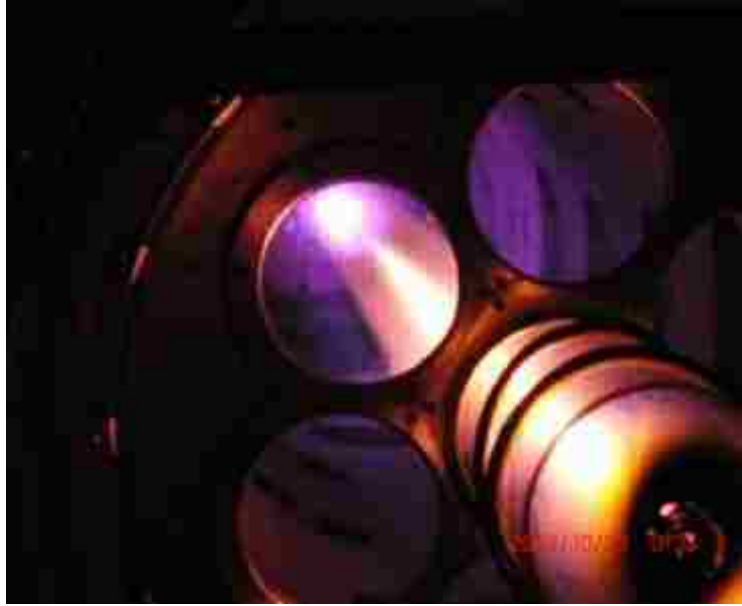
The vacuum chamber has four 10 in ports (Port 4) at 47 cm from the source. These ports are arranged azimuthally, such that they are at 0° , 90° , 180° , and 270° with 0° being at the horizontal mid-plane of the chamber. The chamber also has 8 in. ports located 87.5 cm (Port 5) and 127.5 cm (Port 6) from the source. There are multiple ports at each location arranged so that there is a port every 60 degree around the circumference of the chamber; that is, 0° , 60° , 120° , 180° , 240° , and 300° . For this paper, Port 4, Port 5, and Port 6 refer

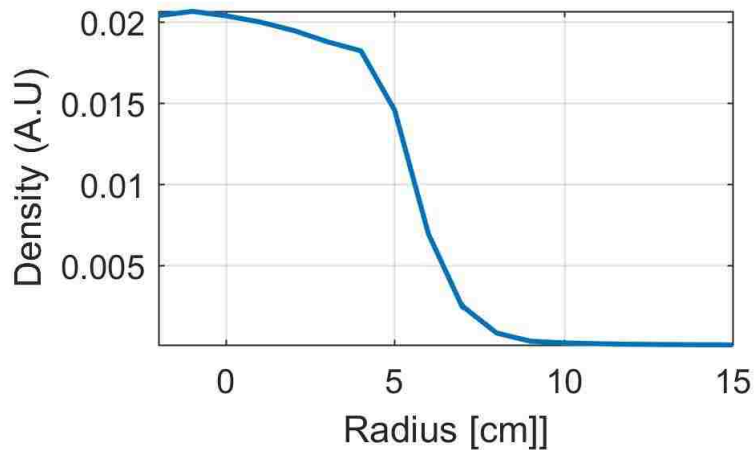


to the ports located at 0° unless otherwise specified. The rectangular window on the north end of the machine was used for axial laser injection and optical alignment. The helicon source is to the right of the rectangular aluminum box in Figure 2.1.2.

For these experiments, a Helicon antenna 25 cm long and 13 cm in diameter with a single $m = 1$ helical half-twist [80] was used to create argon plasma. The helicon source was operated in pulsed mode at 10 MHz with approximately 1800 W of power, a pulse length of 250 ms and a rep-rate of 500 mHz. Power was provided to the antenna network via a three-stage amplifier, i.e., an Agilent 33120A Function Generator/Arbitrary Waveform Generator provides a user defined AM modulated pulse to a Henry Radio, Inc. Model SS750HF RF Linear Solid-State Power Amplifier which amplifies the pulse and directs it to an 8K Ultra HF Linear Communications Amplifier, also by Henry Radio, Inc. Figure 2.1.3 shows a typical helicon plasma discharge.

The typical helicon plasma time behavior is depicted in Figure 2.1.4. Shown is the typical ion saturation current measurement from a single tip Langmuir probe at the center of the plasma (chamber), at Port 6, with an operating pressure of 10 mTorr. The probe is referenced to the grounded vacuum chamber. The initial peak in the signal is due to high RF power used at the beginning of the discharge for neutral gas break down. The steady state section of the discharge, ~ 100 ms to ~ 250 ms, is the region of the plasma used for data measurements, and is the result of the user defined pulse generated by the function generator. The radial ion density profile for 10 mTorr argon is shown in Figure 2.1.5. For a more complete description of the HelCat plasma device, see References [79], and [80].





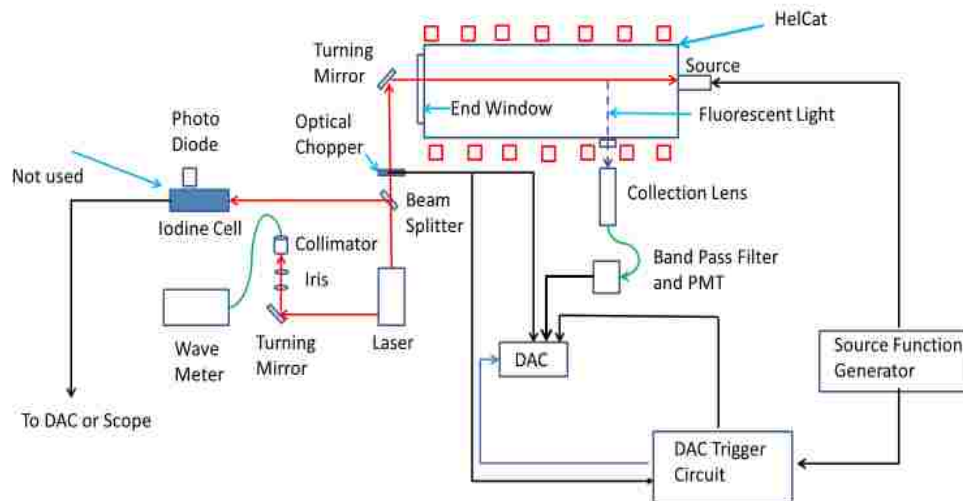
2.2 The LIF System

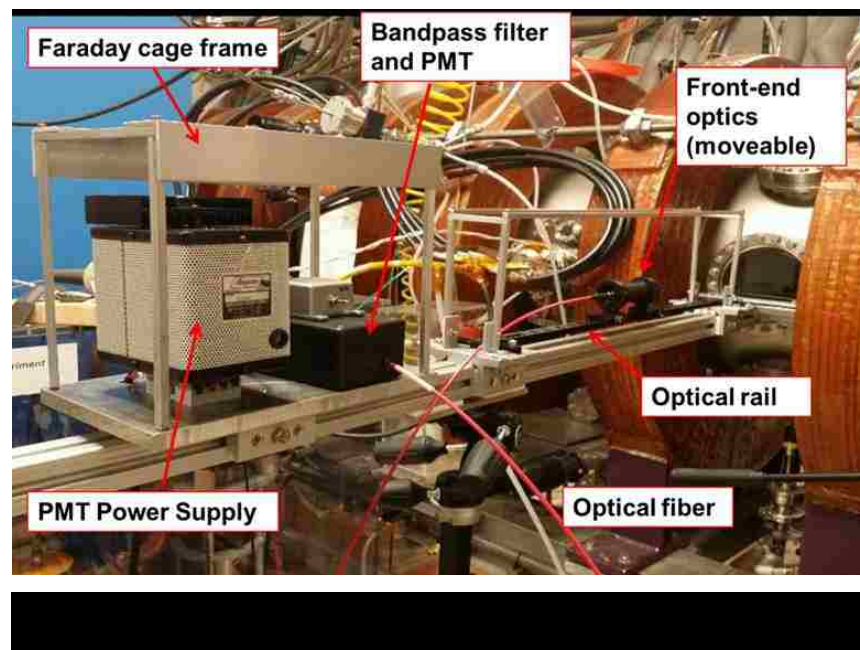
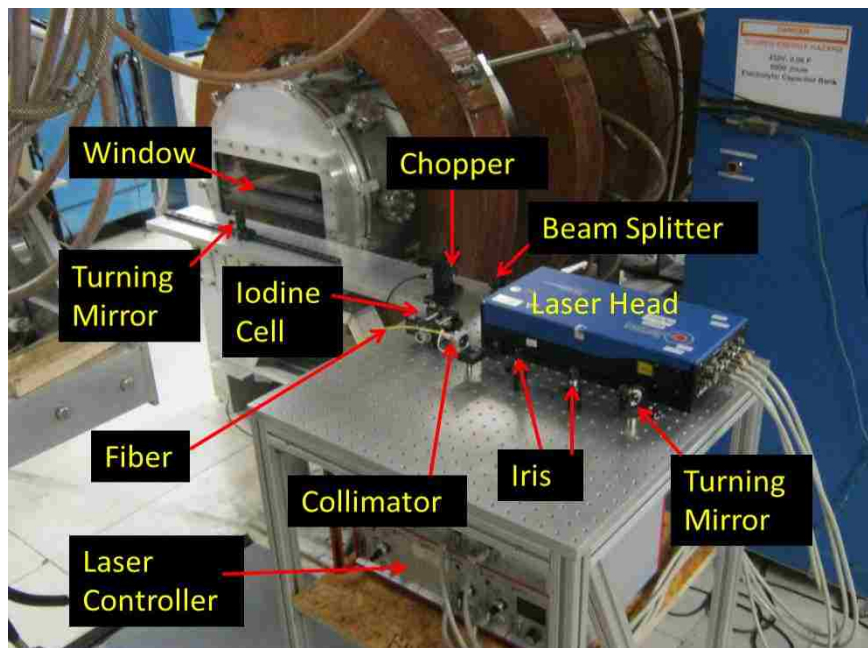
The LIF system developed is based on the design used by *Earl Scime, et al*, at West Virginia University [36]. The LIF system has two major sections: the injection side, and the collection side. The injection side consists of an injected laser beam, an optical chopper, a wavemeter, and a turning mirror. The collection side consists of focusing lenses, an optical fiber, an optical line filter, and a photomultiplier tube (PMT). These parts are shown schematically in Figure 2.2.1. The actual components are shown in Figure 2.2.2, and Figure 2.2.3. Both injection and collections sides are mounted on optical rails to allow the optics to be moved radially across the machine.

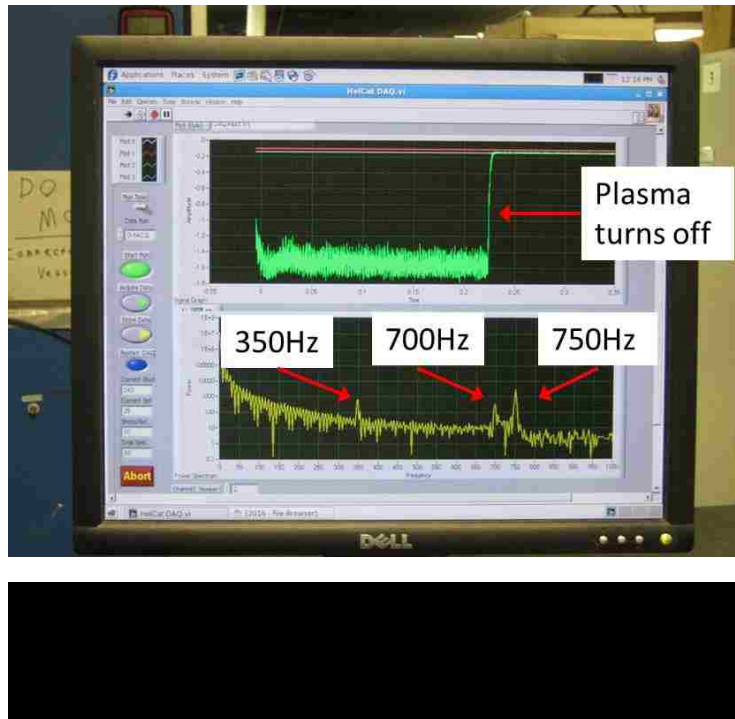
The laser beam is directed through a ThorLabs MC2000 Optical Chopper and onto an optical mirror turned at 45° . This directs the laser beam down the length of the chamber. The fluorescent light is observed by a set of focusing lenses. This light is directed to a line filter with an optical fiber. The light passing through the filter is collected and converted

to an electrical signal by a photomultiplier tube (PMT), and the signal is sent to the data acquisition (DAQ) system. The DAQ displays the raw data and the power spectrum of the data, Figure 2.2.4, and records the data for later analysis. There are three peaks in the power spectrum. The peak in the power spectrum at 350Hz is from the plasma fluctuations, the peak at 700Hz is a harmonic of the 350Hz, and the peak at 750Hz is the response due to the chopper cutting the laser at that frequency. When the laser is off resonance, the peak at 750Hz does not appear in the power spectrum. Thus, there is visual confirmation that the transition of interest is being excited.

The laser head has a side port for measuring the wavelength of the laser beam produced. This light was directed onto a turning mirror and then into a ThorLabs PAF-X-15-B collimator. This focusses the laser into a 9 μ m core diameter, single-mode optical fiber. This fiber then directs the light to the wavemeter for monitoring of the laser wavelength, or frequency.





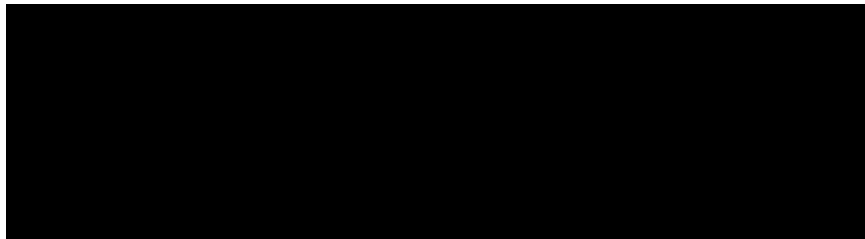
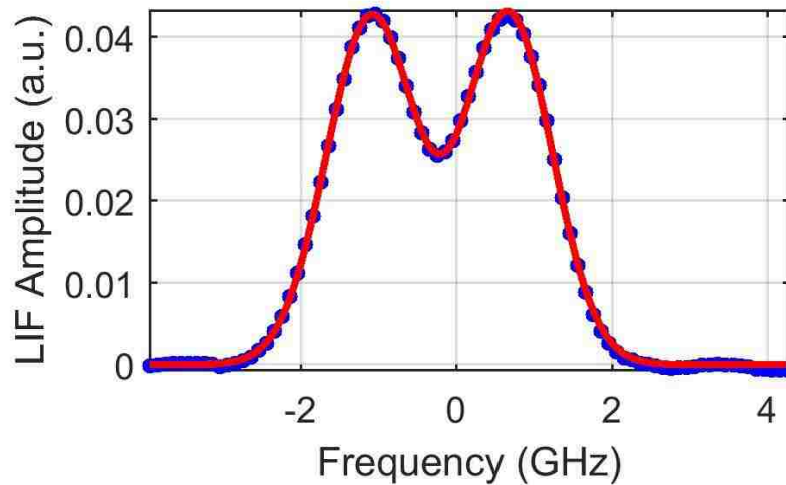


2.2.1 The Laser

The laser used in these experiments was a Toptica TA pro-2V0_13271 Tunable Diode Laser with an output of ~ 250 mW max over a range of 684 nm to 699 nm. The laser has a mode hop free tuning range of 50 GHz and a linewidth < 1 MHz. The laser can be swept through this range by hand, by internal sweep reference, or by an external input. For these experiments, the laser was swept through the wavelengths of interest by hand using the controls provided on the front panel.

Since it was easier to ensure the correct values when using frequency instead of wavelength, the wavemeter (described in the next section) was set to output GHz. For the neutral argon line, the resonance wavelength (frequency) is 696.7352 nm (430281.71 GHz) in vacuum. The laser was swept from 430278.05 GHz to 430286.05 GHz in 0.1 GHz steps. Ten sets of data were collected and averaged for each frequency step. A typical set of data for an entire frequency sweep is shown in Figure 2.2.5. Data processing techniques will be

described in Section 2.3.1.1 The double peak in the plot is due the Zeeman splitting discussed in Section 1.3.3.



2.2.2 Wavemeter

The wavemeter used for this research was a Burleigh Wa-1500. This wavemeter has an Absolute accuracy of $\pm 2 \times 10^{-7}$, or 0.2 ppm, or 0.00014 nm @ 700 nm. The resolution at 1000 nm is ± 0.0001 nm, or 0.01 GHz which translates to ± 60 m/s. This sets a lower limit on error analysis for velocity measurements.

2.2.3 Optics

2.2.3.1 The Injection Side

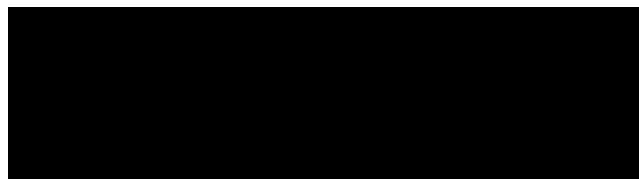
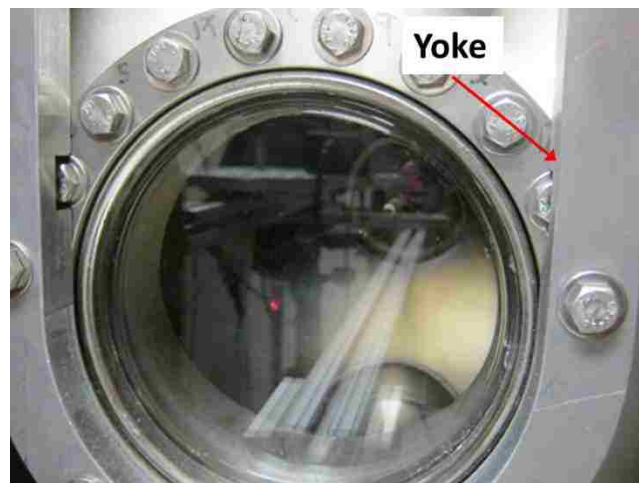
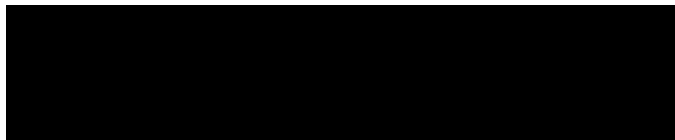
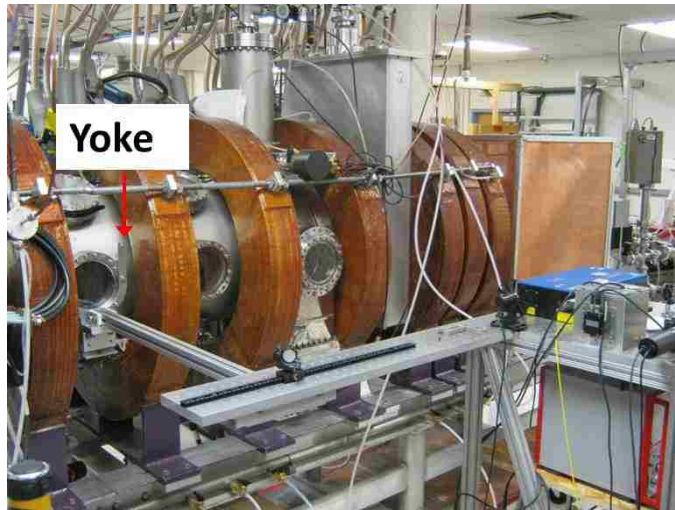
As can be seen in Figure 2.2.2, an optical table was made to hold the laser and the injection side optics. The optical bread board used for this research was manufactured by Unique Services, LLC, here in Albuquerque. The support for the table was designed by

Heitek Automation using 1.5in x 1.5in 80/20 Aluminum extrusion. Shelves were installed to hold the laser controller, the wavemeter, the chopper controller, and the iodine cell heater controller (discussed in Section 2.2.5).

The entire table was then attached to the flange with the rectangular window at the end of the machine, as shown in Figure 2.2.2. The laser head and all the optics were mounted to the optical bread board, and an optical mirror mounted on an optical rail was used to direct the injection laser down the length of the machine. Having the mirror mounted to the rail allowed the laser to be scanned radially across the machine (plasma), (Figure 2.2.1).

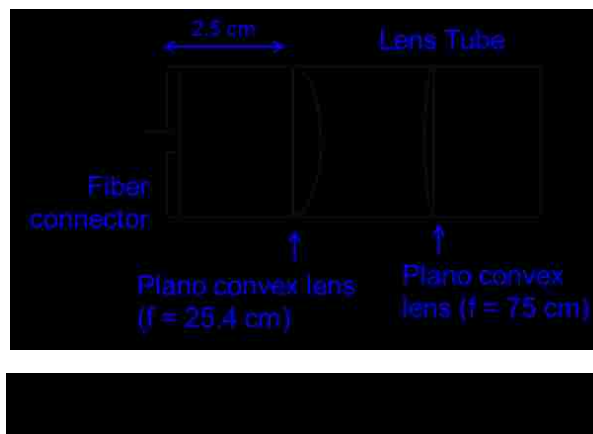
2.2.3.2 The Collection Side

All the components of the collection side of the LIF system were mounted on a 1.5in x 1.5in 80/20 Aluminum extrusion. The extrusion was mounted to Port 6 with a custom-made Aluminum yoke, shown in Figure 2.2.6. The yoke was made to fit around the port window, over the bolt heads, and hold the optics at the center of the window, Figure 2.2.7.

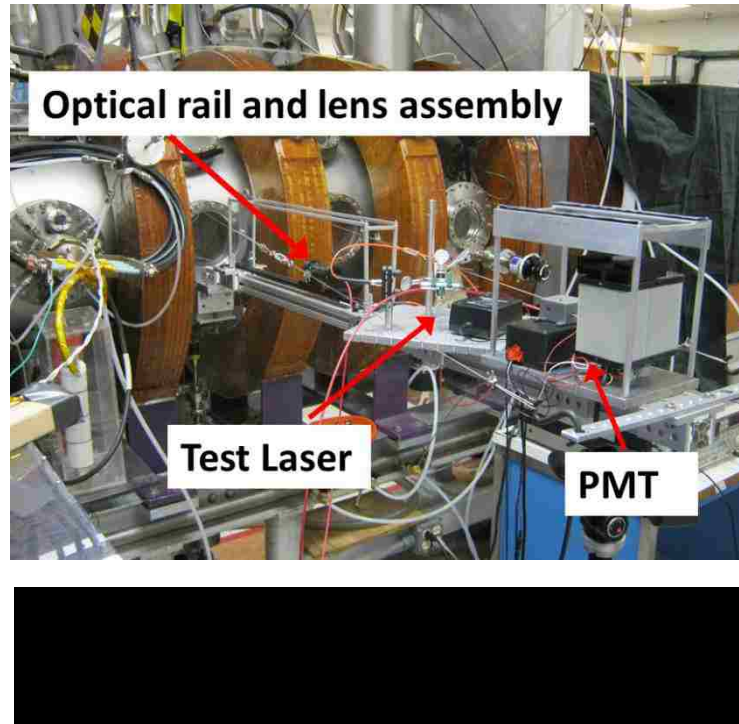


The collection optics use a set of plano-convex lenses held in a lens tube. The first lens has a focal length of 75cm to focus on the center of the chamber, while the second lens has a focal length of 2.54cm to focus the light collected into a 1000 μ m optical fiber, shown

schematically in Figure 2.2.8. The fiber directs the light collected to a Dell Optics line filter centered at 772.08nm, with a FWHM line width of 1.06 nm. (This line filter is for neutral LIF. Other filters were used for ion measurements.) The light passing through the filter is collected and converted to an electrical signal by a Hamamatsu H10721-20 PMT with a spectral response from 230 to 920nm. A Faraday cage was constructed around the PMT to reduce the RF pick-up from the helicon source.



The lens tube is mounted to an optical rail which was mounted to the Al extrusion. This arrangement allowed the collection lenses to be focused to the same radial position as the injection mirror, Figure 2.2.9. Also shown in the figure are the PMT (without the Faraday cage), and the test laser used for alignment.

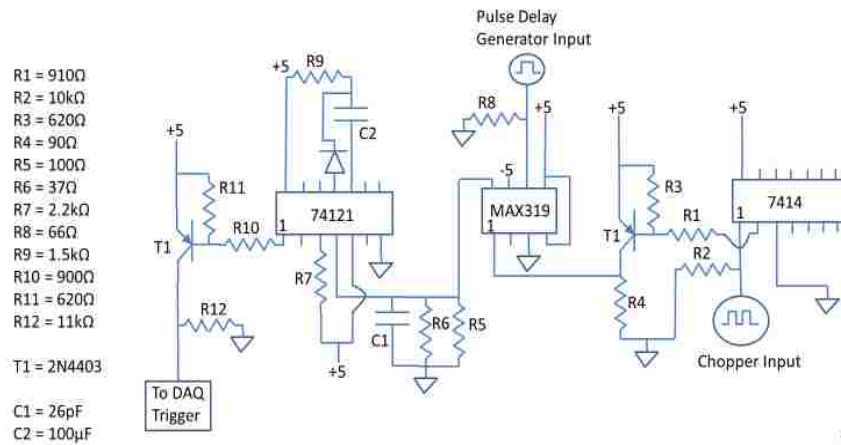


2.2.4 DAQ Trigger Circuit

Data collection for this research was performed using a Linux-based ACQ196 data acquisition card (DAQ) from D-tAcq Solutions with a LabView Interface. Normally the DAQ is triggered by the function generator that drives the helicon amplifiers and creates the plasma. For this research, it was necessary to synchronize the DAQ to the chopper signal. To accomplish this, a DAQ Trigger Circuit was constructed to ensure correct triggering of the DAQ. The circuit schematic is shown in Figure 2.2.10.

The optical chopper produces a square wave signal at the frequency that the laser beam is being chopped. This signal is directed to a SN7414 Schmitt-Trigger Inverter which acts as an input signal buffer. The output of this chip is inverted and sent to a 2N4403 transistor which acts as a driver for the next stage.

DAQ Trigger Circuit



A BNC Model 555 Pulse/Delay Generator was used to convert the TTL pulse from the source function generator to a 50 ms long, +10V square pulse with a 50ms delay. The 50 ms delay was used to ensure that the plasma had attained a quasi-steady state. The 50 ms long pulse was to ensure that the DAQ did not receive multiple triggers during a plasma discharge.

A MAX319 analog switch used the output from the pulse/delay generator and the output of the transistor to trigger the SN74121N. The MAX319 allowed the signal from the chopper through to the rest of the circuit only when it received a signal from the pulse/delay generator. The output signal of the MAX319 was still a square wave at the same frequency as the chopper, but only 50ms long.

This signal was then directed to the SN74121N One-Shot which produces a high, or low square pulse output. The configuration used was such that a downward transition in the square wave from the chopper produced an output “low” square pulse. The pulse duration was set by R9 and C2 through the relation:

$$t_W = K R_X C_X \quad (2.2.1)$$

where K is a calibration constant ~ 0.7 , t_W is in nano seconds and is the pulse duration, R_X is the resistor value in $k\Omega$, and C_X is the capacitor value in pF. For the values listed, this gives a pulse duration of 105ms, which then ensures that the DAQ will not receive multiple triggers during a plasma discharge.

The output of the One-Shot is sent to the final stage of the circuit which consists of a second 2N4403 transistor. This acts as an output buffer and inverts the signal again to produce a square “high” pulse which is used to trigger the DAQ.

DC power for this circuit was provided by a 110VAC to +5VDC converter and a RECOM RKZ-0505D DC/DC converter.

2.2.5 Iodine Cell

As stated in Section 2.2.2, the wavemeter has a minimum resolution in velocity space of ± 60 m/s. To decrease this limit on the velocity, other researchers have employed an iodine cell in their LIF systems [36], [47], and [45]. These systems rely on the fact that iodine has a distinct spectral line signature. If the transition being excited in the plasma is close to one of the lines of iodine, then this can be used as a calibration for the LIF system, and can lower the limit on the velocity to $\sim \pm 25$ m/s.

This method was partially implemented in the course of this research. The iodine cell is indicated in Figure 2.2.1 and Figure 2.2.2. A BP058 $\emptyset 1/2$ " Pellicle Beam splitter with an 8:92 ratio was installed to direct a small percentage of the injection laser beam to the iodine cell. It was found that there are two reasonably strong spectral lines for iodine near the 696.7652nm neutral line. The Laboratoire Aimé Cotton has done extensive work identifying the excitation lines of Iodine. They have developed the Atlas du Spectre Iodine

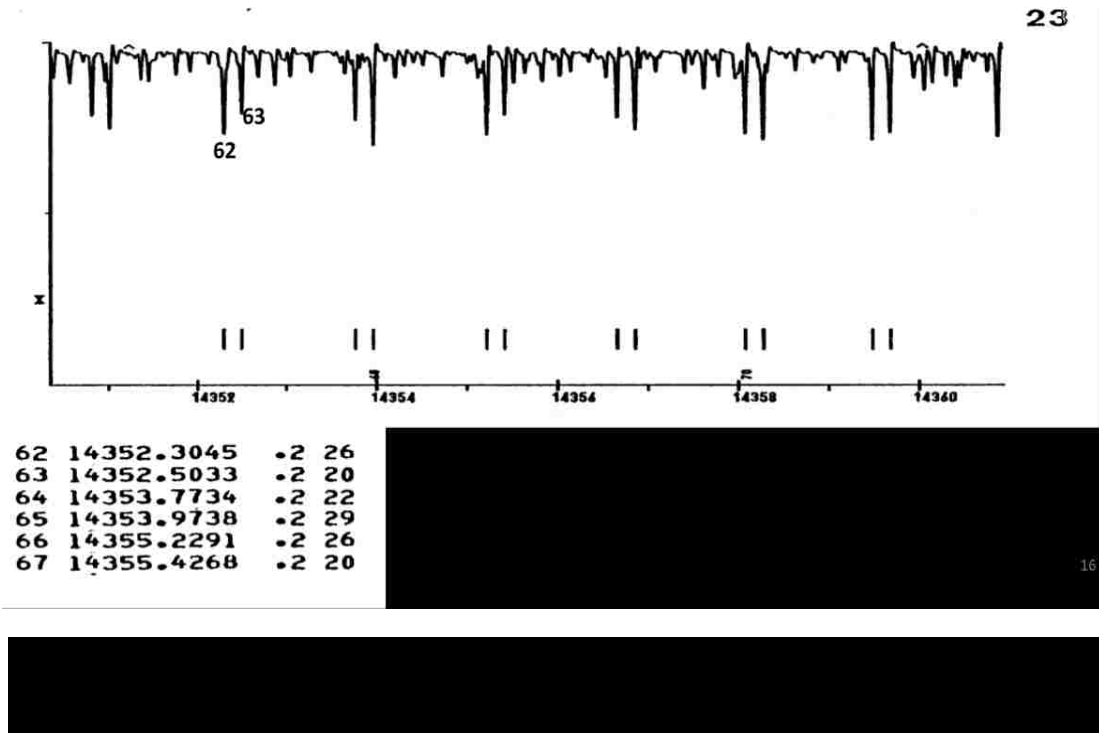
in which they show the most thorough line spectra for iodine and give the corresponding wave number values along with their intensities. Figure 2.2.11 shows the line spectrum and the corresponding wave number values for a small section of the iodine spectrum [81].

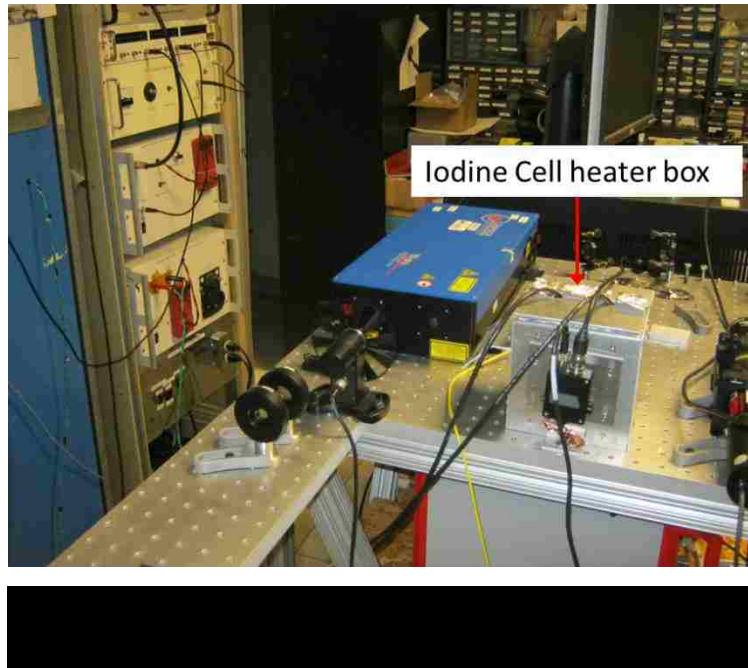
Converting the lines labeled 62 and 63 to GHz, we get:

$$14352.5033\text{cm}^{-1} = 696.7425\text{nm} = 430277.22\text{GHz}$$

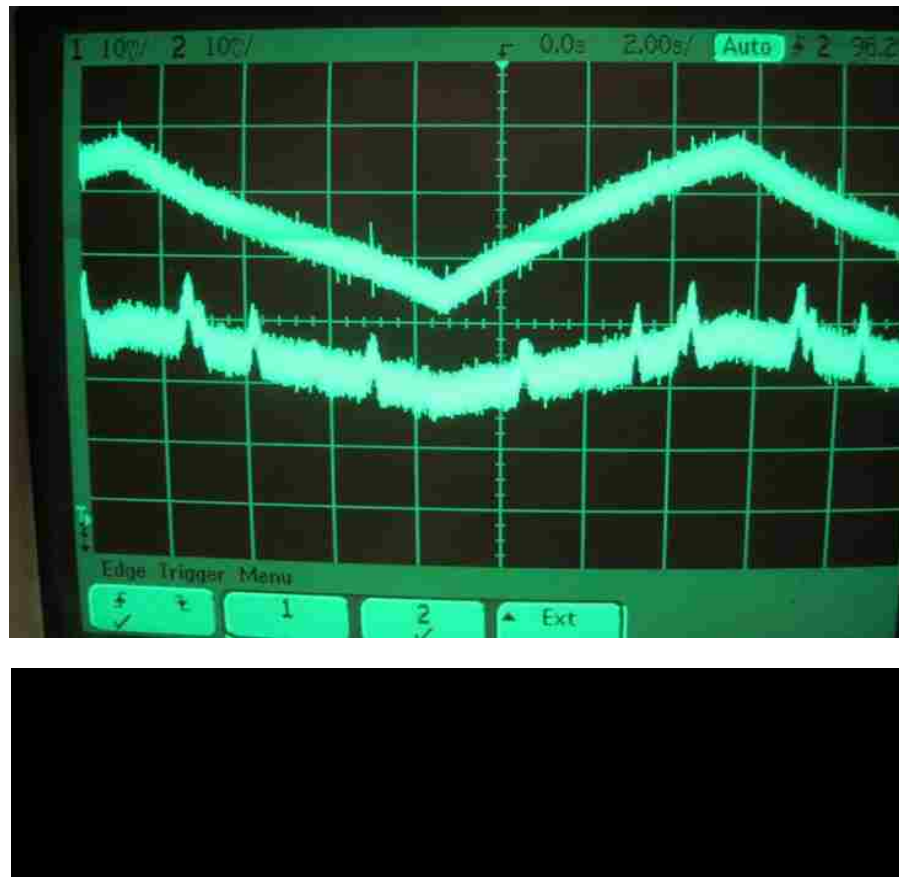
$$14352.3045\text{cm}^{-1} = 696.7522\text{nm} = 430271.26\text{GHz}$$

Since these values are within the mode hop free tuning range of the laser and were the closest to the resonant frequency of 430281.71GHz, the sweep of the laser was increased to include these lines. The response of the iodine cell was observed with a ThorLabs PDA36A Photodetector. It was determined that the iodine cell needed to be heated for the fluorescence to be observable and an insulating cage was built around the iodine cell to help increase the temperature, Figure 2.2.12.

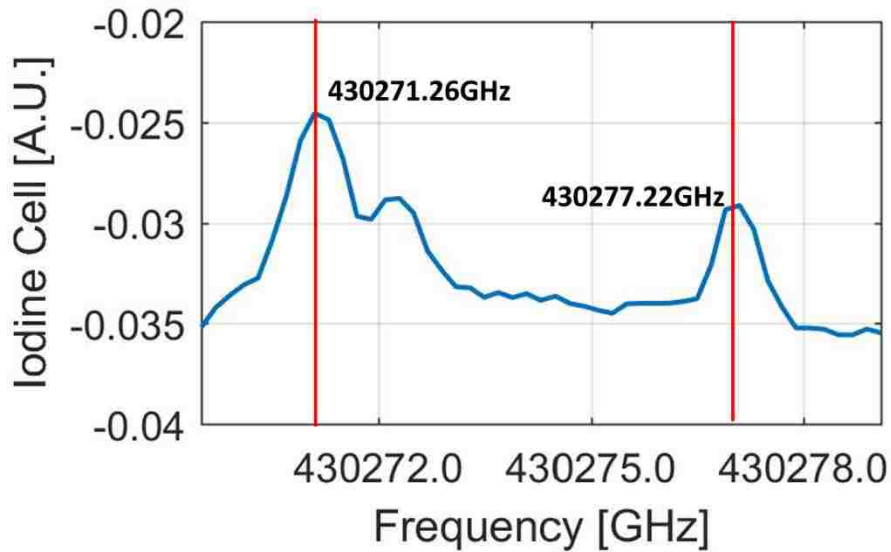




It was found that the temperature had to be maintained at $\sim 100^{\circ}\text{C}$ to get enough fluorescence for the photodetector to respond. Figure 2.2.13 shows this response on an oscilloscope. The upper trace is the output of the laser control. The lower trace is the response of the iodine cell as the laser is swept through the resonances of interest indicating that the cell is functioning correctly.



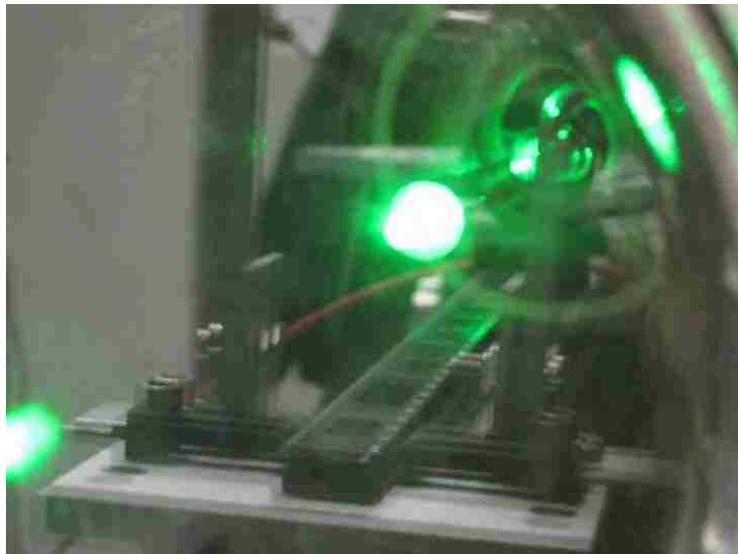
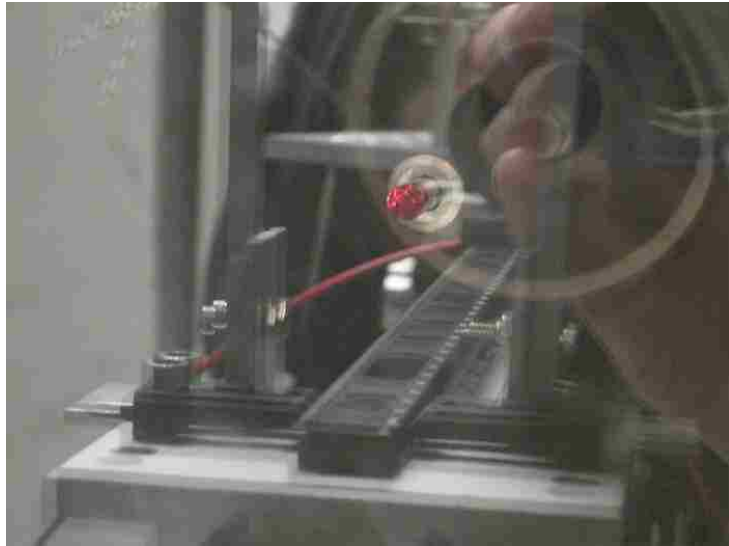
Once this was accomplished, data were collected with the DAQ. This is shown in Figure 2.2.14. As can be seen in the plot, the fluorescence from the iodine cell can be resolved with our system. However, to use this method effectively, the other experimenters used the internal sweep on the laser and swept through the frequencies of interest ~100 times. They had steady-state plasma and data acquisition systems that allowed them to record data continuously. Since our system is pulsed and our data acquisition system cannot record continuously, the iodine cell was not pursued further for this research.



2.3 Neutral LIF

For neutral argon, as discussed in Section 1.3.2, the resonant frequency is 430281.77GHz. Therefore, the laser was swept from 430278.05GHz to 430286.05GHz in 0.1GHz steps to ensure capturing of the entire Doppler shifted, temperature broadened line width. Ten sets of data were recorded at each sweep position. Initially, the optics were set at $r = 0$ cm (the center of the machine). Alignment between the injection side and the collection side was accomplished by observing the injection laser on a probe tip, and then shining a test laser backward through the collection optics and onto the same probe tip. The laser shining on the probe tip is shown in Figure 2.3.1 and Figure 2.3.2. The collection optics have an observation spot diameter of ~ 5 mm, and the laser has a spot diameter of ~ 5 mm, resulting in a total measurement volume of ~ 0.67 cm³ [10]. This method of

alignment ensured that both the injection and collection optics were focused to the same point in the chamber.

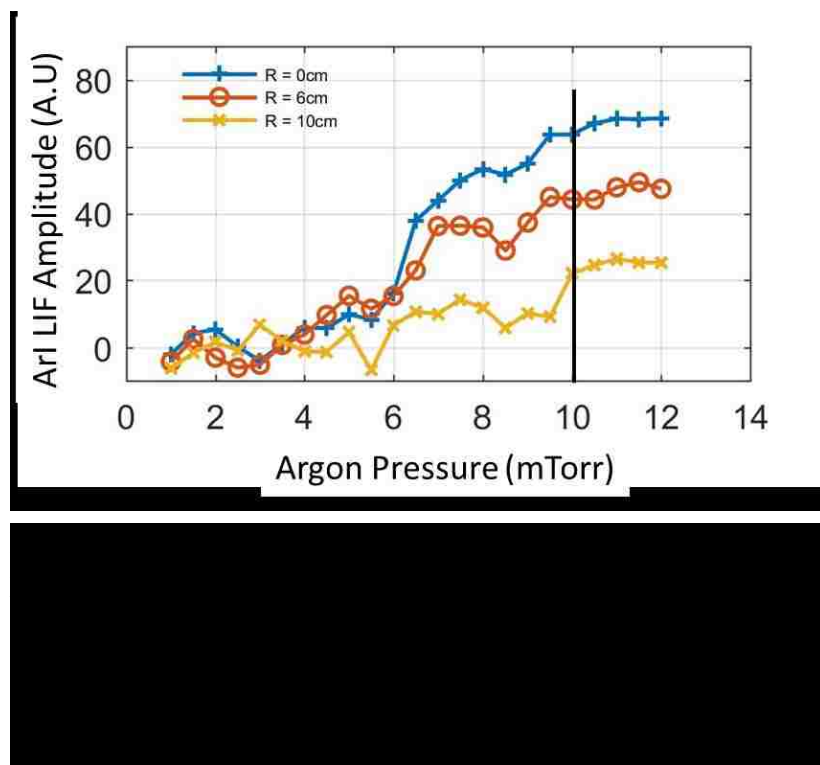


2.3.1 Axial Velocity Measurements

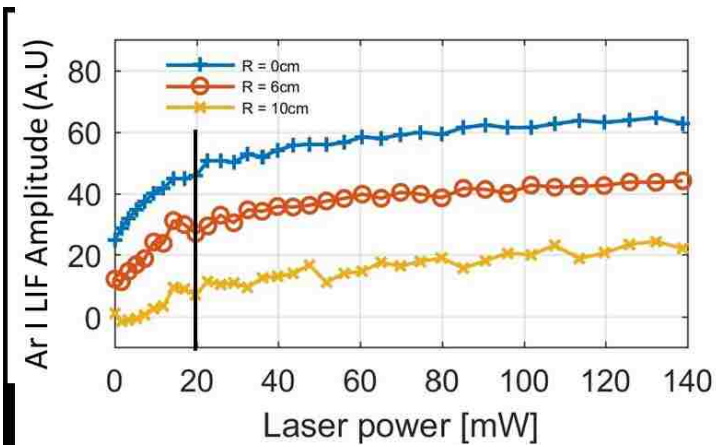
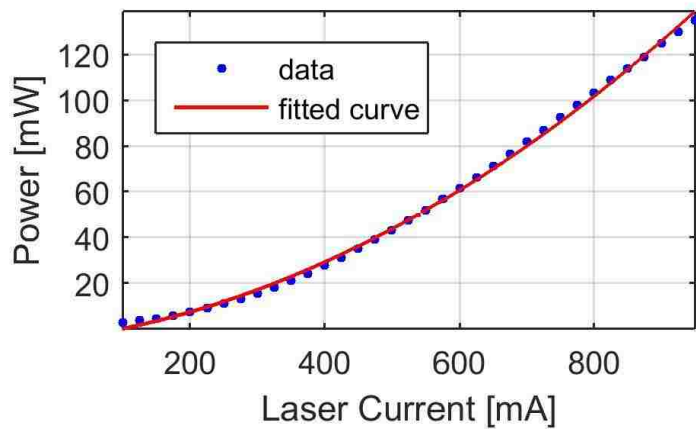
As started in Section 2.1, for axial measurement, that is axial flow and temperature, and a radial density profile measured in the axial direction, the laser was injected from the end of the chamber after passing through the beam splitter, and the optical chopper. The same method was used for both neutral argon (ArI), and singly-ionized argon (ArII).

2.3.1.1 Port 6

To ensure that adequate LIF signal would be collected, and that the data would not be affected by power broadening, parameter scans of argon pressure and laser power were performed. It was found that for some Argon pressures, there was no observable response. As such, a scan of the pressure was performed to determine the best Argon pressure at which to run the machine at. This scan was accomplished by setting the laser to the resonant frequency of the first Zeeman split peak (~ 430280.95 GHz), recording ten sets of data, then increasing the pressure by 0.5 mTorr. The scans were started at 1.0 mTorr and stopped at 12 mTorr. Then a plot of LIF signal response versus pressure was constructed. This process was performed at $r = 0$ cm (the center of the machine), $r = 6$ cm, and $r = 10$ cm. Figure 2.3.3. For Port 6, it was decided that 10 mTorr was the best pressure as there was good signal response, and the turbo-pump on HelCat was not stressed too much. In addition, the LIF signal was significantly decreased at 10 cm. Since it was desired to go further toward the edge of the chamber, there was concern that any lower operating pressure might not provide a usable response beyond 10 cm.



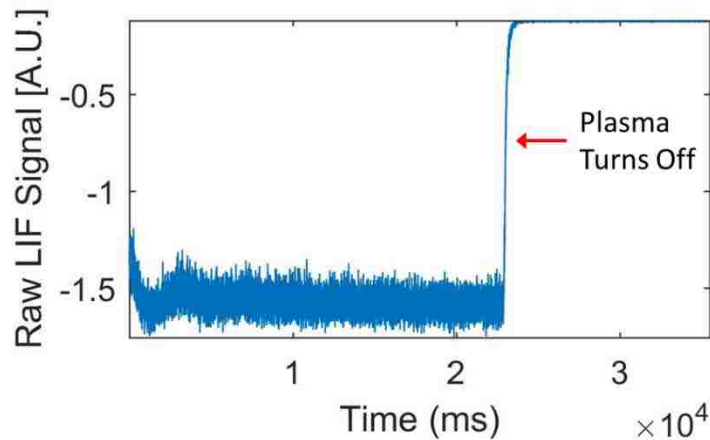
As discussed in Section 1.3.4, power broadening was also a concern as our laser has the capability of producing a beam of approximately 250mW. As such, power scans were performed at the same radii as the pressure scans. Since the laser controller displays the current to the laser head, a calibration curve was constructed to convert the current to laser power. A ThorLabs PM100D Optical Power Meter was used to measure the laser power after the beam splitter. The laser current was increased in steps of 25 mA, starting at 100 mA and stopping at 950 mA, as 960 mA is the max input laser current allowed, Figure 2.3.4. The power scans were then performed by recording the neutral LIF response with the laser set at ~ 430280.95 GHz, and varying the laser current as was done for the calibration curve. These scans are shown in Figure 2.3.5.



As can be seen in Figure 2.3.5, the power does saturate above approximately 40 mW. Even with the reduced signal observed at the other radial locations, the saturation

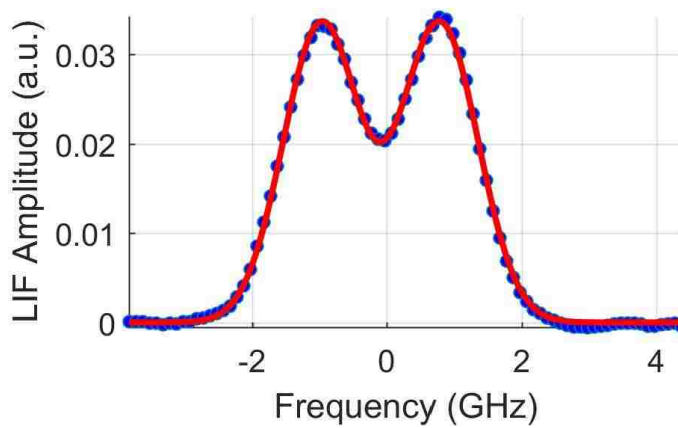
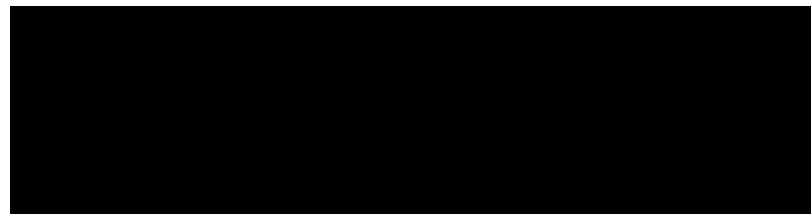
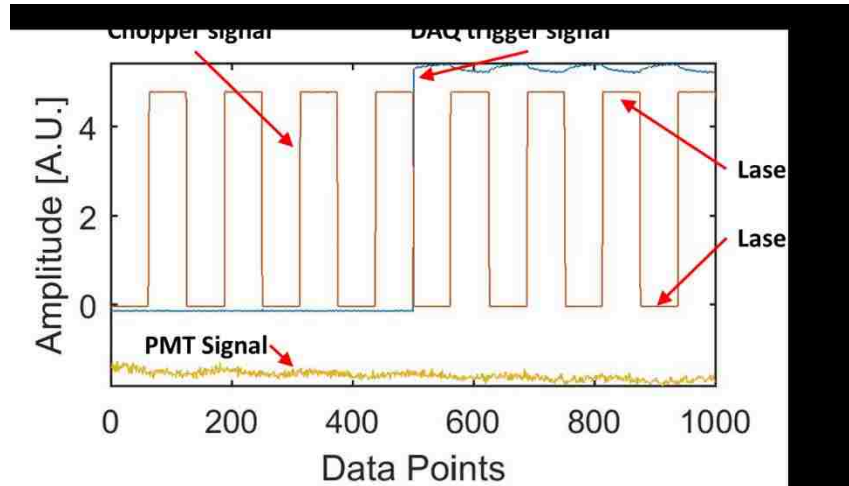
occurs at about the same laser power. Therefore, it was decided to perform the experiments at 20 mW of laser power which corresponds to a laser head input current of 325 mA.

Once the argon pressure and laser power were determined, the actual frequency sweeps could be performed. As stated above, for neutral argon, the sweep was started at 430278.05 GHz \pm 0.01 GHz, and stopped at 430286.05 GHz \pm 0.01 GHz with a step size of 0.1 GHz \pm 0.01 GHz. Ten sets of data were collected at each frequency step. Since observation of the raw data gave no indication of a response to the input laser, as shown in Figure 2.3.6, a MatLab code was developed to process the data using the timing from the chopper.



Since the DAQ circuit, described above, was designed to trigger the DAQ on a “down” of the chopper signal, it was possible to cut the data according to the chopper frequency. And, since there should be a difference between the laser “on,” and the laser “off” conditions provided by the chopper, the “off” data was subtracted from the “on” data (Figure 2.3.7). This subtraction was performed for each set of on/off data in each shot of data. These values were then averaged, and the results of the ten shots of data were

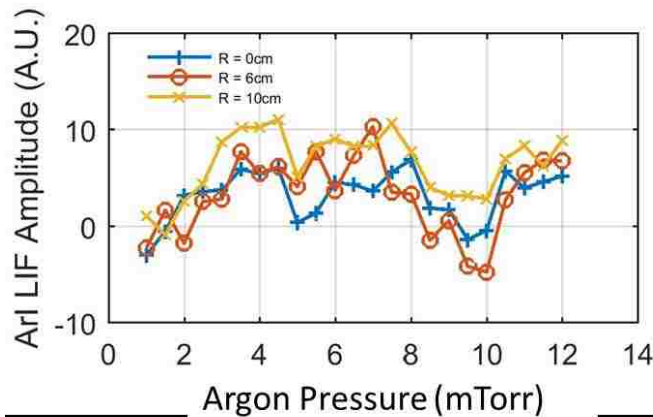
averaged. This gave a value of the LIF amplitude for a particular laser frequency. The laser frequency was then changed, and the process repeated. The amplitudes were then plotted as a function of the frequency step as shown in Figure 2.3.8. In the figure, the frequencies have been shifted so that the resonant frequency is at 0GHz.



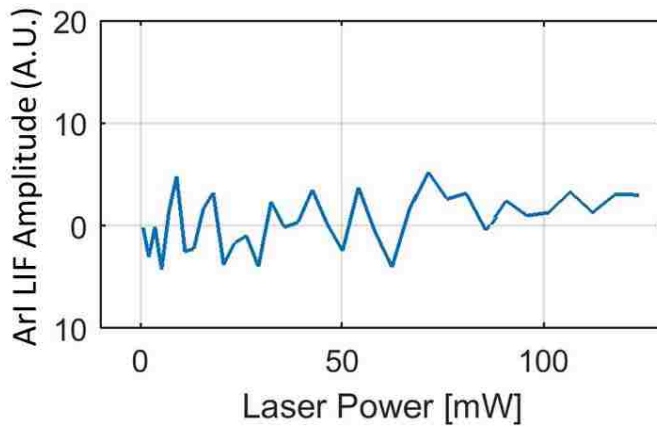
This procedure was then repeated radially across the plasma from $r = 0$ cm (the center of the plasma (chamber) to $r = 15$ cm in 1 cm increments. From these frequency scans, neutral density, temperature and velocity can be determined and plotted as a function of position. This will be described in more detail in Section 4.1

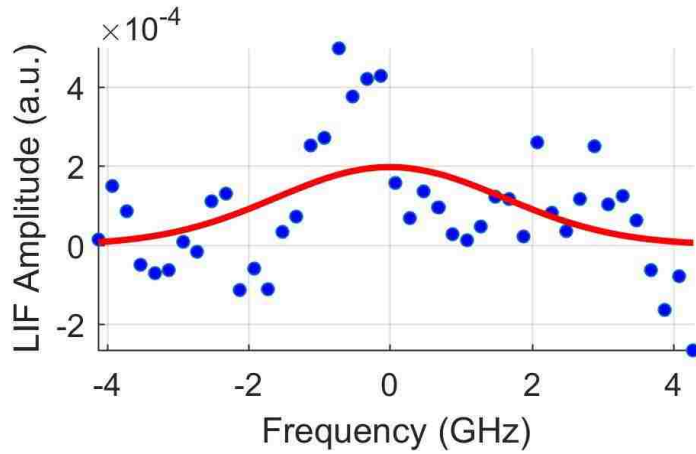
2.3.1.2 Port 4

This entire process was repeated at Port 4. Since the injection side optics were attached to the end of the machine, they did not have to be moved. And, since the collection side optics were on a self-contained yoke and rail assembly, this was moved from Port 6 to Port 4 relatively easily. The laser had already been calibrated, so there was no need to repeat that part of the procedure. The pressure and power scans were repeated at $R = 0$ cm, $R = 6$ cm, and $R = 10$ cm, as shown in Figure 2.3.9.



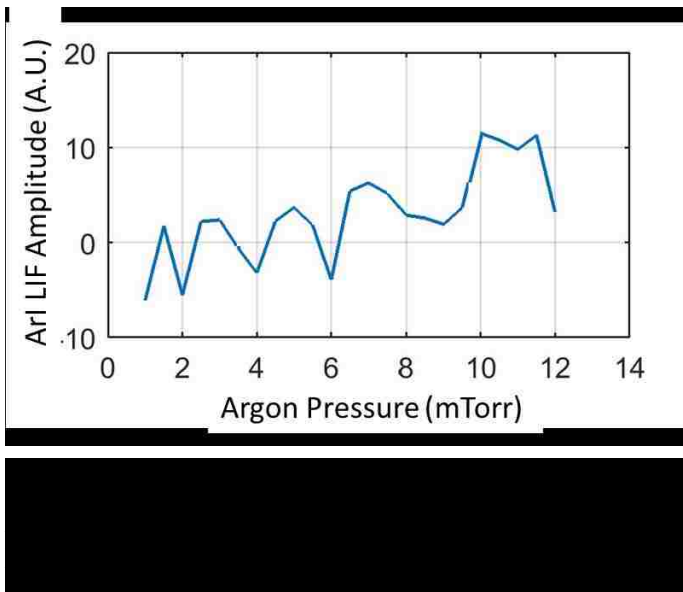
As can be seen in the previous plots, there is not much response at any of the radial position for any of the argon pressures. However, it was decided to try a power scan and a frequency scan at $r = 6$ cm. These scans are shown in Figure 2.3.10, and Figure 2.3.11, respectively. It was obvious from these plots that the neutral LIF scheme would not produce any usable results at Port 4, and no further attempts to obtain neutral LIF data were made at this port.





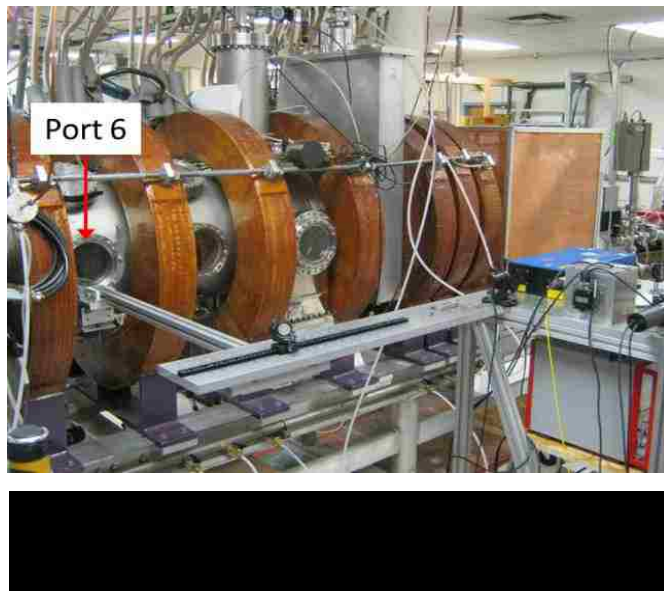
2.3.1.3 Port 5

To be thorough, the collection side optics were moved from Port 4 to Port 5. Applying lessons learned at Port 4, a pressure scan was performed at $r = 6$ cm only, as shown in Figure 2.3.12. As this scan did not show any appreciable response, no further neutral LIF measurements were attempted at Port 5.



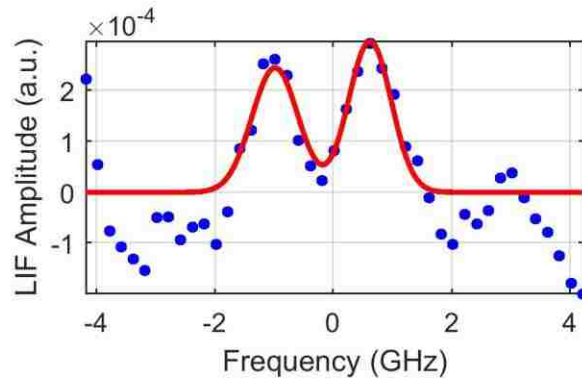
2.3.2 Radial Velocity Measurements

In order to make measurements that were sensitive to radial velocity, the optics were first reversed so that the injection side was located at Port 6 and the collection side was at the end of the machine. The laser injection system attached to Port 6 is shown in Figure 2.3.13. The neutral LIF line filter was reinstalled in the collection optics, and frequency scans were attempted. This did work; however, the signal was diminished to such an extent that it would not have been possible to collect data for the entire radial scan as planned. The neutral LIF amplitude versus laser frequency at $r = 0$ cm is shown in Figure 2.3.14. As these scans were performed at 10 mTorr argon and full power on the laser, it was decided not to do pressure, or power scans.

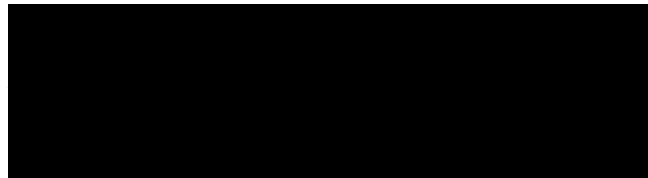
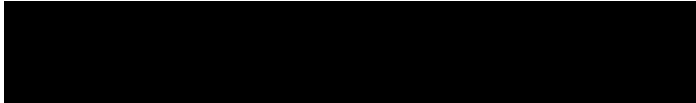


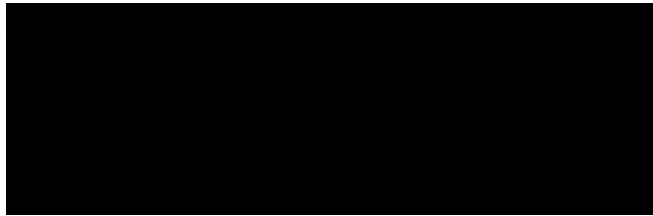
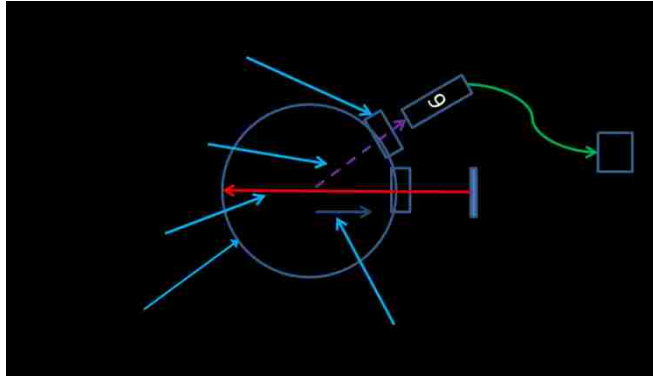
It is believed that the diminished LIF response is due to shielding from neutral particles in the length of the chamber. That is, light emitted by neutrals excited by the laser

at Port 6 would be reabsorbed by other neutrals before it had a chance to travel the length of the chamber to the collection optics indicating that the plasma is optically thick in this direction. This would make sense as it is expected that the plasma at the end of the chamber opposite from the helicon source would be dominated by neutral particles. It was then decided to move the collection side optics to the port at 60° at the Port 6 location.

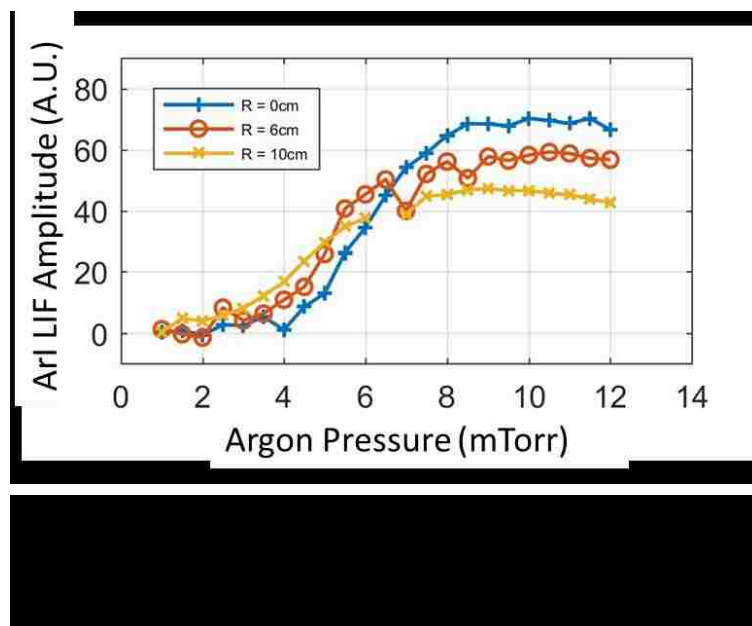


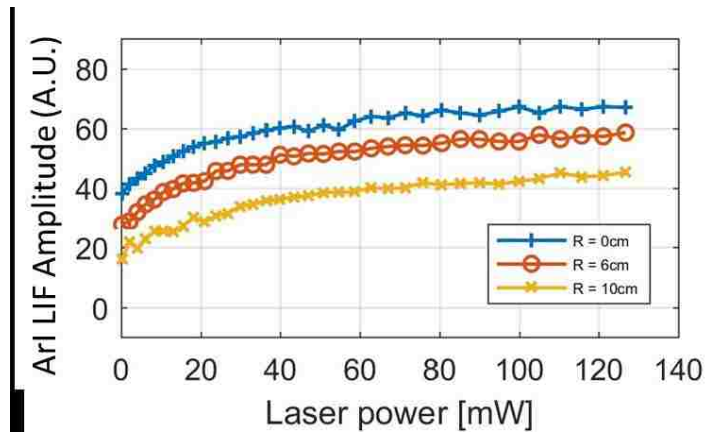
Since it was found that neutral LIF would not work at any pressure for Port 4 and Port 5, the remaining neutral LIF research was restricted to Port 6. And, since it was found that having the collection optics at the end of the machine would not work satisfactorily, a new aluminum yoke was made to hold the collection optics on the port located 60° azimuthally from Port 6, as shown in Figure 2.3.15. An optical bread board was also fabricated to facilitate moving the collections side optics. A ThorLabs PRO1 High-Precision Rotation Mount was employed to allow alignment of the collection optics with the probe tip as it was scanned radially across the machine (Figure 2.3.16). Figure 2.3.17 shows, schematically, the orientation of the optics and the direction of the scan.



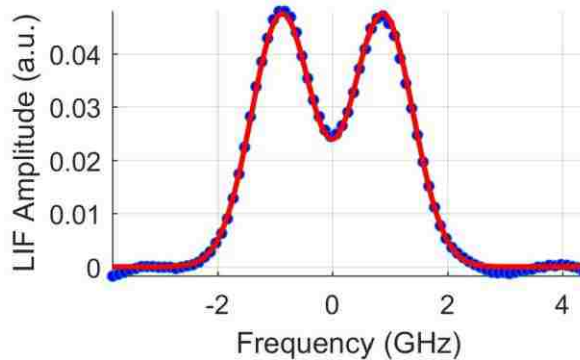


Once the optical mount was installed and tested, new pressure and power scans were performed, shown in Figure 2.3.18, and Figure 2.3.19, respectively. From these plots, it was decided, once again, that the best parameters for this orientation would be 10 mTorr argon and 20 mW of laser power.





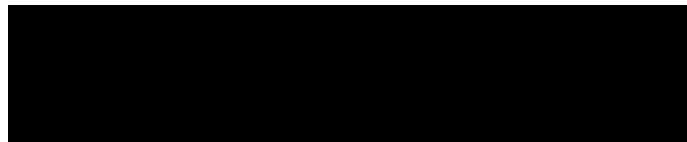
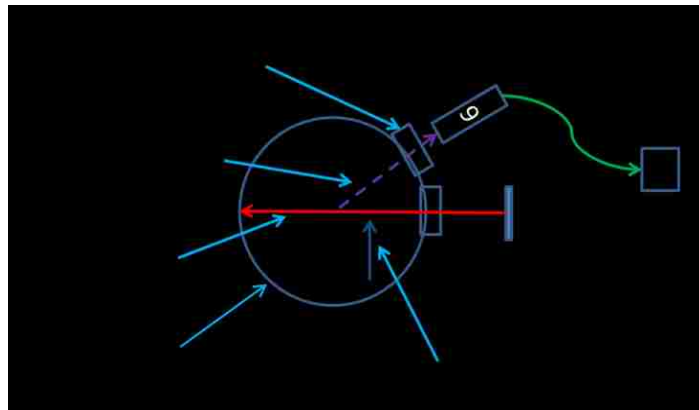
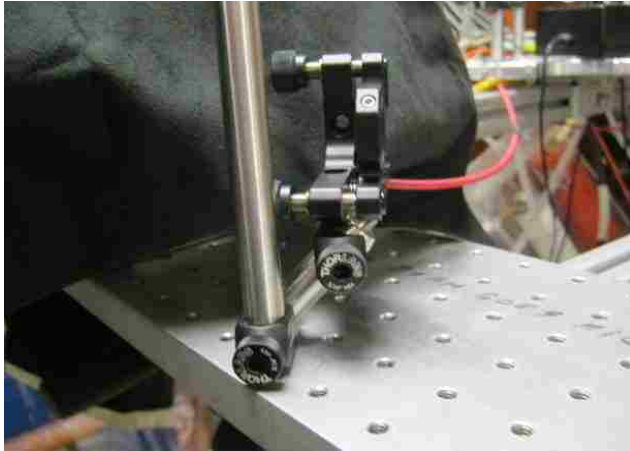
Once these parameters were determined, frequency scans were performed as before starting at $r = 0$ cm and moving radially outward in 1cm increments to $r = 15$ cm. A typical plot of a frequency scan is shown in Figure 2.3.20. Plots of the Doppler shifted velocity, neutral temperature, and neutral density were then created and will be discussed in more detail in Section 4.1

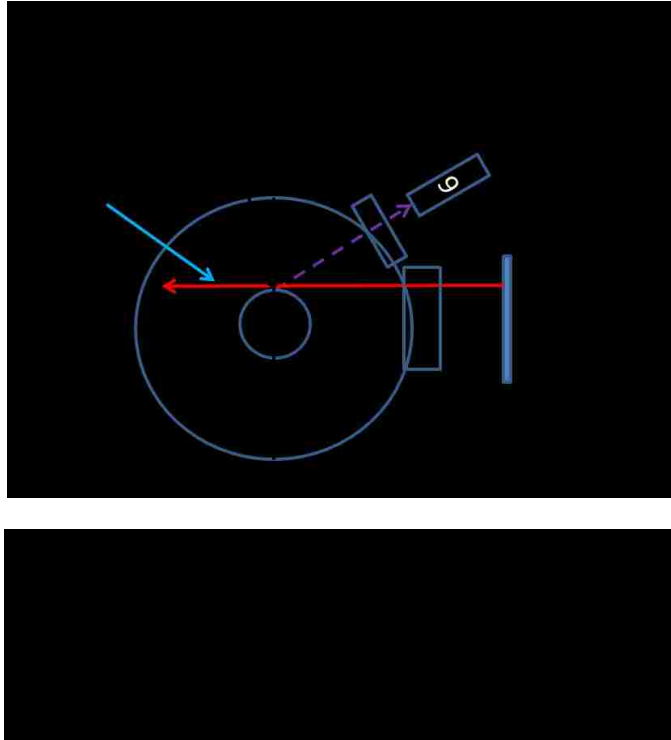


2.3.3 Azimuthal Measurements

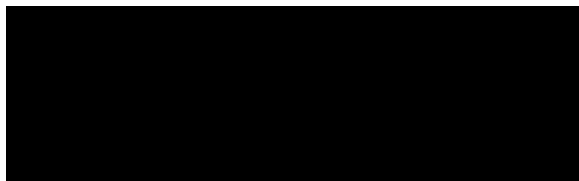
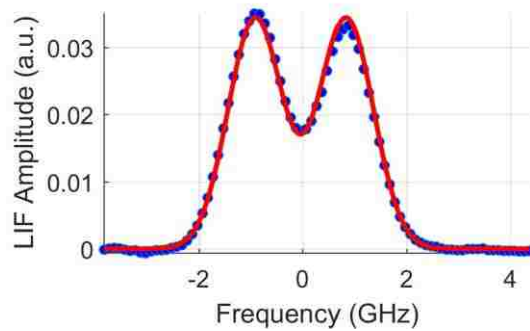
Once the radial LIF measurements were complete, new optical mounts were used to allow the injection laser to be scanned in the vertical direction, thus obtaining azimuthal data via a tangent-radial measurement. The new mounts can be seen in Figure 2.3.21 and Figure 2.3.22, and a schematic depiction of the system is shown in Figure 2.3.23. Figure 2.3.24 shows a schematic of how raising the laser vertically can probe an azimuthal velocity.







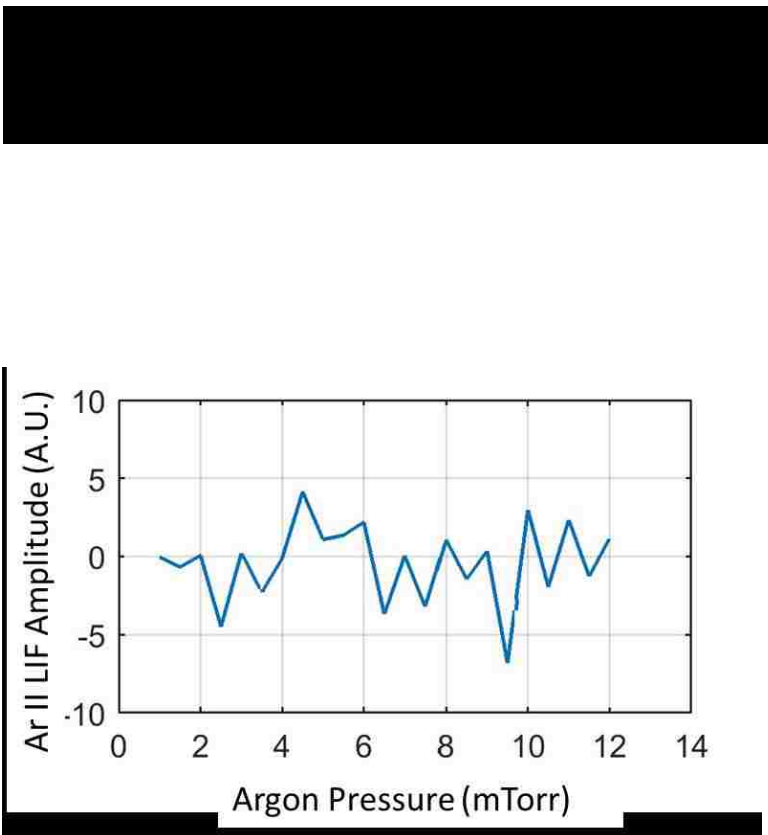
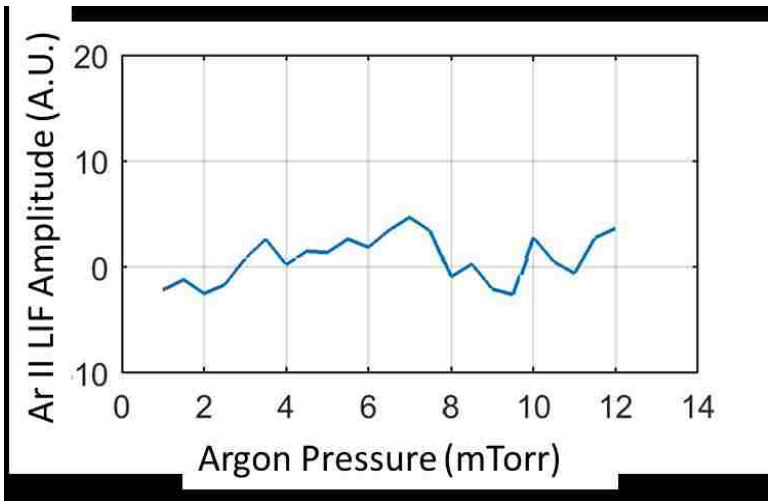
Since the optics were in the same location as for the radial measurements, no pressure, or power scans were performed. Data collection for the azimuthal scans was performed at 10 mTorr argon and 20 mW of laser power. Frequency scans were performed in the same manner as described before. The laser was moved vertically from $R = 0\text{cm}$ to $R = 6\text{cm}$ in 1cm increments. The 8in window at Port 6 was the limiting factor in the azimuthal direction. A typical plot of a frequency scan is shown in Figure 2.3.25. Once again, plots of the Doppler shifted velocity, the neutral temperature and the neutral density profile were produced and will be discussed in Section 4.1



2.4 ArII (singly-ionized argon) LIF

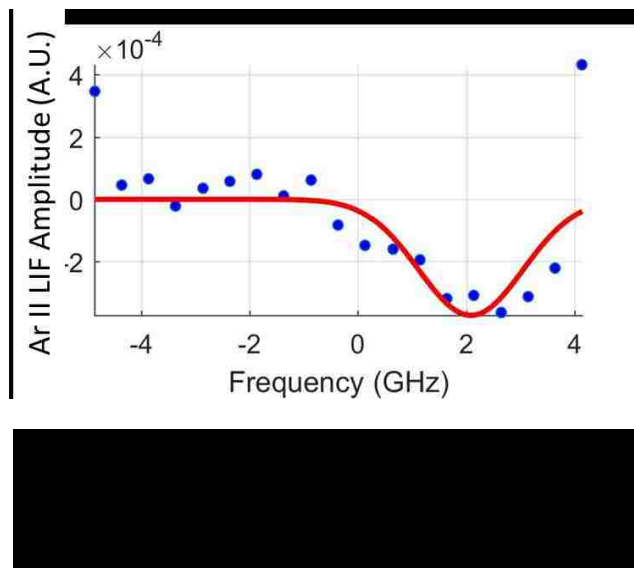
2.4.1 688 Ion Line

As discussed in Section 1.4.2, two different ion lines were within the tuning range of the laser. The first ion line has a pump line resonance at 688.8512nm which corresponds to 435206.41GHz. This is one of the three-level schemes suggested by Severn [32], and has the decay line at 434.9285nm. (A Dell Optics line filter centered at 434.81nm with a FWHM line width of approximately 1.0nm was installed before the PMT on the collections side optics.) Unfortunately, this line also has a relative intensity of 26 [58]. Due to the very low relative intensity, no usable data was recorded for this ion line at Ports 4 and 5, Figure 2.4.1 and Figure 2.4.2. For Port 6, no pressure scan was recorded, however a frequency scan at 1 mTorr was obtained and indicated that this ion line was not going to produce usable results (Figure 2.4.3). Considering the data and conversations with *Dr. Earl Scime* [77], it was decided to abandon this LIF scheme.

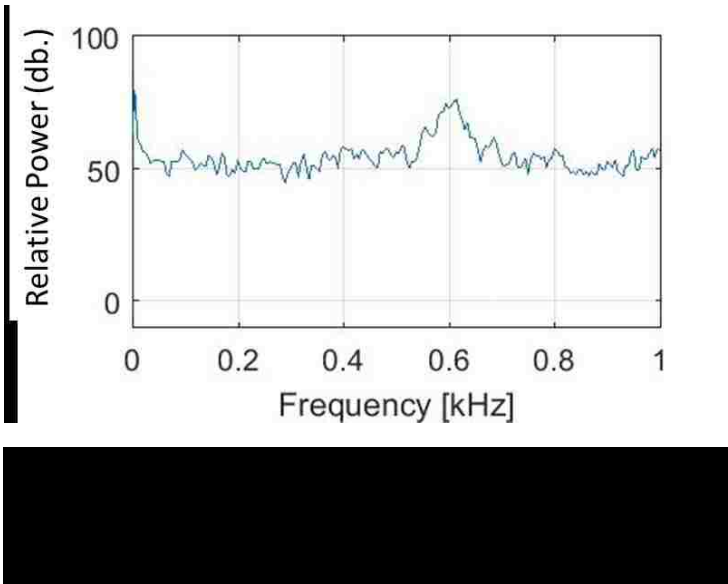
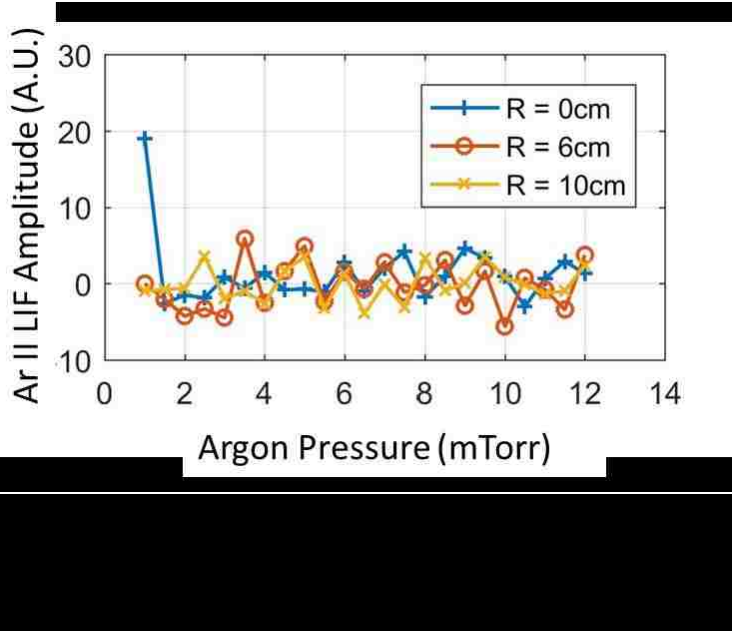


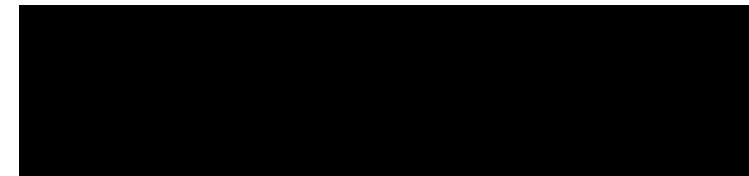
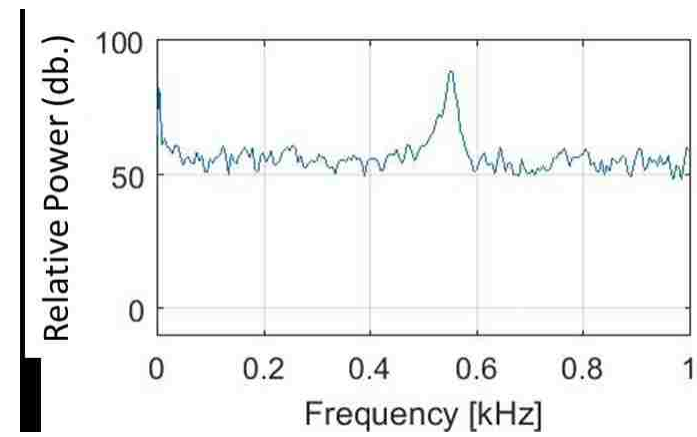
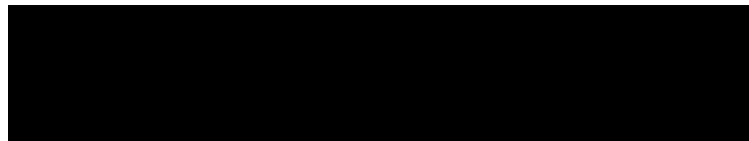
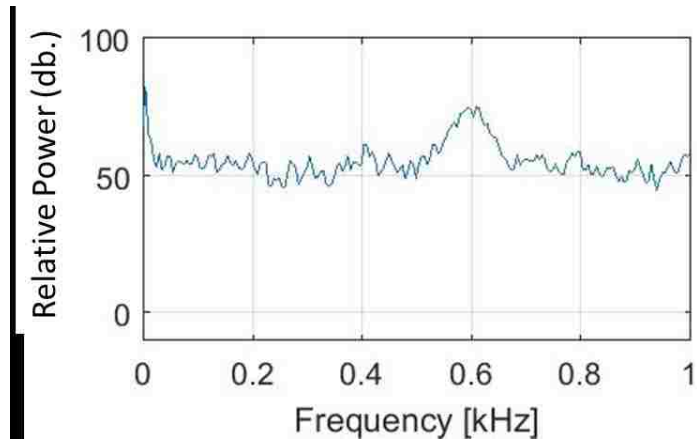
2.4.2 686 Ion Line

The second ion line discussed in Section 1.3.2 is the line suggested by *Dr. Earl Scime* [77]. This pump line is at 686.3162nm (436813.90 GHz) and the decay line is at 476.6197 nm. Therefore, a dell Optics line filter centered at 476.5 nm with a FWHM line width of approximately 1.0 nm was inserted before the PMT. This pump line has a relative intensity of 112 [58].



The tests with this ion line started at Port 6. Pressure scans were performed at $r = 0$ cm, $r = 6$ cm, and $r = 10$ cm. The data for these scans is shown in Figure 2.4.2.1. The peak for $r = 0$ cm in Figure 2.4.4 is due to plasma fluctuations, not LIF response as can be seen in the power spectrum for 1 mTorr and no laser on (Figure 2.4.5) as compared to 1 mTorr with the laser on (Figure 2.4.6). At 1.5mTorr the plasma peak moves so that it is not overlapping with the chopper frequency which was set at 600Hz, as shown in Figure 2.4.7.

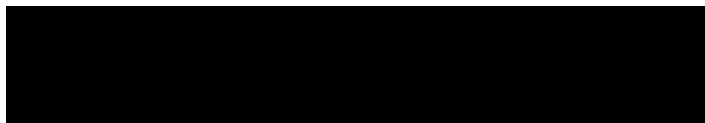
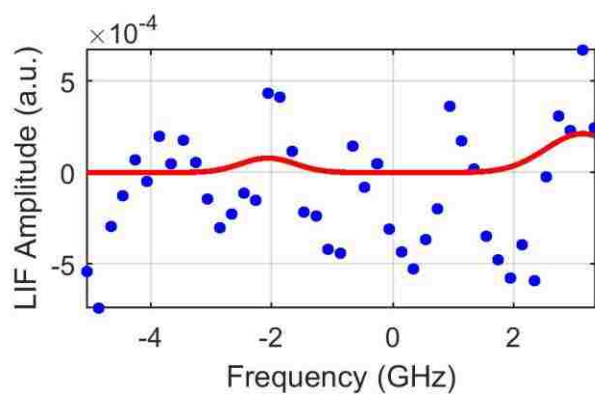


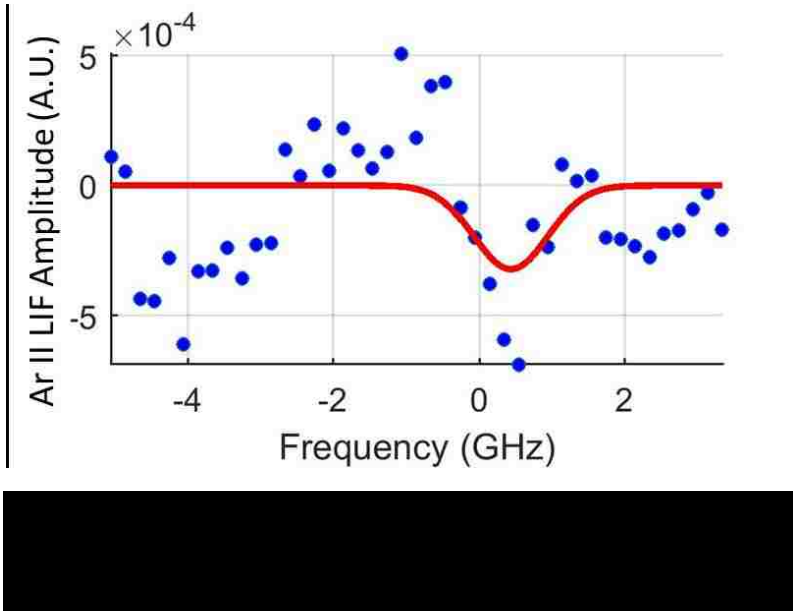
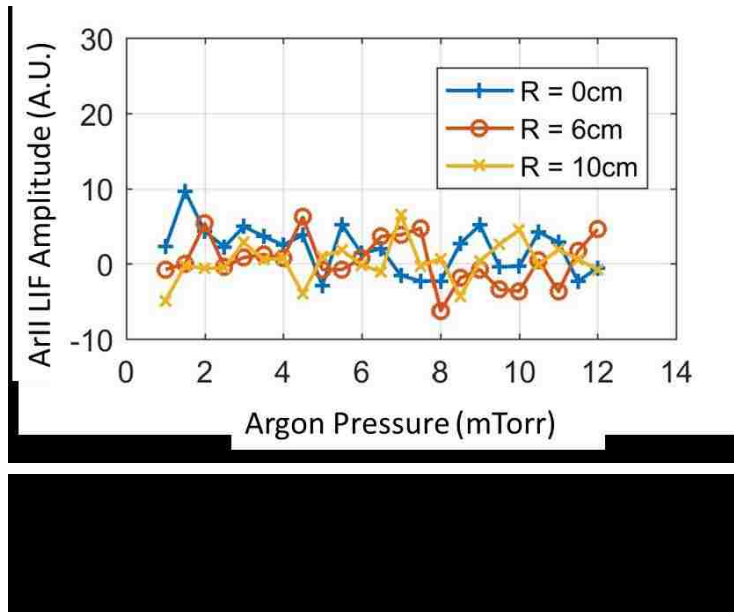


No power scans were performed at this port, but frequency scans were acquired at the same radial positions. These scans were acquired in a similar fashion as those for the

neutral line except that the laser was swept from 436809.05 GHz to 436817.05 GHz in 0.2 GHz steps. Figure 2.4.8 shows the frequency response for 10 mTorr argon at $r = 0$ cm. The frequency response at $r = 6$ cm and $r = 10$ cm are similar. All of these data indicate that there was no LIF response for the 686.3162 nm transition at this port.

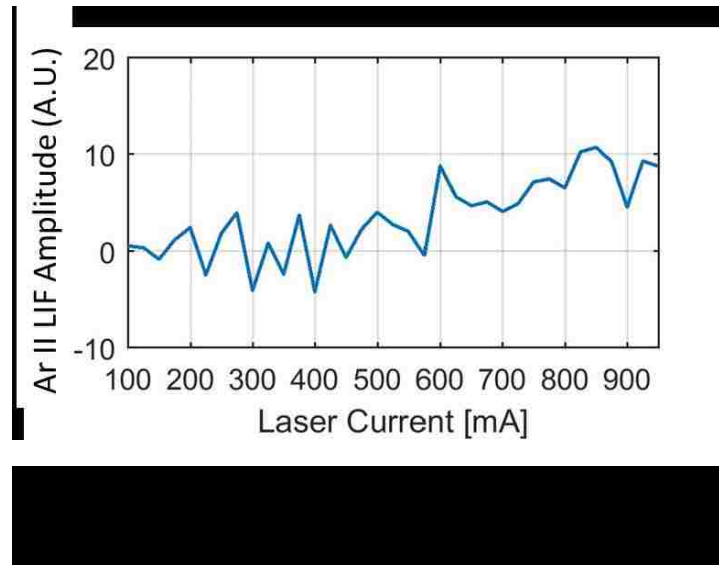
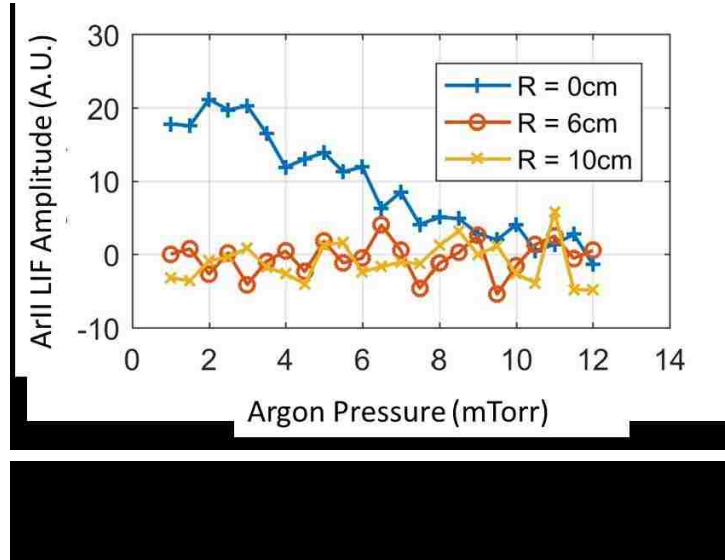
The collection side optics were then moved to Port 5, and pressure and frequency scans were performed as at Port 6. The pressure scans are shown in Figure 2.4.9, and the frequency scan at $r = 0$ cm with 10 mTorr argon is shown in Figure 2.4.10. The frequency scans at $r = 6$ cm and $r = 10$ cm are similar. Once again, there was no observable LIF response for this ion transition at Port 5.

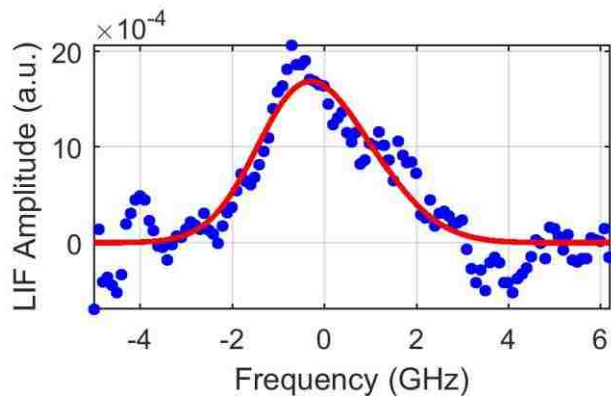




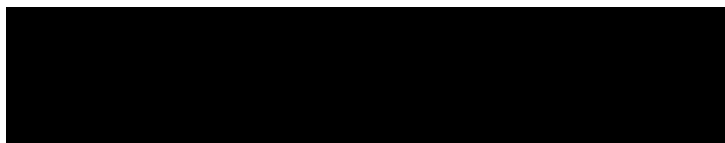
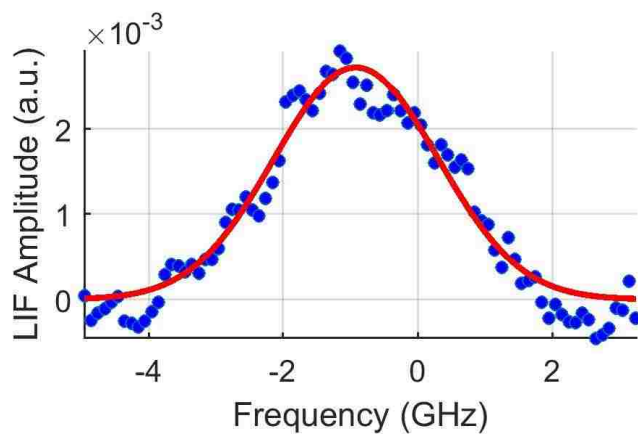
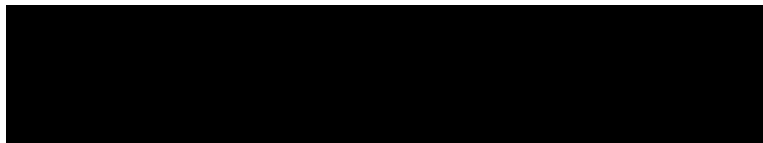
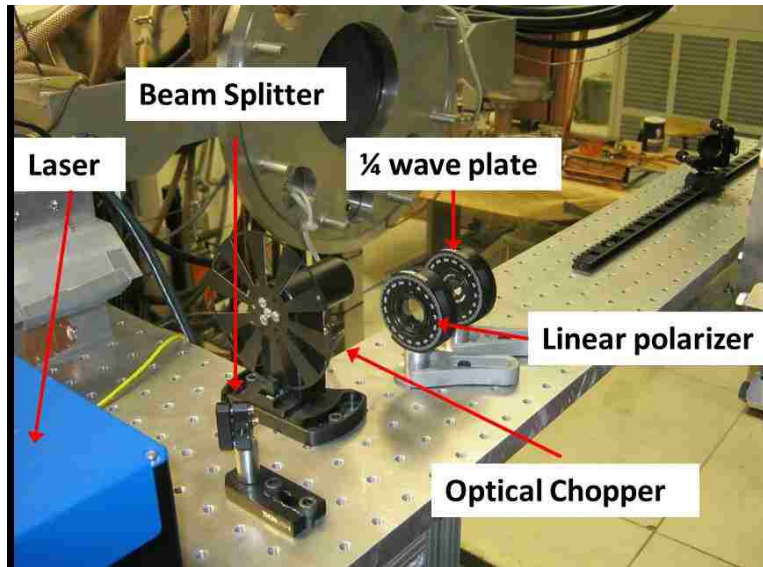
The collection side optics were moved to Port 4, and the pressure scans were repeated, as shown in Figure 2.4.11. This time there was a different response. Since these scans indicated an LIF response at low pressure and the center of the machine, attempts were made to further resolve this signal. A power scan was performed at the center of the

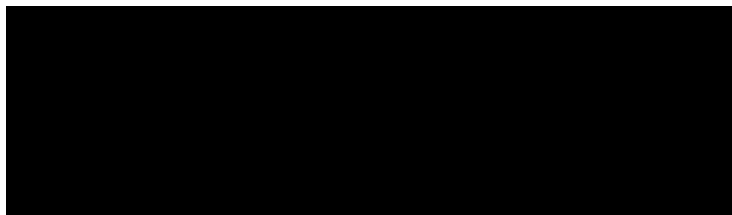
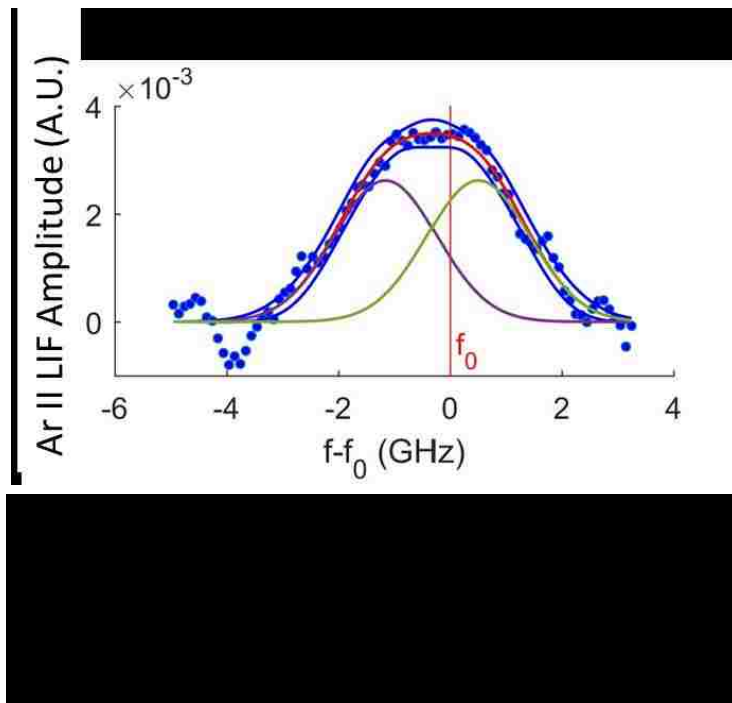
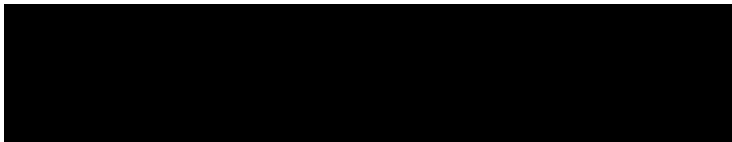
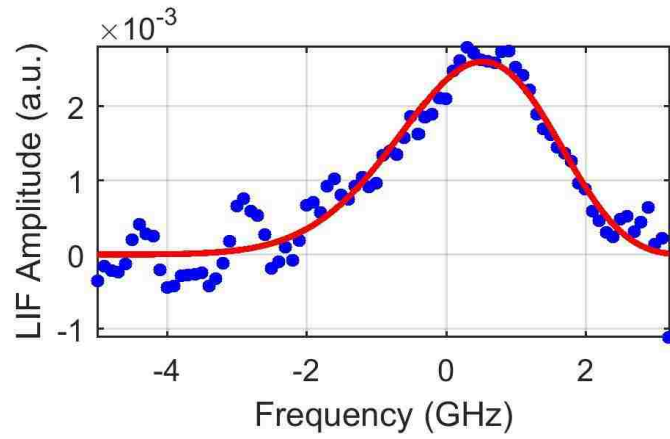
machine and 2.5 mTorr argon (Figure 2.4.12). As it did not appear that saturation would be an issue, a frequency scan was performed (Figure 2.4.13).





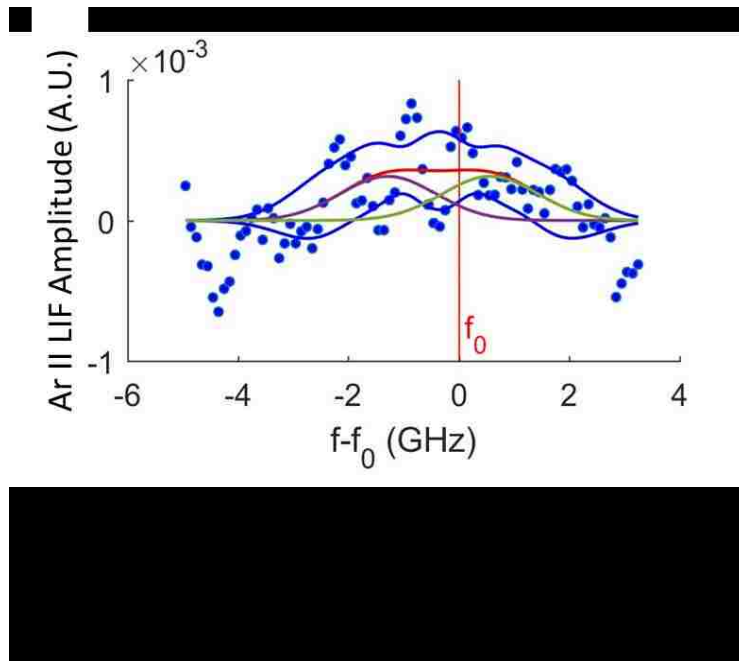
This response shows that there is a signal for this ion line, however, it did not have the characteristic double peak as expected from Zeeman splitting. To determine if this was a single peak, or if it was not enough signal to resolve the peaks, a quarter-wave plate was installed on the injection side of the optics after the optical chopper, as shown in Figure 2.4.14. Frequency scans were performed again; one with the quarter-wave plate at 45° , and a second with the quarter-wave plate at -45° , as shown in Figure 2.4.15, and Figure 2.4.16, respectively. These two plots show that Zeeman splitting is occurring, but that it cannot be resolved as the neutral LIF could. To investigate this further, the MatLab code used to analyze the raw data was modified to show a double Gaussian fit of the data. Figure 2.4.17 shows the analyzed data, the fit line, the confidence intervals, and the double Gaussian fit under the main peak. This shows that the Zeeman splitting for this line is very small and the peaks are compressed into one central peak.





Once it was determined that this response was actual LIF signal, frequency scans versus radial position were performed. For neutral LIF these scans were performed from

the center of the machine out to $r = 15$ cm. For this ion LIF line, data was collected for only $r = 0$ cm, $r = 1$ cm, and $r = 2$ cm as by this radial position, the LIF response was too small to be extracted from the noise, as shown in Figure 2.4.18. As the signal was so badly degraded, and the plots of signal versus pressure indicated no response for $r = 6$ cm and $r = 10$ cm, no further data was collected for this LIF line at this port.



As there was no usable response for either ion line at Port 6, or Port 5, no measurements were attempted for radial LIF at these ports. Since there was a response at Port 4 for the 686 Ion line, it was discussed to try radial laser injection. However, Port 4 is a 10-in. port, not an 8 in. port like those at ports 5 and 6. Therefore, to obtain radial LIF measurements at this port would have required making yet another yoke to hold the collection optics, and the removal of existing equipment from the top port at the Port 4 location. It was decided that the expected results were not worth the required effort, and no further ion data were collected.

2.5 Summary of LIF Measurements

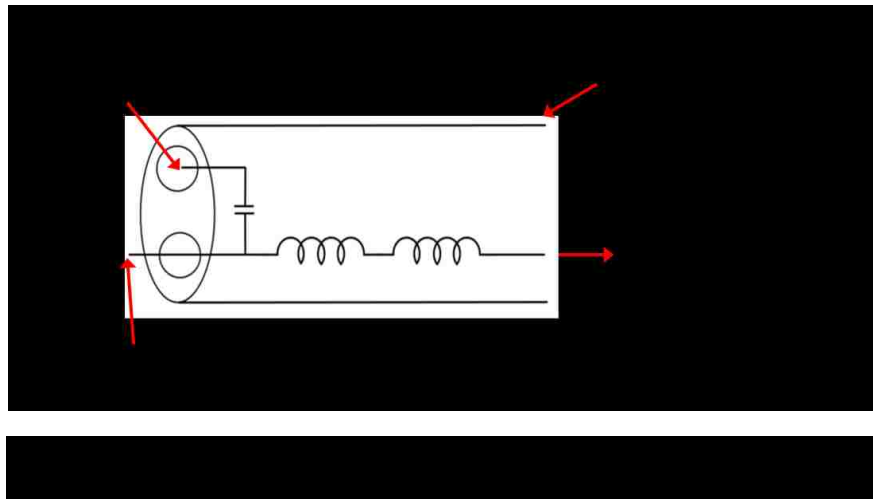
To summarize and clarify the preceding LIF measurements, Table 2.5.1 lists the different LIF schemes, (Ar I at 696 nm, Ar II at 688 nm, and Ar II at 686 nm), the ports, and the directions. A bold x, **X**, indicates this configuration was not attempted.

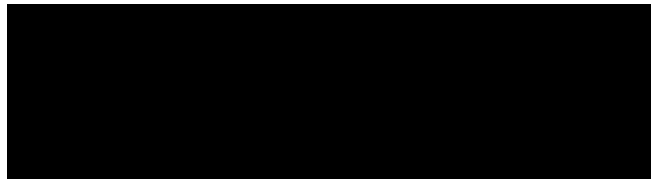
Table 2.5.1. Summary of LIF schemes attempted and the results.

		Ar I at 696 nm	Ar II at 688 nm	Ar II at 686 nm
Port 6	Axial	Data Recorded at 10 mTorr	Tried—Did not work	Tried—Did not work
	Radial	Data Recorded at 10 mTorr	X	X
	Azimuthal	Data Recorded at 10 mTorr	X	X
Port 5	Axial	Tried—Did not work	Tried—Did not work	Tried—Did not work
	Radial	X	X	X
	Azimuthal	X	X	X
Port 4	Axial	Tried—Did not work	Tried—Did not work	Minimal data recorded at 2.5 mTorr
	Radial	X	X	X
	Azimuthal	X	X	X

2.6 Swept Probe

Since two of the inputs for the CR model described in Section 1.3.5 are the electron temperature profile and the ion density profile for the given plasma, a radio frequency (RF) compensated probe was used to obtain a temperature and density profiles. *Desjardins* constructed and used this probe for dissertation research. The probe is shown in Figure 2.6.1 and Figure 2.6.2 [82]. A planar tip measuring 1.84 mm wide and 2.53 mm long (4.65 mm^2) was used for this probe. The inductor used has a self-resonant frequency (SRF) 10.8 MHz and acts as a RF choke providing a 38dB decrease in power of the 10 MHz from the Helicon antenna. The capacitor improves the time response of the probe, and gives stray capacitance a path to ground [82].

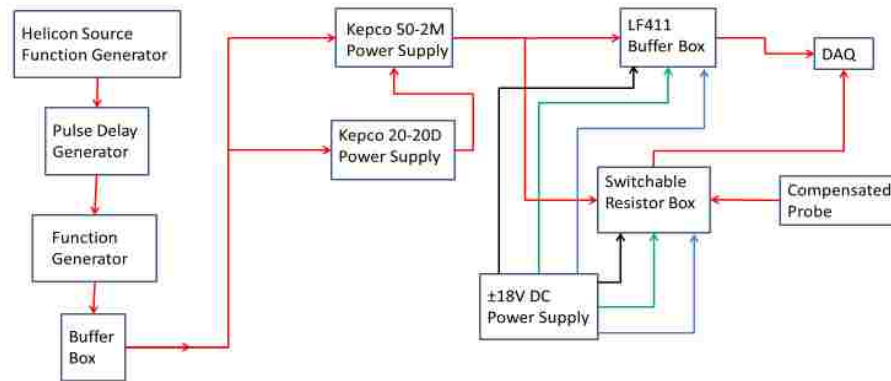




To obtain electron temperature, it was necessary to sweep the probe, i.e., apply a varying bias to the probe to be able to measure the response as a function of bias voltage. For this research, a triangle wave with a sweep rate of 150 Hz with and an amplitude of $\pm 70\text{V}$ was used to sweep the compensated probe. This was accomplished using a BNC Model 555 Pulse/Delay Generator, an Agilent 33120A Function Generator, a Kepco Model 50-2M Bipolar Operational Power Supply/Amplifier, a Kepco Model 20-20D Bipolar Operational Power Supply/Amplifier, and a switchable resistor box. Figure 2.6.3 shows a schematic of the bias voltage system.

Raw data from this probe are shown in Figure 2.6.4. The red trace is the bias applied to the probe (V_{bias}). A voltage divider of 1/11 was used to allow the signal to be collected on the DAQ. The blue is the response of the compensated probe (V_{probe}). The current is found by dividing by the resistor used in the resistor box. The part of the trace prior to the

Swept Probe Electronics Layout

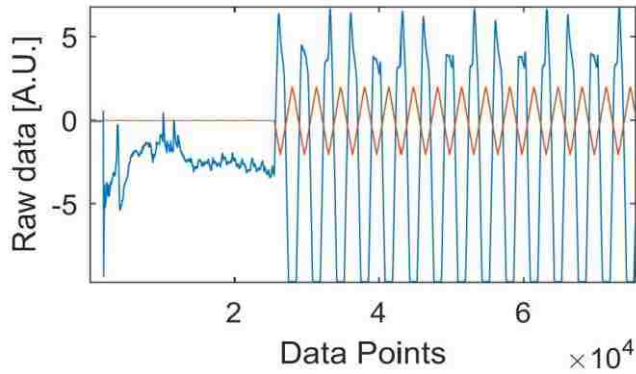


35

bias turning on is from the plasma without biasing. Observation of Figure 2.6.4 shows that V_{probe} is cut off on the negative side of the sweep. This is due to the limitations of the DAQ. To compensate for this limitation, two sets of data were taken at each radial position. One resistor was chosen to capture as much of the positive (ion) side of the sweep, and a second resistor was chosen to capture the negative (electron) side of the sweep.

By plotting the current versus the bias voltage, an I-V curve can be obtained, as shown in Figure 2.6.5. The blue trace in the plot is “ion” side of the data, and the red trace is the “electron” side of the data. Since the current is a combination of ion current and electron current, the standard procedure is to subtract the ion current from the I-V curve before attempting to fit the electron temperature [83]. Once this is done, the electron temperature can be found from the relation:

$$I_e = nev_{the} e^{\frac{(V_p - V_B)}{KT_e}} \quad (2.6.1)$$

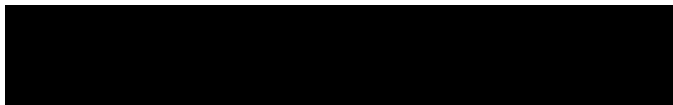
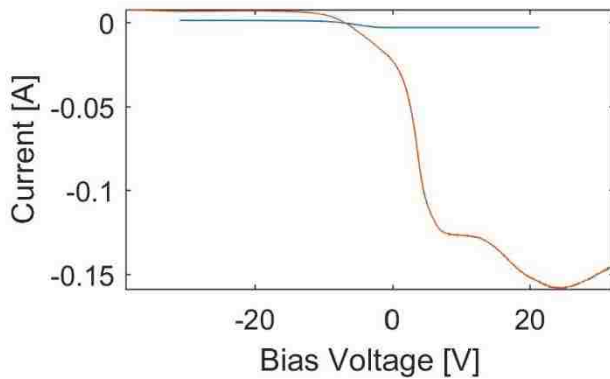


where n is the electron density, e is the electron charge, v_{the} is the electron thermal speed,

$$v_{the} = \sqrt{\frac{8KT_e}{\pi m_e}},$$

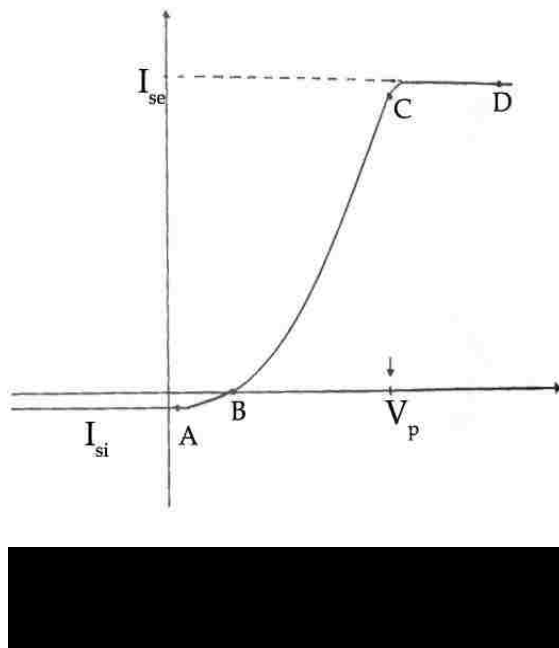
V_p is the plasma potential, V_B is the bias voltage, K is the Boltzmann

constant, T_e is the electron temperature, and m_e is the electron mass [83].



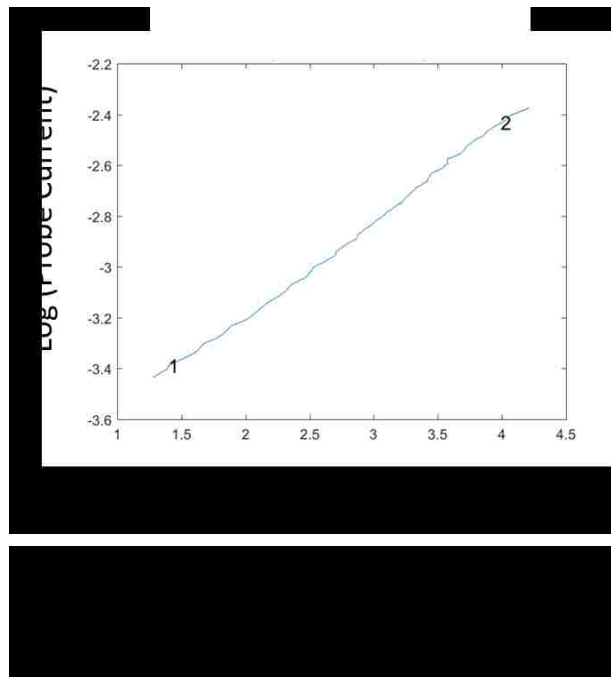
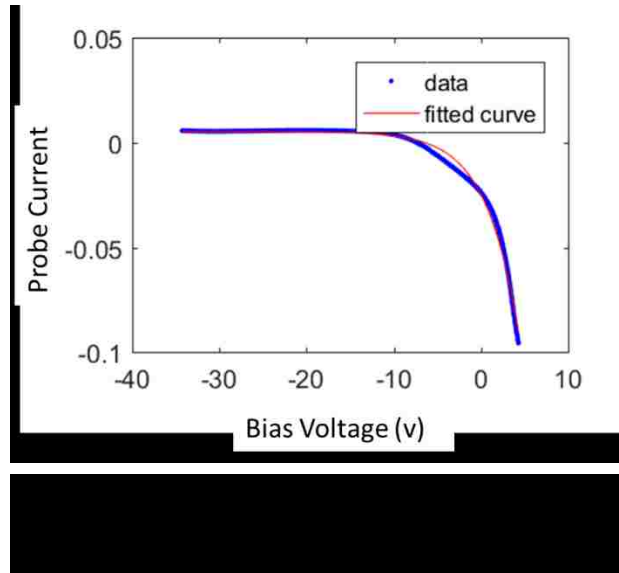
The ideal I-V curve shown in Figure 2.6.6 depicts how several pieces of information can be obtained. The ion saturation current, Point A, on the plot is the voltage at which the

probe is biased to a large enough negative value that no more electron current is collected. The floating potential, Point B, is the point the current goes to zero, i.e., no current is drawn for a given bias voltage. The plasma potential, Point C, is the point where the I-V curve rolls over to electron saturation, also called the “knee” of the curve. Point D is the electron saturation region where the only current is due to electron. On a real data plot, this is almost never “flat,” but will have some continued increase with applied voltage. The electron temperature is found by fitting an exponential to the portion of the I-V curve between Point B and Point C [82].

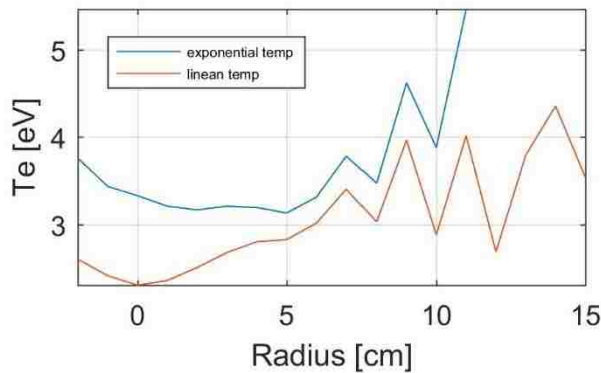


Two different methods for fitting an exponential to the data were used. The first method is to fit an exponential to the part of the curve above the ion saturation current, but below where the electrons start to saturate, i.e., the exponential part of the curve. This method is shown in Figure 2.6.7. The temperature is then found from the fitting parameters. The second method of determining the electron temperature is to plot the log of the current

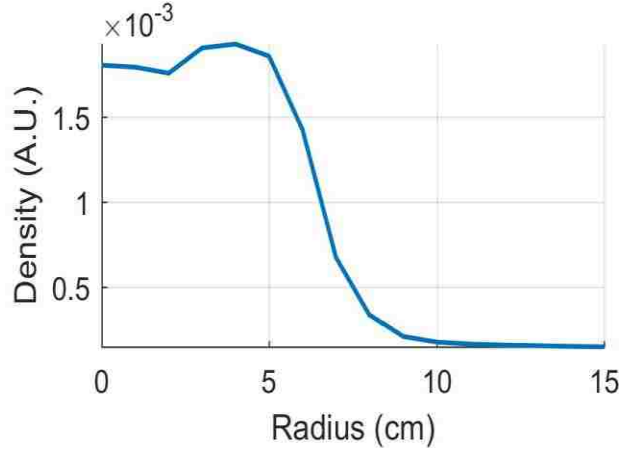
versus the bias voltage for the part of the curve that is exponential. The temperature is then found by taking the inverse of the slope of the resulting line [84], [83], as shown in Figure 2.6.8.



Both methods were used for this research and the radial profiles are shown in Figure 2.6.9. The exponential fit gives a slightly higher temperature, but the shape of the profiles is similar for radial positions to $r = 10$ cm. Data beyond 10 cm was not used in the CR model which will be discussed in more detail in Section 3.2



In addition to electron temperature profiles, an ion density profile, shown in Figure 2.6.10, was created from the “ion” side of the data. This was accomplished by creating a linear fit between the left end of the ion trace and a point on the ion trace where it starts to become exponential. This line was then extended to the left to where the bias voltage would be ~ -60 V. Since there were ten sets of data at each radial position, the mean of the shots was used as that point value and the standard deviation was used as the error. The mean values were then used as the ion saturation current and plotted as a function of radius.



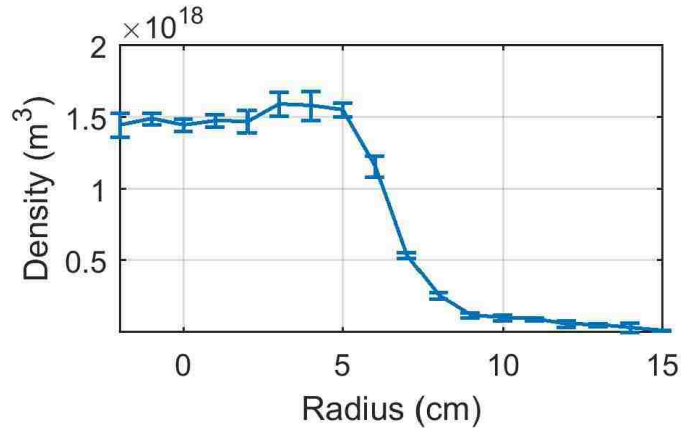
The absolute ion density profile was determined from:

$$I_{sat} = 0.6qn_iA\sqrt{\frac{kT_e}{m_i}} \quad (2.6.2)$$

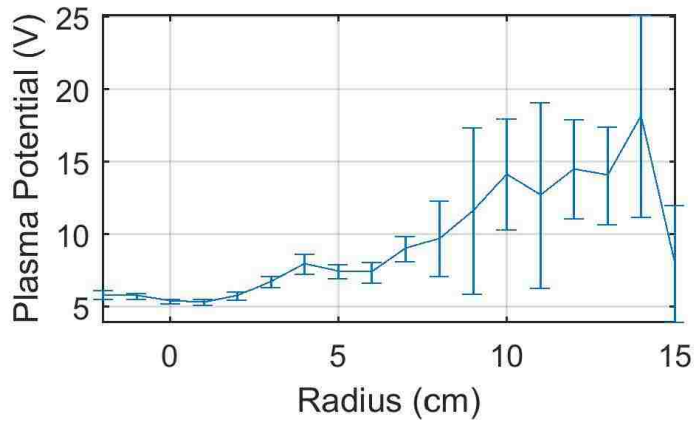
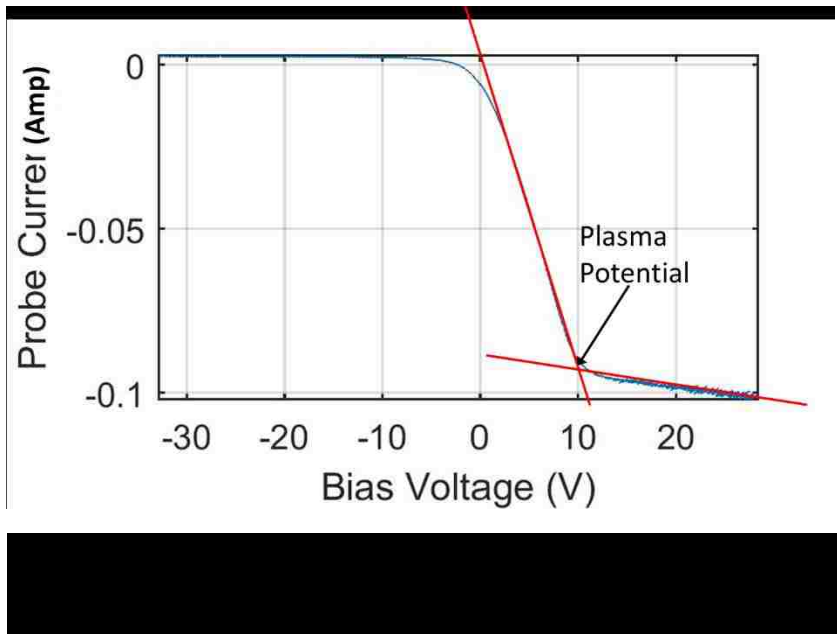
Where q is the electron charge, n_i is the ion density, A is the area of the probe tip, k is the Boltzmann constant, T_e is the electron temperature, and m_i is the ion mass. For this calculation, an average of the electron temperatures found above was used for T_e . The error for the ion density was calculated using quadrature analysis:

$$\Delta n = \sqrt{\Delta I_{sat} \left(\frac{\partial n}{\partial I_{sat}} \right) + \Delta T_e \left(\frac{\partial n}{\partial T_e} \right)} \quad (2.6.3)$$

Where Δn is the error in the ion density, ΔI_{sat} is the standard deviation discussed above, ΔT_e is the error in the electron temperature, $\frac{\partial n}{\partial I_{sat}}$ is the derivative of the ion density with respect to I_{sat} , and $\frac{\partial n}{\partial T_e}$ is the derivative with respect to electron temperature. The absolute ion density is shown in Figure 2.6.11.

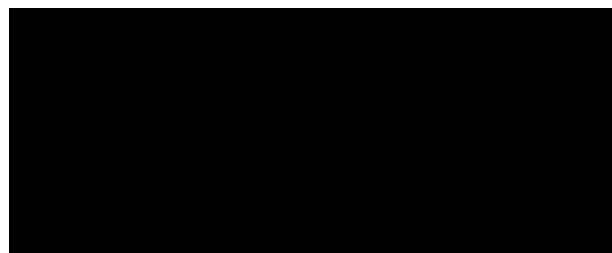
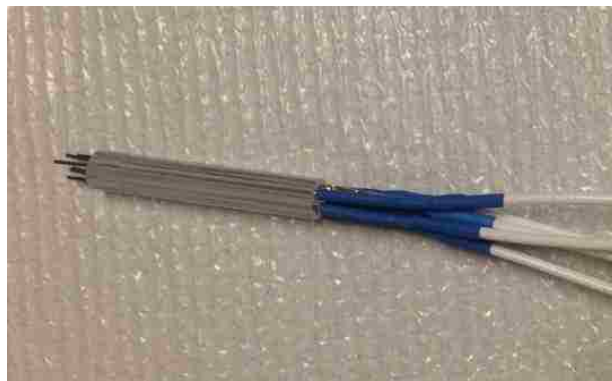
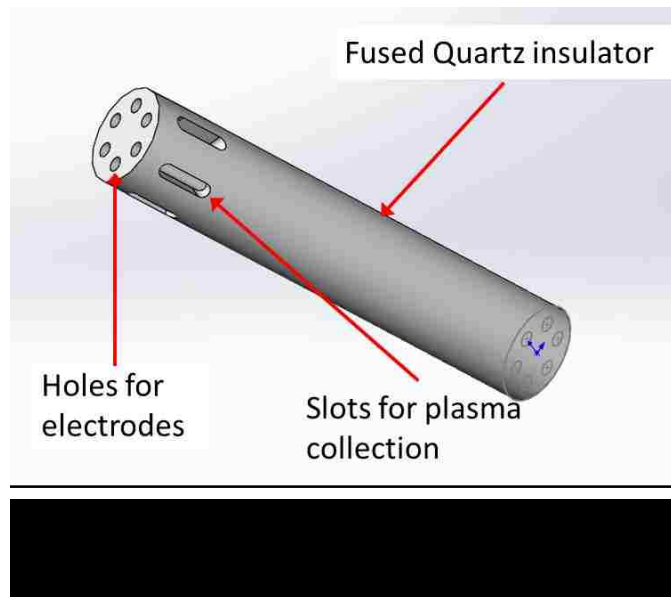


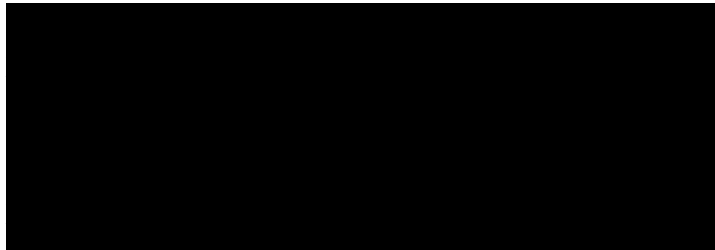
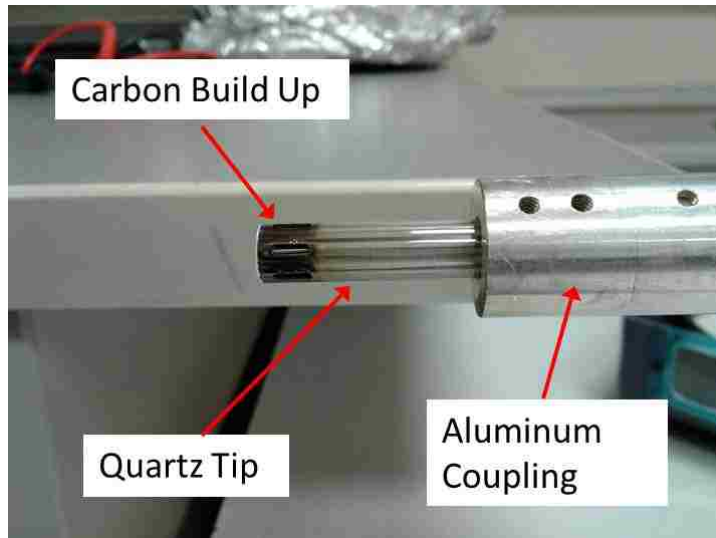
Finally, the swept probe data was used to produce a floating potential profile. As stated above the plasma potential is found from the “knee” of the I-V curve. This was accomplished by fitting two lines to the data and taking the intersection as the “knee,” or plasma potential. This technique is shown in Figure 2.6.12. This was repeated for each set of data and averaged as before to produce the profile of plasma potential versus radius shown in Figure 2.6.13.



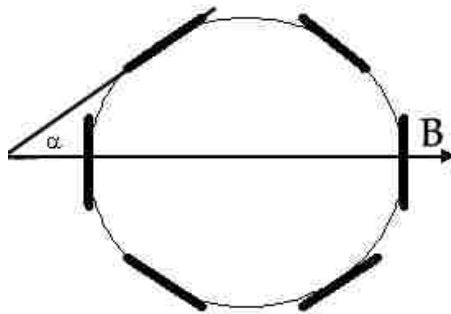
2.7 Mach Probe

Since this research was concerned with the effect of neutral particle motion with regards to the overall plasma response, i.e., the ion motion, it was decided to include ion flow measurements collected with a Mach probe. The probe used was based on the design used by *Dr. Desjardins* [82]. In her research *Dr. Desjardins* used a ceramic tip for the Mach probe. The new design incorporates a quartz tip manufactured by GM Associates Inc., but still has the six-tip configuration. The new quartz tip is 8 mm in diameter, 45 mm long, has six through holes 1.3 mm in diameter, and has six slots measuring 1.3 mm by 2.54 mm aligned with the trough holes. The original design of this quartz tip had the holes for the electrodes drilled all the way through the quartz, as shown in Figure 2.7.1 and Figure 2.7.2. It was found that debris (carbon from the chamber and tantalum from the electrodes) would build up on the end of the tip and short between the tips, as shown in Figure 2.7.3. High Desert Frameworks was able to fuse the end of the quartz so that this was no longer an issue. However, the tip still had shorting issues and it was found, using a scanning electron microscope (SEM) with energy dispersive X-ray (EDX) technology, that the carbon and sputtered tantalum were coating the outside of the quartz. High Desert Frameworks suggested that the tip be soaked in Etchall Reusable Glass & Mirror Dip 'n etch Liquid to remove the debris, as shown in Figure 2.7.4. This did work as described and reliable data has been collected with the Mach probe by *M. W. Hatch*.





The analysis of the data collected with the Mach probe was done in the same manner as described by *Desjardins* [82]. Figure 2.7.5 shows the basic design of the Mach probe. Each tip will collect current that from particles (ions) that hit that tip. The tips perpendicular to the magnetic field will collect current from plasma flowing in the direction of the field. They will not collect current from plasma flowing in other directions. Using the ratio, R , of the collected ion saturation current between the upstream tip and the downstream tip, it is possible to calculate the ion flow speed in the direction of the magnetic field (axial direction in this case).



Azimuthal ion flow (perpendicular to the magnetic field, B) is determined by the current that is collected by the tips at an angle other than 90° to the magnetic field. These tips collect both axial and azimuthal current, but the currents can be decoupled using the following equations [82]:

$$\frac{1}{c} \ln(R) = M_{\parallel} - M_{\perp} \cot(\alpha) \quad (2.7.1)$$

$$C = 1 + 0.14 \cosh\left(\frac{M_{\parallel}}{0.862}\right) \approx 2.3 - 2.5 \quad (2.7.2)$$

$$R = \frac{I_{up}}{I_{down}} \quad (2.7.3)$$

$$M = \frac{v}{C_s} \quad (2.7.4)$$

where:

I_{up} = Ion saturation current upstream (toward the source)

I_{down} = Ion saturation current downstream (away from the source)

C_s = Sound speed

v = Ion flow speed

M_{\parallel} = Parallel Mach number

M_{\perp} = Perpendicular Mach number

If this had been a four-tip probe, with the tips at 90° to each other, then it would have been possible to use Equation 2.7.1 without modification. Since the tip used has six tips at 60° to each other, it is necessary to solve the following equations for the unknown, M_{\perp} :

$$\frac{1}{C} \ln(R_1) = M_{\parallel} - M_{\perp} \cot(\alpha_1) \quad (2.7.5)$$

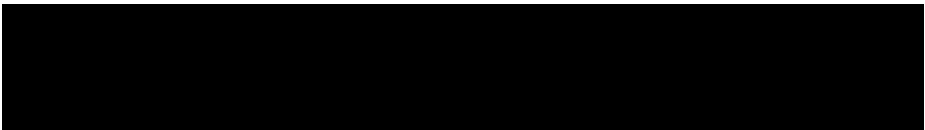
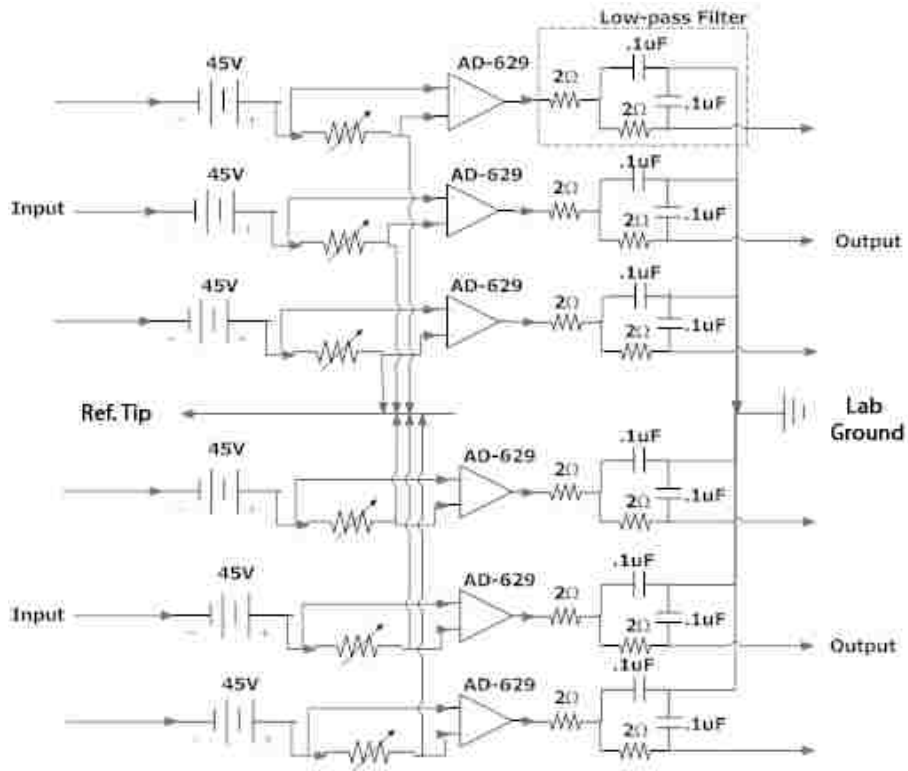
$$\frac{1}{C} \ln(R_2) = M_{\parallel} - M_{\perp} \cot(\alpha_2) \quad (2.7.6)$$

$$\frac{1}{C} \ln\left(\frac{R_1}{R_2}\right) = -M_{\perp} (\cot(\alpha_1) - \cot(\alpha_2)) \quad (2.7.7)$$

Equation 2.7.7 can then be used to solve for M_{\perp} since all of the other variables are known [82].

The electrical circuit for the Mach probe is shown in Figure 2.7.6. For this research, the 45 VDC bias was replaced with 90 VDC bias [82]. To account for variation in tip

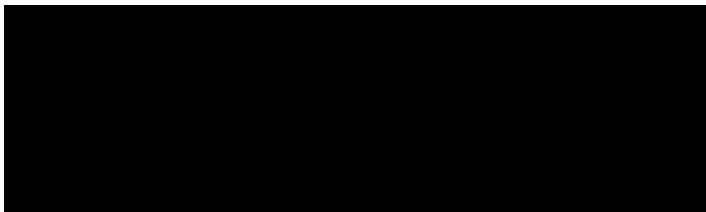
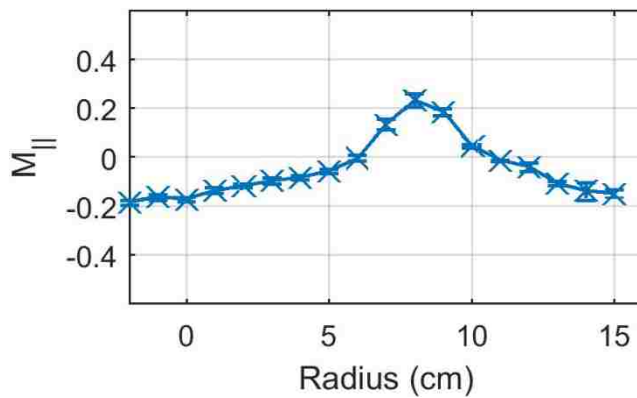
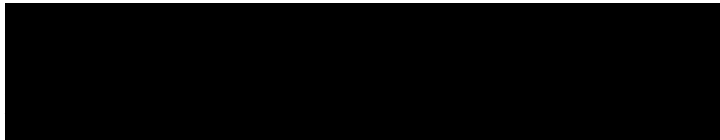
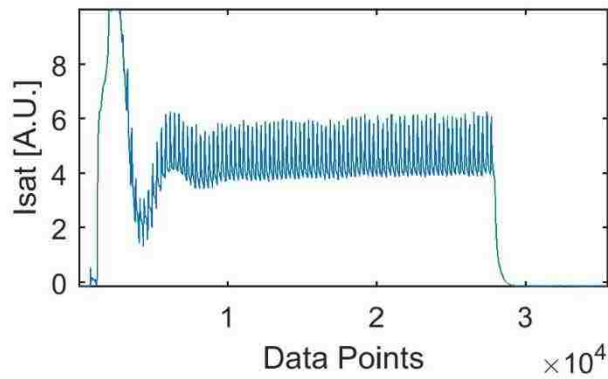
collecting area, the tips were calibrated to each other by setting a single tip toward the helicon source, adjusting the variable resistor to a value on the DAQ, then rotating the probe so the next tip was pointed toward the source and adjusting its resistor until it showed the same value as the first tip. This procedure was repeated for all six tips.

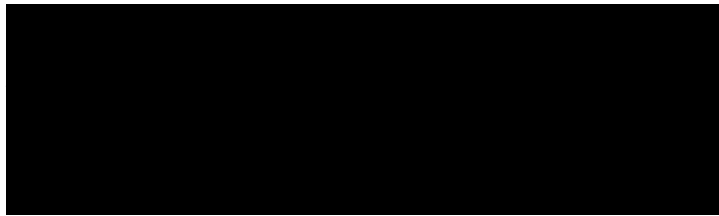
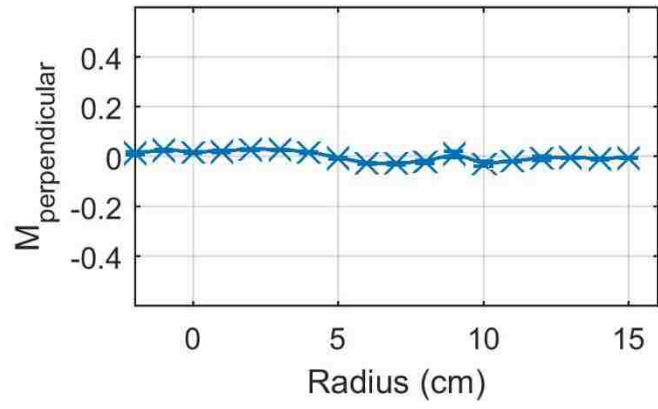


Once the tips were calibrated to each other, data collection could begin. The probe was rotated so that Tip 1 (this is arbitrary, but labeled for reference) was directed toward the helicon source for a reference position. Data were collected in 1cm increments starting at $r = -2$ cm and continuing to $r = 15$ cm, with $r = 0$ cm being the center of the chamber. Figure 2.7.7 shows the raw data for a typical plasma discharge, and Figure 2.7.8 and Figure

2.7.9 show the resulting ion velocity measurements. These will be discussed in more detail in Section 4.1.

The current Mach probe was constructed and tested by *M. W. Hatch*. The data presented here was collected by *M. W. Hatch*, and presented at the American Physical Society (APS) Division of Plasma Physics (DPP) 2017 Conference [24].



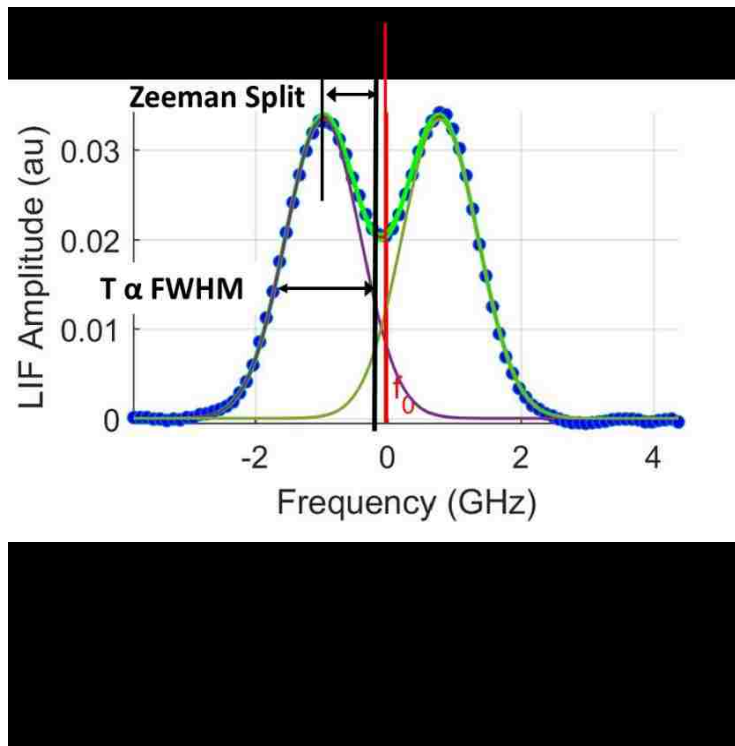


Chapter 3: Experimental Results and Analysis

3.1 Neutral Density, Temperature and Flow Measurements

From the neutral LIF signal versus frequency plots, it is possible to calculate the amplitude, temperature, velocity, and Zeeman split for each radial position. These values can then be plotted versus radius to give amplitude (relative density), temperature and velocity profiles. The Zeeman splitting can be compared to theory; there is no need to plot it as a function of radius since the background magnetic field is constant.

Figure 3.1.1 shows a typical plot of the neutral LIF response as a function of frequency. Also shown in the figure is the Zeeman split due to the magnetic field, the velocity, and the full width at half maximum (FWHM) used to calculate the neutral doppler shift of the data from the resonant frequency, f_0 , used to calculate the neutral temperature.



Determining the amplitude is straight forward. It is just the max value of the LIF signal recorded for each frequency scan. The Zeeman splitting was found from the fit of the curve (Equation 1.3.17) to the data. These values are shown in Table 3.1.1. As can be seen these values are in good agreement with the calculated Zeeman splitting values in Section 1.3.3, i.e., the Zeeman Split = 0.9274 GHz \pm 0.0549 GHz.

For the velocity, the difference between the center frequency (f_0) and the center of the Zeeman split peaks (f) was used in the equation for Doppler shift:

$$f = \frac{\Delta v}{c} f_0 \quad (3.1.1)$$

In this equation, c is the speed of light in vacuum, and Δv is the Doppler shifted velocity. The direction is found from [85]:

$$\omega_s = \omega_0 + \mathbf{k} \cdot \mathbf{v} \quad (3.1.2)$$

where ω_s is the Doppler shifted frequency, ω_0 is the resonant frequency of the atomic transition, \mathbf{k} is the wave vector in the direction of the injected laser, and \mathbf{v} is the velocity of the particle observed. For all of the neutral velocity measurements, the Doppler shifted frequency is down shifted from the resonant frequency, indicating that the velocity is negative, and the particles are moving toward the laser injection point.

The neutral temperature was calculated using:

$$\Delta f_{FWHM} = \sqrt{\frac{8kT \ln 2}{mc^2}} f_0 \quad (3.1.3)$$

Δf_{FWHM} is the change in frequency for the full width, half maximum value of the fit to the data, k is the Boltzmann constant, T is the temperature in eV, and m is the mass of the argon ion.

Table 3.1.1. Measured values of Zeeman splitting for $B = 0.044T$.

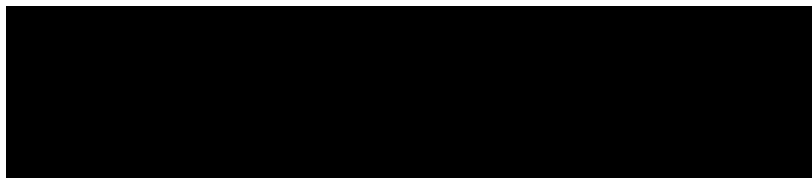
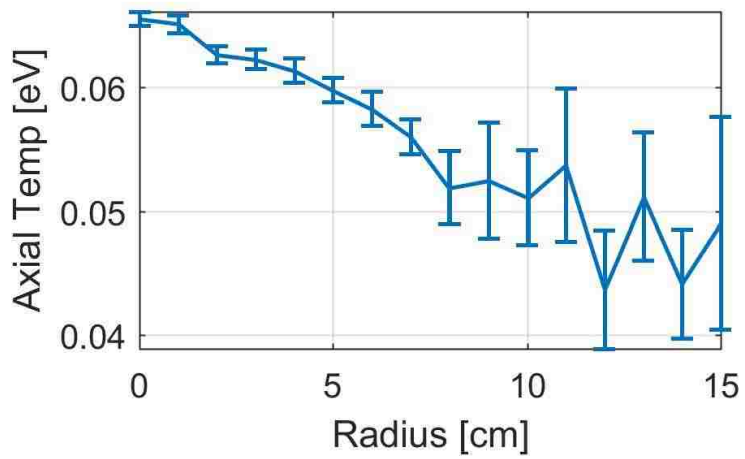
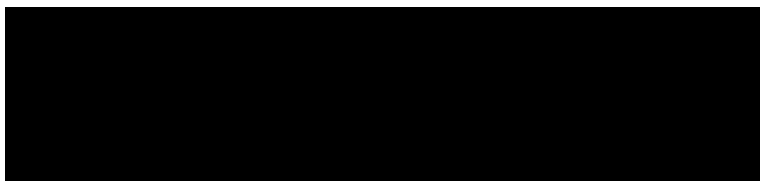
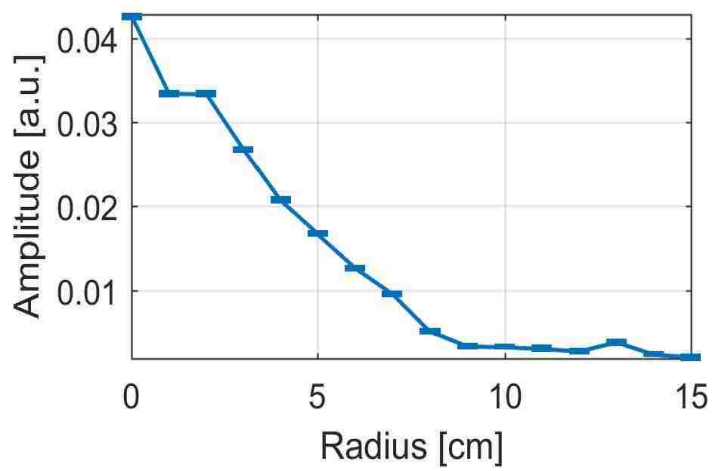
radius (cm)	Zeeman Split (GHz)	Error (GHz)
0	0.8806	0.0047
1	0.8771	0.0061
2	0.8822	0.0057
3	0.8843	0.0068
4	0.8850	0.0084
5	0.8586	0.0084
6	0.8694	0.0117
7	0.8587	0.0132
8	0.8625	0.0293
9	0.8512	0.0448
10	0.8612	0.0370
11	0.8923	0.0622
12	0.8334	0.0524
13	0.8898	0.0559
14	0.8823	0.0513
15	0.8706	0.0895

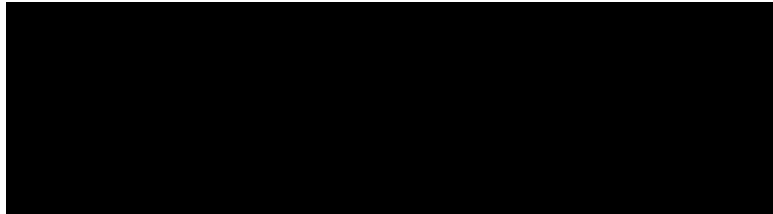
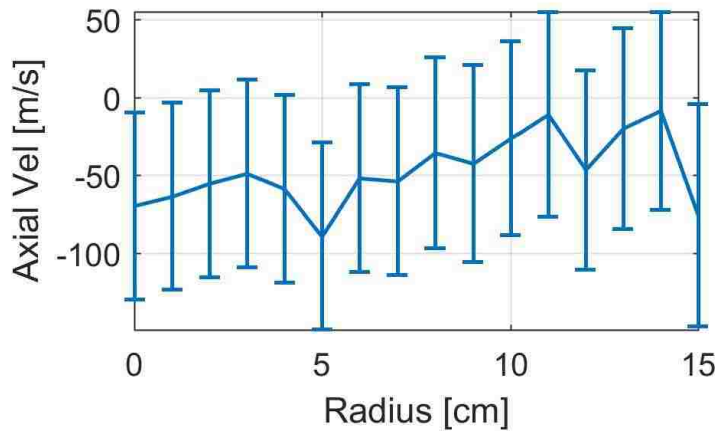
3.1.1 Measurements using Axial Laser Injection

Once all the data was processed, density, temperature and velocity profiles were constructed as a function of radius. This was repeated for the axial, radial, and azimuthal data.

Figure 2.2.1 shows the laser injection and collection optics orientation for axial LIF measurements. The following plots show the density (amplitude) profile (Figure 3.1.2), the temperature profile (Figure 3.1.3), and the axial (parallel) velocity (Figure 3.1.4) for ArI. For the density profile, it appears that the profile is peaked at the center. It should be remembered that this is for state #2 of the 65 neutral states. As will be shown in Section 3.2, the ground state neutral density profile is depleted in the center. In Figure 3.1.4, the velocity is in the negative direction which is away from the helicon source, and approximately 50 m/s. The axial neutral temperature is ~ 0.05 eV. Error bars for the amplitude and temperature were obtained from the confidence intervals (CI) of the fit to the data (Equation 1.3.17). The error in the velocity measurements is a combination the confidence intervals of the fit to the data and the absolute resolution of the wavemeter (WE). The absolute resolution of the wavemeter is 60 m/s. These errors were added in quadrature, i.e.,

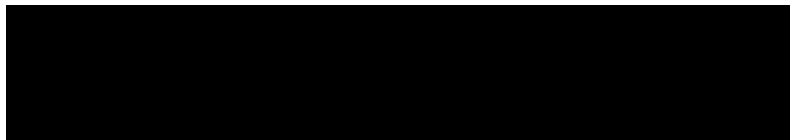
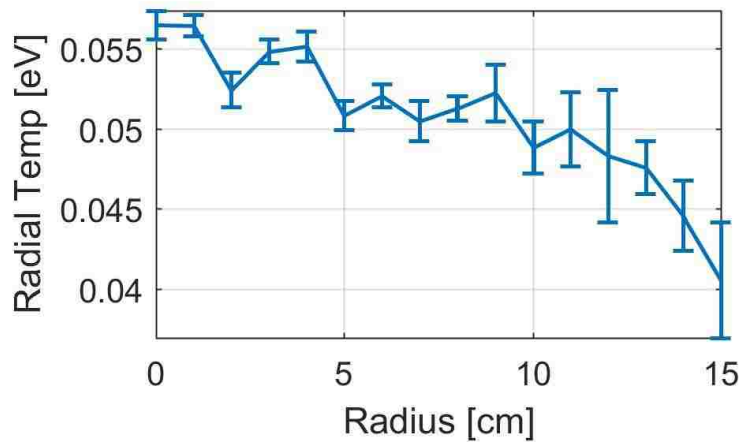
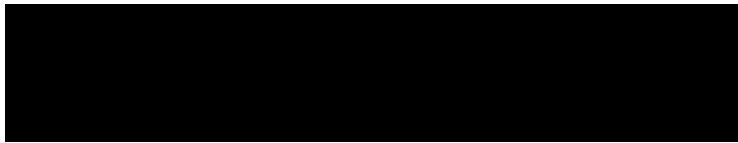
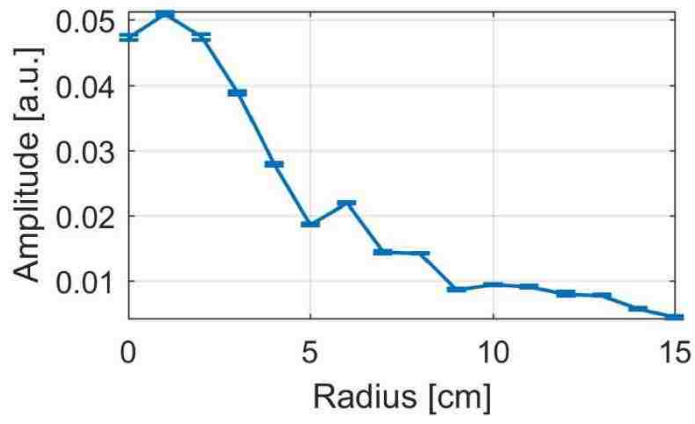
$$v_{error} = \sqrt{CI_{velocity}^2 + WE^2} \quad (3.1.4)$$

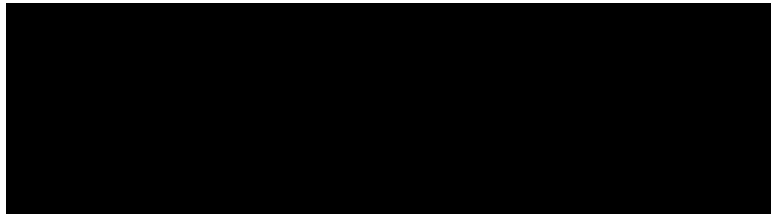
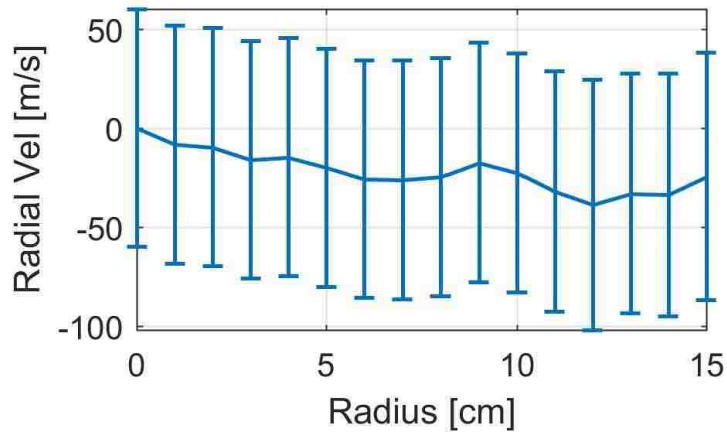




3.1.2 Measurements using Radial Laser Injection

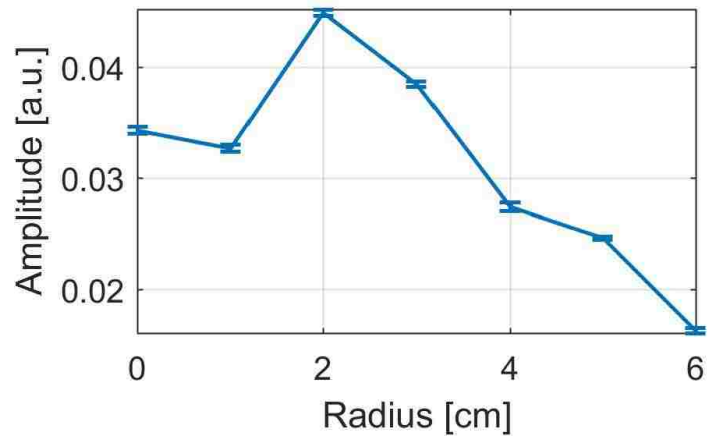
Figure 2.4.1 and Figure 2.4.3 show the configuration of the injection laser and collection optics used for radial LIF measurements. As stated in Section 2.4.1, all of the radial LIF measurements were performed at Port 6 with the collection optics at the 60° degree port. The neutral (ArI) LIF amplitude (density) profile, temperature profile, and radial velocity are shown in Figure 3.1.5, Figure 3.1.6, and Figure 3.1.7, respectively. Once again it would appear that the density is peaked toward the center of the machine, but that would be a naive assessment as will be explained in Section 3.2. In this case, the negative velocity indicates flow radially outward from the center of the machine and less than 50 m/s. The radial temperature is ~0.05 eV.

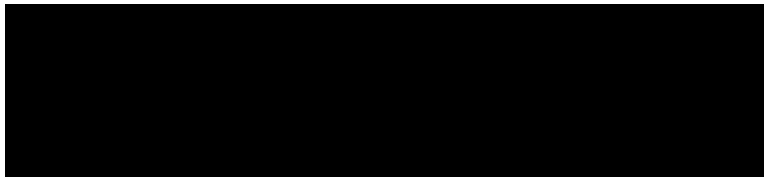
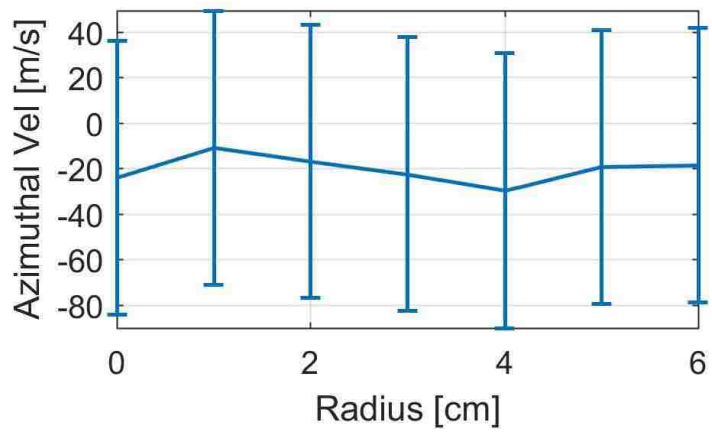
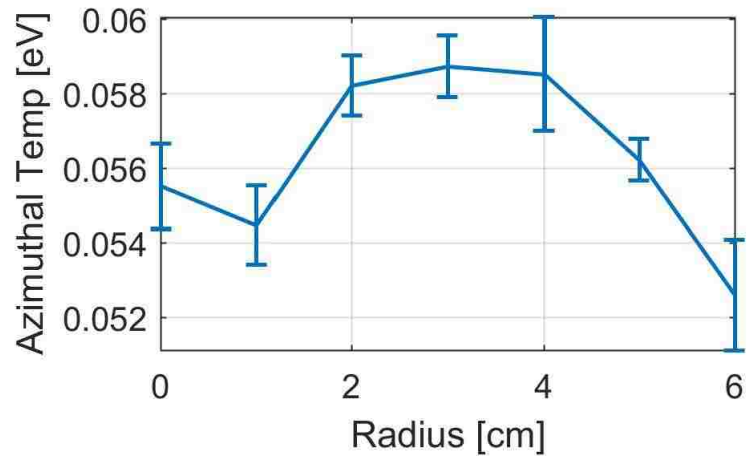




3.1.3 Azimuthal Measurements

For azimuthal LIF measurements, the laser and collection optics remained in the same orientation as for the radial measurements except that in this case, the laser was moved vertically using a system of optical mirrors, see Figure 2.3.20, Figure 2.3.21 and Figure 2.3.22. The scan was limited to 6cm due to the 8in conflat window at Port 6. The amplitude (density), temperature and azimuthal (perpendicular) velocity profiles are shown in Figure 3.1.8, Figure 3.1.9, and Figure 3.1.10. In this case the negative velocity indicates neutral flow in the electron diamagnetic direction (EDD) and approximately 20 m/s. The azimuthal temperature was ~ 0.055 eV.

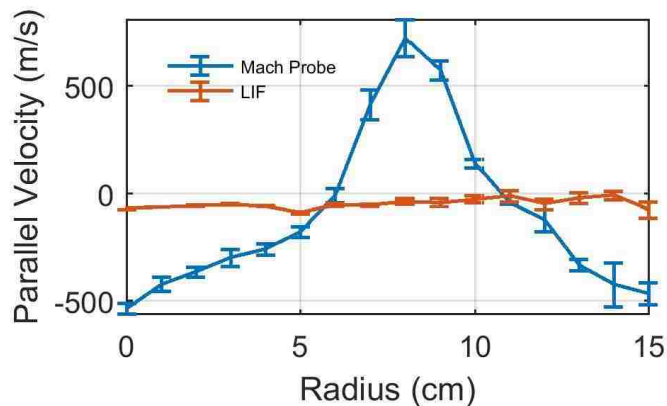




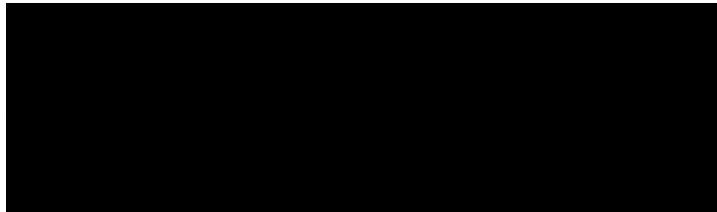
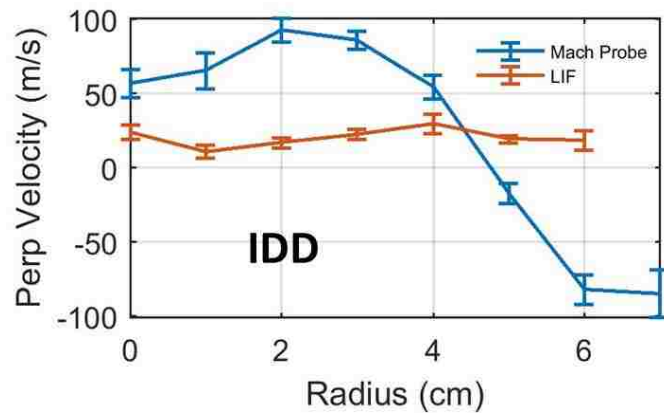
3.2 Comparison with Mach Probe Measurements

Since we now have neutral velocity measurements, it is possible to compare these to the Mach probe measurements of the ion velocities. To plot these on the same scale, the Mach probe velocities were multiplied by the sound speed, $C_s = \sqrt{\frac{qTe}{m_i}}$, (3.0972×10^3 m/s), to obtain velocities in m/s. The parallel (axial) and perpendicular (azimuthal) velocity comparisons are shown in Figure 3.2.1, and Figure 3.2.2, respectively.

For the parallel velocity, the neutral flow is all away the source and less than 50 m/s. The ion flow, on the other hand, the ion flow is away from the source for $r = 0$ cm (the center of the machine) to $r = 6$ cm. It then reverses direction to flow toward the source from $r = 6$ cm to $r = 11$ cm, and reverses again to flow away from the source. The velocity varies from ~ 550 m/s away from the source to ~ 700 m/s toward the source.



The perpendicular ion velocity also shows flow reversal. The flow in the plasma center is in the electron diamagnetic direction (EDD) and changes to the ion diamagnetic direction (IDD) at ~ 5 cm. The neutral particle velocity does not change direction and is in the EDD. The neutral velocities are less than 20 m/s, where the ion velocities range from ~ 90 m/s in the EDD, to ~ 80 m/s in the IDD.



3.3 CR Model Fit

The neutral and ion flows shown in the previous section would seem to indicate that the neutral flow has little effect on the ion flow. However, it is the neutral radial velocity that would contribute to an $\mathbf{F} \times \mathbf{B}$ drift described in Section 1.1.3. Recall from the momentum equation given by *Vranješ* [22], the ion-neutral collision force term has the form:

$$\mathbf{F}_{ni} = v_{in} m_i n_i \mathbf{v}_n \quad (3.3.1)$$

with:

$$v_{in} = n_0 \sigma_s^i \sqrt{\frac{kT_i}{m_i}} \quad (3.3.2)$$

In these equations, v_{in} is the ion-neutral collision frequency, m_i is the ion mass, n_i is the ion density, v_n is the neutral velocity, n_0 is the ground state neutral density, σ_s^i is the ion-neutral collision cross section, $\sim 5 \times 10^{-15} \text{cm}^2$, k is the Boltzmann constant, and T_i is the ion temperature [86].

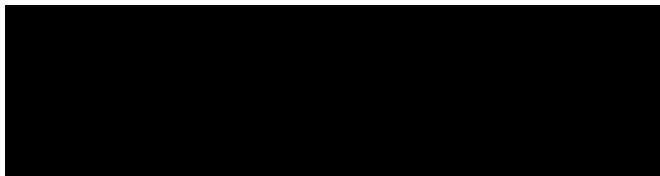
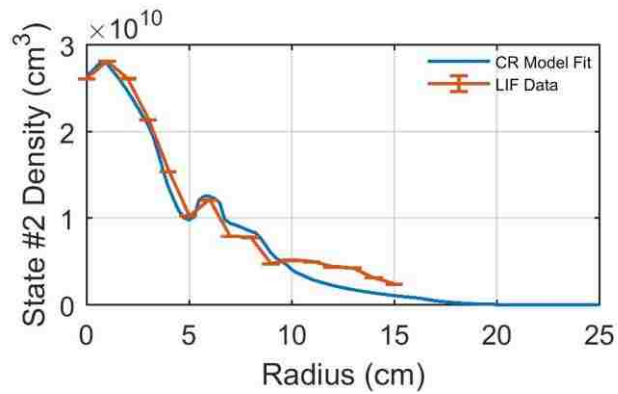
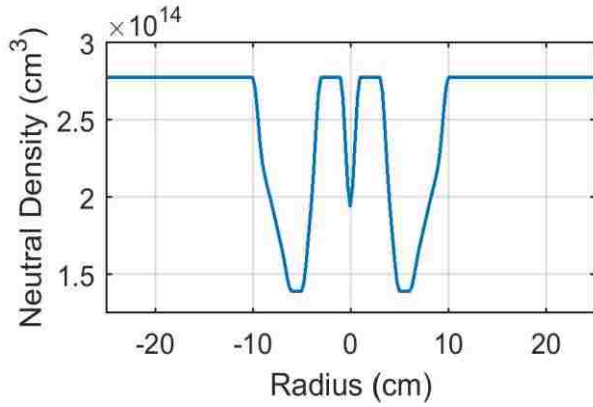
Using this force, the FxB drift can be calculated from:

$$\mathbf{F} \times \mathbf{B}_{Drift} = \frac{1}{q} \frac{\mathbf{F} \times \mathbf{B}}{B^2} \quad (3.3.3)$$

Since the collision frequency is a function of the ground state neutral density, the CR model described in Section 1.3.5 was used to obtain a ground state neutral density profile. The model requires the electron temperature and density profile as inputs. These were provided by the swept probe described in Section 2.6. The other input is a test ground state neutral density profile. The output is the density profiles of all 64 excited neutral argon states. These are compared to the measured density profile, in this case state #2, i.e., the $(^2P_{3/2}^0)4s\ ^2[3/2]_2^0$ energy level. Once a reasonable fit is obtained, the input ground state neutral density profile is taken as the best estimate.

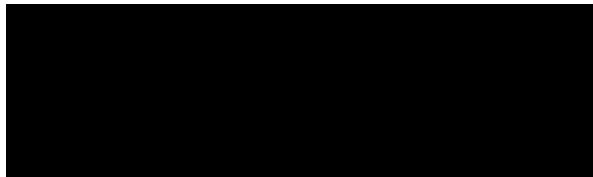
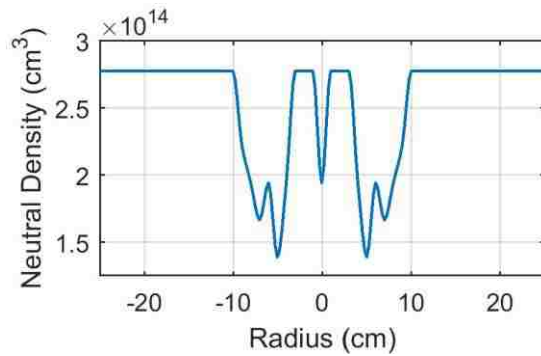
For the measured radial excited state neutral density profile, the ground state profile used is shown in Figure 3.3.1, and the fit of excited state #2 to the data is shown in Figure 3.3.2. A MatLab code using the piecewise cubic Hermite interpolating polynomial (pchip) fitting function was used to obtain the ground state neutral density profile. This ground state density profile shows a depletion of $\sim 30\%$ and 2 cm wide at the center of the plasma. It has a second depletion region at 5 cm of $\sim 50\%$ and 6 cm wide.

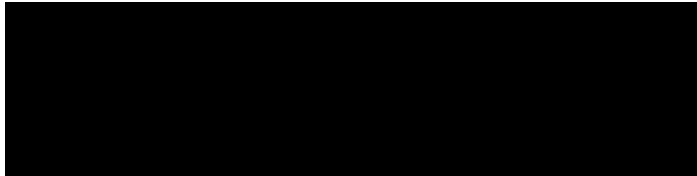
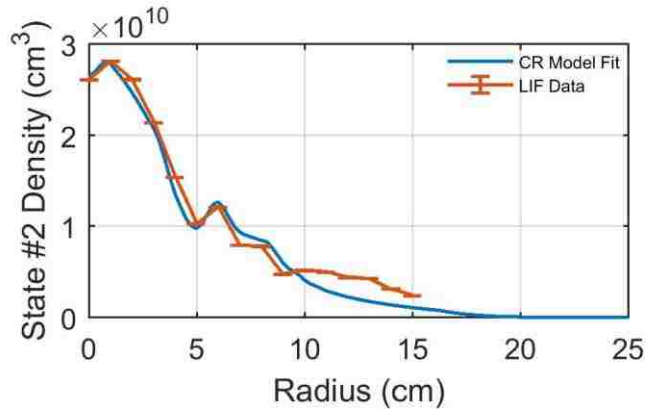
The output of the CR model is a reasonable match to the LIF data for the excited state #2. The CR model can also include an electron beam. This feature was used to match the increase in LIF signal at 6 cm. The beam had an energy of 15.5eV and a temperature of 0.01eV, and was located at 6 cm.



If the electron beam is not included, then a modification of the depletion region at 5cm needs to be included. This modification requires the depletion to be ~ 30% at 6 cm, then back to ~ 40% at 7 cm. The depletion region is then allowed to come back to 0% by 10 cm. Figure 3.3.3 shows the new ground state neutral density profile and Figure 3.3.4 shows the fit from the CR model to the data. As can be seen, both methods give good agreement with the measured neutral state #2 profile.

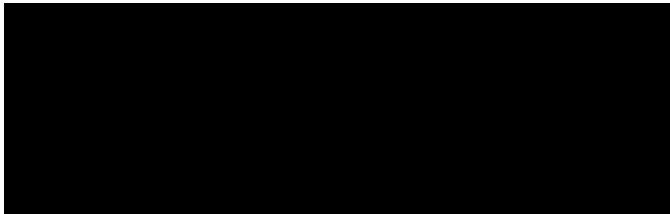
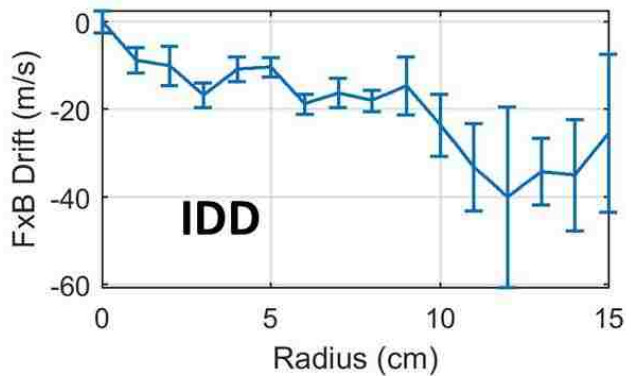
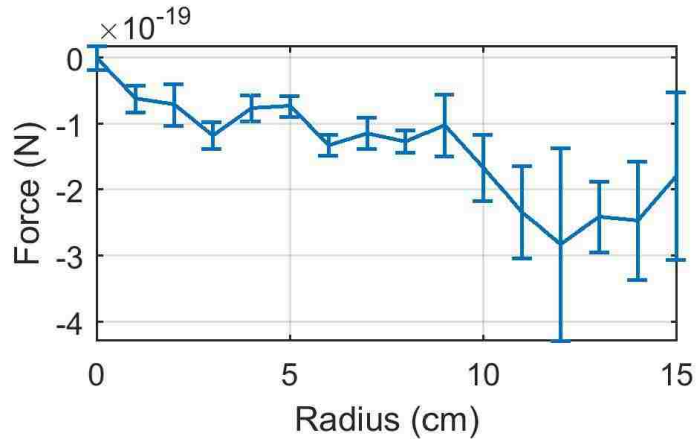
Since the neutral ground state density profile shown in Figure 3.3.1 makes more physical sense than the one shown in Figure 3.3.3, there may be an electron beam in the plasma located at $r = 6$ cm. This will need to be investigated further as there have been no attempts to measure electron beams in HelCat thus far, and if there is an electron beam it may have an effect on other plasma properties.





The mismatch between the data and the fit past 10 cm may be evidence of a second electron beam, or may be simply that the signal to noise ratio of the data was very small in this region.

Once the ground state neutral density profile was created, the neutral-ion collision force and the $\mathbf{F} \times \mathbf{B}$ drift velocity could be computed. The ion temperature found from the ion LIF measurements at Port 4 was used as T_i in the neutral-ion collision frequency term. Figure 3.3.5 show the ion-neutral collision force versus radius, and Figure 3.3.6 shows the resulting $\mathbf{F} \times \mathbf{B}$ drift velocity. This drift is in the ion diamagnetic direction (IDD), and on the order of 40 m/s at its maximum value.



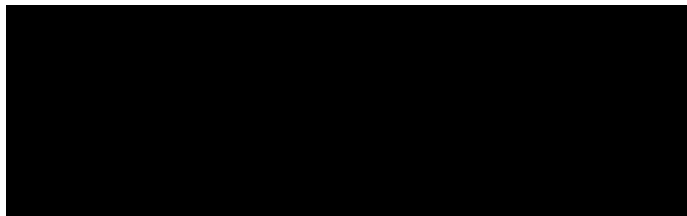
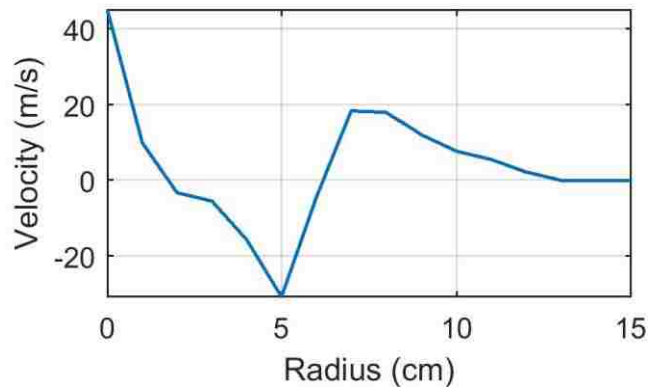
For the force calculated above, the measured neutral radial velocity was used. Since the radial velocity can also be calculated from the neutral density profile through the diffusion flux:

$$v_n = -D_n \frac{\nabla n_n}{n_n} \quad (3.3.4)$$

with;

$$D_n = \frac{kT_n}{mv_{in}} \quad (3.3.5)$$

In these equations, D_n is the diffusion constant of neutrals, n_n is the density of the neutrals, k is the Boltzmann constant, T_n is the neutral temperature, m is the mass of the neutral, and v_i is the ion-neutral collision frequency [22]. This velocity is plotted as a function of radius in Figure 3.3.7. The magnitude of the calculated velocity is approximately the same as that measured with LIF, however, the shape is due to the variation in the ground state radial density profile, and does not match the measured profile shown in Figure 3.1.2.3, but is within the error bars on the LIF measurements.



3.4 Calculation of Remaining Drift Velocities and Comparison to Mach Probe Flow Measurements

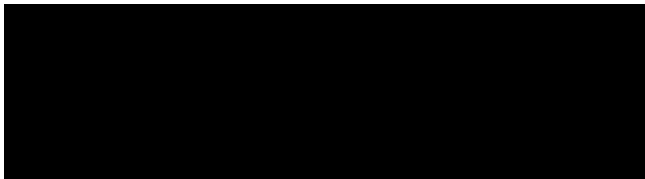
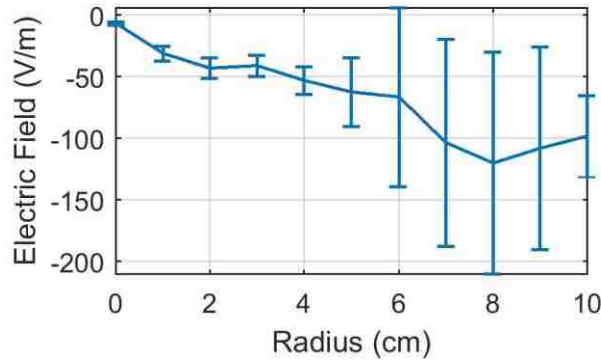
As the intent of this research was to try to determine if the neutral particles could have an effect on the ion motion, it was deemed necessary to calculate the other drift

velocities that would be expected in a helicon plasma, i.e., the $\mathbf{E} \times \mathbf{B}$ drift, v_{ExB} , and the diamagnetic drift, v_{dia} .

The electric field, E , can be found from the negative of the gradient of the plasma potential:

$$\mathbf{E} = -\nabla\phi \quad (3.4.1)$$

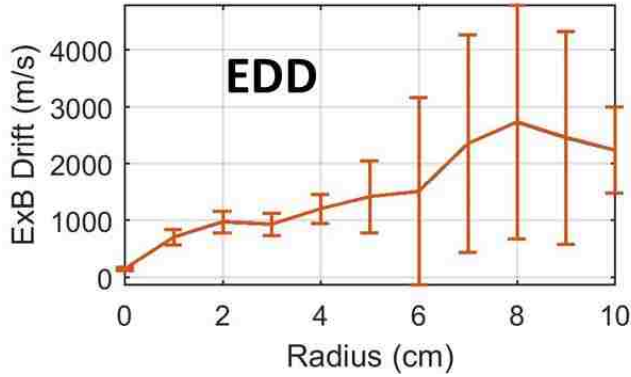
where ϕ is the plasma potential found from the swept probe data (Figure 2.6.11). Since β is small as was discussed in Section 1.1, the electrostatic approximation for calculating the electric field is valid. The resultant radial electric field is shown in Figure 3.4.1. The negative values indicate that the E-field is directed radially inward.



The $\mathbf{E} \times \mathbf{B}$ drift velocity is found from:

$$\mathbf{v}_{ExB} = \frac{\mathbf{E} \times \mathbf{B}}{B^2} \quad (3.4.2)$$

and is shown in Figure 3.4.2. This drift is in the electron diamagnetic direction (EDD).



As noted in Section 1.1.4, the ratio of the ion cyclotron frequency, ω_{ci} , to the ion-neutral collision frequency, ν_{in} , plays an important role in plasma drifts in the ionosphere. For a plasma in HelCat at 10 mTorr argon, $B = 0.044$ T:

$$\omega_{ci} = \frac{qB}{m_i} \approx 105 \text{ kHz} \quad (3.4.3)$$

And:

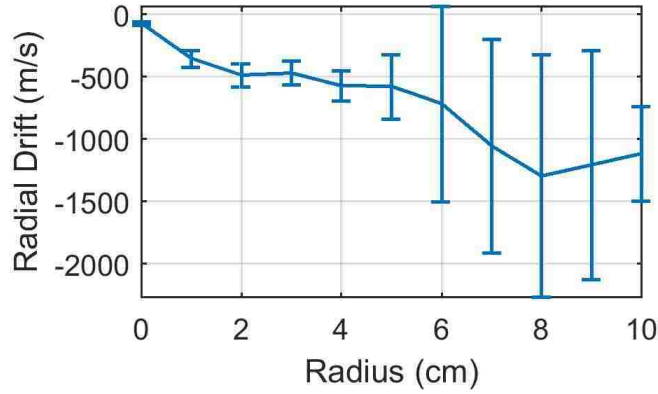
$$\nu_{in} = n_0 \sigma \sqrt{\frac{kT_i}{m_i}} \approx 118 \text{ kHz} \quad (3.4.4)$$

Since the ratio is approximately 1, the neutral particles will probably have an effect on the ion flow in HelCat. The total ion drift can be written as [16]:

$$\mathbf{v}_i = \frac{k_i}{1+k_i^2} \frac{\mathbf{E}}{B} + \frac{k_i^2}{1+k_i^2} \frac{\mathbf{E} \times \mathbf{B}}{B^2} \quad (3.4.5)$$

The first term in Equation 3.4.5 indicates that there should be a flow in the direction of \mathbf{E} that is modified by the ion-neutral collisions, Figure 3.4.3. The second term in Equation 3.4.5 is the $\mathbf{E} \times \mathbf{B}$ drift modified by the ion-neutral collisions. This correction to the $\mathbf{E} \times \mathbf{B}$

drift is shown in Figure 3.4.4. As can be seen from the plot, the inclusion of the effects of the neutral particles in the form of the Pedersen conductivity reduces the calculated $\mathbf{E} \times \mathbf{B}$ drift.



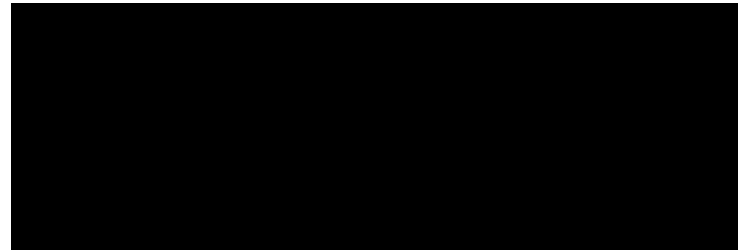
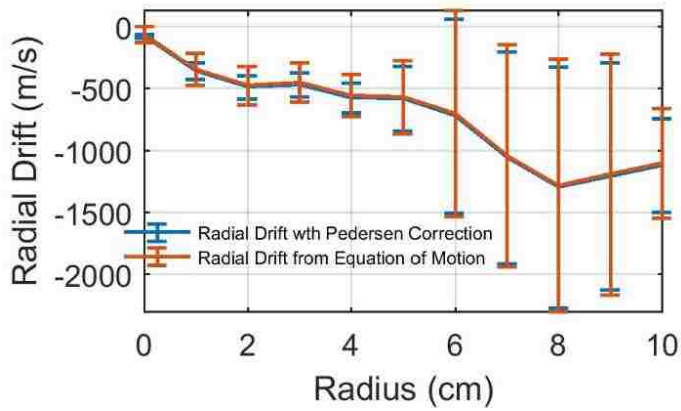
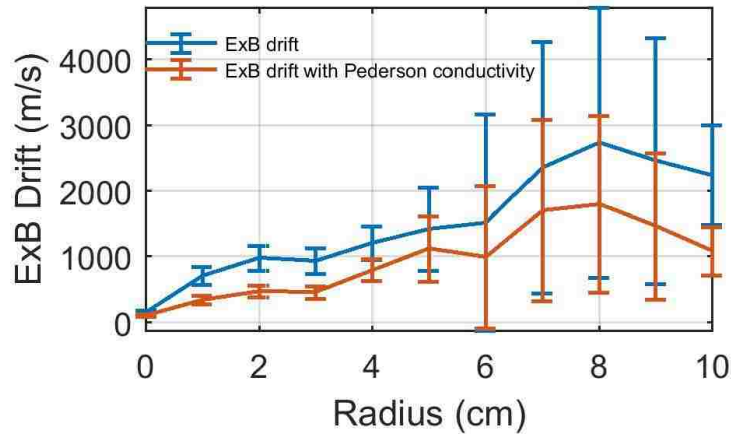
As stated in Section 1.1.2, the ion motion equation with the Pedersen conductivities included, does not include the neutral velocity. Likewise, the $\mathbf{F} \times \mathbf{B}$ force, calculated and shown in Section 3.3, does not properly include all of the ion-neutral collision effects. To include the neutral velocity and the collisional affects, Equations 1.1.1.13 and 1.1.1.14 were derived in Section 1.1.1, and reprinted here as:

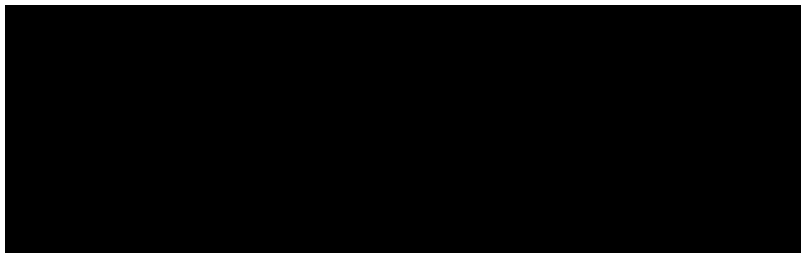
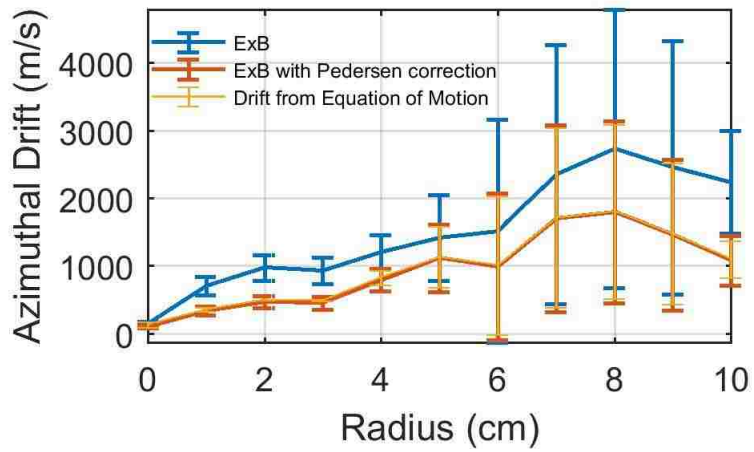
$$v_{i\theta} = -\frac{k^2}{k^2+1} \frac{E_r}{B_0} + \frac{1}{k^2+1} v_{n\theta} - \frac{k}{k^2+1} v_{nr} \quad (3.4.6)$$

$$v_{ir} = \frac{k}{k^2+1} \frac{E_r}{B_0} + \frac{1}{k^2+1} v_{nr} + \frac{k}{k^2+1} v_{n\theta} \quad (3.4.7)$$

Figure 3.4.5 shows the comparison of Equations 3.4.5 and 3.4.7 for the radial ion velocity, and Figure 3.4.6 show that comparison of Equations 3.4.5 and 3.4.6 for the azimuthal ion

velocity. As can be seen in both figures, the addition of the neutral velocity terms provides very little change compared to the ion velocities found through Pedersen conductivity. Had the neutral velocity been larger, this may have had more of an effect.





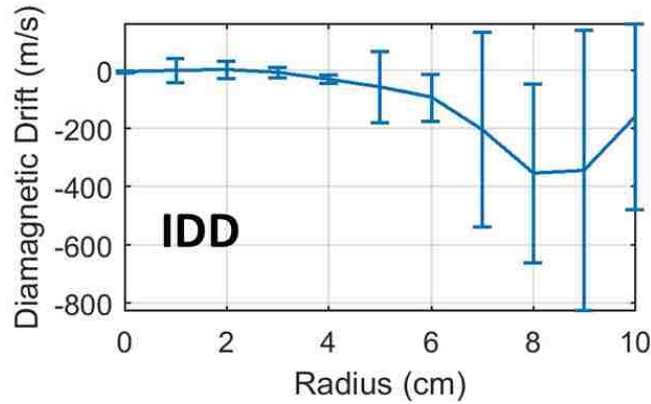
The ion diamagnetic drift can be found from:

$$v_{dia} = \frac{\nabla p}{qnB} \quad (3.4.8)$$

and,

$$\nabla p = qT_i \nabla n \quad (3.4.9)$$

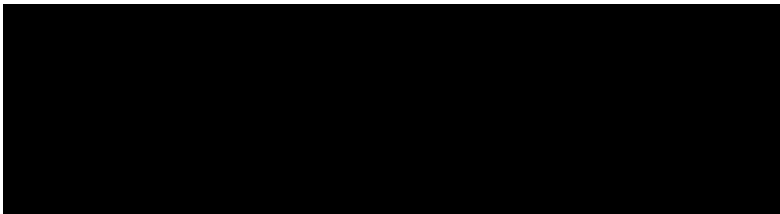
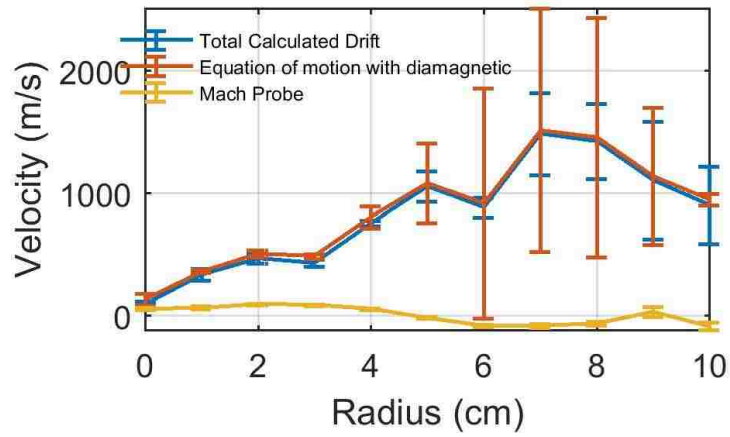
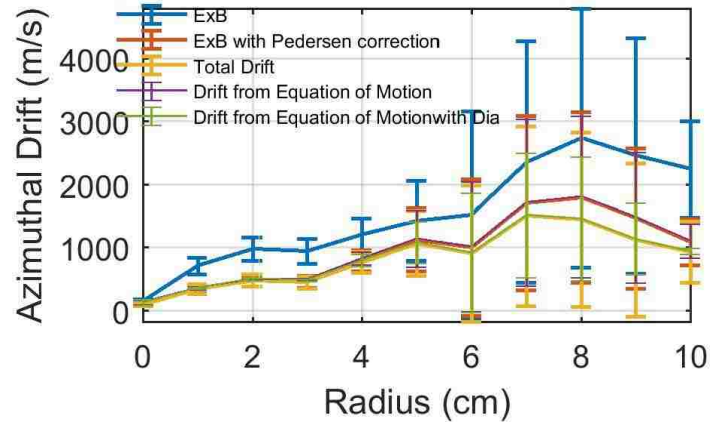
In these equations, q is the electron charge, n is the ion density, and T_i is the ion temperature. Figure 3.4.7 shows that this drift is in the ion diamagnetic direction (IDD).



These drifts can be combined to obtain a total drift:

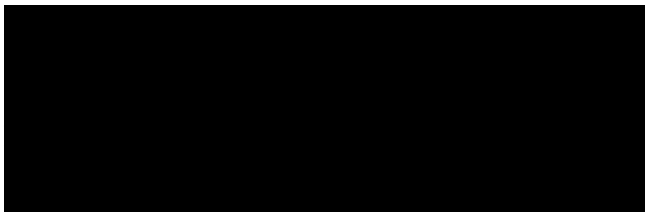
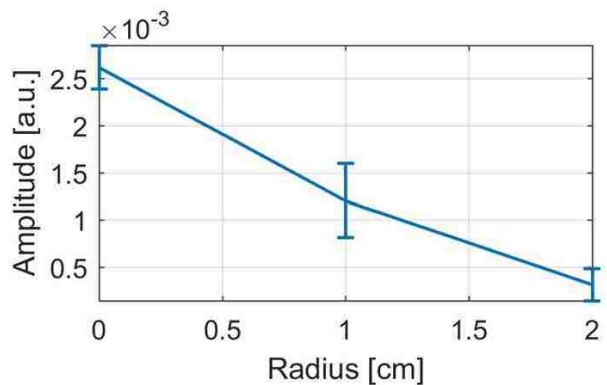
$$v_{total\ drift} = v_{ExB} - v_{dia} + v_{FxB} \quad (3.4.10)$$

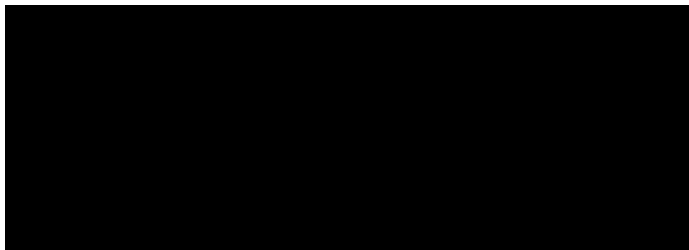
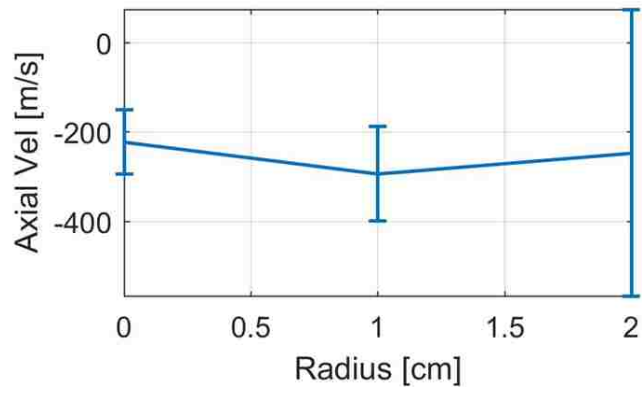
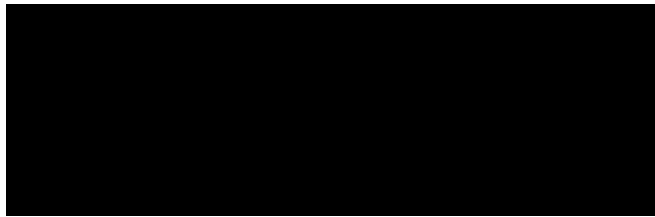
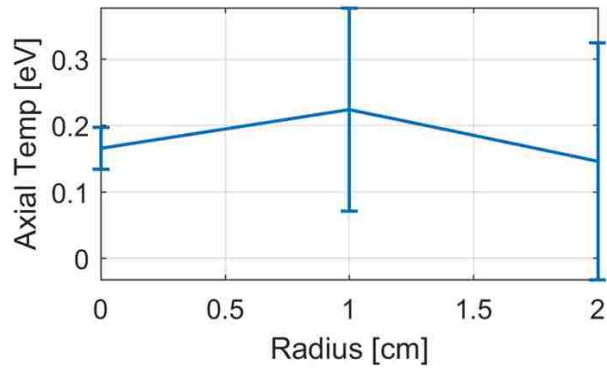
This total drift is shown in Figure 3.4.8 and is in the electron diamagnetic direction (EDD). In the figure, the blue trace is the $\mathbf{E} \times \mathbf{B}$ drift; the red and purple traces are on top of each other and are the $\mathbf{E} \times \mathbf{B}$ with Pedersen conductivity and the ion equation of motion; the yellow and green traces, also on top of each other, are the total azimuthal ion drift velocity. Figure 3.4.9 shows the total drift and the azimuthal (perpendicular) Mach probe data. The $\mathbf{F} \times \mathbf{B}$ drift is in the ion diamagnetic direction, but since it is very small in magnitude, it does not have a significant effect on the total ion drift velocity. Also shown in Figure 3.4.9 (red trace) is the azimuthal ion velocity computed from the combination of the ion velocity calculated from the momentum equation and the ion velocity calculated from the diamagnetic drift. As can be seen in Figure 3.4.9, the total calculated ion drift velocity does not match the ion velocity measured with the Mach probe.



3.5 Ion Line (ArII) Data

Since no usable data was collected from Port 5, or Port 6, the data displayed is that of Port 4 only. Also, as the ion line excited was a low intensity line and the resulting data showed a very small signal to noise ratio, ion measurements were not pursued further as significant effort would have been required. Therefore, the only ion data available at this time is the axial ion amplitude, temperature, and velocity. These are shown in Figure 3.5.1, Figure 3.5.2, and Figure 3.5.3, respectively. As can be seen in the plot of amplitude versus position, the signal is already less than 10^{-3} at 2 cm. At 3 cm, the signal to noise ratio was on the order of one, and extracting useful data was not possible. The negative velocities measure for the ions indicate that the ions are flowing away the source at approximately 250 m/s. The axial ion temperature was ~ 0.1783 eV.





Chapter 4: Conclusion and Future Work

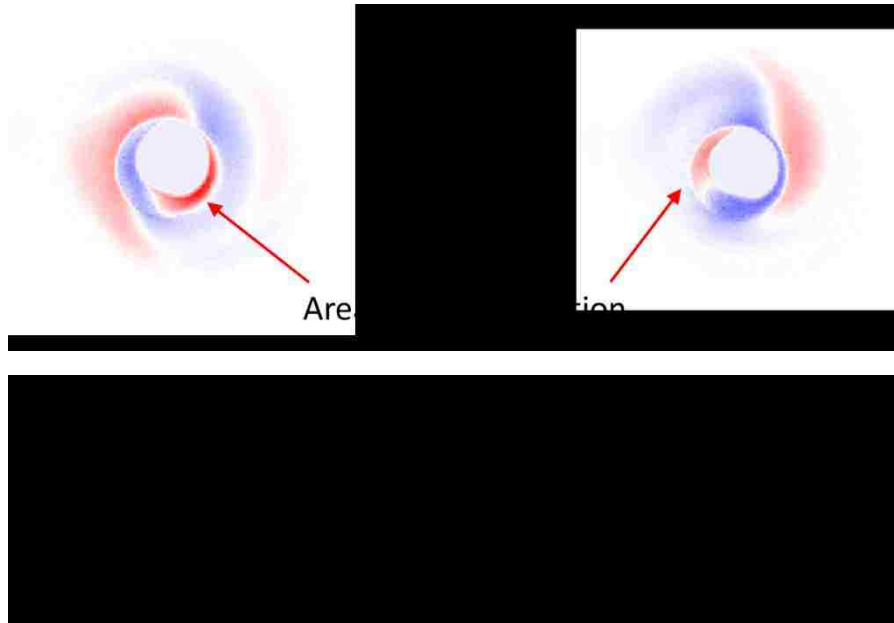
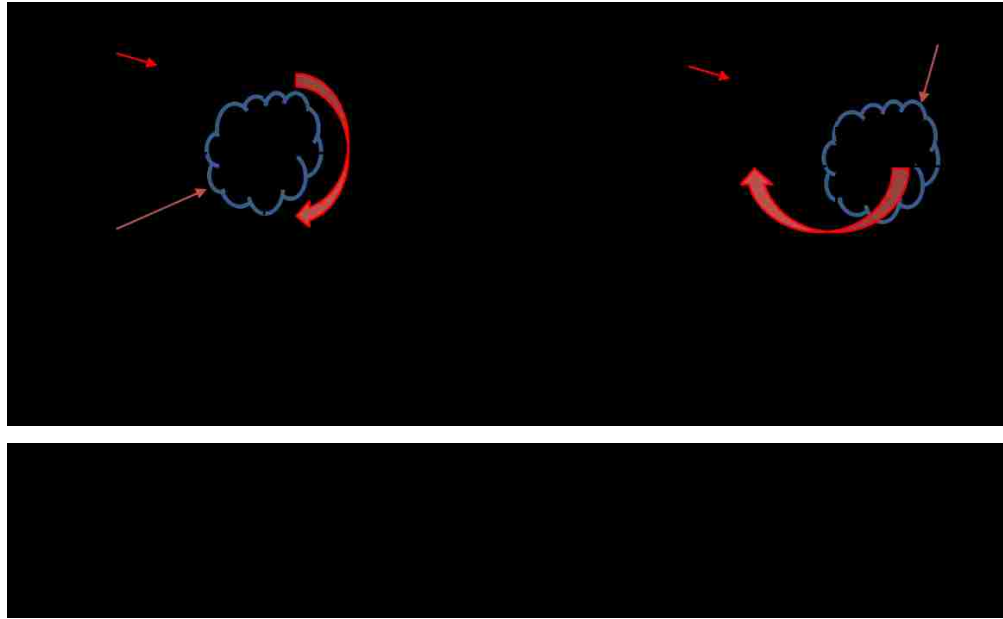
4.1 Conclusions

Laser induced fluorescence (LIF) measurements were collected for neutral argon (ArI) at Port 6 (127.5 cm from the source) with 10 mTorr static fill in the HelCat plasma device. These measurements were used to produce amplitude, temperature and velocity profiles in the axial (parallel), radial and azimuthal directions. The axial and azimuthal velocity profiles were compared to axial and azimuthal ion velocity profiles collected with a Mach probe. There was no obvious correlation between these flows. The neutral axial velocity was away from the helicon plasma source on the order of 50 m/s while the axial ion velocity was away from the helicon source near the center of the machine ($r = 0$ cm to $r = 6$ cm), then changed direction to flow toward the helicon source ($r = 6$ cm to $r = 11$ cm), then changed direction again to flow away from the helicon source ($r = 11$ cm to $r = 15$ cm). The ion velocity varied in magnitude from ~ 550 m/s away from the helicon source to ~ 700 m/s toward the helicon source (the sound speed for ions is $c_s \approx 2,700$ m/s with $T_e \approx 3$ eV). For the azimuthal velocities, the neutral flow was in the electron diamagnetic direction (EDD) at less than 50 m/s while the azimuthal ion flow reversed direction, i.e., near the center of the machine ($r = 0$ cm to $r = 5$ cm) the ion flow was in the electron diamagnetic direction (EDD), and beyond $r = 5$ cm, the azimuthal ion flow was in the ion diamagnetic direction with the maximum magnitudes of velocity in either direction ~ 100 m/s.

The ArI amplitude profiles show that the density of the metastable neutral state, $(^2P_{3/2}^0)4s\ ^2[3/2]_2^0$, decreases with radius after an initial increase near the center of the plasma. The temperature profiles show that the neutral temperature follows a similar trend,

but decreases more slowly, and on average the neutral temperature was $\sim 0.055\text{eV}$ corresponding to a neutral thermal speed, $v_{thn} = \sqrt{\frac{kT_n}{m_n}}$, of $\sim 350\text{m/s}$.

A radio frequency (RF) compensated, swept probe was employed to provide the data used to calculate radial profiles for the electron energy distribution function (eedf), the electron density and the plasma potential for the plasma conditions described above. The eedf and the electron density profile were used as inputs for the collisional-radiative (CR) model. The output of the CR model was compared to the ArI metastable state radial amplitude profile produced from the laser induced fluorescence (LIF) measurements. A ground state neutral argon profile was produced. The ground state neutral profile had a hollow profile with two depletion regions. The center of the machine showed a ground state neutral depletion of $\sim 30\%$. The second region was at about $r = 5\text{ cm}$, and had a depletion in the ground state of $\sim 50\%$. The central depletion region is most likely due to ionization at the core of the plasma which is expected for a helicon plasma. The depletion region at $r = 5\text{ cm}$ may be due to plasma rotation, i.e., the plasma would rotate as a unit about the center of the machine, as shown in Figure 4.1.1. Figure 4.1.2 shows recent fast camera images collected on HelCat that would seem to support this possibility.



An added feature of the CR model is the ability to include an electron beam. This was done to observe the difference in how well the output of the code fit to the radial LIF metastable state profile. The addition of the electron beam allowed the ground state neutral profile to have a smoother curve, i.e., the peak, at $r = 6$ cm, in the second depletion region

is not needed. This indicates that there may be an electron beam in the plasma at $r = \sim 5.5$ cm. More research would need to be performed to determine if this is the case.

An $F \times B$ force and drift velocity were calculated using the neutral radial velocity derived from the LIF measurements and the ground state neutral density profile provided by the CR model. The drift calculated was in the ion diamagnetic direction (IDD) with a maximum value of approximately 40m/s.

The swept probe data were also used to produce a plasma potential profile and an ion density profile. The plasma potential profile was used to calculate a radial electric field, which was then used to calculate an $E \times B$ drift velocity profile. As the plasma potential increased with radius, the calculated electric field was pointed radially inward (toward the center of the machine) which then caused the drift velocity to be in the electron diamagnetic direction (EDD) and increasing in magnitude with increasing radius. The ion density profile was used to calculate the diamagnetic drift. This drift was in the ion diamagnetic direction (IDD) but not large in magnitude compared to the $E \times B$ drift.

It was found that for the plasma parameters used in this experiment that the ion cyclotron frequency, ω_{ci} , and the ion-neutral collision frequency, ν_{in} , were nearly equivalent in magnitude. As such, a drift velocity was calculated using theory that included ion-neutral collisions. This drift had two components; a radial component in the direction of the electric field, and a component in the direction of the $E \times B$ drift but modified by the ion-neutral collisions. The modified $E \times B$ drift was used in subsequent calculations. The radial component of this drift became quite large with increasing radius. Unfortunately, currently, we do not have a method to measure the radial component of the ion velocity.

The methods discussed above for including the neutral particle effects in the calculation of the azimuthal ion velocities both ignored some of these effects. The calculation of the $\mathbf{F} \times \mathbf{B}$ drift did not include the ion-neutral collisions as they affect the ion velocity directly, and the ion velocity calculated from the Pedersen conductivity did not include the neutral velocity. To ensure that our analysis captured all of the possible effects of the neutral particle interactions, a third analysis method was employed. This method started with the momentum equation, and after some simplifying assumptions, the ion velocities in the radial and azimuthal directions were derived. This method included the correction from the Pedersen conductivity and the neutral particle velocity. It was found that this method yielded results that were almost identical to those obtained using just the Pedersen correction term. Since the neutral velocities were extremely slow, this is to be expected. Had the neutral velocities been larger, there may have been more of an effect.

The estimated azimuthal ion drift velocities ($V_{E \times B}$ (with the Pedersen correction) + $V_{\text{diamagnetic}} + V_{F \times B}$) were added together, and the azimuthal ion velocity calculated from the momentum equation was combined with the diamagnetic drift velocity to provide two methods of determining the total estimated azimuthal ion velocity. These velocities were then compared to the measured azimuthal ion flow. The total calculated drift velocities were almost identical and in the electron diamagnetic direction (EDD), and increased in magnitude to about $r = 7$ cm, then began to decrease. These total drift velocities did not match the measured azimuthal ion velocity as they were larger in magnitude and did not reverse direction as shown by the ion velocity measured with the Mach probe (Figure 3.4.7).

From the above discussion, the neutral particles do affect the plasma (ion) flow through ion-neutral collisions. The $\mathbf{F} \times \mathbf{B}$ drift did not have much of an effect, although it was in the opposite azimuthal direction to that of the $\mathbf{E} \times \mathbf{B}$ drift. The correction term from the Pedersen conductivity had more of an effect on the total drift velocity. In this formalization, the neutrals had the effect of a drag force rather than a driving force. However, the inclusion of the neutral particle effects still does not explain the measured azimuthal ion flow in HelCat.

In addition, the laser induced fluorescence (LIF) system was used to observe singly ionized argon (ArII) at Port 4 with 2.5mTorr argon using the 686.3162 nm transition. The magnetic field and the helicon power were the same as for the neutral LIF measurements. Data were collected, and profiles produced for amplitude, temperature, and velocity in the axial direction. The average ion temperature ($T_i \approx 0.1783$ eV) was used in calculations which required an ion temperature. The ion velocity was directed away from the source at approximately 250 m/s. As the signal to noise ratio for these measurements was extremely small, data was collected for only three radial positions. Due to the configuration of the machine, obtaining radial and azimuthal data for ArII would have required fabrication of new mounting plates and removal of existing equipment. For the reasons listed above no radial, or azimuthal, ion measurements were attempted.

In a helicon plasma device such as HelCat, one would expect that, on average, the ions would flow away from the source, radially outward, and the azimuthal flow would be dominated by the $\mathbf{E} \times \mathbf{B}$ drift which would be in the ion diamagnetic direction. The measured ion flow in HelCat shows more complex behavior. The Mach probe data indicates that the ions do flow away from the source near the center of the machine, but

they reverse direction to flow toward the source, and then reverse again. The azimuthal ion flow also shows a reversal. The ion flow is in the electron diamagnetic direction until about $r = 5$ cm, then there is a shear and the ions reverse direction. The calculated azimuthal ion drift velocity is in the electron diamagnetic direction and an order of magnitude larger depending on radius.

4.2 Future Work

As stated above, the azimuthal ion velocity measured using a Mach probe does not agree with the calculated azimuthal ion velocity. There are several possible causes for this discrepancy. First, the Mach probe analysis may not be correct. Second, the swept probe measurements and data analysis may be faulty. Third, the LIF measurements and analysis may be incorrect. Finally, there may be other processes involved in the plasma in HelCat.

The Mach probe measurements should not be an issue as data were collected for each of the six tips facing towards the helicon source and the profiles produced were almost identical, indicating that the probe was recording the same values regardless of orientation. The theory for Mach probe analysis in plasmas with strong magnetic fields has been developed by I. H. Hutchinson [87]. A strong magnetic field is defined as being such that the ion gyro radius is “substantially smaller” than the probe radius. The ion gyro radius is:

$$\rho_i = \frac{v_{\perp}}{\omega_{ci}} \quad (4.2.1)$$

where v_{\perp} is the perpendicular ion velocity, and ω_{ci} is the ion cyclotron frequency defined before. The ion cyclotron frequency in HelCat for the conditions of this experiment was found to be ~ 105 GHz. If $v_{\perp} \approx v_{thi} = \sqrt{\frac{k_B T_i}{m_i}}$, then $v_{\perp} \approx 650$ m/s, and $\rho_i \approx 6$ mm.

Since the Mach probe diameter is 8 mm, this does not satisfy the requirement that ρ_i is

“substantially smaller” than the radius of the probe. Therefore, the analysis used may, or may not be correct. This issue will have to be addressed. An LIF system capable of performing ArII measurements would help determine if the Mach probe analysis is correct.

As stated in Section 2.6, the swept probe measurements had to be ‘stitched’ together to obtain a complete I-V curve. This problem is due to the high bias voltage needed to obtain ion saturation and electron saturation during the same voltage sweep. The current data acquisition system (DAQ) cannot record this much of a voltage sweep accurately. This issue needs to be addressed to ensure correct analysis.

As to the LIF measurements, more could be done to improve the resolution of the data, as was done by the group working on HYPER-1 at the National Institute for Fusion Science in Japan [8] [9] [46]. This was not done for the research presented here as the additional equipment was cost prohibitive, and improved resolution would probably not change the overall physics.

This leaves other process in the plasma that could account for the observed ion flow. One possibility that has been discussed is flow due do Reynold’s stress [88]. In Equation 4.2.2, ν_{in} is the ion-neutral collision frequency, μ_{ii} is the ion-ion collisional viscosity, $\langle V_\theta \rangle$ is the time-averaged azimuthal ion velocity, and $\langle \tilde{V}_r \rangle$ and $\langle \tilde{V}_\theta \rangle$ are the time-averaged fluctuations of the radial and azimuthal velocities. Since this flow is driven by the fluctuations of the radial and azimuthal velocities, and fairly large fluctuations have been recorded in HelCat, depending on radius, this could have an effect on the overall ion flow. This is something that should be investigated.

$$\frac{1}{r^2} \frac{\partial}{\partial r} (r^2 \langle \tilde{V}_r \tilde{V}_\theta \rangle) = -\nu_{in} \langle V_\theta \rangle + \mu_{ii} \left(\frac{1}{r} \frac{\partial}{\partial r} \left(r \frac{\partial \langle V_\theta \rangle}{\partial r} \right) - \frac{\langle V_\theta \rangle}{r^2} \right) \quad (4.2.2)$$

If the fluctuations of the radial velocity, \tilde{V}_r , and the azimuthal velocity, \tilde{V}_θ , are large and correlated in time, that is, they do not average to zero, i.e., $\langle \tilde{V}_r \tilde{V}_\theta \rangle \neq 0$, then they can couple to drive an azimuthal velocity, $\langle V_\theta \rangle$ which could be different from the ion velocity calculated from the drift velocities.

A second possibility of processes that are not understood is that the plasma may not be rotating around the physical center of the machine, as described in Section 4.1. This would produce anomalous ion flows. Recently, fast camera imaging has indicated that this may be the case in HelCat. This is currently being investigated.

Finally, and probably most importantly, an argon ion (ArII) LIF system needs to be used on HelCat so that the Mach probe data can be corroborated. This would have to be a system that can excite one of the strong ion lines such as those use by *Keese* and others at West Virginia University [35], [39].

One simple test that could be performed is to change the direction of the magnetic field. This should not have an effect on the neutrals, but the ions should reverse direction for the azimuthal flows. This would be a good test once a laser is available to measure ion velocities.

References

- [1] "Merriam-Webster Online Dictionary," [Online]. Available: <https://www.merriam-webster.com/dictionary/plasma>. [Accessed 28 November 2017].
- [2] R. A. Stern and J. A. Johnson III, "Plasma Ion Diagnostics using Resonant Fluorescence," *Physical Review Letters*, vol. 34, no. 25, pp. 1548-1551, 1975.
- [3] N. Beverini, G. Cicconi, G. L. Genovesi and E. Piano, "4s3P2 metastable level density and temperature in a low-density argon plasma," *Plasma Sources Science and Technology*, vol. 6, p. 185, 1997.
- [4] W. G. Schrenk, *Analytical Atomic Spectroscopy*, New York: Plenum Press, 1975.
- [5] R. M. Magee, M. E. Galante, J. Carr jr, G. Lusk, D. W. McCarren and E. E. Scime, "Neutral Depletion and the helicon limit," *Physics of plasmas*, vol. 20, no. 12, pp. 123511.1-123511.5, 2013.
- [6] S. Houshmandyar and E. E. Scime, "Enhanced neutral depletion in a static helium helicon discharge," *Plasma Sources Science and Technology*, vol. 21, p. 035008, 2012.

- [7] A. Keesee, *Neutral Density Profiles in Argon Helicon Plasmas*, Morgantown, West Virginia: Dissertation, 2006.
- [8] M. Aramaki, K. Ogiwara, S. Etoh, S. Yoshimura and M. Y. Tanaka, "High resolution laser induced fluorescence Doppler velocimetry utilizing saturated absorption spectroscopy," *Review of Scientific Instruments*, vol. 80, p. 053505, 2009.
- [9] S. Etoh, M. Aramaki, K. Ogiwara, S. Yoshimura and M. Y. Tanaka, "Development of high resolution LIF spectroscopy with saturated absorption spectrum," *Journal of Plasma Fusion Research*, vol. 8, pp. 20-24, 2009.
- [10] R. F. Kelly, K. D. Meaney, M. Gilmore, T. R. Desjardins and Y. Zhang, "ArI/ArII laser induced fluorescence system for measurement of neutral and ion dynamics in a large scale helicon plasma," *Review of Scientific Instruments*, vol. 87, no. 11, p. 11E560, 2016.
- [11] F. F. Chen, *Introduction to Plasma Physics and Controlled Fusion; Volume 1*, Springer, 2006.
- [12] D. Elliott, D. Sutherland, U. Siddiqui, E. Scime, C. Everson, K. Morgan, A. Hossack, B. Nelson and T. Jarboe, "Two-photon LIF on the HIT-SI3 experiment: Absolute density and temperature measurements of deuterium neutrals," *Review of Scientific Instruments*, vol. 87, no. 11, pp. 11E506.1-11E506.4, 2016.

- [13] D. Elliott, E. Scime and Z. Short, "Novel xenon calibration for two-photon absorption laser induced fluorescence of hydrogen," *Review of Scientific Instruments*, vol. 87, no. 11, pp. 11E504.1-11E504.3, 2016.
- [14] T. R. Pedersen, *Personal Correspondence*, 2017.
- [15] H. Rishbeth and O. K. Garriott, *Introduction to Ionospheric Physics*, New York: Academic Press, 1969.
- [16] A. Brekke, *Physics of the Upper Polar Atmosphere*, Chichester: John Wiley & Sons, 1997.
- [17] W. Baumjohann and R. A. Treumann, *Basic Space Plasma Physics*, London: Imperial College Press, 1997.
- [18] N. R. C. Committee on Solar and Space Physics, *Plasma Physics of the Local Cosmos*, Washington, D.C.: The National Academies Press, 2004.
- [19] M. Gilmore, R. Kelly, A. G. Lynn, T. R. Desjardins, N. Boynton, L. Nguyen, A. Scruggs and J. Romero, "ArI LASER INDUCED FLUORESCENCE SYSTEM FOR MEASUREMENT OF NEUTRAL DYNAMICS IN A LARGE SCALE HELICON PLASMA," in *ICOPS*, 2015.
- [20] G. R. Tynan, M. J. Burin, C. Holland, G. Antar, N. Crocker and P. H. Diamond, "Radially sheared azimuthal flows and turbulent transport in a cylindrical plasma," *Physics of Plasmas*, vol. 11, no. 11, pp. 5195-5203, 2004.

- [21] Y. Sakawa, C. Joshi, P. K. Kaw, F. F. Chen and V. K. Jain, "Excitation of the modified Simon-Hoh instability in an electron beam produced plasma," *Physics of Fluids B: Plasma Physics*, vol. 5, no. 6, p. 1681, 1993.
- [22] J. Vranjes, A. Okamoto, S. Yoshimura, S. Peodts, M. Kono and M. Y. Tanaka, "Analytical Description of a Neutral-Induced Tripole Vortex in a Plasma," *Physical Review Letters*, vol. 89, no. 26, p. 265002, 2002.
- [23] S. I. Braginskii, "Transport Processes in a Plasma," in *Reviews of Plasma Physics, Volume 1*, 1965, pp. 205-311.
- [24] M. W. Hatch, R. F. Kelly, D. M. Fisher, M. Gilmore and R. H. Dwyer, "Mach Probe Measurements in a Large-Scale Helicon Plasma," in *American Physical Society (APS) Division of Plasma Physics (DPP)*, Milwaukee, Wisconsin, 2017.
- [25] N. Bjorna, "Derivation of Ion-Neutral Collision Frequencies From a Combined Ion Line/Plasma Line Incoherent Scatter Experiment," *Journal of Geophysical Research*, vol. 94, no. A4, pp. 3799-3804, 1989.
- [26] A. V. Tolmacheva, "Results of the Ion-Neutral Collision Frequency Measurements in the Lower Thermosphere by the Method of Resonance Scattering of Radio Waves by Artificial Periodic Irregularities," *Radiophysics and Quantum Electronics*, vol. 58, no. 4, pp. 245-252, 2015.

- [27] S. Chapman, "The electrical conductivity of the ionosphere," *Nuovo Cimento*, vol. 4, no. 10, pp. 1385-1412, 1956.
- [28] W. G. Baker and D. F. Martyn, "Electric currents in the Ionosphere. 1. The Conductivity," *Philosophical Transactions of the Royal Society of London. Series A, Mathematical and Physical Sciences*, vol. 246, no. 913, pp. 281-294, 1953.
- [29] S. Maus, "Conductivity of the Ionosphere," CIRES, University of Colorado, 2006.
- [30] C. E. Wieman and L. Hollberg, "Using diode lasers for atomic physics," *Review of Scientific Instruments*, vol. 62, no. 1, pp. 1-20, 1991.
- [31] K. Muraoka and M. Maeda, "Application of laser-induced fluorescence to high-temperature plasmas," *Plasma Physics and Controlled Fusion*, vol. 35, pp. 633-656, 1993.
- [32] G. D. Severn, D. A. Edrich and R. McWilliams, "Argon ion laser-induced fluorescence with diode lasers," *Review of Scientific Instruments*, vol. 69, no. 1, pp. 10-15, 1998.
- [33] R. Engeln, S. Mazouffre, P. Vankan, D. C. Schram and N. Sadeghi, "Flow dynamics and invasion by background gas of a supersonically expanding thermal plasma," *Plasma Sources Science and Technology*, vol. 10, p. 595, 2001.

- [34] R. F. Boivin and E. E. Scime, "Laser induced fluorescence in Ar and He plasmas with a tunable diode laser," *Review of Scientific Instruments*, vol. 74, p. 4352, 2003.
- [35] A. M. Keesee, E. E. Scime and R. F. Boivin, "Laser-induced fluorescence measurement of three plasma species with a tunable diode laser," *Review of Scientific Instruments*, vol. 75, no. 10, p. 4091, 2004.
- [36] E. Scime, C. Biloiu, C. Compton, F. Doss, D. Venture, J. Heard, E. Choueiri and R. Spektor, "Laser induced fluorescence in a pulsed argon plasma," *Review of Scientific Instruments*, vol. 76, no. 2, pp. 026107 1-3, 2005.
- [37] A. M. Keesee and E. E. Scime, "Neutral argon density profile determination by comparison of spectroscopic measurements and a collisional-radiative model," *Review of Scientific Instruments*, vol. 77, p. 10F304, 2006.
- [38] A. M. Keesee and E. E. Scime, "Neutral density profiles in argon helicon plasmas," *Plasma Sources Science and Technology*, vol. 16, p. 742, 2007.
- [39] I. A. Biloiu, X. Sun and E. E. Scime, "High time resolution laser induced fluorescence in pulsed argon plasma," *Review of Scientific Instruments*, vol. 77, p. 10F301, 2006.

- [40] I. A. Biloiu, *Laser Induced Fluorescence studies of Ion Acceleration in Single and Multiple Species Expanding Plasmas*, Morgantown: West Virginia University, 2009.
- [41] S. C. Thakur, *Understanding Plasmas through Ion Velocity Distribution Function measurements*, Morgantown: West Virginia University, 2010.
- [42] R. VanDervort, D. Elliott, D. McCarren, J. McKee, M. Soderholm, S. Sears and E. Scime, "Optimization of confocal laser induced fluorescence in a plasma," *Review of Scientific Instruments*, vol. 85, p. 11E408, 2014.
- [43] Z. D. Short, M. U. Siddiqui, M. F. Henriquez, J. S. McKee and E. E. Scime, "A novel laser-induced fluorescence scheme for Ar-I in a plasma," *Review of Scientific Instruments*, vol. 87, no. 1, pp. 013505.1-013505.7, 2016.
- [44] A. Okamoto, K. Hara, K. Nagaoka, S. Yoshimura, J. Vranjes, M. Kono and M. Y. Tanaka, "Experimental observation of a tripolar vortex in a plasma," *Physics of plasmas*, vol. 10, no. 6, p. 2211, 2003.
- [45] K. Ogiwara, S. Etoh, M. Aramaki, S. Yoshimura and M. Y. Tanaka, "Neutral Flow Measurement Using a Tunable Diode Laser," *Proceedings of ITC/ISHW2007*, 2007.

- [46] M. Aramaki, K. Ogiwara, S. Etoh, S. Yoshimura and M. Y. Tanaka, "Measurement of neutral flow velocity in an ECR plasma using tunable diode laser LIF spectroscopy combined with saturated absorption spectroscopy," *Journal of Physics: Conference Series*, vol. 227, p. 012008, 2010.
- [47] H.-J. Woo, K.-S. Chung, T. Lho and R. McWilliams, "A Newly Calibrated Laser-Induced Fluorescence (LIF) System for Ar Ions with a Single Tunable Diode Laser," *Journal of the Korean Physical Society*, vol. 48, no. 2, pp. 260-265, 2006.
- [48] T. Bieber, X. Glad, L. de Poucques, R. Hugon, J.-L. Vasseur and J. Bougdira, "Argon Ion and Neutral Metastable Levels Destruction in a Magnetically Enhanced Inductively coupled Plasma Reactor," *The Open Plasma Physics Journal*, vol. 6, pp. 32-43, 2013.
- [49] N. Teshigahara, S. Shinohara, Y. Yamagata, D. Kuwahara, Watanabe and Masaki, "Development of 2D Laser-Induced Fluorescence (LIF) System in High-Density Helicon Plasma," *Plasma Fusion and REsearch: Regular Articles*, vol. 9, p. 3406055, 2014.
- [50] D. Kuwahara, Y. Tanida, M. Watanabe, N. Teshigahara and Y. S. S. Yamagata, "Development of Ar I and AR II Measuring System using Laser-Induced Fluorescence Methods in High-Density Helicon Plasma," *Plasma and Fusion Research: Regular Articles*, vol. 10, p. 3401057, 2015.

- [51] T. Nakano, N. Sadeghi, D. J. Trevor, R. A. Gottscho and R. W. Boswell, "Metastable chlorine ion transport in a diverging field electron cyclotron resonance plasma," *Journal of Applied Physics*, vol. 72, no. 8, p. 3384, 1992.
- [52] R. A. Dougal, P. F. Williams and D. C. Pease, "Time-resolved two-dimensional imaging of groundstate species using laser-induced fluorescence," *Review of Scientific Instruments*, vol. 54, no. 5, p. 572, 1983.
- [53] A. Rex and F. Fink, "Applications of laser-induced fluorescence spectroscopy for the determination of NADH in experimental neuroscience," *Laser Physics Letters*, vol. 3, no. 9, p. 452, 2006.
- [54] "Chapter 10. Atomic Spectroscopy," in *Springer Handbook of Atomic, Molecular, and Optical Physics*, Springer-Verlag New York, 2006, pp. 175-198.
- [55] Z. Rudzikas, *Theoretical Atomic Spectroscopy*, Cambridge: Cambridge University Press, 1997.
- [56] G. V. Marr, "VII Spectral Radiation in the Presence of External Fields," in *Plasma Spectroscopy*, New York, Elsevier Publishing Company, 1968, p. 190.
- [57] G. Racah, "On a New Type of Vector Coupling in Complex Spectra," *Physical Review*, vol. 61, p. 537, 1942.

- [58] "NIST Atomic Spectra Database Lines Form," [Online]. Available: https://physics.nist.gov/PhysRefData/ASD/lines_form.html. [Accessed 27 9 2017].
- [59] L. Pauling and S. Goudsmit, *The structure of Line Spectra*, New York: McGraw-Hill Book Company, Inc., 1930.
- [60] H. N. Russell and F. A. Saunders, "New Regularities in the Spectra of the Alkaline Earths," *American Astronomical Society*, vol. 61, p. 38, 1925.
- [61] R. F. Boivin, "Study of the Different Line broadening Mechanisms for the Laser Induced Fluorescence Diagnostic of the HELIX and LEIA Plasmas Internal Report," West Virginia University, Morgantown, 1998.
- [62] G. V. Marr, "Chapter III The Absorption and Emission of Radiation," in *Plasma Spectroscopy*, Amsterdam, Elsevier Publishing Company, 1968, pp. 27-33.
- [63] R. F. Boivin, "Zeeman Splitting for LIF transitions and Deconvolution Technique to Extract Ion Temperature Internal Report PL-050," West Virginia University, Morgantown, WV, 2001.
- [64] G. Herzberg, in *Atomic Spectra and Atomic Structure*, New York, Dover Publications, 1944, pp. 96-112.

- [65] M. J. Goeckner and J. Goree, "Laser-induced fluorescence measurement of plasma ion temperatures: Corrections for power saturation," *Journal of Vacuum Science and Technology A*, vol. 7, no. 3, p. 977, 1989.
- [66] E. Castanos-Martinez and M. Moisan, "Absorption spectroscopy measurements of resonant and metastable atom densities in atmospheric-pressure discharges using a low-pressure lamp as a spectral-line source and comparison with a collisional-radiative model," *Spectrochimica Acta Part B*, vol. 65, pp. 199-209, 2010.
- [67] X.-M. Zhu and Y.-K. Pu, "A simple collisional-radiative model for low pressure argon discharges," *Journal of Physics D: Applied Physics*, vol. 40, pp. 2533-2538, 2007.
- [68] A. Yanguas-Gil, J. Cotrino and A. R. Gonzalez-Elipe, "Influence of the excited states on the electron-energy distribution function in low-pressure microwave argon plasmas," *Physical Review E*, vol. 72, pp. 016401.1-016401.9, 2005.
- [69] J. Vlcek, "A collisional-radiative model applicable to argon discharges over a wide range of conditions: 1. Formulation and basic data," *Journal of Physics D: Applied Physics*, vol. 22, pp. 623-631, 1989.
- [70] A. Bogaerts, R. Gijbels and J. Vlcek, "Collisional-radiative model for an argon glow discharge," *Journal of Applied Physics*, vol. 84, no. 1, pp. 121-136, 1998.

- [71] R. M. Magee, M. E. Galante, D. McCarren, E. Scime, R. L. Boivin, N. H. Brooks, R. J. Groebner, D. N. Hill and G. Porter, "A two photon absorption laser induced fluorescence diagnostic for fusion plasmas," *Review of Scientific Instruments*, vol. 83, no. 10, pp. 701-703, 2012.
- [72] M. E. Galante, R. M. magee and E. E. Scime, "Two photon absorption laser induced fluorescence measurements of neutral density in a helicon plasma," *Physics of Plasmas*, vol. 21, no. 5, pp. 055704.1-055704.7, 2014.
- [73] R. M. Magee, M. E. Galante, N. Gulbrandsen, D. W. McCarren and E. E. Scime, "Direct measurements of the ionization profile in krypton helicon plasmas," *Physics of Plasmas*, vol. 19, no. 12, pp. 123506.1-123506.6, 2012.
- [74] B. H. Seo, J. H. Kim and S. J. You, "Metastable argon atoms under significant neutral depletion in helicon plasmas by laser-induced fluorescence," *Current Applied Physics*, vol. 17, no. 10, pp. 1254-1259, 2017.
- [75] P. Schef, A. Derkatch, P. Lundin, S. Mannervik, L. -O. Norlin, D. Rostohar, P. Royen and E. Biemont, "Lifetimes of Metastable Levels in ArII," *The European Physical Journal D*, vol. 29, pp. 195-199, 2004.
- [76] S. G. Rautian and A. S. Yatsenko, "Grotrian Diagrams," *Uspekhi Fizicheskikh Nauk*, vol. 42, no. 2, pp. 205-208, 1999.
- [77] E. E. Scime, *LIF schemes*, Personal Communication, 2016.

- [78] Y. Zhang, *Experimental Investigation of Plasam Dynamics in Jets and Bubbles using a Compact Coaxial Plasma Gun in a Background Magnetized Plasma*, Albuquerque: UNM Dissertation, 2016.
- [79] M. Gilmore, A. G. Lynn, T. R. Desjardins, Y. Zhang, C. Watts, S. C. Hsu, S. Betts, R. Kelly and E. Schamiloglu, "The HelCat basic plasma science device," *Journal of Plasma Physics*, vol. 81, no. 1, 2015.
- [80] A. G. Lynn, M. Gilmore, C. Watts, J. Herrea, R. Kelly, S. W. S. X. L. Yan and Y. Zhang, "The HelCat dual-source plasma device," *Review of Scientific Instruments*, vol. 80, no. 10, p. 103501, 2009.
- [81] S. Gerstenkorn and P. Luc, "C_IODE_14000_15600_0001," in *Atlas du Spectre Iodine*, Orsay Cedex, France, Laboratoire Aimé Cotton, publié le 3 octobre 2013, mis à jour le 26 mai 2014 à 13h58min, p. 23.
- [82] T. Desjardins, *Dynamics of Turbulence and Flows in a Helicon Plasma Under Electrode Biasing*, Albuquerque: Dissertation, University of New Mexico, 2016.
- [83] F. F. Chen, "Langmuir probe measurements in the intense RF field of a helicon discharge," *Plasma Sources Science and Technology*, vol. 21, no. 5, pp. 055013 1-11, 2012.

- [84] R. L. Merlino, "Understanding Langmuir probe current-voltage characteristics," *American Journal of Physics*, vol. 75, no. 12, pp. 1078-1085, 2007.
- [85] I. H. Hutchinson, *Principles of Plasma Diagnostics*, Cambridge, Ma: Cambridge University Press, 2005.
- [86] J. D. Huba, *NRL Plasma Formulary*, Washington: Naval Research Laboratory, 2016.
- [87] I. H. Hutchinson, "Ion Collection by Probes in Strong Magnetic Fields with Plasma Flow," *Physical Review A*, vol. 37, no. 11, p. 4358, 1988.
- [88] C. Holland, J. H. Yu, D. Nishijima, M. Shimada, N. Taheri and G. R. Tynan, "Observation of Turbulent-Driven Shear Flow in a Cylindrical Laboratory Plasma Device," *Physical Review Letters*, vol. 96, p. 195002, 2006.
- [89] J. Huba, *NRL Plasma Formulary*, Washington, DC: Naval Research Laboratory, 2016.
- [90] L. Schott, "Electrical Probes," in *Plasma Diagnostics*, Woodbury, American Institute of Physics, 1995, pp. 668-731.
- [91] W. G. Baker and D. F. Martyn, "Conductivity of the Ionosphere," *Nature*, vol. 170, no. 4339, pp. 1090-1092, 1952.

[92] D. Elliott, D. Sutherland, U. Siddiqui, E. E. C. Scime, K. Morgan and
A. Hossack.

Appendix A

In Section 1.1.1, the momentum equation was presented as:

$$m_i n_i \left(\frac{\partial}{\partial t} + \mathbf{V}_i \cdot \nabla \right) \mathbf{V}_i = q_i n_i (-\nabla \phi + \mathbf{V}_i \times \mathbf{B}_0) - \nabla p_i - \nabla \cdot \boldsymbol{\pi}_i - \mathbf{R} - m_i n_i \nu_{in} \mathbf{V}_i + m_i n_i \nu_{in} \mathbf{V}_n \quad \text{A.1}$$

It was stated without proof that the collisional momentum transfer term, \mathbf{R} , was small. To show that this is a valid assumption, this term will be compared to the $\mathbf{V}_i \times \mathbf{B}_0$ term.

The NRL Plasma Formulary [89] defines \mathbf{R} as:

$$\mathbf{R} = \mathbf{R}_u + \mathbf{R}_T \quad \text{A.2}$$

where \mathbf{R}_u is the frictional force, and \mathbf{R}_T is the thermal force and are defined as:

$$\mathbf{R}_u = \frac{ne}{\sigma_0} (0.51 \mathbf{j}_{\parallel} + \mathbf{j}_{\perp}) \quad \text{A.3}$$

$$\sigma_0 = \frac{ne^2 \tau_e}{m_e} \quad \text{A.4}$$

And:

$$\mathbf{R}_T = -0.71 n \nabla_{\parallel} (kT_e) - \frac{3n}{2\omega_{ce} \tau_e} \mathbf{b} \times \nabla_{\perp} (kT_e) \quad \text{A.5}$$

Since these equations are given in Gaussian units, the following calculations are performed using Gaussian units.

In the previous equations, the electron gyrofrequency, ω_{ce} , is defined as:

$$\omega_{ce} = \frac{eB}{m_e c} \quad \text{A.6}$$

The collision time, τ_e is:

$$\tau_e = \frac{3\sqrt{m_e}(kT_e)^{3/2}}{4\sqrt{2\pi n}\lambda e^4} \quad \text{A.7}$$

And, the current density, \mathbf{j} , is:

$$\mathbf{j} = -ne\mathbf{u} = -ne(\mathbf{V}_e - \mathbf{V}_i) \quad \text{A.8}$$

Where e is the electronic charge, B is the magnitude of the magnetic field, \mathbf{b} is the magnetic field direction ($\mathbf{B} = B\mathbf{b}$), m_e is the mass of an electron, c is the speed of light, k is the Boltzmann constant, T_e is the electron temperature, n is the electron density, and λ is the Coulomb Logarithm ($= 10$ for this calculation), and \mathbf{V}_e and \mathbf{V}_i are the electron and ion velocities.

For the conditions of this research, $\omega_{ce} \cong 7.73\text{GHz}$, $\tau_e \cong 1.12 \times 10^{-7}\text{s}$, and $\omega_{ce}\tau_e \cong 865 \gg 1$. In this limit, we have:

$$\frac{en}{c} \mathbf{V}_i \times \mathbf{B} \gg \mathbf{R}_u = \frac{ne}{\sigma_0} \mathbf{j}_\perp \quad \text{A.9}$$

After some math, this can be written as:

$$\omega_{ce}\tau_e \frac{V_i}{V_i - V_e} \gg 1 \quad \text{A.10}$$

which holds if $V_e \ll 865 V_i$. Since we do not have a measurement for the electron velocity, we are unable to determine if the above inequality is true, and the importance of \mathbf{R}_u remains undetermined.

To investigate the relation between the ion velocity and the thermal force, the relation $\omega_{ci}\tau_i \ll 1$ must hold. The ion gyrofrequency and the ion collision time are: $\omega_{ci} \approx 1.05 \times 10^5 \text{ s}^{-1}$, and $\tau_i \approx 6.2 \times 10^{-7} \text{ s}$. This gives $\omega_{ci}\tau_i \approx 0.065 \ll 1$.

In this limit, the relation between the $V_i \times B_0$ term and R_T is:

$$\frac{en}{c} V_i \times B \gg R_T = -0.71n\nabla_{\perp}(kT_e) \quad \text{A.11}$$

After some math, this can be written as:

$$V_i \gg \frac{c}{eB} * 0.71\nabla_{\perp}(kT_e) \quad \text{A.12}$$

Inserting numbers and assuming the derivative of the temperature is approximately 0.1eV/cm yields:

$$V_i \gg 1.6 \times 10^4 \text{ cm/s} \quad \text{A.13}$$

Since the measured value if V_i is $\approx 1.0 \times 10^4$ cm/s, this would indicate that R_T may be important. However, if the value of the ion velocity calculated from the $E \times B$ drift is used ($V_i \approx 1.8 \times 10^5$ cm/s), then this inequality does hold and the RT term can be neglected.

As stated in the conclusion, the discrepancy between the measured and calculated ion velocities needs to be investigated further. In addition, the electron velocity will have to be determined before a final assessment can be made as to whether the momentum transfer term, R , is of importance.

Appendix B

B.1 The collisional-radiative (CR) model code

As stated in Section 1.3.5, a collisional-radiative (CR) model was used in this research to obtain a ground state neutral argon (ArI) density profile from the radial amplitude profile for the metastable excited state #2. This code was borrowed from *Amy Keese* at West Virginia University [7]. This code was originally developed by *Vlček* in 1989 [69]. *Annemie Bogaerts* also used this code in 1998 [70].

The CR code was updated to reflect the configuration and type of machine every time it was used by a different researcher. This process was continued for the research presented here. *D. M. Fisher* performed the modifications to the code for this research. These modifications mounted to changing the configuration of the parameters in the code to reflect the physical dimensions of HeICat, updating the code from Fortran 77 to Fortran 90, and writing a MatLab routine to allow for a user defined ground state neutral density profile. There is also a MatLab file to compare the output of the Cr model to the radial density (amplitude) profile for the metastable argon state as measured with the LIF system. (Without his assistance, this research would have taken much longer.)

The current version of this code uses three input files. The first of these files uses electron temperature and density measurements to create electron energy distribution functions (eedf) and electron density profiles from swept probe data. The second code allows the user to create a neutral ground state profile. The third file contains the machine parameters. These codes are presented next, followed by the CR code.

B.1.1 The Electron Energy Distribution Function Code

The MatLab code for creating the eedf and electron density profile follows. % symbols indicate comments:

```
% DUSTIN_EEDFCREATOR: Script to create electron energy distribution
%                       function along with temp. and dens. fits for
%                       AMK CR model.
% + Weighting should be used to make models more robust during fitting
% + Density data may be scaled AFTER fitting an approximate peak density;
%   The veracity of this should be checked.
clear;
close all;

% Variables
peakdensity = 1.6e12; % [cm^-3] Approximate peak density
radius = 25.0;      % [cm] Laser path (in this case the machine radius)
zsize = 201;       % Number of points in fitting array
Esize = 1140;      % Number of points in energy array

% Electron Beam
Tbeam = .01;      % eV
Ebeam = 15.5;    % eV
beam = 1;        % Use beam=1, don't use beam=0

% Constants
me = 9.11E-31;   % mass of electron [kg]

% Load HelCat Ne and Te data
ne_data = load('C:\Users\ralph\Documents\LIF\data\LIF Port 6\Swept
probe\Run 17_08_23; 17.27_2\Ion_Density_udsweep12_shot10.txt');
%   ne_data = load('profiles/Maren_Langmuir_10mT/density vs
radius_noresistor.txt');
ne_dataX = ne_data(:,1); % LP density data, X
% ne_dataX = ne_data(1,:); % LP density data, X
ne_dataX = ne_dataX + 1; % SHIFTING DATA BY 1 CM DUE TO CENTRAL
PEAK OFFSET
ne_dataY = ne_data(:,2); % LP density data, Y
ne_ndata = 2*size(ne_dataX,1); % Number of data points taken
ne_data_radLimit = ne_dataX(end); % Radial limit of data collection

te_data = load('profiles/temp_data_dustin.mat');
te_dataX = 0:1:17;
te_dataY = nanmean(squeeze(te_data.temperature_exp_1),2)';
% te_dataY_1 = nanmean(squeeze(te_data.temperature_exp_1),2)';
```

```

% te_dataY_2 = nanmean(squeeze(te_data.temp_linear_1),2)';
% te_dataY = (te_dataY_1 + te_dataY_2)/2;
te_ndata = 2*size(te_dataX,2);
te_data_radLimit = te_dataX(end);

% Interpolate data and mirror about r=0 assuming source/dynamic symmetry
%>>>> Density
helcatNeX = zeros(1,(2*ne_ndata-1));
helcatNeY = zeros(1,(2*ne_ndata-1));
tempX = linspace(0,ne_data_radLimit,ne_ndata);
tempY = interp1(ne_dataX,ne_dataY,tempX);
for i=1:ne_ndata-1
    helcatNeX(i) = -tempX(ne_ndata-i+1);
    helcatNeY(i) = tempY(ne_ndata-i+1);
end
for i=1:ne_ndata
    helcatNeX(i+ne_ndata-1) = tempX(i);
    helcatNeY(i+ne_ndata-1) = tempY(i);
end

% for i=1:ne_ndata-1
%     helcatNeX(i) = -tempX(ne_ndata-i+1);
%     helcatNeY(i) = tempY(ne_ndata-i+1);
% end
% for i=1:ne_ndata
%     helcatNeX(i+ne_ndata-1) = tempX(i);
%     helcatNeY(i+ne_ndata-1) = tempY(i);
% end

%>>>> Temperature
helcatTeX = zeros(1,(2*te_ndata-1));
helcatTeY = zeros(1,(2*te_ndata-1));
tempX = linspace(0,te_data_radLimit,te_ndata);
tempY = interp1(te_dataX,te_dataY,tempX);
for i=1:te_ndata-1
    helcatTeX(i) = -tempX(te_ndata-i+1);
    helcatTeY(i) = tempY(te_ndata-i+1);
end
for i=1:te_ndata-1
    helcatTeX(i+te_ndata-1) = tempX(i);
    helcatTeY(i+te_ndata-1) = tempY(i);
end

% Allocate arrays
maxz = radius;
z = zeros(1,zsize);
eedf = zeros(Esize,zsize);
beamedf = zeros(Esize,zsize);
te = zeros(1,zsize);
test = zeros(1,Esize);
beamtest = zeros(1,Esize);
E = zeros(1,Esize);
axis = zeros(1,zsize);
axise = zeros(1,Esize);

% Create z values

```

```

for i=1:zsize
    axis(i) = i;
    z(i) = 2.0*(maxz/(zsize-1))*(i-1)-maxz;
end
%plot(axis,z);
%title('axis vs z')
%pause;

% Create E values
for j=1:Esize
    axise(j) = j;
    if (j<=11)
        E(j)=(j-1)*.001;
    elseif (j<=20)
        E(j)=(j-10)*.01;
    elseif (j<=29)
        E(j)=(j-19)*.1;
    elseif (j<=43)
        E(j)=(j-29)*.2+1.0;
    else
        E(j)=(j-44)+4.0;
    end
end
%plot(axise,E);
%title('axise vs E')
%pause;

% Normalize density
scaling = peakdensity/max(helcatNeY);

%% New fitting routines for Te and Ne from LP data - (DMF,04.2017)
% Fitting routines can be a dark-art. Beware traveller...
% I recommend dynamically testing equations in grapher or the like to
% arrive at reasonable guess values before making a coding attempt. (DMF)

%fit_exponential = @(a,x) ( a(1)*exp(-x.^2/a(2)) + a(3) );
%guess = [1e13,10,0];
%nlml = fitnlm(helcatNeX,helcatNeY,fit_exponential,guess);
%ne = predict(nlml,z');

%fit_poly_5 = @(a,x) ( a(1) + a(2)*x.^2 + a(3)*x.^3 + a(4)*x.^4 ...
%                    + a(5)*x.^5 + a(6)*x.^6 ).*exp(-a(7)*abs(x));
%guess = [1,1,1,1,1,1,1];
%nlml = fitnlm(helcatTeX,helcatTeY,fit_poly_5,guess);
%te = predict(nlml,z');

% fit_crazy = @(a,x) (a(5) + a(4)*exp(-a(1)*x.^2).*(-a(2) - a(3)*x.^2));
% guess = [1,0.4,3,0.8,4];
% nlml = fitnlm(helcatTeX(1+5:end-5),helcatTeY(1+5:end-5),fit_crazy,guess);
% te = predict(nlml,z');

% Flat temperature of 3eV
%for i=1:zsize

```

```

%   te(i) = 3;
%end
newvalue_1 = helcatTeY(19)
te = spline(helcatTeX(1+5:end-5),helcatTeY(1+5:end-5),z);

for i=1:zsize
    if ( z(i) >abs(helcatTeX(19)) )
%       te(i) = helcatTeY(15);
        te(i) = newvalue_1;
        te(zsize+1-i) = newvalue_1;
        newvalue_1 = newvalue_1*.99
    end
end
% te = te*0.5;

% fit_exp_poly = @(a,x) ( a(1) + a(2).*exp(-a(3)*x.^2) + a(4)*x.^2 );
% guess = [1,1,1,1];
% nlm1 = fitnlm(helcatNeX,helcatNeY,fit_exp_poly,guess);
% ne = predict(nlm1,z');

%fit_tanh = @(a,x) a(1)*(1-tanh((abs(x)-a(2))/a(3)))/2 ...
%           - a(4)*exp(-a(5)*x.^2);
%guess = [1e13,5,1,5,0.1];
%nlm1 = fitnlm(helcatNeX,helcatNeY*scaling,fit_tanh,guess);
%ne = predict(nlm1,z');

%p1 = polyfit(helcatNeX,helcatNeY*scaling,6);
%ne = polyval(p1,z);

ne = spline(helcatNeX,helcatNeY*scaling,z);
% Make tails of ne go to last measured value ~5e10 cm^3 or fixed value
newvalue = helcatNeY(end)*scaling;
for i=1:zsize
    if ( z(i) > helcatNeX(end) )
        ne(i) = newvalue;
        ne(zsize+1-i) = newvalue;
        newvalue = newvalue*.9;
    end
end

% Plot fit and input density curves
figure
subplot(2,1,1);
plot(ne_dataX,ne_dataY*scaling,'-o','LineWidth',2); alpha 0.5; hold
on;
plot(helcatNeX,helcatNeY*scaling);
plot(z,ne);
xlim([-25,25])
legend('Original LP ne data','Mirrored data around r=0','Nonlinear
fit');
title('Density, ne');
xlabel('r [cm]');
ylabel('n [cm^3]');
hold off;
subplot(2,1,2);
plot(te_dataX,te_dataY,'-o','LineWidth',2); alpha 0.5; hold on;

```

```

plot(helcatTeX,helcatTeY);
plot(z,te);
xlim([-25,25])
legend('Original LIF Te data','Mirrored data around r=0','Nonlinear
fit');
title('Temperature, Te');
xlabel('r [cm]')
ylabel('Te [eV]')
hold off;

% ===== Temperature
%fit_simpleTe = @(a,x) a(1)*exp(-a(2)*x.^2) + a(3);
%guess = [3,0.2,0.01];
%plot(z,fit_simpleTe(guess,z)); hold on;
%plot(z,ne)
%legend('Simple Te guess');
%xlabel('r [cm]');
%ylabel('Te [eV]');
%hold off;
%pause;

%% For each te create a Maxwellian distribution
for i=1:zsize
    for j=1:Esize
        if j==1
            eedf(j,i) = ne(i)*sqrt(me/(2*pi*1.6E-19*te(i))) ...
                *exp(-E(j)/te(i))*(100*1.6E-19*(.001)/me);
        else
            % f(v)v dv to get cm^-2 s^-1
            eedf(j,i) = ne(i)*sqrt(me/(2*pi*1.6E-19*te(i))) ...
                *exp(-E(j)/te(i))*(100*1.6E-19*(E(j)-E(j-
1))/me);
        end
        test(j) = eedf(j,i);
    end
    %if i==20
    %figure(1)
    %plot(E,test);
    %title('E vs test')
    %pause;
    %end
end

%% Add electron beam to +/- 1 cm if selected
if beam==1
    for i=1:zsize
        if ((z(i)>=-6.5)&&(z(i)<=-5.5)) || ((z(i)>=5.5)&&(z(i)<=6.5))
            for j=1:Esize
                if j==1
                    beamedf(j,i) = ne(i)*sqrt(me/(2*pi*1.6E-19*Tbeam))
...
                    *exp(-(sqrt(E(j))-sqrt(Ebeam))^2/Tbeam)
...
                    *(100*1.6E-19*(.001)/me);
                else

```



```

        beamedf(j,i) = ne(i)*sqrt(me/(2*pi*1.6E-19*Tbeam))
...
        *exp(-(sqrt(E(j))-sqrt(Ebeam))^2/Tbeam)
...
        *(100*1.6E-19*(E(j)-E(j-1))/me);
    end
    beamtest(j) = beamedf(j,i);
    basiceedf = eedf(j,i);
    eedf(j,i) = 0.999*basiceedf + 0.001*beamedf(j,i);
    test(j) = eedf(j,i);
end
figure(1)
plot(E,beamtest);
title('E vs beamtest')
%
    pause;
figure(1)
plot(E,test);
title('E vs test')
%pause;
end
end
end

%figure(1)
%plot(E,test);
%title('E vs test')
%pause;

% Write eedf and ne to input file for code
save eedf.dat eedf -ascii;
save ne.dat ne -ascii;
%
```

B.1.1.2 The Ground State Neutral Density Code

The MatLab code for creating the ground state neutral density profile

follows. % symbols indicate comments:

```

% Neutral density profile
% Deep Patel and Dustin Fisher
% 10.06.17
close all;
xlz = 50; % diameter in cm
Nz=200; % number of data points-1
xrad = xlz/2; % z-center
precz = xlz/Nz; % dz
P_1 = 0.3; %depletion percentage for center zone
```

```

P_2 = 0.5; %depletion percentage for outer zones
wid_1 = 1.5; %width of depletion region for center
wid_2 = 8.0; %width of depletion region for outer
zones
pres=10; %pressure in mT
Pres = (pres)*10^-3*133.322; %pressure in Pascals
r = 0.25; %radius in m
rval = 5.2; %center of two off axis depletion
regions
a_1 = -0.3; %linear slope of fit left hand side
a_2 = -a_1; %linear slope of fit right hand side
b = 2; % division factor to locate the end
of the linear slope
l = 4; %length of machine in m
V = pi*r^2*l; %Volume of machine in m_3
xtgas=348; %temp of neutrals in K
T = xtgas;
k = 1.38064852e-23; %Boltzman constant

z = zeros(1,Nz+1); %initialize z

xn0 = zeros(1,Nz+1); %Initialize n0

for iz=0:Nz
    z(iz+1) = iz*precz - xrad;
end

% depletion for center zone
% ! P is depletion percentage (11%=.11) if P>.5 then dd=1/(1-P)
% ! if P<.5 then dd=1/P, da=1-P
if P_1>0.5
    dd_1 = 1/(1-P_1);
else
    dd_1 = 1/P_1;
end
da_1 = 1 - P_1;

% depletion for outer zones
% ! P is depletion percentage (11%=.11) if P>.5 then dd=1/(1-P)
% ! if P<.5 then dd=1/P, da=1-P
if P_2>0.5
    dd_2 = 1/(1-P_2);
else
    dd_2 = 1/P_2;
end
da_2 = 1 - P_2;

% ! Calculations for depletion zone
    wl = xrad - (wid_1/2); %left side of center depletion
region
    wr = xrad + (wid_1/2); %right side of center depletion
region
    zrval = xrad - rval; %left location of depletion region
    zrrval = xrad + rval; %right location of depletion
region
    wll = xrad - (wid_2/2) - rval; %left end of left depletion region

```

```

    wrl = xrad + (wid_2/2) - rval;           %right end of left depletion
region
    wlr = xrad - (wid_2/2) + rval;           %left end of right depletion
region
    wrr = xrad + (wid_2/2) + rval;           %right end of right depletion
region
    wl_1 = xrad - xrad/b;                   %left end of linear depletion
region
    wr_1 = xrad + xrad/b;                   %right end of linear depletion
region

for iz=0:Nz

    zval = precz*iz;

    if ((zval >= wl_1) && (zval <= wll) && (zval <= xrad))
        xn0(iz+1) = ((Pres)/(k*T)/1e6) * ...
            (1.02 + a_1*precz*iz/100);

    elseif ((zval >= wll) && (zval <= wrl) && (zval <= xrad))

        xn0(iz+1) = ((Pres)/(k*T)/1e6)*...
            (((2*zrval/wid_2)*(precz*iz/zrval
1.0))^2)/dd_2 + da_2);

    elseif ((zval >= wlr) && (zval <= wrr) && (zval > xrad))

        xn0(iz+1) = ((Pres)/(k*T)/1e6)*...
            (((2*zrval/wid_2)*((precz*iz
(2*rval))/zrval - 1.0))^2)/dd_2 + da_2);

    elseif ((zval >= wrr) && (zval <= wr_1) && (zval > xrad))

        xn0(iz+1) = ((Pres)/(k*T)/1e6) * ...
            (0.88 + a_2*precz*iz/100);

    elseif ((zval >= wl)&&(zval <= wr))

        xn0(iz+1) = ((Pres)/(k*T)/1e6)*...
            (((xlz/wid_1)*(precz*iz/xrad-1.0))^2)/dd_1
+ da_1);

    else xn0(iz+1) = ((Pres)/(k*T)/1e6);

    end

end

% for iz=0:Nz
%     zval = precz*iz;
%     if ((zval >= wl)&&(zval <= wr))
%
%         xn0(iz+1) = 3.535d16*pres/1000*273/xtgas*...

```

```

%                                     (((xlz/wid)*(precz*iz/xrad-1.0))^2)/dd +
da);
%                                     else
%                                     xn0(iz+1) = 3.535d16*pres/1000*273/xtgas;
%                                     end
% end

% for iz=0:Nz
%     zval = precz*iz;
%     if ((zval >= wl)&&(zval <= wr))
%
%         xn0(iz+1) = ((Pres)/(k*T)/1e6)*...
%                     (((xlz/wid)*(precz*iz/xrad-1.0))^2)/dd +
da);
%     else
%         xn0(iz+1) = ((Pres)/(k*T)/1e6);           %pressure in
chamber in cm-3
%     end
% end

simpx = [0, 1,2,3, 4, 5, 6, 7, 8, 9,10,11,12,25];
simpy = [0.7,1,1,1,.7,.5,.7,.6,.7,.8,1, 1, 1, 1]*((Pres)/(k*T)/1e6);
n = length(simpx);

xx = zeros(1,2*n-1);
xx(1:n) = -fliplr(simpx);
xx(n+1:end) = simpx(2:end);

yy = zeros(1,2*n-1);
yy(1:n) = fliplr(simpy);
yy(n+1:end) = simpy(2:end);

zz = zeros(1,Nz+1);
for iz=0:Nz
    zz(iz+1) = iz*precz - xrad;
end

xn0_new = pchip(xx,yy,zz); % Piecewise cubic hermite interpolating
polynomial

figure(1)

    plot(z,xn0_new,'lineWidth',1.2);
%     plot(r(3:13),v_perp(3:13),'LineWidth',1.2)
%     plot(r(3:13),ExB_drift(3:13),'LineWidth',1.2)

    xlabel('Radius (cm)')
    ylabel('Neutral Density (cm^-3)')
    axis tight
    set(gcf, 'PaperUnits', 'centimeters','PaperPosition', [2.5 2.5 8.5
5]);
    set(gcf,'Units','centimeters','Position',[2 2 8.5 5])%See changes on
screen
    grid on
    ylim([1.25e14 3e14]);

```

```

%                                     legend({'Mach
Probe','LIF'},'Position',[0.27,0.32,1,1],'FontSize',6);
%     legend('boxoff');
print('Neutral_density_profile_without_E_beam.jpg','-djpeg','-
r300')

    savefig('figure(1)');

figure(2)
plot(z,xn0);
xlabel('Radius (cm)')
ylabel('Density in cm^-3')

savefig('figure(2)');
% save(figure);
% xtest = [-25,-20,-10,-5,0,5,10,20,25];
% ytest = [2.8e14,2.5e14,2.5e14,1e14,2e14,1e14,2.5e14,2.5e14,2.8e14];
% yspline = spline(xtest,ytest,z);
% figure
% plot(xtest,ytest); hold on;
% plot(z,yspline)

% save deepxn0.dat xn0 -ascii;
save deepxn0.dat xn0_new -ascii;
save xn0creator_Dustin_P_0_3_wid_1_5_workspace.mat

% xn0_out = [P,wid,z,xn0];
%
% write_out_2=[temp,temp_pm,vel,vel_pm,vel_pm_total,amp,amp_pm,zeeman,zee
man_pm]; %Temp, velocit and amplitude, _pm ar the error bars (+ or -)
% save(['Nuetral_profile_fit_parameters_P = ' num2str(P) ' width = '
num2str(wid) '.txt'],'xn0_out','-ascii')
% save('data_2.txt','write_out_2','-ascii')

```

B.1.1.3 The machine parameters input file

The input file for the Fortran code that has the machine parameters. The exclamation symbol, !, is used for comments in this file.

```

! CR code input file 11/21/16 (DMF)
&BASIC
    Nz = 200          ! Number of radial points MINUS ONE
    Ntot = 65        ! Energy states (should not change unless revamping
code)
    NE = 1139        ! Number of energy points in eedf MINUS ONE
    xlz = 50.0       ! Chamber diameter in cm
    pres = 10.0      ! Gas pressure in mTorr (use fill, no plasma)
    xtgas = 348      ! Gas temperature in K

```

```

dt = 1d-5
xn0_profile = 6 ! 1: Flat ground state profile
                ! 2: Parabolic profile with depletion P
                ! 3: Profile using LP data for cerertain parameters
                ! 4: Profile with depletion of width wid
                ! 5: 2 off-axis depltns. of width wid centered at
r=+/-rval
                ! 6:
P = 0.30        ! Depletion percentage (eg. 11%=.11)
wid = 1.5       ! Depletion width
rval = 5.0      ! Center for 2 off-axis depletion
Eth = 0.05      ! Thermal energy in eV      |\ Thermalized
vth = 4.89d4    ! Thermal velocity in cm/s  |/\  atoms
mult = 100      ! Update counter for time loop
nt = 10000000  ! Number of time steps
devlim = 1d-6  ! Max deviation for time loop
Emeane = 4.0    ! 3/2KT=mean energy of all electrons
Ebulk = 0.4     ! Used for calculation of contributions, does not matter
/
&CDS
  cathode_dark_space = F
  Ncnds = 20
  dc = 0.15
/

```

B.1.1.4 The Output Comparison Code

The MatLab code for comparing the output of the CR code to the neutral argon state of interest (state #2 in this case) follows. % symbols indicate comments:

```

% Read CR model data
% Dustin M. Fisher
% 09.26.17
close all

ne = importdata('ne.dat');
eedf = importdata('eedf.dat');
z = importdata('z.dat');
z = z - 25; % Center radius at zero

load('xn0creator_Dustin_P_0_3_wid_1_5_workspace.mat'); %,'P','wid');
% P;
% wid;

%crlb = importdata('crlb.dat',' '); % open crlb.dat; level populations
%levels = crlb(1,:);
%poplevels = crlb(2:end,:);
popdata = dlmread('crlb.dat');
levels = popdata(1,2:end);
poplevels = popdata(2:end,2:end);

% Load LIF amp profile data

```

```

lif_amp = load('profiles/LIF_amp.mat');
lif_amp_1 = lif_amp.amp;
lif_amp_1_pm = lif_amp.amp_pm;

% Density versus machine radius
%figure
%   plot(z,log10(poplevels))
%   title('Density versus machine radius')
%   xlabel('Radius')
%   ylabel('LOG(Density (arb))')

% Density versus energy level
%figure
%   plot(levels,log10(poplevels))
%   title('Density versus Ar Energy Level')
%   xlabel('Ar Energy Level')
%   ylabel('LOG(Density (arb))')

% Density as function of energy level and radius
%figure
%   pcolor(levels,z,log10(poplevels))
%   shading 'flat'
%   title('Density as a function of Ar Energy level and Radius')
%   xlabel('Ar Energy Level')
%   ylabel('Radius (cm)')
%   cb = colorbar();
%   cb.Label.String = 'LOG(Density (arb))';

% INPUT: electron density from Isat data
%figure
%   plot(z,ne)
%   title('INPUT to CR: n_e from Isat')
%   xlabel('Radius (cm)')
%   ylabel('Electron density, n_e')

% INPUT: electron energy distribution function, eedf from Te and ne
%figure
%   plot(eedf)
%   title('INPUT to CR: eedf')
%   xlabel('')
%   ylabel('')

figure
%   subplot(1,1,1);
%   plot(z,poplevels(:,3),'LineWidth',1.2);
%   hold on;
%   plot(0:1:15,lif_amp.amp*max(poplevels(:,4)/max(lif_amp.amp)))

errorbar(0:1:15,lif_amp_1*max(poplevels(:,3)/max(lif_amp_1)),lif_amp_1_
pm*max(poplevels(:,3)),'-','LineWidth',1.2);
%   xlim([0 z(end)])
%   xlabel('Radius (cm)')
%   ylabel('State #2 Density (cm^-3)')
%   plot(r(3:13),v_perp(3:13),'LineWidth',1.2)
%   plot(r(3:13),ExB_drift(3:13),'LineWidth',1.2)

```

```

%   xlabel('Radius (cm)')
%   ylabel('Neutral Density (cm^3)')
%   axis tight
set(gcf, 'PaperUnits', 'centimeters', 'PaperPosition', [2.5 2.5 8.5
5]);
set(gcf, 'Units', 'centimeters', 'Position', [2 2 8.5 5])%See changes on
screen
grid on
%   ylim([1.25e14 3e14]);
legend({'CR          Model          Fit', 'LIF
Data'}, 'Position', [0.27,0.32,1,1], 'FontSize', 6);
legend('boxoff');
print('State#2_density_profile_without_E_beam.jpg', '-djpeg', '-
r300')
savefig('figure');

save read_population_P_0_3_wid_1_5_workspace.mat
%subplot(3,1,2);
%plot(z, log10(poplevels(:,4)))
%xlim([0 z(end)])
%xlabel('Radius (cm)')
%ylabel('LOG(Population)')
%subplot(3,1,3);
%plot(0:1:15, lif_amp.amp*max(poplevels(:,4)/max(lif_amp.amp)))
%xlim([0 z(end)])
%xlabel('Radius (cm)')
%ylabel('Population (arb)')
%   poplevels_1 = transpose(poplevels(:,4));
%   z = transpose(z);
%   read_population_out = [P,wid,z,poplevels_1];
%
write_out_2=[temp,temp_pm,vel,vel_pm,vel_pm_total,amp,amp_pm,zeeman,zee
man_pm]; %Temp, velocit and amplitude, _pm ar the error bars (+ or -)
%   save(['Fit_to_LIF_data_P = ' num2str(P) ' width = ' num2str(wid)
' .txt'],'read_population_out','-ascii')
%   save('data_2.txt','write_out_2','-ascii')

```

b.1.1.5 The Collisional-Radiative (CR) Code

The Fortran 90 code modified by D. M. Fisher for use in this research. The exclamation point is used to indicate comments.

```

PROGRAM main
!
! Collisional radiative model (1D)
! Recieved by Amy Keese (AMK) from Annemie Bogaerts on 09/17/03
! Modified 09/22/03 by AMK
!      12/02/03

```



```

!           12/18/03 Ee(0:NE), zero added to force indexing from
zero
!           that had been causing NaN problems
!           02/17/04 Modifications to read eedf from matlab
calculations,
!           no need from nm or atom edf, no need for Ncds
!           02/17/04 NE changed from 1200
!           10/11/04 add r(0:Nz)
!           10/12/04 add iz dependence to xn0
!           11/19/16 Code ported to F90 by Dustin M. Fisher (DMF);
!           optimized for speed, readability, and usr input
!
USE array
IMPLICIT NONE
INTEGER :: iz, i, j, l, it

! Read in parameter variables to namelist
NAMELIST /BASIC/ Nz, Ntot, NE, xlz, pres, xtgas, dt
NAMELIST /BASIC/ xn0_profile, P, wid, rval, Eth, vth, mult
NAMELIST /BASIC/ nt, devlim, Ebulk, Emeane
NAMELIST /CDS/ cathode_dark_space, Ncds, dc
READ(*,BASIC)
READ(*,CDS)

! Allocate arrays
CALL allocation

! Input files
OPEN(UNIT=1,FILE='levels1.dat',STATUS='OLD') ! cross sections
& trans. prob.
OPEN(UNIT=2,FILE='levels2.dat',STATUS='OLD') ! "
OPEN(UNIT=3,FILE='levels3.dat',STATUS='OLD') ! "
OPEN(UNIT=4,FILE='eedf.dat',STATUS='OLD')      ! EEDF of
electrons
OPEN(UNIT=8,FILE='ne.dat',STATUS='OLD')      ! electron density

! Output files
OPEN(UNIT=14,FILE='cr1b.dat',STATUS='REPLACE') ! level pops.
OPEN(UNIT=15,FILE='cr2b.dat',STATUS='REPLACE') ! contrib.of
prod.-loss
OPEN(UNIT=16,FILE='cr3b.dat',STATUS='REPLACE') ! coll.
processes
OPEN(UNIT=17,FILE='cr4b.dat',STATUS='REPLACE') ! "
OPEN(UNIT=18,FILE='cr5b.dat',STATUS='REPLACE') ! "
OPEN(UNIT=22,FILE='xn0.dat',STATUS='REPLACE') ! xn0 profile
OPEN(UNIT=23,FILE='z.dat',STATUS='REPLACE') ! z array
OPEN(UNIT=24,FILE='Esc.dat',STATUS='REPLACE') ! Escape
factors

OPEN(UNIT=77,FILE='r.dat',STATUS='REPLACE',FORM='UNFORMATTED', &
ACCESS='DIRECT',RECL=(Nz+1)*8)
OPEN(UNIT=88,FILE='level_populations.dat',STATUS='REPLACE', &

```

```

        FORM='UNFORMATTED',ACCESS='DIRECT', RECL=(Nz+1)*Ntot*8)
OPEN(UNIT=99,FILE='debug.dat',STATUS='REPLACE') ! debug only

! Input of data from files
!
=====
=====
! Data necessary for cross sections; read ionization+excitation
energy, and
! degeneracies of the levels
READ(1,'(a80)') cstr
DO i=1,Ntot

!READ(1,'(i2,2(1x,f6.3),1x,f5.0,1x,f5.3,1x,f2.0,1x,f8.4)') &
!   n, Eion(n), Eexc(n), g(n), g0(n), gi(n), gam(n)
READ(1,*) n, Eion(n), Eexc(n), g(n), g0(n), gi(n), gam(n)
IF (gi(n).EQ.6) THEN
    fac(n) = 1.0
ELSE IF (gi(n).EQ.4) THEN
    fac(n) = 2.0d0/3.0d0
ELSE IF (gi(n).EQ.2) THEN
    fac(n) = 1.0d0/3.0d0
ELSE
    WRITE(*,*) 'ERROR: metastable level not recognized.'
    STOP
END IF
END DO
WRITE(*,*) 'The following variables were populated: ' //
TRIM(cstr)

! Read aA*fmn (allowed) and aP (forbidden) coef. for elec.excit
! Read Amn (trans. probab.)
READ(2,'(a80)') cstr
WRITE(*,*) 'The following variables were populated: ' //
TRIM(cstr)
READ(3,'(a80)') cstr
WRITE(*,*) 'The following variables were populated: ' //
TRIM(cstr)
DO i=1,Ntot
    DO j=i+1,Ntot
        READ(2,*) n, m, aAf(n,m), aP(n,m)
        READ(3,*) n, m, A(n,m)
        !READ(2,'(2(1x,i2),2(1x,e8.2))') n, m, aAf(n,m),
aP(n,m)
        !READ(3,'(2(1x,i2),1x,e8.2)') n, m, A(n,m)
    END DO
END DO

! Electron energy distribution function
iEe = 0
DO i=0,NE
    IF (iEe.LT.11) THEN

```

```

        Ee(iEe) = iEe*0.001d0
    ELSE IF ((iEe.GE.11) .AND. (iEe.LT.20)) THEN
        Ee(iEe) = (iEe-9)*0.01d0
    ELSE IF ((iEe.GE.20) .AND. (iEe.LT.29)) THEN
        Ee(iEe) = (iEe-18)*0.1d0
    ELSE IF ((iEe.GE.29) .AND. (iEe.LT.43)) THEN
        Ee(iEe) = (iEe-28)*0.2d0 + 1.0d0
    ELSE
        Ee(iEe) = (iEe-43) + 4.0
    END IF
    READ(4,*) (fe(iEe,iz), iz=0,Nz)
    iEe = iEe + 1
END DO

! Read in electron density profile, ne, assuming ne=ni
READ(8,*) (nes(iz), iz=0,Nz)
DO iz=0,Nz
    ni(iz) = nes(iz)
END DO

! Close input files
CLOSE(1)
CLOSE(2)
CLOSE(3)
CLOSE(4)
CLOSE(8)

! Input of data, general (geometry, precisions, discharge
conditions)
!
=====
=====
    xrad = xlz/2.0d0      ! z-center
    precz = xlz/DBLE(Nz) ! dz

! P is depletion percentage (11%=.11) if P>.5 then dd=1/(1-P)
! if P<.5 then dd=1/P, da=1-P
IF (P>0.5d0) THEN
    dd = 1.0d0/(1.0d0-P)
ELSE
    dd = 1.0d0/P
END IF
da = 1.0d0 - P

! Calculations for depletion zone
wl = xrad - (wid/2.0d0)
wr = xrad + (wid/2.0d0)
zrval = xrad - rval
zrrval = xrad + rval
wll = xrad - (wid/2.0d0) - rval
wrl = xrad + (wid/2.0d0) - rval
wlr = xrad - (wid/2.0d0) + rval

```

```

wrr = xrad + (wid/2.0d0) + rval

! Set xn0 profile
SELECT CASE(xn0_profile)
CASE(1)
  ! Flat ground state profile
  WRITE(*,*) 'xn0: Flat ground state profile'
  DO iz=0,Nz
    xn0(iz) = 3.535d16*pres/1000*273/xtgas
    WRITE(22,'(e10.5)') xn0(iz)
  END DO
CASE(2)
  ! Parabolic profile with depletion P
  WRITE(*,*) 'xn0: Parabolic profile with depletion P'
  DO iz=0,Nz
    xn0(iz) = 3.535d16*pres/1000*273/xtgas* &
      (((precz*iz/xrad - 1.0D0)**2)/dd + da)
    WRITE(22,'(e10.5)') xn0(iz)
  END DO
CASE(3)
  ! Profile using Langmuir probe data for certain parameters
  WRITE(*,*) 'xn0: Profile using LP data for certain
parameters'
  DO iz=0,Nz
    xn0(iz) = 1.0d14*(1.25-0.218*EXP(-(precz*iz-5+1.066d-
7)**2/2.27)) + &
      0.000444*(precz*iz-5)**2)
    WRITE(22,'(e10.5)') xn0(iz)
  END DO
CASE(4)
  ! Profile with depletion of width wid
  WRITE(*,*) 'xn0: Profile with depletion of width wid'
  DO iz=0,Nz
    zval = precz*iz
    IF ((zval.GE.wl).AND.(zval.LE.wr)) THEN
      xn0(iz) = 3.535d16*pres/1000*273/xtgas*
&
      (((xlz/wid)*(precz*iz/xrad-
1.0))**2)/dd + da)
    ELSE
      xn0(iz) = 3.535d16*pres/1000*273/xtgas
    END IF
    WRITE(22,'(e10.5)') xn0(iz)
  END DO
CASE(5)
  ! Profile with two off-axis depletions of width wid
centered at
  ! r=+/-rval
  WRITE(*,*) 'xn0: Profile with two off-axis depletions of
width wid &
centered at r=+/-rval'
  DO iz=0,Nz

```

```

        zval = precz*iz
        IF
((zval.GE.wll).AND.(zval.LE.wrl).AND.(zval.LE.xrad)) THEN
            xn0(iz) = 3.535d16*pres/1000*273/xtgas*
&
            (((2*zrval/wid)*(precz*iz/zrval-
1.0))**2)/dd + da)
        ELSE
            IF
((zval.GE.wlr).AND.(zval.LE.wrr).AND.(zval.GT.xrad)) THEN
            xn0(iz) = 3.535d16*pres/1000*273/xtgas*
&
            (((2*zrval/wid)*((precz*iz-
(2*rval))/zrval-1.0))**2 &
            )/dd + da)
        ELSE
            xn0(iz) = 3.535d16*pres/1000*273/xtgas
        END IF
        WRITE(22,'(e10.5)') xn0(iz)
    END DO
CASE(6)
    ! Deep Patel's xn0 model
    OPEN(UNIT=33,FILE='deepxn0.dat',STATUS='OLD')
    WRITE(*,*) 'xn0: Deep Patel user profile'
    READ(33,*) (xn0(iz), iz=0,Nz)
    CLOSE(33)
    WRITE(22,'(e10.5)') xn0(iz)
END SELECT

! Cathode dark space for iz <= Ncds
IF (cathode_dark_space) THEN
    precz1 = dc/Ncds
    precz2 = (xlz-dc)/(Nz-Ncds)
    DO iz=0,Nz
        IF (iz .LE. Ncds) THEN
            z(iz) = iz*precz1
        ELSE
            z(iz) = dc + (iz-Ncds)*precz2
        END IF
        IF (iz .LT. Ncds) THEN
            zh(iz) = (iz+0.5)*precz1
        ELSE
            zh(iz) = dc + (iz+0.5-Ncds)*precz2
        END IF
        WRITE(23,'(e10.5)') z(iz)
    END DO
ELSE
    DO iz=0,Nz
        z(iz) = iz*precz ! z-array
        zh(iz) = (iz+0.5d0)*precz ! half-step z-array
        WRITE(23,'(e10.5)') z(iz)
    END DO
END IF

```

```

! Create centered z-array
DO iz=0,Nz
    r(iz) = z(iz) - xrad
END DO

! Set various z arrays and derivatives
DO iz=0,Nz-1
    dz(iz) = z(iz+1)-z(iz)          ! 1st simple derivative of
z
    IF (iz .NE. 0) THEN
        dzz(iz) = zh(iz) - zh(iz-1) ! 1st simple derivative of
zh
    END IF
END DO

! Loss of metastable atoms (n=2 and n=4) due to diffusion,
described by
! coefficient D
D(2) = 74.6*1000/pres*xtgas/300
D(4) = 74.6*1000/pres*xtgas/300
WRITE(*,*) 'Loss of metastable atoms (n=2,4) due to diffusion;
coeff D'
WRITE(*,*) 'D(2) =',D(2),'D(4) =',D(4)

xkmet = 6.4d-10 ! metastable-metastable atom coll. rate coef.
[cm^3/s]
xkpi = 2.36d-10
k2b(2) = 2.3d-15 ! two-body coll. w/ therm. ground state atoms
(n=2)
k3b(2) = 1.4d-32 ! three-body coll. w/ therm. ground state
atoms (n=2)
k2b(4) = 4.3d-15 ! (n=4)
k3b(4) = 1.5d-32 ! (n=4)
!
=====
! Calculation of coll.'rates' (r: rate (in cm-3 s-1), k: per
pop=1 (in s-1))
DO iz=1,Nz-1
    DO n=1,Ntot
        !IF (iz.EQ.2) STOP
        !IF (n.EQ.1) THEN
            ! WRITE(*,*) 'iz:',iz
        !END IF

        ! Electrons
        DO iEe=0,NE
            kione(n,iz)          =          kione(n,iz)          +
fe(iEe,iz)*Sione(Ee(iEe),n,Eion(n))
            rrecl(n,iz)          =          rrecl(n,iz)          +
fe(iEe,iz)*Srecl(Ee(iEe),n, &

```

```

Eion(n),gam(n),g(n),gi(n))*fac(n)*ni(iz)
      rrec2e(n,iz) = rrec2e(n,iz) +
fe(iEe,iz)*Srec2e(Ee(iEe),n, &
Eion(n),g(n),gi(n))*nes(iz)*fac(n)*ni(iz)
      DO m=n+1,Ntot
          kexce(n,m,iz) = kexce(n,m,iz) +
&
fe(iEe,iz)*Sexce(Ee(iEe),n,m,Eexc(n), &
Eexc(m),aAf(n,m),aP(n,m),g(n),g(m))
      END DO
      DO l=1,n-1
          kdeexe(n,l,iz) = kdeexe(n,l,iz) +
&
fe(iEe,iz)*Sdeexe(Ee(iEe),n,l,Eexc(n), &
Eexc(l),aAf(l,n),aP(l,n),g(n),g(l),g0(n))
      END DO
      END DO
      END DO
      END DO

! Thermalized atoms (E=0.06 eV -> v=5.36e4 cm/s) (k: perp
pop=1, in s-1)
DO n=1,Ntot
  DO iz=0,Nz
    kionth(n,iz) = Sionth(n,Eion(n))*vth*xn0(iz)
    rrecth(n,iz) = Sreci(Eth,n,Eion(n),g(n),gi(n))* &
      vth*xn0(iz)*nes(iz)*fac(n)*ni(iz)
    DO m=n+1,Ntot
      kexcth(n,m,iz) =
Sexcth(n,m,Eexc(n),Eexc(m),gi(n),gi(m))* &
      vth*xn0(iz)
    END DO
    DO l=1,n-1
      kdeexth(n,l,iz) =
Sdeexth(n,l,Eexc(n),Eexc(l),g(n),g(l), &
      gi(n),gi(l),g0(n))*vth*xn0(iz)
    END DO
  END DO
END DO

! Calculation of the escape factors
DO n=2,Ntot
  DO iz=0,Nz
    IF (A(1,n).NE.0.0) THEN
      xkR = 2.1d-
17/(Eexc(n)**3)*g(n)/(xtgas**0.5)*A(1,n)*xn0(iz)*xrad

```

```

      xa = A(1,n)*(1+3.225d-
14/(Eexc(n)**3)*g(n)*xn0(iz))* &
      4.839d-9/Eexc(n)/(xtgas**0.5)
      Td = 1/(xkR*(pi*LOG(xkR))**0.5)
      Tc = (xa/(pi**0.5*xkR))**0.5
      Tcd = 2*xa/(pi*(LOG(xkR))**0.5)
      Esc(n,iz) = 1.9*Td*EXP(-pi*Tcd**2/(4.0*Tc**2)) + &
      1.3*Tc*DERF(pi**0.5*Tcd/(2.0*Tc))
      ELSE
      Esc(n,iz) = 1.0d0
      END IF
    END DO
  END DO
DO iz=0,Nz
  WRITE(24,'(65(e10.5,1x))') (Esc(n,iz),n=1,Ntot)
END DO
!
=====
=====
! Calculation of the level populations

! Initial values: all populations=0, pop(ground; n=1)=xngas
DO iz=0,Nz
  pop(1,iz) = xn0(iz)
  DO n=2,Ntot
    pop(n,iz) = 0.0d0
  END DO
END DO

! ct terms (indep. of time) for all levels: loss by:
DO n=2,Ntot
  DO iz=1,Nz-1
    Kloss(n,iz) = 0.0d0
    ! * electron, ion, fast atom, therm.atom excitation to
higher levels
    DO m=n+1,Ntot
      Kloss(n,iz) = Kloss(n,iz) + kexce(n,m,iz) +
kexci(n,m,iz) + &
      kexca(n,m,iz) + kexcth(n,m,iz)
    END DO
    ! * elec,ion,fast atom, therm.atom deexcit,
radiat.decay to lower
! levels (includes escape factors to level 1)
    DO l=1,n-1
      IF (l.EQ.1) THEN
        Arad = A(1,n)*Esc(n,iz)
      ELSE
        Arad = A(1,n)
      END IF
      Kloss(n,iz) = Kloss(n,iz) + kdeexe(n,l,iz) +
kdeexi(n,l,iz) + &

```



```

                                kdeexa(n,l,iz) + kdeexth(n,l,iz) +
Arad
                                END DO
                                ! * electron, ion, fast atom, therm.atom ionization
                                Kloss(n,iz) = Kloss(n,iz) + kione(n,iz) + kioni(n,iz)
+ &
                                kiona(n,iz) + kionth(n,iz)
                                END DO
END DO

! ct. terms (indep.of time) for metast: 2,4
DO n=2,4,2
  DO iz=1,Nz-1
    Kloss(n,iz) = Kloss(n,iz) + nm(iz)*xkpi +
xn0(iz)*k2b(n) + &
                                xn0(iz)**2*k3b(n)
    ai(n,iz) = -D(n)/(dzz(iz)*dz(iz-1))
    ci(n,iz) = -D(n)/(dzz(iz)*dz(iz))
    bbi(n,iz) = 1/dt + D(n)/dzz(iz)*(1/dz(iz) + 1/dz(iz-
1)) + &
                                Kloss(n,iz)
                                END DO
  END DO
  !
=====
=====
! Each timestep (pop(1->n-1) known at t, pop(n+1->Ntot) known
at t-1)
t = 0.0
DO it=1,nt
  t = t + dt
  ! Old values
  DO n=2,Ntot
    DO iz=0,Nz
      popold(n,iz) = pop(n,iz)
    END DO
  END DO

  ! Each level

  ! Metastable levels: 2,4
  DO n=2,4,2
    DO iz=1,Nz-1
      ! Additional loss (met-met coll; incorpor.in bi)
      IF (n.EQ.2) THEN
        pop2 = pop(n+2,iz)
      END IF
      IF (n.EQ.4) THEN
        pop2 = pop(n-2,iz)
      END IF
      bi = bbi(n,iz) + 2*xkmet*pop(n,iz) + xkmet*pop2
      prod = 0.0d0
    END DO
  END DO

```

```

! Prod: excitation from lower levels
DO l=1,n-1
    prod = prod + (kexce(l,n,iz) + kexci(l,n,iz) +
&
    kexca(l,n,iz) +
kexcth(l,n,iz))*pop(l,iz)
END DO
! Prod: deexcitation + rad.decay from higher levels
DO m=n+1,Ntot
    prod = prod + (kdeexe(m,n,iz) + kdeexi(m,n,iz)
+
&
    kdeexa(m,n,iz) + kdeexth(m,n,iz) +
A(n,m))*pop(m,iz)
END DO
! Prod: Recombination -> total prod
prod = prod + rrecl(n,iz) + rrec2e(n,iz) +
rreci(n,iz) + &
    rreca(n,iz) + rrecth(n,iz)
di = popold(n,iz)/dt + prod

! Thomas algorithm
IF (iz.EQ.1) THEN
    bbeta(iz) = bi
    ggamma(iz) = di
ELSE
    bbeta(iz) = bi - ai(n,iz)*ci(n,iz-1)/bbeta(iz-
1)
    ggamma(iz) = di - ai(n,iz)*ggamma(iz-
1)/bbeta(iz-1)
END IF
END DO
pop(n,Nz-1) = ggamma(Nz-1)/bbeta(Nz-1)
DO iz=Nz-2,1,-1
    pop(n,iz) = (ggamma(iz) -
ci(n,iz)*pop(n,iz+1))/bbeta(iz)
END DO
END DO

! Other levels
DO n=3,Ntot
    IF (n.EQ.4) THEN
n=4'
        !WRITE(*,*) '** Original code exits at Energy level
        !WRITE(*,*) '** Exiting loop at Energy level n=',n
        !EXIT
    ELSE
        DO iz=1,Nz-1
            ! Production: sum over all levels
            prod = 0.0d0
            ! Prod: Excitation from lower levels
            DO l=1,n-1

```

```

                                prod = prod + (kexce(l,n,iz) +
kexci(l,n,iz) + &
                                kexca(l,n,iz) +
kexcth(l,n,iz))*pop(l,iz)
                                END DO
                                ! Prod: Deexcitation + rad.decay from higher
levels
                                DO m=n+1,Ntot
                                prod = prod + (kdeexe(m,n,iz) +
kdeexi(m,n,iz) + &
                                kdeexa(m,n,iz) + kdeexth(m,n,iz) +
&
                                A(n,m))*pop(m,iz)
                                END DO
                                ! Prod: Recomb -> total prod
                                prod = prod + rrecln(n,iz) + rrec2e(n,iz) + &
                                rreci(n,iz) + rreca(n,iz) +
rrecth(n,iz)
                                pop(n,iz) = (pop(n,iz) + dt*prod)/(1 +
Kloss(n,iz)*dt)
                                END DO
                                END IF
                                END DO

                                ! New timestep: Calculate deviation
                                xmaxdev = 0.0d0
                                DO n=2,Ntot
                                DO iz=1,Nz-1
                                IF ((pop(n,iz).NE.0.0).OR.(popold(n,iz).NE.0.0))
THEN
                                dev = ABS(pop(n,iz) - popold(n,iz))* &
                                2/(pop(n,iz)+popold(n,iz))
                                END IF
                                xmaxdev = max(xmaxdev,dev)
                                END DO
                                END DO
                                IF (MOD(it,mult)==0.0) THEN
                                WRITE(*,*) it
                                END IF
                                IF (xmaxdev.LT.devlm) THEN
                                EXIT ! exits the outer time do-loop
                                END IF

                                END DO ! end of time loop
                                WRITE(*,*) 't:', t
                                WRITE(*,*) 'xmaxdev:', xmaxdev
                                !
=====
=====
                                ! Output

                                ! Level populations

```

```

DO n=1,Ntot
    n2(n) = n
END DO
WRITE(14, '(f7.5,65(1x,i9))') z(0), (n2(n),n=1,Ntot)
DO iz=0,Nz
    WRITE(14, '(f10.5,65(1x,e10.5))') r(iz),
(pop(n,iz),n=1,Ntot)
END DO
WRITE(88,REC=1) pop(1:Ntot,0:Nz)
WRITE(77,REC=1) r(0:Nz)

CLOSE(14)
CLOSE(15)
CLOSE(16)
CLOSE(17)
CLOSE(18)
CLOSE(22)
CLOSE(23)
CLOSE(24)
CLOSE(77)
CLOSE(88)
CLOSE(99)

```

STOP

```

!\
!           |           Original           stop           in           code
=====
!/>

```

```

! Contributions of production, loss processes
WRITE(15,*) 'n: prod: recle, rec2e, reci, reca, recth'
WRITE(15,*) 'e: exc(from l), deexc(from m)'
WRITE(15,*) 'i: exc(from l), deexc(from m)'
WRITE(15,*) 'a: exc(from l), deexc(from m)'
WRITE(15,*) 'th: exc(from l), deexc(from m)'
WRITE(15,*) 'rad.decay (from m)'
WRITE(15,*) 'n: loss: ione,ioni,iona,ionth'
WRITE(15,*) 'e: exc(to m), deexc(to l)'
WRITE(15,*) 'i: exc(to m), deexc(to l)'
WRITE(15,*) 'a: exc(to m), deexc(to l)'
WRITE(15,*) 'th: exc(to m), deexc(to l)'
WRITE(15,*) 'rad.decay (to l)'
WRITE(15,*) 'for metast: pi,2b,3b,met-met (with same, other)'

```

! Calculate contributions

```

DO n=2,Ntot
    trecle = 0.0d0
    trec2e = 0.0d0
    treci = 0.0d0
    treca = 0.0d0
    trecth = 0.0d0
    tione = 0.0d0

```

```

tioni = 0.0d0
tiona = 0.0d0
tionth = 0.0d0
tpi = 0.0d0
t2b = 0.0d0
t3b = 0.0d0
tmet1 = 0.0d0
tmet2 = 0.0d0
DO m=1,Ntot
  texce(m) = 0.0d0
  texci(m) = 0.0d0
  texca(m) = 0.0d0
  texcth(m) = 0.0d0
  tdeexe(m) = 0.0d0
  tdeexi(m) = 0.0d0
  tdeexa(m) = 0.0d0
  tdeexth(m) = 0.0d0
  trad(m) = 0.0d0
END DO
! Sum over all positions
DO iz=1,Nz-1
  ! Recomb(prod), ioniz(loss)
  trecle = trecle + rrecle(n,iz)*dzz(iz)
  trec2e = trec2e + rrec2e(n,iz)*dzz(iz)
  treci = treci + rreci(n,iz)*dzz(iz)
  treca = treca + rreca(n,iz)*dzz(iz)
  trecth = trecth + rrecth(n,iz)*dzz(iz)
  tione = tione + kione(n,iz)*dzz(iz)*pop(n,iz)
  tioni = tioni + kioni(n,iz)*dzz(iz)*pop(n,iz)
  tiona = tiona + kiona(n,iz)*dzz(iz)*pop(n,iz)
  tionth = tionth + kionth(n,iz)*dzz(iz)*pop(n,iz)

  ! For metastables: pi,2b,3b,met-met: additional loss
  IF ((n.EQ.2).OR.(n.EQ.4)) THEN
    tpi = tpi + xkpi*nm(iz)*pop(n,iz)*dzz(iz)
    t2b = t2b + k2b(n)*xn0(iz)*pop(n,iz)*dzz(iz)
    t3b = t3b + k3b(n)*xn0(iz)**2*pop(n,iz)*dzz(iz)
    IF (n.EQ.2) THEN
      pop2 = pop(n+2,iz)
    END IF
    IF (n.EQ.4) THEN
      pop2 = pop(n-2,iz)
    END IF
    tmet1 = tmet1 + 2*xkmet*pop(n,iz)**2*dzz(iz)
    tmet2 = tmet2 + xkmet*pop2*pop(n,iz)*dzz(iz)
  END IF

  ! from/to higher: excit(loss), deexcit+rad(prod)
  DO m=n+1,Ntot
    texce(m) = texce(m) +
kexce(n,m,iz)*dzz(iz)*pop(n,iz)

```

```

          texci(m)           =          texci(m)           +
kexci(n,m,iz)*dzz(iz)*pop(n,iz)
          texca(m)           =          texca(m)           +
kexca(n,m,iz)*dzz(iz)*pop(n,iz)
          texcth(m)          =          texcth(m)          +
kexcth(n,m,iz)*dzz(iz)*pop(n,iz)
          ! Note the switch from n->m in 'pop' (from
original)
          tdeexe(m)          =          tdeexe(m)          +
kdeexe(m,n,iz)*dzz(iz)*pop(m,iz)
          tdeexi(m)          =          tdeexi(m)          +
kdeexi(m,n,iz)*dzz(iz)*pop(m,iz)
          tdeexa(m)          =          tdeexa(m)          +
kdeexa(m,n,iz)*dzz(iz)*pop(m,iz)
          tdeexth(m)         =          tdeexth(m)         +
kdeexth(m,n,iz)*dzz(iz)*pop(m,iz)
          trad(m) = trad(m) + A(n,m)*dzz(iz)*pop(m,iz)
          END DO
          ! from/to lower: excit(prod), deexcit+rad(loss)
          DO l=1,n-1
          tdeexe(l)          =          tdeexe(l)          +
kdeexe(n,l,iz)*dzz(iz)*pop(n,iz)
          tdeexi(l)          =          tdeexi(l)          +
kdeexi(n,l,iz)*dzz(iz)*pop(n,iz)
          tdeexa(l)          =          tdeexa(l)          +
kdeexa(n,l,iz)*dzz(iz)*pop(n,iz)
          tdeexth(l)         =          tdeexth(l)         +
kdeexth(n,l,iz)*dzz(iz)*pop(n,iz)
          IF (l.EQ.1) THEN
              Arad = A(l,n)*Esc(n,iz)
          ELSE
              Arad = A(l,n)
          END IF
          trad(l) = trad(l) + Arad*dzz(iz)*pop(n,iz)
          texce(l)           =          texce(l)           +
kexce(l,n,iz)*dzz(iz)*pop(l,iz)
          texci(l)           =          texci(l)           +
kexci(l,n,iz)*dzz(iz)*pop(l,iz)
          texca(l)           =          texca(l)           +
kexca(l,n,iz)*dzz(iz)*pop(l,iz)
          texcth(l)          =          texcth(l)          +
kexcth(l,n,iz)*dzz(iz)*pop(l,iz)
          END DO
          END DO

          ! Sum over all processes
          tprod = trecle + trec2e + treci + treca + trecth
          tloss = tione + tioni + tiona + tionth
          IF ((n.EQ.2).OR.(n.EQ.4)) THEN
              tloss = tloss + tpi + t2b + t3b + tmet1 + tmet2
          END IF
          DO m=n+1,Ntot

```

```

        tprod = tprod + tdeexe(m) + tdeexi(m) + tdeexa(m) + &
                tdeexth(m) + trad(m)
        tloss = tloss + texce(m) + texci(m) + texca(m) +
texcth(m)
    END DO
    DO l=1,n-1
        tprod = tprod + texce(l) + texci(l) + texca(l) +
texcth(l)
        tloss = tloss + tdeexe(l) + tdeexi(l) + tdeexa(l) + &
                tdeexth(l) + trad(l)
    END DO

! Calculation of contributions for each process
IF (tprod.NE.0) THEN
    trecle = trecle/tprod*100
    trec2e = trec2e/tprod*100
    treci = treci/tprod*100
    treca = treca/tprod*100
    trecth = trecth/tprod*100
    tione = tione/tloss*100
    tioni = tioni/tloss*100
    tiona = tiona/tloss*100
    tionth = tionth/tloss*100
    IF ((n.EQ.2).OR.(n.EQ.4)) THEN
        tpi = tpi/tloss*100
        t2b = t2b/tloss*100
        t3b = t3b/tloss*100
        tmet1 = tmet1/tloss*100
        tmet2 = tmet2/tloss*100
    END IF
    DO m=n+1,Ntot
        tdeexe(m) = tdeexe(m)/tprod*100
        tdeexi(m) = tdeexi(m)/tprod*100
        tdeexa(m) = tdeexa(m)/tprod*100
        tdeexth(m) = tdeexth(m)/tprod*100
        trad(m) = trad(m)/tprod*100
        texce(m) = texce(m)/tloss*100
        texci(m) = texci(m)/tloss*100
        texca(m) = texca(m)/tloss*100
        texcth(m) = texcth(m)/tloss*100
    END DO
    DO l=1,n-1
        texce(l) = texce(l)/tprod*100
        texci(l) = texci(l)/tprod*100
        texca(l) = texca(l)/tprod*100
        texcth(l) = texcth(l)/tprod*100
        tdeexe(l) = tdeexe(l)/tloss*100
        tdeexi(l) = tdeexi(l)/tloss*100
        tdeexa(l) = tdeexa(l)/tloss*100
        tdeexth(l) = tdeexth(l)/tloss*100
        trad(l) = trad(l)/tloss*100
    END DO

```

```

! Final output: contributions in %
WRITE(15,*) 'n', n
WRITE(15,*) 'prod'
WRITE(15,*) trecle, trec2e, treci, treca, trecth
WRITE(15,*)
WRITE(15, '(64(2x,e9.3))') (texce(1),l=1,n-
1), (tdeexe(m),m=n+1,Ntot)
WRITE(15,*)
WRITE(15, '(64(2x,e9.3))') (texci(1),l=1,n-
1), (tdeexi(m),m=n+1,Ntot)
WRITE(15,*)
WRITE(15, '(64(2x,e9.3))') (texca(1),l=1,n-
1), (tdeexa(m),m=n+1,Ntot)
WRITE(15,*)
WRITE(15, '(64(2x,e9.3))') (texcth(1),l=1,n-
1), (tdeexth(m),m=n+1,Ntot)
WRITE(15,*)
WRITE(15,*) (trad(m),m=n+1,Ntot)
WRITE(15,*)
WRITE(15,*) 'loss'
WRITE(15,*) tione, tioni, tiona, tionth
WRITE(15,*)
WRITE(15, '(64(2x,e9.3))')
(texce(m),m=n+1,Ntot), (tdeexe(1),l=1,n-1)
WRITE(15,*)
WRITE(15, '(64(2x,e9.3))')
(texci(m),m=n+1,Ntot), (tdeexi(1),l=1,n-1)
WRITE(15,*)
WRITE(15, '(64(2x,e9.3))')
(texca(m),m=n+1,Ntot), (tdeexa(1),l=1,n-1)
WRITE(15,*)
WRITE(15, '(64(2x,e9.3))')
(texcth(m),m=n+1,Ntot), (tdeexth(1),l=1,n-1)
WRITE(15,*)
WRITE(15,*) (trad(1),l=1,n-1)
IF ((n.EQ.2).OR.(n.EQ.4)) THEN
WRITE(15,*) 'metast'
WRITE(15,*) tpi, t2b, t3b, tmet1, tmet2
END IF
WRITE(15,*)
END IF
END DO ! end of contributions calculation

STOP ! Original code has a STOP here

! Calculation of relative roles of electron, ion, atom
collisions

!=====
=====
! Electrons

```



```

DO iz=0,Nz
  WRITE(*,*) 'elec', iz
  rtot(iz) = 0.0d0
  rtot2(iz) = 0.0d0
  DO iEe=0,NE
    ftote(iz) = ftote(iz) + fe(iEe,iz)
    relae(iz) = relae(iz) +
fe(iEe,iz)*Selae(Ee(iEe))*xn0(iz)
    ree(iz) = ree(iz) +
fe(iEe,iz)*See(Ee(iEe),Ebulk)*nes(iz)
    rione(iz) = rione(iz) +
fe(iEe,iz)*Sione(Ee(iEe),1,Eion(1))*xn0(iz)
    telae = telae +
fe(iEe,iz)*Selae(Ee(iEe))*xn0(iz)*dz(iz)
    tee = tee +
fe(iEe,iz)*See(Ee(iEe),Ebulk)*nes(iz)*dz(iz)
    rtot(iz) = rtot(iz) +
fe(iEe,iz)*(Selae(Ee(iEe))*xn0(iz) + &
See(Ee(iEe),Ebulk)*nes(iz))
    DO n=1,Ntot
      IF (n.EQ.1) THEN
        pop(n,iz) = xn0(iz)
      END IF
      rtot2(iz) = rtot2(iz) +
&
fe(iEe,iz)*(Sione(Ee(iEe),n,Eion(n))*pop(n,iz) + &
Srec1e(Ee(iEe),n,Eion(n),gam(n),g(n),gi(n))*
fac(n)*ni(iz) +
Srec2e(Ee(iEe),n,Eion(n),g(n),
&
gi(n))*nes(iz)*fac(n)*ni(iz))
    ttione(n) = ttione(n) +
fe(iEe,iz)*Sione(Ee(iEe),n,Eion(n))* &
pop(n,iz)*dz(iz)
    ttrec1e(n) = ttrec1e(n) +
fe(iEe,iz)*Srec1e(Ee(iEe),n,
&
Eion(n),gam(n),g(n),gi(n))*fac(n)*ni(iz)*dz(iz)
    ttrec2e(n) = ttrec2e(n) +
fe(iEe,iz)*Srec2e(Ee(iEe),n,
&
Eion(n),g(n),gi(n))*nes(iz)*fac(n)*ni(iz)*dz(iz)
    !WRITE(*,*) iz, n, rtot2(iz)
    DO m=n+1,Ntot
      rtot2(iz) = rtot2(iz) +
fe(iEe,iz)*Sexce(Ee(iEe),n,m,
&
Eexc(n),Eexc(m),aAf(n,m),aP(n,m),g(n),g(m)) &
*pop(n,iz)
    ttexce(n,m) = ttexce(n,m) +
fe(iEe,iz)*Sexce(Ee(iEe),
&

```

```

n,m,Eexc(n),Eexc(m),aAf(n,m),aP(n,m),      &
      g(n),g(m))*pop(n,iz)*dz(iz)
      !WRITE(*,*) iz, n, m, rtot2(iz)
      END DO
      DO l=1,n-1
        rtot2(iz) = rtot2(iz) +
fe(iEe,iz)*Sdeexe(Ee(iEe),n,l, &
Eexc(n),Eexc(l),aAf(l,n),aP(l,n),g(n),g(l), &
      g0(n))*pop(n,iz)
      ttdeexe(n,l) = ttdeexe(n,l) +
fe(iEe,iz)*Sdeexe(Ee(iEe), &
n,l,Eexc(n),Eexc(l),aAf(l,n),aP(l,n), &
g(n),g(l),g0(n))*pop(n,iz)*dz(iz)
      !WRITE(*,*) iz, n, m, l, rtot2(iz)
      END DO
      END DO
      ! Original STOP here
      END DO

      !WRITE(*,*) iz, rtot(iz), rtot2(iz)
      rtot(iz) = rtot(iz) + rtot2(iz)
      !WRITE(16,'(f7.5,10(1x,e9.3))') z(iz), rtot(iz),
relae(iz), ree(iz), &
      ! rione(iz), ftote(iz),
&
      ! rtot(iz)/ftote(iz),
&
      ! relae(iz)/ftote(iz),
&
      ! ree(iz)/ftote(iz),
rione(iz)/ftote(iz)
      END DO

      tote = telae + tee
      tote2 = 0.0d0
      DO n=1,Ntot
        tote2 = tote2 + ttione(n) + ttrecl1e(n) + ttrecl2e(n)
        DO m=n+1,Ntot
          tote2 = tote2 + ttexce(n,m)
        END DO
        DO l=1,n-1
          tote2 = tote2 + ttdeexe(n,l)
        END DO
      END DO
      !WRITE(*,*) 'tote, tote2', tote, tote2
      tote = tote + tote2

      ! Write % contrib.of each collsion

```



```

IMPLICIT NONE
INTEGER, INTENT(IN) :: n
DOUBLE PRECISION, INTENT(IN) :: E
DOUBLE PRECISION, INTENT(IN) :: Eion
DOUBLE PRECISION :: a, b, EE

Sione = 0.0d0
IF (E.GE.Eion) THEN
  IF (n.EQ.1) THEN
    a = (E-Eion)/2.0d0
    EE = 1.2d0 - 250.0d0/(E+2.0d0*Eion)
    Sione = 1.0d-16*23.9d0/E*LOG((E+150d0/E)/Eion)*4.6d0*
&
    (ATAN((a-EE)/4.6d0) - ATAN(-EE/4.6d0))
  ELSE
    IF ((n.GE.2).AND.(n.LE.5)) THEN
      a = 0.35d0
    ELSEIF (n.EQ.6) THEN
      a = 0.45d0
    ELSEIF ((n.GE.7).AND.(n.LE.9)) THEN
      a = 0.39d0
    ELSEIF ((n.GE.10).AND.(n.LE.11)) THEN
      a = 0.32d0
    ELSE
      a = 0.67d0
    END IF
    IF ((n.GE.2).AND.(n.LE.11)) THEN
      b = 4.0d0
    ELSE
      b = 1.0d0
    END IF
    Sione = 6.783d-14/Eion**2*a*(Eion/E)**2*      &
    (E/Eion-1.0d0)*LOG(1.25d0*b*E/Eion)
  END IF
END IF

RETURN
!
END FUNCTION Sione
!-----
-----
DOUBLE PRECISION FUNCTION SreclE(E,n,Eion,gam,gn,gin)
! Radiative recombination (from photoionization; inverse process)
IMPLICIT NONE
INTEGER, INTENT(IN) :: n
DOUBLE PRECISION, INTENT(IN) :: E
DOUBLE PRECISION, INTENT(IN) :: Eion
DOUBLE PRECISION, INTENT(IN) :: gam
DOUBLE PRECISION, INTENT(IN) :: gn
DOUBLE PRECISION, INTENT(IN) :: gin
DOUBLE PRECISION :: Elh
PARAMETER(Elh = 13.884d0)

```

```

DOUBLE PRECISION :: hv, Sp

Srec1e = 0.0d0
hv = E + Eion
IF (E.GT.0.0) THEN
  IF (n.EQ.1) THEN
    IF ((hv.GE.Eion).AND.(hv.LE.(2*E1h))) THEN
      Sp = 3.5d-17
    END IF
    IF (hv.GT.(2*E1h)) THEN
      Sp = 2.8d-16*(E1h/hv)**3
    END IF
  ELSEIF ((n.GE.2).AND.(n.LE.5)) THEN
    IF ((hv.GE.Eion).AND.(hv.LE.(0.59*E1h))) THEN
      Sp = 2d-18*gam
    END IF
    IF (hv.GT.(0.59*E1h)) THEN
      Sp = 7.91d-18*gam*(Eion/E1h)**2.5*(E1h/hv)**3
    END IF
  ELSE
    IF (hv.GT.Eion) THEN
      Sp = gam*7.91d-18*(Eion/E1h)**2.5*(E1h/hv)**3
    END IF
  END IF
  Srec1e = gn/(2*gin*5.1173d5)*hv**2/E*Sp
END IF

RETURN
!
END FUNCTION Srec1e
!-----
-----
DOUBLE PRECISION FUNCTION Srec2e(E,n,Eion,gn,gin)
! Electron 3b recombination (from ionization; inverse process)
! Srec2ne = sigma/n_e
! 3/2 kT = mean energy of all electrons, assume: Ee=10 eV
! fac32 = (h**2/(2pi*M_e))**3/2 : in eV**3/2 (cfr kT) cm**3 (cfr
n_e)
  USE array, ONLY: Emeane
  IMPLICIT NONE
  INTEGER, INTENT(IN) :: n
  DOUBLE PRECISION, INTENT(IN) :: E
  DOUBLE PRECISION, INTENT(IN) :: Eion
  DOUBLE PRECISION, INTENT(IN) :: gn
  DOUBLE PRECISION, INTENT(IN) :: gin
  DOUBLE PRECISION :: fac32
  PARAMETER(fac32 = 3.313d-22)
  DOUBLE PRECISION :: xkT, fac32b, E2

  Srec2e = 0.0d0
  IF (E.GT.0.0) THEN
    xkT = 2.0d0*Emeane/3.0d0

```

```

        fac32b = fac32/xkT**1.5
        E2 = E + Eion
        Srec2e = gn/(2*gin)*fac32b*E2/E*Siene(E2,n,Eion)
END IF

RETURN

!
END FUNCTION Srec2e
!-----
-----
DOUBLE PRECISION FUNCTION Sexce(E,n,m,Eexcn,Eexcm,aAf,aP,gn,gm)
! Excitation of different Ar* levels to different Ar* levels (from
Vlcek)
    IMPLICIT NONE
    INTEGER, INTENT(IN) :: n
    INTEGER, INTENT(IN) :: m
    DOUBLE PRECISION, INTENT(IN) :: E
    DOUBLE PRECISION, INTENT(IN) :: Eexcn
    DOUBLE PRECISION, INTENT(IN) :: Eexcm
    DOUBLE PRECISION, INTENT(IN) :: aAf
    DOUBLE PRECISION, INTENT(IN) :: aP
    DOUBLE PRECISION, INTENT(IN) :: gn
    DOUBLE PRECISION, INTENT(IN) :: gm
    DOUBLE PRECISION :: Emn, Q, b, SexcA, SexcF

    Emn = Eexcm - Eexcn
    Sexce = 0.0d0
    IF (E.GE.Emn) THEN
        IF ((n.GE.2).AND.(n.LE.3).AND.(m.GE.3).AND.(m.LE.5)) THEN
            IF ((n.EQ.2).AND.(m.EQ.3)) THEN
                Q = 1.0d0
            END IF
            IF ((m.EQ.4).OR.(m.EQ.5)) THEN
                Q = 0.1d0
            END IF
            Sexce = gm/gn*(E-Emn)/E*5.797d-15*Q*(E-Emn)**(-0.54)
        ELSEIF ((n.EQ.4).AND.(m.EQ.5)) THEN
            Sexce = gm/gn*(E-Emn)/E*8.111d-16*(E-Emn)**(-1.04)
        ELSEIF ((aAf.EQ.0.0).AND.(aP.EQ.0.0)) THEN
            Sexce = 0.0d0
        ELSE
            IF (n.GE.1) THEN
                b = 1.0d0
            END IF
            IF ((n.EQ.1).AND.
                ((m.EQ.3).OR.(m.EQ.5).OR.(m.EQ.15).OR.(m.EQ.16))) &
THEN
                b = 4.0d0
            END IF
            IF ((n.EQ.1).AND.(m.EQ.17)) THEN
                b = 2.0d0
            END IF

```

```

      IF ((n.EQ.1).AND.
          ( (m.EQ.20).OR.(m.EQ.21).OR.(m.EQ.26).OR. &
            (m.EQ.27).OR.(m.EQ.33))) THEN
          b = 1.0d0
      END IF
      SexcA = 6.783d-14/Emn**2*aAf*(Emn/E)**2*(E/Emn-
1)*LOG(1.25*b*E/Emn)
      SexcF = 3.519d-16*aP*(Emn/E)*(1-(Emn/E))
      IF ((n.EQ.1).AND.
          ((m.EQ.2).OR.(m.EQ.4).OR.(m.EQ.12).OR.(m.EQ.13))) &
      THEN
          SexcF = 3.519d-16*aP*(Emn/E)**3*(1-(Emn/E)**2)
      END IF
      Sexce = SexcA + SexcF
    END IF
  END IF

  RETURN
!
END FUNCTION Sexce
!-----
-----
DOUBLE PRECISION FUNCTION
Sdeexe(E,m,n,Eexcm,Eexcn,aAf,aP,gm,gn,g0m)
! Superelastic (deexcitation) collisions from Ar*(m) to Ar*(n):
from excit
! (detailed balancing)
  IMPLICIT NONE
  INTEGER, INTENT(IN) :: m
  INTEGER, INTENT(IN) :: n
  DOUBLE PRECISION, INTENT(IN) :: E
  DOUBLE PRECISION, INTENT(IN) :: Eexcm
  DOUBLE PRECISION, INTENT(IN) :: Eexcn
  DOUBLE PRECISION, INTENT(IN) :: aAf
  DOUBLE PRECISION, INTENT(IN) :: aP
  DOUBLE PRECISION, INTENT(IN) :: gm
  DOUBLE PRECISION, INTENT(IN) :: gn
  DOUBLE PRECISION, INTENT(IN) :: g0m
  DOUBLE PRECISION :: Emn

  Sdeexe = 0.0d0
  IF (E.GT.0.0) THEN
    Emn = Eexcm - Eexcn
    IF (n.EQ.1) THEN
      ! gn = g0m; orig. mixes the intent of gn (DMF)
      Sdeexe =
g0m/gm*(E+Emn)/E*Sexce(E+Emn,n,m,Eexcn,Eexcm,aAf,aP,g0m,gm)
    ELSE
      Sdeexe =
gn/gm*(E+Emn)/E*Sexce(E+Emn,n,m,Eexcn,Eexcm,aAf,aP,gn,gm)
    END IF
  END IF
END IF

```

```

        RETURN
    !
END FUNCTION Sdeexe
!-----
-----
DOUBLE PRECISION FUNCTION Sionth(n,Eion)
! Thermalized Ar atoms: Tg=500 K -> E=3/2kTg=0.06 eV (changed to
usr input; DMF)
    USE array, ONLY: Eth
    IMPLICIT NONE
    INTEGER, INTENT(IN) :: n
    DOUBLE PRECISION, INTENT(IN) :: Eion
    DOUBLE PRECISION :: bn

    Sionth = 0.0d0
    IF (Eth.GT.Eion) THEN
        bn = 8.69d-18*Eion**(-2.26)
        Sionth = bn*(Eth-Eion)
    END IF

    RETURN
!
END FUNCTION Sionth
!-----
-----
DOUBLE PRECISION FUNCTION Sreci(E,n,Eion,gn,gin)
! Ion+atom recombination to level n (from ionization: Siona)
! Will not be used in MC; Srec=sigma/ne
    USE array, ONLY: Emeane
    IMPLICIT NONE
    INTEGER, INTENT(IN) :: n
    DOUBLE PRECISION, INTENT(IN) :: E
    DOUBLE PRECISION, INTENT(IN) :: Eion
    DOUBLE PRECISION, INTENT(IN) :: gn
    DOUBLE PRECISION, INTENT(IN) :: gin
    DOUBLE PRECISION :: fac32
    PARAMETER(fac32 = 3.313d-22)
    DOUBLE PRECISION :: xkT, fac32b, E2

    Sreci = 0.0d0
    IF (E.GT.0.0) THEN
        xkT = 2.0d0*Emeane/3.0d0
        fac32b = fac32/xkT**1.5
        E2 = E + Eion
        Sreci = gn/(2*gin)*fac32b*E2/E*Siona(E2,n,Eion)
    END IF

    RETURN
!
END FUNCTION Sreci

```



```

!-----
-----
DOUBLE PRECISION FUNCTION Siona(E,n,Eion)
  IMPLICIT NONE
  INTEGER, INTENT(IN) :: n
  DOUBLE PRECISION, INTENT(IN) :: E
  DOUBLE PRECISION, INTENT(IN) :: Eion
  DOUBLE PRECISION :: xmea, fac

  Siona = 0.0d0
  IF (E.GE.Eion) THEN
    IF (n.EQ.1) THEN
      ! cfr vroeger (fit from data)
      IF (E.LE.75) THEN
        Siona = 10**(-29.175+6.554*LOG10(E))
      ELSEIF ((E.GT.75).AND.(E.LE.100)) THEN
        Siona = 10**(-23.7+3.636*LOG10(E))
      ELSEIF ((E.GT.100).AND.(E.LE.133.4)) THEN
        Siona = 10**(-20.125+1.8468*LOG10(E))
      ELSEIF ((E.GT.133.4).AND.(E.LE.237)) THEN
        Siona = 10**(-18.518+1.0938*LOG10(E))
      ELSEIF ((E.GT.237).AND.(E.LE.1000)) THEN
        Siona = 10**(-16.875+0.4018*LOG10(E))
      ELSE
        Siona = 10**(-16.373+0.2346*LOG10(E))
      END IF
    ELSE
      ! ion+atom ionization from level n (from Vlcek)
      xmea = 2.725d-5
      fac = 7.3258d-17
      Siona = fac/Eion**2*(E/Eion-1)/(1+xmea*(E/Eion-1))**2
    END IF
  END IF

  RETURN
!
END FUNCTION Siona
!-----
-----
DOUBLE PRECISION FUNCTION Sexcth(n,m,Eexcn,Eexcm,gin,gim)
! Thermalized Ar atoms: Tg=450 K -> E=3/2kTg=0.06 eV (usr input;
DMF)
! Includes 2-4,2-5,3-4,3-5 previously excluded by no
intercombination AMK
  USE array, ONLY: Eth
  IMPLICIT NONE
  INTEGER, INTENT(IN) :: n
  INTEGER, INTENT(IN) :: m
  DOUBLE PRECISION, INTENT(IN) :: Eexcn
  DOUBLE PRECISION, INTENT(IN) :: Eexcm
  DOUBLE PRECISION, INTENT(IN) :: gin
  DOUBLE PRECISION, INTENT(IN) :: gim

```

```

DOUBLE PRECISION :: bmn, Emn

Sexcth = 0.0d0
bmn = 0.0d0
Emn = ABS(Eexcm-Eexcن)
IF ((Eth.GT.Emn).AND.(n.LT.m)) THEN
  IF (((n.EQ.2).AND.(m.EQ.4).OR.(m.EQ.5)).OR. &
      ((n.EQ.3).AND.(m.EQ.4).OR.(m.EQ.5))) THEN
    bmn = 4.8d-22*Emn**(-2.26)
  END IF
  IF (gin.EQ.gim) THEN
    IF
      ((n.EQ.2).AND.(m.EQ.3)).OR.((n.EQ.4).AND.(m.EQ.5)) THEN
        bmn = 1.79d-20*Emn**(-2.26)
      ELSEIF (((n.EQ.2).AND.(m.EQ.4).OR.(m.EQ.5)).OR. &
              ((n.EQ.3).AND.(m.EQ.4).OR.(m.EQ.5))) THEN
        bmn = 4.8d-22*Emn**(-2.26)
      ELSE
        bmn = 8.69d-18*Emn**(-2.26)
      END IF
    END IF
    Sexcth = bmn*(Eth-Emn)
  END IF

RETURN

!
END FUNCTION Sexcth
!-----
-----
DOUBLE PRECISION FUNCTION
Sdeexth(m,n,Eexcm,Eexcن,gm,gn,gim,gin,g0m)
! Thermalized Ar atoms: Tg=500 K -> E=3/2kTg=0.06 eV (usr input;
DMF)
! ion+atom deexcitation from level m to level n (from excitation)
! Modified to include 2-4,2-5,3-4,3-5 previously excluded by no
intercomb; AMK
USE array, ONLY: Eth
IMPLICIT NONE
INTEGER, INTENT(IN) :: m
INTEGER, INTENT(IN) :: n
DOUBLE PRECISION, INTENT(IN) :: Eexcm
DOUBLE PRECISION, INTENT(IN) :: Eexcن
DOUBLE PRECISION, INTENT(IN) :: gm
DOUBLE PRECISION, INTENT(IN) :: gn
DOUBLE PRECISION, INTENT(IN) :: gim
DOUBLE PRECISION, INTENT(IN) :: gin
DOUBLE PRECISION, INTENT(IN) :: g0m
DOUBLE PRECISION :: bmn, Emn, Eext, Sext

Sdeexth = 0.0d0
bmn = 0.0d0
Emn = ABS(Eexcm-Eexcن)

```

```

IF ((Eth.Gt.Emn).AND.(n.LT.m)) THEN
  Eext = Eth + Emn
  IF (((n.EQ.2).AND.((m.EQ.4).OR.(m.EQ.5))).OR. &
      ((n.EQ.3).AND.((m.EQ.4).OR.(m.EQ.5)))) THEN
    bmn = 4.8d-22*Emn**(-2.26)
  END IF
  IF (gin.EQ.gim) THEN
    IF
      ((n.EQ.2).AND.(m.EQ.3)).OR.((n.EQ.4).AND.(m.EQ.5)) THEN
        bmn = 1.79d-20*Emn**(-2.26)
      ELSEIF (((n.EQ.2).AND.((m.EQ.4).OR.(m.EQ.5))).OR. &
              ((n.EQ.3).AND.((m.EQ.4).OR.(m.EQ.5)))) THEN
        bmn = 4.8d-22*Emn**(-2.26)
      ELSE
        bmn = 8.69d-18*Emn**(-2.26)
      END IF
    END IF
    Sext = bmn*(Eth-Emn)
    IF (n.EQ.1) THEN
      ! gn = g0m; In the orig. code this mixed the intent of
gn (DMF)
      Sdeexth = g0m/gm*Eth/(Eth-Emn)*Sext
    ELSE
      Sdeexth = gn/gm*Eth/(Eth-Emn)*Sext
    END IF
  END IF

  RETURN
!
END FUNCTION Sdeexth
!-----
-----
DOUBLE PRECISION FUNCTION Selae(E)
! Elastic with Ar0 (from CR6: Bretagne et.al, J.Phys.D, 15, 2205
('82))
! At high energy: idem Vroeger
  IMPLICIT NONE
  DOUBLE PRECISION, INTENT(IN) :: E
  DOUBLE PRECISION :: a1, a2, a3, a4, a5, a6, a7
  PARAMETER(a1 = -18.146)
  PARAMETER(a2 = 201.739)
  PARAMETER(a3 = -595.64)
  PARAMETER(a4 = 832.739)
  PARAMETER(a5 = -611.768)
  PARAMETER(a6 = 230.268)
  PARAMETER(a7 = -35.192)

  Selae = 0.0d0
  IF ((E.GT.0.0).AND.(E.LT.4)) THEN
    Selae = ((E/(E+0.3))**0.5*LOG(E+0.3)*(a1+a2/(E+0.3)**0.5 +
&

```

```

        a3/(E+0.3) + a4/(E+0.3)**1.5 + a5/(E+0.3)**2 +
&
        a6/(E+0.3)**2.5 + a7/(E+0.3)**3) - 1.319*LOG(E) +
&
        0.231)*1d-16
ELSEIF ((E.GE.4).AND.(E.LE.16)) THEN
    Selae = 1.56798d-16 + 5.96811d-17*E + 2.95251d-17*E**2 -
&
        1.98062d-18*E**3 + 2.67756d-20*E**4
ELSEIF ((E.GT.16).AND.(E.LE.100)) THEN
    Selae = 4.65827d-15 - 2.07313d-16*E + 4.50635d-18*E**2 -
&
        4.97379d-20*E**3 + 2.68443d-22*E**4 - 5.61251d-
25*E**5
    ELSE
        Selae = 5.90086d-15*E**(-0.544327)
    END IF

    RETURN
!
END FUNCTION Selae
!-----
-----
DOUBLE PRECISION FUNCTION See(E,Ebulk)
! Electron-electron collisions
    IMPLICIT NONE
    DOUBLE PRECISION, INTENT(IN) :: E
    DOUBLE PRECISION, INTENT(IN) :: Ebulk
    DOUBLE PRECISION :: Erel, b0

    See = 0.0d0
    Erel = ABS(E-Ebulk)
    IF (Erel.GT.0.0) THEN
        b0 = 2.882d-7/Erel
        IF (b0.NE.0.0) THEN
            See = 25.13*b0**2*LOG(0.003/b0)
        END IF
    END IF

    RETURN
!
END FUNCTION See
!-----
-----

!
END PROGRAM main

```